Magnetic Order and Excitation in Frustrated Pyrochlore 5d - Transition Metal Oxides

Von der Fakultät für Mathematik, Informatik und Naturwissenschaften der RWTH Aachen University zur Erlangung des akademischen Grades eines Doktors der Naturwissenschaften genehmigte Dissertation

vorgelegt von

Master of Science
Erxi Feng
aus
Baiyin, China

Berichter: Univ.-Prof. Dr. rer. nat. Thomas Brückel
Univ.-Prof. Dr. rer. nat. Carsten Honerkamp

Tag der mündlichen Prüfung: 28.09.2018

Diese Dissertation ist auf den Internetseiten der Universitätsbibliothek verfügbar.

Abstract

Motivated by the recent experimental realizations of novel magnetic phases and emergent quasiparticles, such as magnetic monopoles and Majorana fermions, in frustrated and topological quantum magnets, this thesis focuses on the studies of the magnetic ground state of a complete series of pyrochlore 5d transition metal oxides, including the $Ln_2Ir_2O_7$ (Ln = rare-earth elements) family and $Nd_2Hf_2O_7$, via in-house specific heat and magnetization measurements as well as advanced neutron scattering techniques. This has allowed us to establish a global phase diagram of the magnetic ground state of $Ln_2Ir_2O_7$. Except for $Pr_2Ir_2O_7$, other pyrochlore iridates exhibit a transition at finite temperature from a paramagnetic metal to an antiferromagnetic semimetal with the "all-in-all-out" magnetic order of the Ir^{4+} sublattice. The magnetic ground-state of Ln^{3+} is strongly dependent on the Ln^{3+} single-ion anisotropy and the molecular magnetic field generated by the surrounding Ir^{4+} sublattice. For the Ln^{3+} ions with an easy-axis anisotropy along the local [1 1 1] axis, which is parallel to the molecular field, an "all-in-all-out" long-range magnetic order is universally observed on the Ln^{3+} sublattice. On the contrary, for the Ln^{3+} ions with an easy-plane anisotropy, a dynamic spin liquid phase persists down to the sub-Kelvin temperature range.

Furthermore, aided by the magnetic structure refinements, sum-rule analysis of the total magnetic moments, quantitative analyses of low-temperature magnetic entropy and simulations of inelastic neutron scattering spectra, a deeper understanding on the exotic magnetic order and emergent quantum excitations in the ground state of two representative 5d pyrochlore compounds, the metallic spin-ice $Pr_2Ir_2O_7$ and insulating quantum spin-ice candidate $Nd_2Hf_2O_7$, have been obtained. $Pr_2Ir_2O_7$ undergoes a magnetic transition from paramagnetic state to the "2-in-2-out" long-range order of Pr^{3+} below 0.76 K, signalized by a slightly dispersive gapped magnetic excitation. $Nd_2Hf_2O_7$ shows an "all-in-all-out" long-range order of Nd^{3+} below 0.53 K. Its magnetic excitation consists of a flat band mode centered at 0.1 meV and a dispersive mode up to 0.23 meV in the ordered state. The XYZ model based on the "dipole-octupole" ground-state doublet is introduced to explain these observations. The Occurrence of exotic quantum fragmentation of magnetic moments in $Nd_2Hf_2O_7$ can thus be confirmed.

Zusammenfassung

In frustrierten und topologischen Quantenmagneten wurden kürzlich neuartige magnetische Phasen und Quasiteilchen, wie magnetische Monopole und Majorana-Fermionen, experimentell nachgewiesen. Um die Forschung auf diesem Gebiet voranzutreiben, konzentriert sich diese Arbeit auf die Untersuchung des magnetischen Grundzustands einer kompletten Serie von 5d Übergangsmetalloxiden, der Pyrochlorphase. Die $Ln_2Ir_2O_7$ (Ln = Elemente der seltenen Erden) Familie und $Nd_2Hf_2O_7$ wurden mithilfe von Wärmekapizitäts- und Magnetisierungsmessungen, sowie Neutronenstreumethoden, systematisch untersucht. Ein globales Phasendiagram des magnetischen Grundzustandes von $Ln_2Ir_2O_7$ konnte somit erstellt werden. Mit der Ausnahme von $Pr_2Ir_2O_7$ zeigen Iridate in der Pyrochlorphase einen Übergang bei endlicher Temperatur von einem paramagnetischem Metall zu einem antiferromagnetischem Halbmetall mit einer „alle-hinein-alle-heraus" magnetischen Struktur des Ir^{4+} Untergitters. Der magnetische Grundzustand der Ln^{3+} Ionen ist stark von der Ln^{3+} Einzelionenanisotropie und des molekularen magnetischen Feldes des umliegenden Ln^{4+} Untergitters abhängig. Ln^{3+} Ionen mit einer leichten Achse in die lokale [1 1 1] Richtung, parallel zum molekularen Feld, nehmen eine magnetisch langreichweitige „alle-hinein-alle-heraus" Ordnung im Ln^{3+} Untergitter an. Im Gegensatz dazu bilden Ln^{3+} Ionen mit Anisotropie in der Ebene eine dynamische Spinflüssigkeitsphase, bis zu Temperaturen unterhalb eines Kelvins. Die Verfeinerung der magnetischen Struktur, Summenregelanalyse des gesamten magnetischen Moments, quantitative Analyse der magnetischen Entropie für tiefe Temperaturen und Simulation der Spektren unelastischer Neutronenstreuexperimente, ermöglichen das Verständnis der exotischen magnetischen Ordnung und der Quantenanregung des Grundzustandes zweier repräsentativer 5d Pyrochlor Materialien, des metallischen Spin-Eis $Pr_2Ir_2O_7$ und des nichtleitenden und möglichen Quanten-Spin-Eises $Nd_2Hf_2O_7$. $Pr_2Ir_2O_7$ zeigt einen magnetischen Phasenübergang von einer paramagnetischen zu einer langreichweitigen „2-hinein-2-hinaus" Ordnung der Pr^{3+} Atome unterhalb von 0,76 K, die durch eine leicht dispersive magnetische Anregung mit Energielücke messbar wird. $Nd_2Hf_2O_7$ zeigt eine langreichweitige „alle-hinein-alle-heraus" Ordnung der Nd^{3+} Ionen unterhalb von 0,53 K. Die magnetischen Anregungen bestehen aus einer flachen Bandmode um 0.1 meV und einer dispersiven Mode bis zu 0.23 meV im geordneten Zustand. Das auf dem Dipol-Oktopol Grundzustandsdoublet basierende XYZ Model wird zu Beschreibung dieser Beobachtungen eingeführt. Die exotische Fragmentierung der magnetischen Momente in $Nd_2Hf_2O_7$ kann somit bestätigt werden.

Contents

Chapter 1. Introduction

The search for novel quantum phenomena such as exotic phases and emergent excitations is one of the main topics of research in condensed matter physics. "More is different", the famous dictum of Philip W. Anderson [1], captures the idea that novel phases may emerge in interacting many-body systems where the collective behavior of many-particles cannot be understood simply based on the properties of a few particles. In the field of strongly correlated electron systems, the greatly pronounced electron-electron interaction in $3d$ transition metal oxides has led to a variety of important discoveries, such as Mott insulators, high-T_c superconductors, multiferroics, heavy fermions, and so on. Recent studies of $5d$ transition metal oxides have shown that the spin-orbit coupling (SOC) plays an important role in the emergence of non-trivial quantum ground states, for example, the novel $J_{eff} = 1/2$ state in Sr_2IrO_4 [2]. Benefitting from the introduction of the concept of topology in the description of the band structure, exotic phases (e.g. topological Mott insulator, Weyl semimetal, etc.) are predicted in $5d$ transition metal oxides [3]. On the other hand, the competing interactions between spins in a lattice, the so-called magnetic frustration, may prevent the conventional magnetic long-range order transition and lead to a disordered ground state. The exotic magnetic phases, such as quantum spin liquid and the emergent gauge-field excitations could be found in frustrated magnets. For instance, the pyrochlore magnet $Ho_2Ti_2O_7$ exhibits a short-range ordered state with a "2-in-2-out" spin configuration in each spin tetrahedron, called spin-ice as analogy of water ice [4], and its thermally excited state is identified as magnetic monopoles [5].

One class of iridium oxides, rare-earth pyrochlore iridates $Ln_2Ir_2O_7$ (Ln is a lanthanide element), sits at the intersection of geometrical frustrated magnetism, strongly correlated electrons system with strong spin-orbit coupling, and band topology. The coexistence and competition of these interactions may result in an incredibly rich number of interesting or novel ground states, which have attracted intensive attention. Although plenty of recent work have discussed the properties of Ir, very few of them have focused on the magnetism of Ln^{3+}. The scope of this dissertation is to systematically determine the magnetic structures and observe the collective magnetic excitations of Ln^{3+} at finite temperature in pyrochlore iridates,

by employing in-house characterization and neutron scattering, as well as in the 5d pyrochlore insulator $Nd_2Hf_2O_7$.

The rest of this thesis consists of the following chapters:

Chapter 2 presents a short introduction of the geometrical frustrated magnetism, an overview of the magnetic properties of pyrochlore compounds and a discussion of SOC and the Ln-Ir interaction in pyrochlore iridates.

Chapter 3 gives detailed explanations of the experimental techniques that have been used in this thesis. It will include details of the sample synthesis, an explanation of x-ray powder diffraction, DC-magnetization, specific heat measurement and a brief overview of neutron scattering techniques.

Chapter 4 focuses on the properties of the $Ln_2Ir_2O_7$ with metal-to-insulator transition. The metal-to-insulator transition is determined according to the DC magnetization of the compounds. A magnetic phase diagram as function of rare-earth atomic radius and temperature will be given based on the polarized neutron scattering experiments.

Chapter 5 is dedicated to the metallic compound $Pr_2Ir_2O_7$. The crystal-field ground state of Pr^{3+} is determined according to the inelastic neutron scattering experiments. By employing the XYZ-polarization analysis of neutron scattering, we solve the magnetic structure of the long-range ordered state. Via cold neutron inelastic scattering, we observe its low-energy magnetic excitation for the first time.

Chapter 6 addresses the 5d pyrochlore compounds $Nd_2Hf_2O_7$. As indicated by the specific heat anomaly for the magnetic phase transition, the magnetic phase below T_N is determined according to the polarized neutron scattering result. Its magnetic excitations are observed by inelastic neutron scattering and explained by the linear spin wave theory based on XYZ model.

Chapter 7 summarizes the major conclusion from the above chapters and discusses the prospect of future studies of these compounds.

Chapter 2. Theoretical Background and Pervious Studies

2.1. Frustrated magnetism

The spin system in magnetic compounds often undergoes a phase transition at finite temperatures, which can be understood using the Landau theory. Below the transition temperature a long-range magnetic order phase is established. Employ the simple Heisenberg Hamiltonian for the exchange interaction of spins:

$$\mathcal{H}_{Heisenberg} = \mathcal{J} \sum_{i,j} \hat{S}_i \cdot \hat{S}_j \tag{2.1.1}$$

where $\mathcal{J}$ is the exchange coupling constant between two spins $\hat{S}_i$ and $\hat{S}_j$. The summation is over all possible bonds in spin pairs. For the simple cases, the spins usually arrange themselves either in parallel ($\mathcal{J} < 0$ implies ferromagnetic interaction), known as ferromagnetic order, or in antiparallel ($\mathcal{J} > 0$ implies antiferromagnetic interaction), known as antiferromagnetic order. However, there are two things that can prevent the occurrence of magnetic long-range order. One is fluctuation, including the thermal fluctuation that is controlled by temperature in the energy scale $\sim k_B T$, and the quantum fluctuation that is determined by Heisenberg's uncertainty principle [6]. Another one is magnetic frustration, which will be discussed below.

2.1.1. Introduction to magnetic frustration

The concept of frustration was first used in the publications on spin glasses by Toulouse and Villain in 1977 [7,8]. However, the studies of frustrated magnetism, e.g. geometrically frustrated antiferromagnets, can be traced back to the investigation of the antiferromagnetically coupled Ising spins on a triangular and spinel lattice in 1950s [9-12].

The term 'frustration' in magnetism means that the local magnetic interactions and the global free energy cannot be minimized simultaneously, subsequently leading to degeneracy in the classical ground state. In a perfect lattice without any site disorder, the nature of magnetic frustration can be classified into two classes: frustration due to the competing interactions of several exchange paths between two magnetic ions, and geometrical

frustration due to the topology of the lattice where the spatial arrangement of the magnetic ions prevents the satisfaction of the magnetic interactions between different spin pairs.
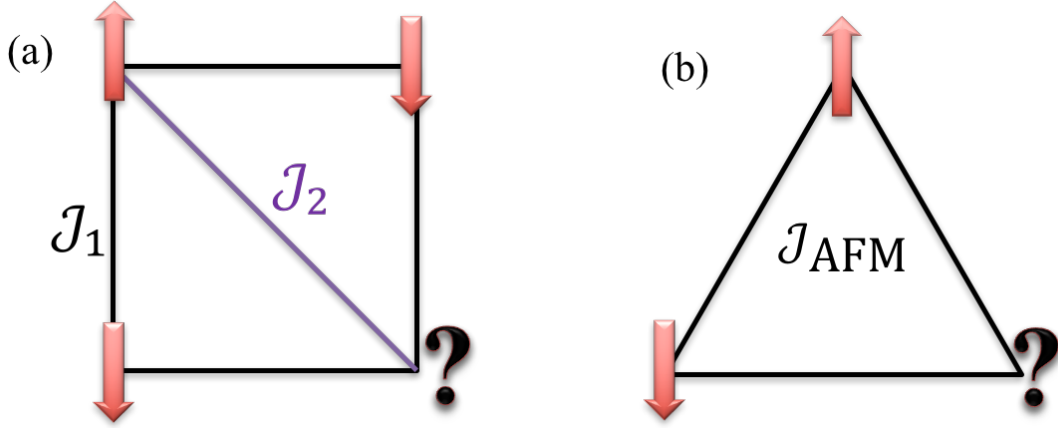
Figure 2.1.1 Examples of the frustrated magnetic systems. (a) Frustration due to the competing antiferromagnetic exchange interactions of the nearest-neighbor coupling $\mathcal{J}_1$ and next-nearest-neighbor coupling $\mathcal{J}_2$ for Ising spins on a square lattice. (b) Geometrical frustration due to the Ising spins with antiferromagnetic interactions in a triangular lattice.

One of the simplest frustration systems due to competing interactions is the $\mathcal{J}_1 - \mathcal{J}_2$ Ising model on a square lattice (Figure 2.1.1 (a)) [13]. (the word 'Ising' indicates the case that the spins are only allowed to point up or down) Besides the nearest-neighbor (NN) antiferromagnetic coupling $\mathcal{J}_1$, the next-nearest-neighbor (NNN) interaction with antiferromagnetic coupling $\mathcal{J}_2$ has to be taken into account:

$$\mathcal{H}_{\mathcal{J}_1 - \mathcal{J}_2} = \mathcal{J}_1 \sum_{NN} \hat{S}_i \cdot \hat{S}_j + \mathcal{J}_2 \sum_{NNN} \hat{S}_i \cdot \hat{S}_j , \quad S_i = \pm 1 \tag{2.1.2}$$

where $\mathcal{J}_i > 0$. If $\mathcal{J}_1$ and $\mathcal{J}_2$ are comparable, the spins cannot satisfy simultaneously the two antiferromagnetic bonds with simply antiparallel arrangement of spins between nearest-neighbor sites. Thus, the ground state of the model depends on the relative strength of the competing interactions $\kappa = \mathcal{J}_2 / \mathcal{J}_1$. Usual Neel state, stripe structure of alternating up and down rows of spins, and novel ground states can be found in the phase diagram [14,15].

The simplest case of geometrical frustration is the equilateral triangle lattice with antiferromagnetic coupled Ising spins located at the corner of the lattice. As shown in Figure 2.1.1(b), when considering only the nearest-neighbor interaction, if one pairwise antiferromagnetic interaction is satisfied with two spins antiparallel, the third spin in the triangular lattice is uncertain since it cannot simultaneously satisfy the two nearest-neighbor antiferromagnetic interactions by pointing either up or down. Obviously, there is no geometrical frustration phenomenon in the one-dimensional spin system, such as spin chain. Among the various lattices leading to geometrical frustration, the most popular two-

dimensional structures are the triangular and the Kagome lattice, in which the common building block is a triangle. The three-dimensional geometrically frustrated lattice includes pyrochlore and spinel lattice, in which the spins reside on a corner-sharing tetrahedral network. In this thesis, I will only focus on the pyrochlore compounds.
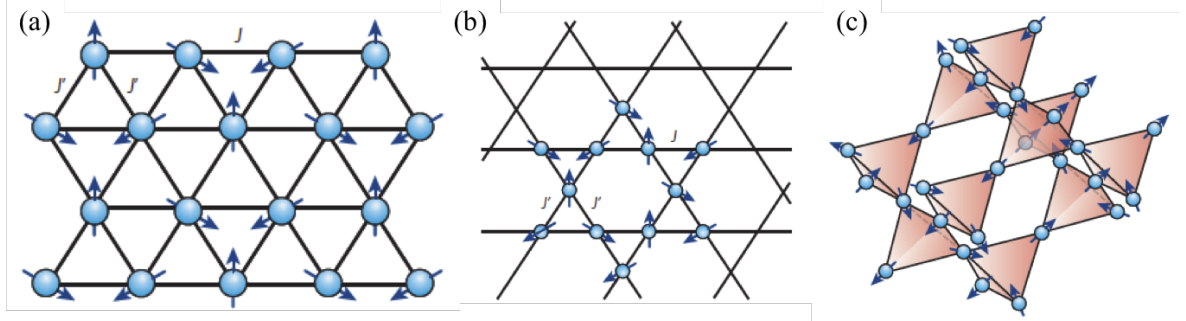
Figure 2.1.2 Geometrical frustrated magnet on 2D and 3D lattices: (a) triangular lattice, (b) kagome lattice and (c) pyrochlore lattice. (taken from [16]).

The frustration index f, introduced by Ramirez [17], is widely used to quantify the degree of frustration:

$$f = |\theta_{CW}|/T_{tran} \tag{2.1.3}$$

where θ_{CW} is the Curie-Weiss temperature, obtained by a linear fitting of the inverse DC susceptibility at high temperatures, where the system is in the trivial paramagnetic state. T_{tran} is the phase transition temperature, where the long-range magnetic order occurs. For instance, $T_{tran} = T_c$ or T_N is the Curie or Neel temperature, respectively, for ferromagnetic or antiferromagnetic ordering. In the spin-glass system T_{tran} would be the freezing temperature. The stronger magnetic frustration of a system is, the lower T_{tran} is compared to θ_{CW} so that a larger f would be. When $f \to \infty$, the system fails to order down to the absolute zero temperature and a novel ground state, known as a "spin liquid", can emerge.

2.1.2. Spin liquids state

A spin liquid state is a state of matter in which the conventional magnetic order is suppressed, however, the spins are highly correlated, and still strongly fluctuating even near the absolute zero temperature [18]. The spin fluctuations in a spin liquid can be *classical* or *quantum* in nature [16]. Classical fluctuations, driven by the thermal energy, dominate in the systems with large-S (S is the spin quantum number, if $S \gg 1/2$, the spin $\hat{S}$ can be treated as three-dimensional vector $\boldsymbol{S}(S^x, S^y, S^z)$). This is referred as classical spin liquid. When the energy

scale becomes too small ($T \rightarrow 0$), classical fluctuations cease and the spins either freeze or order. For small-S systems, e.g. with S comparable to 1/2, the quantum mechanical uncertainty principle produces zero-point motions that persist down to $T = 0$ K. Strong quantum fluctuation may lead to quantum spin liquid (QSL).

QSL shows non-trivial exotic physics such as fractionalization, emergent symmetries and topological order [19]. One example is the resonating valence-bond (RVB) state, proposed by Anderson for the triangular lattice system [20-22]. The wave function of a RVB state is a superposition of spin singlet pairs. While it needs not to break any symmetries of the hosting spin system, this state would be highly entangled and possess non-trivial spin correlations. Breaking one of such singlets will create two unpaired spins, which can then be separated with a small energy cost by rearranging nearby valence bonds. This is known as the fractionalized excitation, spinon [6,19] (see Figure 2.1.3). A spinon carries spin $S = 1/2$ with neutral charge, which cannot be emerged from the magnon-like (spin $S = 1$ and charge neutral) excitation in a conventional magnetic ordered state.
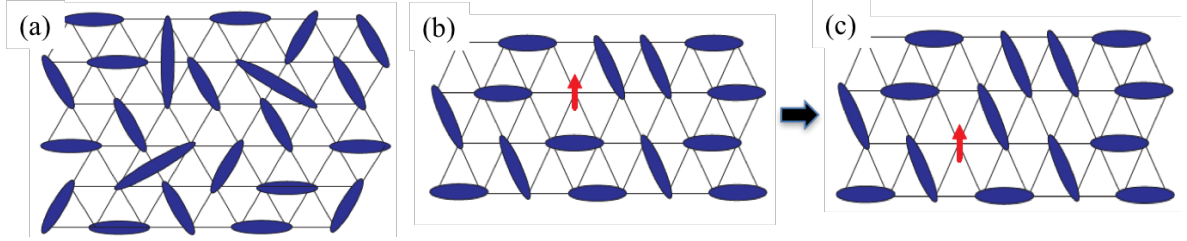
Figure 2.1.3 One possible spin singlet configuration in a resonating valence-bond state (a) and its spinon excitation (b and c) on a triangular lattice. Each blue bond indicates a spin singlet state, $\frac{1}{\sqrt{2}}(|\uparrow\downarrow\rangle - |\downarrow\uparrow\rangle)$. Spinon excitation (red arrow) carries spin $S = 1/2$ with neutral charge and it can move by rearranging nearby bonds (b-c). (taken from [22])

2.2. Pyrochlore Compounds

Pyrochlore compounds offer an excellent playground to investigate magnetic frustration and the resulting exotic states of matter, including classical spin liquids such as the dipolar spin ice compounds $Dy_2Ti_2O_7$ and $Ho_2Ti_2O_7$ [4], and possible quantum spin liquids such as quantum spin ice system $Yb_2Ti_2O_7$[23]. The pyrochlore material gets its name from the mineral $NaCaNb_2O_6F$, which produces a green flame when burned [24]. In this thesis we only focus on the cubic pyrochlore oxides with general formula $A_2B_2O_7$, where A is a trivalent rare earth which includes the lanthanides and Yttrium and B is either a quadravalent transition metal ion or a quadravalent p-block metal ion.

2.2.1. Crystal structure and phase stability

The pyrochlore oxides usually have the cubic space group $Fd\bar{3}m$ (No. 227 in the *International Tables for Crystallography*). Their chemical formula can also be rewritten as $A_2B_2O_6O'$ to illustrate the two distinct oxygen sites. The conventional description using the Wycoff notation is to place the A ion at 16d, B at 16c, O at 48f and O' at 8b, as shown in Table 2.2.1.

Table 2.2.1 The crystallographic positions of the atoms in the pyrochlore oxides using the origin of the second setting for space group $Fd\bar{3}m$. There is only one adjustable positional parameter for the O atom at the 48f site. The point group is given by Schoenflies notation.

Atom	Wyckoff position	Point symmetry	Coordinate
A	16d	D_{3d}	1/2, 1/2, 1/2
B	16c	D_{3d}	0, 0, 0
O	48f	C_{2v}	x, 1/8, 1/8
O'	8b	T_d	3/8, 3/8, 3/8
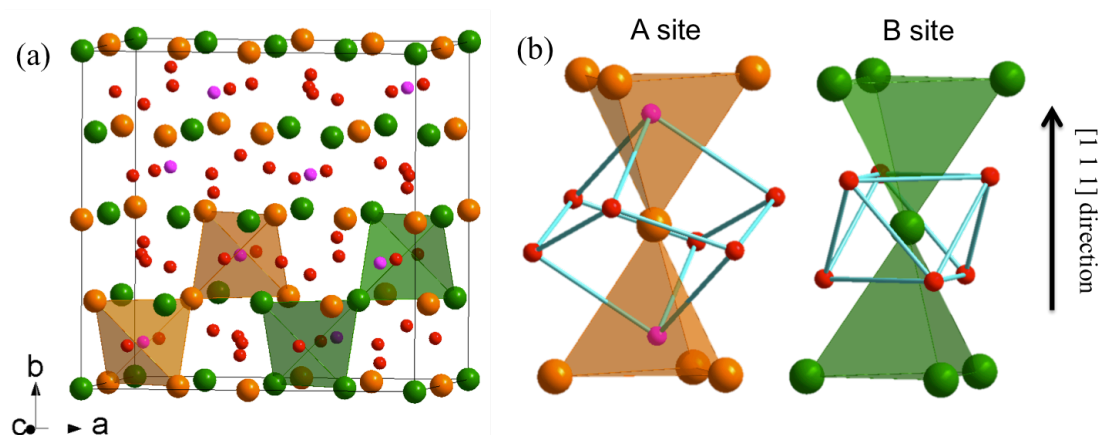
Figure 2.2.1 (a) Crystallographic structure of pyrochlore oxides. A site is orange, B site is green, Oxygen at 48f is red, and oxygen at 8b is purple. (b) The respective oxygen anion environment of the A site and B site.

In the pyrochlore structure, both the 16d and 16c sites form a three-dimensional array of corner-sharing tetrahedra, thus giving rise to canonical geometrically frustrated lattices. The ions A and B are surround by oxygen anions. The coordination geometry of the oxygen environment of A and B is controlled by the 'x' parameter of the 48f site occupied by an oxygen anion. For $x = 0.375$ one has a perfect cubic environment around the A ions on 16d, and the case, $x = 0.3125$, implies a perfect octahedron around the B ions on 16c.

7

   Although about 150 compounds with formula $A_2B_2O_7$ can form the cubic pyrochlore structure, over 15 tetravalent ions are able to reside on the B site [25], any combination of A^{3+} and B^{4+} of the above elements may not be the member of pyrochlore family. One can introduce the tolerance factor to study the phase stability of the pyrochlore structure [26,27]. The frequently used parameter is the ionic radius ratios, r_A/r_B to discuss the stability limits for the pyrochlore phase [28,29]. For example, below $r_A/r_B = 1.46$, the defect-fluorite structure is favored. With the assistance of the high-pressure furnace technique, the ratio r_A/r_B can be extend between 1.36 to 1.71 as shown in Figure 2.2.2. All rare earth iridates can form pyrochlore structure. However, the pyrochlore structure only exists from La to Tb in rare earth hafnates. The A, B sites mixing becomes serious when the rare earth ionic radius ratio is smaller than Tb^{3+} [30].
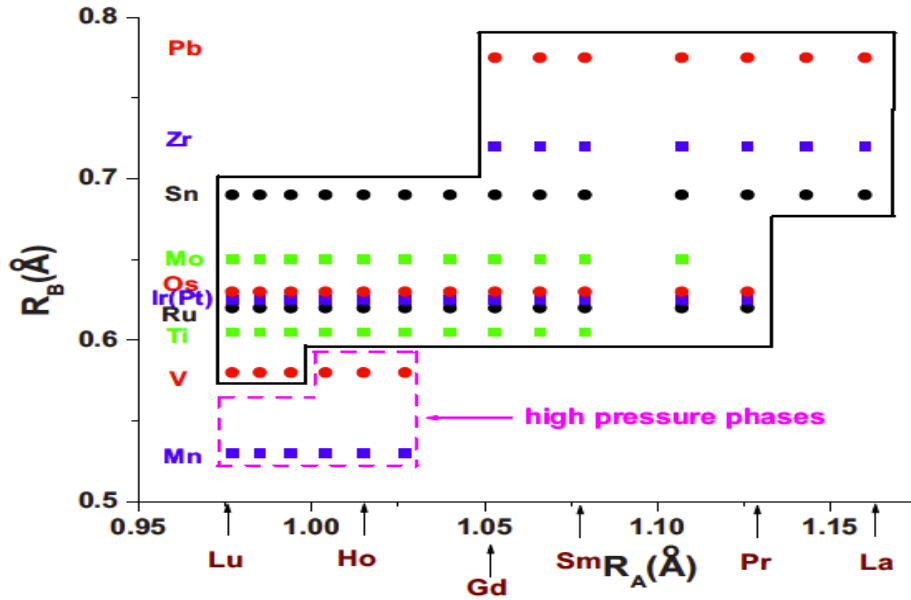
Figure 2.2.2 Stability of the pyrochlore structure for $A_2B_2O_7$ materials. The platinum series are synthesized at high-pressure. (taken from [31] and adapted from [28])

2.2.2. Role of CEF

The crystal electric field (CEF) due to the surrounding anions plays a crucial role on the nature of physic of rare earth ions in the pyrochlore structure. The CEF may cause a considerable reduction of the magnetic moment of the ions, and determines the single-ion anisotropy. Moreover, the origin of non-Ising transvers spin fluctuations in some quantum spin ice materials, for example, in the Pr-based pyrochlore, can be due to the CEF effects.

   The lanthanide series of rare earths starts to fill up the $4f$ shell with cerium and ends with lutetium. The $4f$ shells lie deep inside the $5s$, $5p$, $5d$ and $6s$ shells. Since the rare earths

discussed in this thesis are in the 3+ valence state, the $4f$ electronic shells are shielded by the outmost full-filled $5s$ and $5p$ shells, thus leading to the localization of $4f$ electrons.
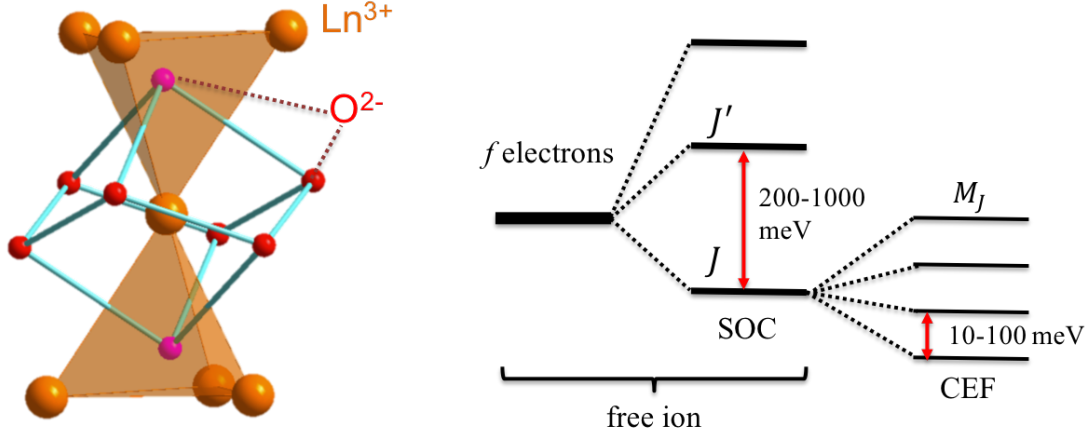
Figure 2.2.3 *Left*: Local oxygen anion environment of the rare earth ions in the pyrochlore lattice structure. The rare earth ions are surrounded by a distorted cubic of O^{2-}, which has a D_{3d} point group symmetry. *Right*: Illustration of the $2J + 1$ degenerate ground-state multiplet originating from SOC, as well as their splitting due to the perturbation of CEF.

In the localized limit, the intra-ionic interaction is taken into account through Hund's rules. As rare-earth ions are relatively heavy, the spin-orbit coupling (SOC) is strong. Its Hamiltonian takes the form:

$$\mathcal{H}_{SO} = \lambda_{SO}\hat{L} \cdot \hat{S} \tag{2.2.1}$$

where $\hat{L}$ and $\hat{S}$ are the total orbital and spin angular momentum operators, respectively, and λ_{SO} represents the spin-orbit coupling strength, which is $\propto Z^4$ (Z is the atomic number in the periodic table). The strong spin-orbit coupling of $4f$ electrons leads to the mixing of states with different quantum numbers M_L and M_S, therefore, L (orbital) and S (spin) are no longer good quantum numbers, instead, the total angular momentum J is a good quantum number. All three of Hund's rules could be used to predict the ground-state J multiplet. For most rare-earth ions, the spin-orbit splitting is larger than 200 meV, which is larger than the thermal energy $k_B T$ in the interesting temperature range. Thus it is a good approximation to consider only the ground-state J multiplet based on Hund's rules.

At sufficiently high temperatures, the free-ion picture discussed above is acceptable. However, the CEF generated by the surrounding ions, such as O^{2-} anion in our cases, has to be taken into account at lower temperature. In f-electron systems, the crystal field is smaller than the spin-orbit coupling due to the shielding effect of the outer electrons. The weakness of the crystal field allows us to apply all three Hund's rules, the CEF therefore can be treated as a perturbation of SOC. Under the influence of CEF, the ground state J multiplet with the

degeneracy of $2J + 1$ splits according to the symmetry of the local environment. The Kramers theorem should be mentioned here. If the ions have an odd number of electrons, i.e. for half-integer J values (Kramers ions), the multiplets arising from the spin-orbit coupling can only be split into doubly degenerated states, where the double degeneracy could only be further lifted by a time-reversal symmetry breaking perturbation such as an external magnetic field. Meanwhile, the wavefunctions of these states are time-conjugated. On the other side, for non-Kramers ions, i.e. with an even number of electrons, no such rule controls the splitting of the multiplets, accidental degenerated states exist and the degeneracy is susceptible to any perturbations, such as weak lattice distortions.

The CEF Hamiltonian $\mathcal{H}_{CEF}$ can be expressed in terms of either the tensor operators or the Stevens operator equivalents. While the tensor operators are more convenient for *ab initio* calculations, the latter we use here are better for the understanding of the origin of single-ion anisotropy. In Stevens notation, the $\mathcal{H}_{CEF}$ reads:

$$\mathcal{H}_{CEF} = \sum_{n,m} B_n^m \hat{O}_n^m(\hat{J}) \tag{2.2.2}$$

where B_n^m are the refinable coefficients for different operators, and $\hat{O}_n^m(\hat{J})$ are the Stevens operators that are polynomial functions of $\hat{J}_z$ and $\hat{J}_\pm$, with $\hat{J}_\pm = \hat{J}_x \pm i\hat{J}_y$. For example, $\hat{O}_2^0 = 3\hat{J}_z^2 - J(J + 1)$. The exact expressions of the Stevens operators can be found in Ref [32].

In the pyrochlore lattice, the rare-earth ions reside at the center of an eight-fold coordinate oxygen anions environment. If $x \neq 0.375$, the 8 O^{2-} anions form a distorted cube compressed along the local [1 1 1] direction, as shown in the left of Figure 2.2.3, the symmetry at the rare earth site is given as the D_{3d} point group, which includes two two-fold and one three-fold rotation axis and an inversion center. If we define that the quantization z-axis is along the local [1 1 1] direction, the CEF Hamiltonian in Eq. (2.2.2) will be reduced to:

$$\hat{\mathcal{H}}_{CEF} = B_2^0 \hat{O}_2^0 + B_4^0 \hat{O}_4^0 + B_4^3 \hat{O}_4^3 + B_6^0 \hat{O}_6^0 + B_6^3 \hat{O}_6^3 + B_6^6 \hat{O}_6^6 \tag{2.2.3}$$

where

$$\hat{O}_2^0 = 3\hat{J}_z^2 - J(J + 1)$$

$$\hat{O}_4^0 = 35\hat{J}_z^4 - 30J(J + 1)\hat{J}_z^2 + 25\hat{J}_z^2 - 6J(J + 1) + 3\hat{J}_z^2(J + 1)^2$$

$$\hat{O}_4^3 = \frac{1}{4}\left\{7\hat{J}_z\left(\hat{J}_+^3 + \hat{J}_-^3\right) + \left(\hat{J}_+^3 + \hat{J}_-^3\right)\hat{J}_z\right\}$$

$$\hat{O}_6^0 = 231\hat{J}_z^6 - 315J(J + 1)\hat{J}_z^4 + 735\hat{J}_z^4 + 105J^2(J + 1)\hat{J}_z^2$$
$$- 525J(J + 1)\hat{J}_z^2 + 294\hat{J}_z^2 - 5J^3(J + 1)^3$$
$$+ 40J^2(J + 1)^2 - 60J(J + 1)$$

$$\hat{O}_6^3 = \frac{1}{4}\left\{\left(11\hat{J}_z^3 - 3\hat{J}_zJ(J+1) - 59\hat{J}_z\right)\left(\hat{J}_+^3 + \hat{J}_-^3\right)\right.$$

$$\left. + \left(\hat{J}_+^3 + \hat{J}_-^3\right)\left(11\hat{J}_z^3 - 3\hat{J}_zJ(J+1) - 59\hat{J}_z\right)\right\}$$

$$\hat{O}_6^6 = \frac{1}{2}\left(\hat{J}_+^6 + \hat{J}_-^6\right)$$

If the Hamiltonian $\mathcal{H}_{\text{CEF}}$ is dominated by the term $B_2^0\hat{O}_2^0$, which is the usual case for rare earth pyrochlore, it is clear that a negative value of B_2^0 would lead to an easy-axis anisotropy and a positive value of B_2^0 would give rise to easy-plane anisotropy [31].

Table 2.2.2 Ground-state properties of some rare-earth ions: the number of electrons in the 4f shells, the Lande factor g_J and the ground states (GS) of Hund's rules. The GS term is labelled as $^{2S+1}L_J$, where L=S, P, D, F, G, H, I correspond to the orbital angular momenta number with 0, 1, 2, 3, 4, 5, 6, respectively. The g tensors corresponding to the local [1 1 1] quantization axis are listed, as well as the type of single-ion anisotropy.

	n(4f)	GS	g_J	$g_\parallel$	$g_\perp$	anisotropy	compounds	Ref.
Pr^{3+}	2	$^3H_4$	4/5	5.17	0	Ising	$Pr_2Sn_2O_7$	[33]
Nd^{3+}	3	$^4I_{9/2}$	8/11	5.3	0	Ising	$Nd_2Zr_2O_7$	[34]
Tb^{3+}	8	$^7F_6$	3/2	10.7	0	Ising	$Tb_2Ti_2O_7$	[35]
Dy^{3+}	9	$^6H_{15/2}$	4/3	19.6	0	Ising	$Dy_2Ti_2O_7$	[36]
Ho^{3+}	10	$^5I_8$	5/4	19.6	0	Ising	$Ho_2Ti_2O_7$	[36]
Er^{3+}	11	$^4I_{15/2}$	6/5	3.9	6.3	XY	$Er_2Ti_2O_7$	[37]
Yb^{3+}	13	$^2F_{7/2}$	8/7	1.92	3.69	XY	$Yb_2Ti_2O_7$	[38]

One can characterize the single-ion anisotropy using the g tensors, which can be obtained from the ground-state wavefunctions of the rare-earth ions.

$$g_\parallel = 2g_J\left|\langle\phi_0^\pm|\hat{J}_z|\phi_0^\pm\rangle\right|,$$

$$g_\perp = g_J\left|\langle\phi_0^+|\hat{J}_+|\phi_0^-\rangle\right| = g_J\left|\langle\phi_0^-|\hat{J}_-|\phi_0^+\rangle\right|$$

(2.2.4)

where $\phi_0^\pm$ are the ground-state wavefunctions, g_J is the Lande factor, $g_\parallel$ and $g_\perp$ are the spectroscopic factors, i.e. g tensor, along and perpendicular to the local trigonal z-axis, respectively. As shown in Table 2.2.2, the rare earth ions in pyrochlore lattice can be classified into two types of single-ion anisotropy. The negligible perpendicular component and large parallel component of the g tensors of Pr^{3+}, Nd^{3+}, Tb^{3+}, Dy^{3+} and Ho^{3+} indicate that these ions have an Ising-type single-ion anisotropy, which would impose the magnetic moment to be oriented along its local [1 1 1] axis. The Ising-type anisotropy is one of the

pre-requisites to realize the spin-ice state, which will be introduced in the next section. Er^{3+} and Yb^{3+}, having a large perpendicular component and relatively small parallel component of the g tensor, can be classified into the XY-type anisotropy. Their magnetic moments would prefer to lay in the plane perpendicular to [1 1 1]. Novel phases, such as the Splayed ferromagnetic long-range order [39], and Palmer-Chalker state [40,41], have been found in the Er^{3+} and Yb^{3+} based pyrochlore compounds.

Beside the single-ion anisotropy determined by CEF, the CEF ground states $\phi_0^{\pm}$ (or wavefunctions) are also important to simplify the magnetic exchange interaction Hamiltonian, for example the Heisenberg model Eq. (2.1.1). It has been demonstrated that the CEF ground states of the rare earth ions in Table 2.2.2 in perfect pyrochlore lattice (no oxygen vacancy, A/B-site mixing and other defect) are doublets, which can be expressed by the bases of $|J, M_J\rangle$ [36]. Meanwhile the energy gap between the ground state and the first excited CEF state is sufficiently large (except for the case of Tb^{3+}), so that an effective $S = 1/2$ (or pseudo spin-1/2) approximation can be introduced to describe the magnetic exchange interactions of the isolated ground state at low temperatures [42,43]. The ground-state doublet based on pseudo spin-1/2 has different properties according to the Karmers theorem introduced above. For the Karmers ions (half-integer J values, Nd^{3+}, Dy^{3+}, Er^{3+}, and Yb^{3+}), the ground-state doublet is protected by time reversal symmetry and can only be split by breaking the time reversal symmetry, for example in magnetic fields. It is worth to note that the high order multipolar components, such as octupole, may play a role and introduce quantum fluctuation into the system, for instance in the systems of Nd^{3+} and Dy^{3+} with $J = 9/2$ and $15/2$, respectively [44]. For the non-Kramers ions (integer J values, Pr^{3+}, Tb^{3+} and Ho^{3+}), without the protection of time reversal symmetry, the ground-state doublet can be easily split by small lattice distortion such as oxygen vacancies. The tiny splitting of the ground-state doublet may introduce an effective transvers field in addition to the Ising component of the pseudo spin and give rise to an enhanced quantum fluctuation in the system [45].

2.3. Diverse magnetic ground states in pyrochlores oxides

The pyrochlore compounds exhibit a rich variety of magnetic ground states. In the case of gadolinium (Gd) based pyrochlore, the Gd^{3+} ion (half-filled $4f$ electronic shell, $4f^7$, with the $^8S_{7/2}$ ground state) has no orbital magnetic moment contribution and the degeneracy of the eight-level ground-state caonnot be lifted by the CEF, which play a large role for other rare-

earth ions as discussed above, beyond a fraction of a Kelvin [46,47]. Thus the spin of Gd^{3+} is expected to be isotropic and to be good realizations of Heisenberg antiferromagnets that have been predicted to be in a collective paramagnetic state with short-range correlations between spins at any nonzero temperature by theoretical calculations [48-50]. However, the Gd-based pyrochlores often possess transitions from paramagnetic state to long-rang order due to dipolar interaction and further neighbor exchange interactions [47]. For instance, the $Gd_2Ti_2O_7$ displays two magnetic transitions, at 0.7 and 1 K, to the magnetic structures with ordering vector $\mathbf{k} = (1/2\ 1/2\ 1/2)$ [51,52], $Gd_2Sn_2O_7$ undergoes a first-order transition into an ordered state with Palmer-Chalker configuration (ordering vector $\mathbf{k} = (1\ 1\ 1)$) near 1 K [53,54]. The investigations of the magnetic ground state and their excitations of Gd-pyrochlore are still ongoing.

Beside the Gd^{3+} and Eu^{3+} (non-magnetic), other trivalent rare-earth ions can be classified into two groups according to the single-ion anisotropy driven by CEF. Here we will briefly discuss the spin ice state for easy-axis anisotropy case and order-by-disorder for easy-plane anisotropy.

2.3.1. Spin ice

A landmark example in frustrated magnetism is spin ice, which was first studied by Harris and colleagues in 1997 [55]. In spin-ices materials, such as $Dy_2Ti_2O_7$, $Ho_2Ti_2O_7$ and $Ho_2Sn_2O_7$, only the rare-earth ions are magnetic, and they form a network of corner-sharing tetrahedral (see Figure 2.2.1). The CEF acting on the rare-earth site constrains spin to align along its local [1 1 1] axis. The name "spin ice" originates from a direct analogy between the configurations, in which two spins point inward and two spins point outward (2-in-2-out) from the center of tetrahedron, and the position of protons in the tetrahedrally coordinated O^{2-} framework of water ice, as shown in Figure 2.3.1. The 2-in-2-out configuration is called "ice rule", as defined in water ice I_h for the 2-strong-2-weak O-H bonds [56]. For a given tetrahedron within 4 Ising spins on the corners, there are 6 configurations obeying the ice rule from in total $2^4 = 16$ configurations. In the pyrochlore lattice with N spins, since each spin is shared by two tetrahedral, the number of microstates satisfying the ice rule is calculated as $\widetilde{\Omega} = 2^N(6/16)^{N/2} = (3/2)^{N/2}$ and the entropy per spin is $S_{CSI} = k_B \ln \widetilde{\Omega} = \frac{k_B}{2} \ln \frac{3}{2}$, corresponding to Pauling's residual entropy for water ice [31].
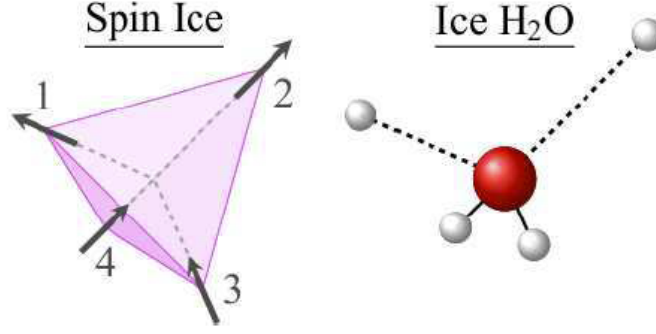
Figure 2.3.1 The analogy between spin ice and water ice: the white spheres are the hydrogen atoms and the red one is the oxygen. A spin pointing *inward* (resp. *outward*) the tetrahedron corresponds to a short covalent bond (resp. long H-bond) for water ice (taken from [57]).

How can we realize the spin ice as the ground state in the pyrochlore lattice? Beginning with the Ising antiferromagnetic Hamiltonian in the pyrochlore lattice with global coordinates (denote as x, y, z), first considered by Anderson [12]:

$$\mathcal{H}_{Ising,AFM} = \mathcal{J}_{\parallel} \sum_{i,j} S_i^z \cdot S_j^z \tag{2.3.1}$$

with $\mathcal{J}_{\parallel} > 0$, and where the sum is carried out over all the nearest-neighbor bonds of the pyrochlore lattice. The Hamiltonian $\mathcal{H}_{Ising,AFM}$ allows an exponentially large number of ground states given by the simple rule that each "up" and "down" tetrahedron must have a vanishing net spin. For each tetrahedron, the configuration with two spins "up" and two spins "down" (2-up-2down) can satisfy this requirement. The 2-up-2-down configuration then can be mapped to the 2-strong-2-weak proton bonds of water ice. However, Anderson's AFM model with Ising spins pointing along the global z direction is unrealistic since the magnetic moment of the rare-earth ion is constrained along the local [1 1 1] direction (denoted as z') by the CEF effect. Considering only nearest neighbor coupling we can write the following [58]:

$$\mathcal{H}_{ex} = -\mathcal{J} \sum_{i,j} \boldsymbol{S}_i \cdot \boldsymbol{S}_j = \frac{\mathcal{J}}{3} \sum_{i,j} \sigma_i^{z'} \sigma_j^{z'}$$

$$\boldsymbol{S}_1 = \pm(-1,-1,+1)/\sqrt{3}, \boldsymbol{S}_2 = \pm(+1,+1,+1)/\sqrt{3},$$

$$\boldsymbol{S}_3 = \pm(+1,-1,-1)/\sqrt{3}, \boldsymbol{S}_4 = \pm(-1,+1,-1)/\sqrt{3}. \tag{2.3.2}$$

where $(\boldsymbol{S}_i \cdot \boldsymbol{S}_j) = -1/3$ for both spins that point out or in the tetrahedron. $\sigma_i^{z'} = +1$ for an "out" spin and $\sigma_i^{z'} = -1$ for an "in" spin. This Hamiltonian matches the above Anderson's AFM model with a global Ising symmetry. The net magnetization for each tetrahedron can

also be derived by using $S_t = \sigma_1^{z'} + \sigma_2^{z'} + \sigma_3^{z'} + \sigma_4^{z'}$ as the total effective Ising spin for the tetrahedron [48]:

$$\mathcal{H}_{ex} = \frac{\mathcal{J}}{6} \sum_{tet} S_t^2 + cc \qquad (2.3.3)$$

So, the ground state of this model is obtained when $S_t = 0$ on every tetrahedron. The lowest energy is related to states of each tetrahedron with two Ising spins directed inside, and two others directed outside the tetrahedron which means two having $\sigma_n^{z'} = +1$, and other two having -1 value. It is important to note that the ferromagnetic exchange between the real magnetic moments in such pyrochlore oxides may still give rise to an effective antiferromagnetic coupling between the effective Ising spins [59,60]. Indeed, the positive Curie-Weiss temperatures have been deduced from the magnetic susceptibility measurements, $\theta_p \approx 0.5, 1.9, 1.8$ and 1.7 K for of $Dy_2Ti_2O_7$ [61], $Ho_2Ti_2O_7$ [55], $Ho_2Sn_2O_7$ [62] and $Dy_2Sn_2O_7$ [62], respectively, implying ferromagnetic exchange interactions. It is worth to notice that antiferromagnetic interactions in (2.3.2) would erase this frustration and favor the 4 in or 4 out (all-in-all-out, AIAO) states [55,63].

Dipolar spin ice

The origin of the ferromagnetic exchange interaction in the classical spin ice compounds is mostly due to the magnetic dipolar interaction between large magnetic moments for instance $\mu \sim 10 \ \mu_B$ for Dy^{3+} and Ho^{3+} ions. An estimation of the dipolar interaction strength is given by $D = \frac{\mu_0}{4\pi} \frac{\mu^2}{r_{nn}^3} \approx 1.4$ K, where $r_{nn} = a_{latt}\sqrt{2}/4$ is the nearest-neighbor distance. The dipolar interaction strength is comparable to the Curie-Weiss temperature. Thus, the dipolar spin-ice model (DSI) was introduced in order to describe the low temperature properties of the classical spin-ice compounds [64]:

$$\mathcal{H}_{DSI} = -\mathcal{J} \sum_{\langle i,j \rangle} \boldsymbol{S}_i \cdot \boldsymbol{S}_j - D r_{nn}^3 \sum_{i>j} \left[\frac{\boldsymbol{S}_i \cdot \boldsymbol{S}_j}{|\boldsymbol{r}_{ij}|^3} - \frac{3(\boldsymbol{S}_i \cdot \boldsymbol{r}_{ij})(\boldsymbol{S}_j \cdot \boldsymbol{r}_{ij})}{|\boldsymbol{r}_{ij}|^5} \right] \qquad (2.3.4)$$

The above DSI model can be simplified according to Eq. (2.3.2):

$$\mathcal{H}_{DSI} = \mathcal{J}_{eff} \sum_{i,j} \sigma_i^{z'} \sigma_j^{z'} \ , \text{where } \mathcal{J}_{eff} = D_{nn} + \mathcal{J}_{nn} = \frac{5D}{3} + \frac{\mathcal{J}}{3} \qquad (2.3.5)$$

The values of $\mathcal{J}_{nn}$ and D_{nn} has been studied by numerical simulations and a phase diagram of the DSI model was built [65]. The spin ice state can be stabilized in a wide range of $\mathcal{J}_{nn}/D_{nn}$ and temperature, as shown in Figure 2.3.2 (a). One key experimental evidence for the existence of the spin-ice state in real materials is that the residual magnetic entropy of

Dy$_2$Ti$_2$O$_7$ recovers the Pauling entropy in water ice [4]. Another powerful technique is neutron scattering that directly measures spin correlations. The observed pinch point in Ho$_2$Ti$_2$O$_7$ is the direct proof of the spin-ice state predicted by the DSI model [66,67]. In addition, several Ho- and Dy-based pyrochlore compounds, such as Ho$_2$Sn$_2$O$_7$ [67,68], Dy$_2$Sn$_2$O$_7$ [62,69], Dy$_2$Ge$_2$O$_7$ [70,71] and Ho$_2$Ge$_2$O$_7$[72], have also been identified as spin ices. These compounds are called classical spin ice in order to be distinguished from quantum spin ice that will be introduced in the next section.
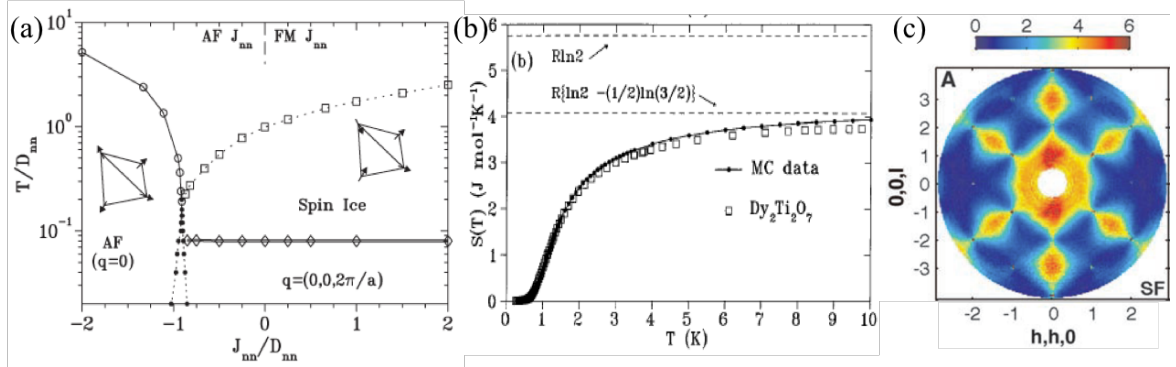
Figure 2.3.2 (a) Calculated phase diagram of the DSI model (taken from [65]). (b) Magnetic entropy of Dy$_2$Ti$_2$O$_7$ revealing the same residual entropy for water ice as explained by [4,64] (taken from [61]). (c) Evidence of the pinch points, associated to the spin-ice state, observed in diffuse magnetic scattering map recorded on the spin-ice compound Ho$_2$Ti$_2$O$_7$ at 1.7 K in the $(h\ h\ l)$ reciprocal space plane (taken from [66]).

Magnetic Monopole and dumbbell model

The magnetic excitations in spin-ice can be obtained by flipping one spin at the center of a pair of corner-sharing tetrahedron, resulting in 3-spins-in-1-spin-out (3I1O) and 1-spin-in-3-spins-out (1I3O) configurations. These excitations are called magnetic monopoles [73]. Catelnovo proposed a dumbbell model to illustrate the DSI Hamiltonian and describe the thermal fluctuations generating the magnetic monopoles [5,74]. The principle is that the Ising spin with a magnetic moment size of μ is treated as two magnetic monopoles with opposite charges $\pm q_m = \mu/a_d$ (dumbbell) separated by a length $a_d = \sqrt{3}a_{latt}/2$, which is the distance between the centers of two neighboring tetrahedra. The magnetic Coulomb interaction between two monopoles is written as:

$$V(r_{\alpha\beta}) \begin{cases} \dfrac{\mu_0 Q_\alpha Q_\beta}{4\pi\ r_{\alpha\beta}} & \text{if } \alpha \neq \beta \\[2mm] \dfrac{v_0 Q_\alpha^2}{2} & \text{if } \alpha = \beta \end{cases} \tag{2.3.6}$$

where $r_{\alpha\beta}$ denotes the distance between two monoples, and ν_0 is the self energy accounting for the dipolar and exchange energy between nearest neighbors. The DSI Hamiltonian Eq. (2.3.4) can be rewrite in terms of the net charges $Q_\alpha = \sum_i q_{m,i} = 0, \pm 2q_m$, and $\pm 4q_m$, where the sum runs over the four magnetic charges inside the tetrahedral, at the centers of the tetrahedral that form a diamond lattice:

$$\mathcal{H}_{DB} = \frac{\mu_0}{4\pi} \sum_{\alpha < \beta} \frac{Q_\alpha Q_\beta}{r_{\alpha\beta}} + \frac{\nu_0}{2} \sum_\alpha Q_\alpha^2 \qquad (2.3.7)$$
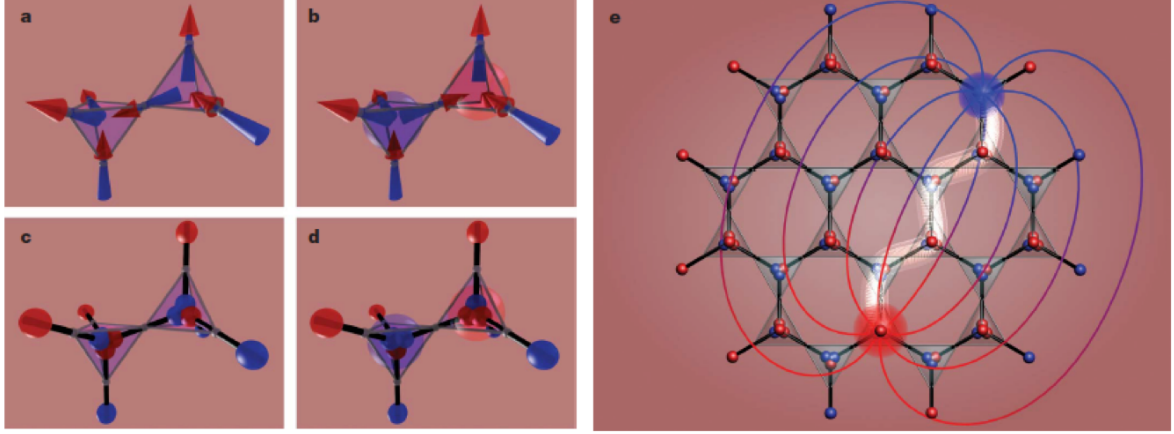
Figure 2.3.3 (a) Spin-ice configuration in two neighboring tetrahedra. (b) 3I1O and 1I3O states obtained by flipping the spin shared by two neighboring tetrahedra. (c, d) The dumbbell picture of the corresponding states in (a, b) obtained by replacing each spin by a pair of opposite magnetic charges. (e) The monopoles can move as diffusion and a pair of monopoles is connected via the Dirac string. (taken from [5])

Many properties of the classical spin ice can be described using the knowledge on the Coulomb gas. For example, considering the spin ice states as a correlated vacuum background, a thermally flipped spin would correspond to the nucleation of pairs of the charged defects, i.e. two magnetic monopoles of opposite charges. These magnetic monopoles reside on a diamond lattice that is formed by connecting the center of the tetrahedral of the pyrochlore lattice. They can be moved apart by flipping a sequence of spins/dumbbells like particle diffusion via a path i.e. the so-called Dirac string [75]. The diffusion of magnetic monopoles costs zero energy along the string since each tetrahedron tends to recover the ground state defined by the ice rule. Some experimental investigations and theoretical predictions have been done in order to obtain the direct evidence of the existence of monopoles in classical spin ice compounds by μSR, neutron scattering, magnetization measurements and so on. However, the interpretation of those results is still a matter of debate [57,75-77].

The dumbbell model of monopole only considers the matter field of monopoles and ignores one of the defining features of spin ice, i.e. its macroscopic zero-point entropy. However, it enlightens us to understand the nature of the ground-state correlations of spin-ice, and also its fractionalized excitations in the aspect of the emergent gauge field. One can map the easy-axis spins $\{S_i\}$ on the pyrochlore lattice to a set of the lattice vector field $\{B_i\}$ on the bonds of the diamond lattice [60]. Then, the 2I2O ice rule can be rewritten as a divergence free coarse-grain field, i.e. $\nabla \times B = 0$. (Note: a nonzero flux of that field means that the ice rule is broken in one tetrahedron.) A gauge field A, an analogy to electromagnetism, could be introduced as $B = \nabla \times A$. Then the correlation functions for the field are

$$\langle B_i(r)B_j(0)\rangle \propto \frac{3r_i r_j - r^2 \delta_{i,j}}{r^5} \tag{2.3.8}$$

which means that the local constraint, i.e., the ice-rule, yields dipolar-like correlations at large distances. These Coulomb correlations are the signature of the so-called "Coulomb phase" in dipolar spin-ices [60,74,78,79], which could be observed in neutron diffuse scattering experiments as the pinch-point feature [66].

Quantum spin ice

So far, we have discussed only the magnetic interaction of the Ising spins in the pyrochlore lattice. A natural question to ask is what are the effects of quantum fluctuation in a spin ice system, i.e. quantum spin ice (QSI). That was originally studied by Hermele *et al*. [80] for the case of the $S = 1/2$ XXZ model for the nearest-neighbor exchange on the pyrochlore lattice [81]:

$$\mathcal{H}_{XXZ} = \mathcal{H}_{CSI} + \mathcal{H}_\perp$$
$$\text{where, } \mathcal{H}_{CSI} = \mathcal{J}_{zz} \sum_{\langle i,j\rangle} \hat{S}_i^{z'} \hat{S}_j^{z'} \tag{2.3.9}$$
$$\text{and, } \mathcal{H}_\perp = -\mathcal{J}_\pm \sum_{\langle i,j\rangle}\left(\hat{S}_i^{+'}\hat{S}_j^{-'} + \hat{S}_i^{-'}\hat{S}_j^{+'}\right)$$

with $0 < \mathcal{J}_\pm \ll \mathcal{J}_{zz}$. The transverse term, $\mathcal{J}_\pm$ can introduce quantum dynamics of the spin-ice configuration. Based on the degenerate perturbation theory in $\mathcal{J}_\pm$ it has been found that the first non-trivial contribution arises at third order, and describes a tunneling process between degenerate spin-ice configurations: a ring exchange running on a hexagonal plaquette [80]. Then, the stability of a gapless spin liquid state, $U(1)$ quantum spin liquid, has been demonstrated numerically in a region of the phase diagram, where the quantum spin ice state is a peculiar case of that phase [80,82-84]. The emergent excitations, such as the

gapless, linearly dispersing photon, and gapped, electric and magnetic charges spinon and vision are predicted according to the gauge theory of quantum electromagnetism [83,85].
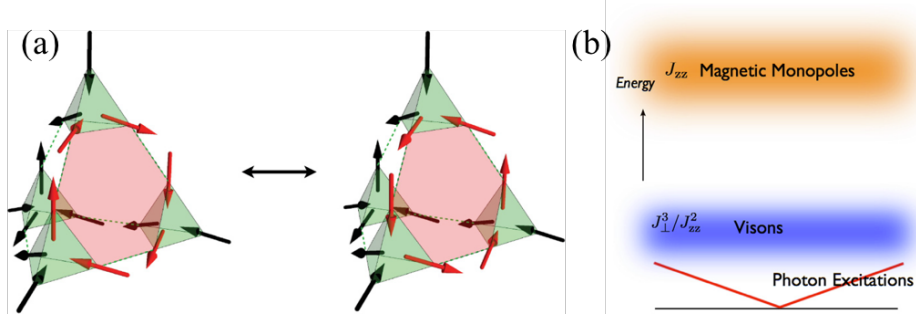

Figure 2.3.4 (a) The tunneling between two spin configurations on a hexagonal plaquette. (taken from ref [83]) (b) Schematic of the spectrum of excitations in quantum spin ice. (taken from ref. [81])

In the real materials, the physical meaning of the transvers term $J_\pm$ depends on the nature of the magnetic ion. A general Hamiltonian for an anisotropic effective spin-1/2 system based on symmetry-allowed nearest-neighbor couplings can be expressed as follow [23,42,43,86]:

$$
\begin{aligned}
\mathcal{H}_{eff-1/2} = \sum_{\langle i,j \rangle} \Big\{ & \mathcal{J}_{zz} \hat{S}_i^{z'} \hat{S}_j^{z'} - \mathcal{J}_\pm \big(\hat{S}_i^{+'} \hat{S}_j^{-'} + \hat{S}_i^{-'} \hat{S}_j^{+'} \big) \\
& + \mathcal{J}_{\pm\pm} \big[\gamma_{ij} \hat{S}_i^{+'} \hat{S}_j^{+'} + \gamma_{ij}^* \hat{S}_i^{-'} \hat{S}_j^{-'} \big] \\
& + \mathcal{J}_{z\pm} \big[\hat{S}_i^{z'} \big(\zeta_{ij} \hat{S}_j^{+'} + \zeta_{ij}^* \hat{S}_j^{-'} \big) + i \leftrightarrow j \big] \Big\}
\end{aligned}
\tag{2.3.10}
$$

where the effective spin is written in terms of local coordinates and the coefficients γ_{ij} is a 4×4 complex matrix, and $\zeta_{ij} = -\gamma_{ij}^*$ (see Ref. [23]). The first term $\mathcal{J}_{zz} \hat{S}_i^{z'} \hat{S}_j^{z'}$ represents the easy-axis Ising interaction in the CSI model, other three terms represent the quantum fluctuations and are allowed by symmetry on the pyrochlore lattice [87]. If we set the terms $\{ \mathcal{J}_{\pm\pm}, \mathcal{J}_{z\pm} \}$ to zero, this expression becomes the minimal model of the QSI Hamiltonian as discussed in Eq. (2.3.9). The four terms $\{ \mathcal{J}_{zz}, \mathcal{J}_\pm, \mathcal{J}_{\pm\pm}, \mathcal{J}_{z\pm} \}$ can be obtained by linear transformations from the original nearest-neighbour interactions: (1) an Ising interaction $\mathcal{J}_{zz} \hat{S}_i^{z'} \hat{S}_j^{z'}$, (2) an isotropic interaction of the form $\mathcal{J}_{iso} \boldsymbol{S}_i \cdot \boldsymbol{S}_j$, (3) a pseudo-dipolar exchange interaction that has the same trigonometric form as magnetostatic dipole-dipole $\mathcal{J}_{pd} \big(\boldsymbol{S}_i \cdot \boldsymbol{S}_j - 3 \boldsymbol{S}_i \cdot \hat{\boldsymbol{r}}_{ij} \, \hat{\boldsymbol{r}}_{ij} \cdot \boldsymbol{S}_j \big)$, and (4) a Dzyaloshinskii-Moriya interaction of the form $\mathcal{J}_{DM} \big(\hat{\boldsymbol{d}}_{ij} \cdot \boldsymbol{S}_i \times \boldsymbol{S}_j \big)$ [88]. The phase diagram for this model has been solved by means of the gauge mean field theory (gMFT) for systems with Kramers ions [89,90] as well as non-Kramers ions [86] (non-Kramers ions must have $\mathcal{J}_{z\pm} = 0$ [86], since $\big| \langle \phi_0^\pm | S^\pm | \phi_0^\pm \rangle \big| = 0$,

where $\phi_0^\pm$ are the wavefunctions of the CEF ground state of rare-earth ions). The existence of the QSI state is predicted for both cases.

Experimentally, to realize the physics of QSI, one needs to look for materials with much reduced dipolar interaction, and enhanced quantum fluctuations. The search for QSI effects has therefore moved away from $Ho_2Ti_2O_7$ or $Dy_2Ti_2O_7$, to materials containing rare-earth ions with smaller magnetic moments [81,91]. There are several QSI candidate materials, such as $Yb_2Ti_2O_7$, $Pr_2X_2O_7$ (X = Sn, Zr, Hf, Ir) and $Tb_2Ti_2O_7$, which have been extensively studied recently [23,92-98]. However, the hallmark signatures of QSI, such as the linear dispersive emergent photon excitation and the continuum spinons excitations, have not been confirmed experimentally so far.

2.3.2. Quantum XY pyrochlores

Table 2.3.1 Ground state magnetic properties of the Er- and Yb- based pyrochlore compounds. T^* denotes the temperature where a broad hump is often observed in magnetic specific heat. The low temperature magnetism of $Yb_2Ti_2O_7$ is strongly sample dependent, here, we take the relevant parameters from the latest report [94]. The magnetic structure of $Yb_2Pt_2O_7$ is not completely determined. PC means Palmer-Chalker states in which the spins are pairwise antiparallel, and collinear with an edge of the tetrahedron [40].

	a (Å)	θ_p (K)	$g_\perp/g_\parallel$	T^* (K)	T_{ord} (K)	Order State	Ref.
$Er_2Ti_2O_7$	10.1	-22	1.6	-	1.2	ψ_2, AFM	[99]
$Er_2Sn_2O_7$	10.4	-14	54	4.3	0.11	Γ_7, PC AFM	[100]
$Er_2Ge_2O_7$	9.9	-22	3.3	-	1.4	ψ_2 or ψ_3, AFM	[101]
$Er_2Pt_2O_7$	10.1	-22	28	1.5	0.30	Γ_7, PC AFM	[102]
$Yb_2Ti_2O_7$	10.0	0.8	1.9	2.5	0.25	Γ_9, FM	[94]
$Yb_2Sn_2O_7$	10.3	0.5	-	1.8	0.15	Γ_9, FM	[39]
$Yb_2Ge_2O_7$	9.8	0.9	1.7	3.7	0.6	ψ_2 or ψ_3, AFM	[101]
$Yb_2Pr_2O_7$	10.1	0.9	-	2.4	0.3	Undeterm. FM	[103]

As a consequence of the CEF effect, Er^{3+} and Yb^{3+} in a pyrochlore lattice possess a strong planar anisotropy within the local coordinate system (see Table 2.2.2). Back to Eq. (2.3.10), if the transverse terms $\{\mathcal{J}_\pm, \mathcal{J}_{\pm\pm}, \mathcal{J}_{z\pm}\}$ dominate over the Ising term $\mathcal{J}_{zz}$, this Hamiltonian could also be used to describe the properties of the easy-plane case, i.e. the so-called quantum XY pyrochlores [104]. Furthermore, the Er- and Yb-based pyrochlore oxides are known to

exhibit strong phases competition between different but nearly degenerate ground states. They often reach an easy-plane long-range ordered state [105]. For example, $Er_2Ti_2O_7$ shows a long-range magnetic order below 1.2 K, in which the spins lie in the XY plane via the order by disorder mechanism [40,106,107]. In contrast, the almost stoichiometric sample of $Yb_2Ti_2O_7$ exhibits a ferromagnetic long-range order below 0.25 K [94]. The experimental results on a number of quantum XY pyrochlore compounds that have been investigated recently are summarized in Table 2.3.1.

2.4. Pyrochlore iridates

So far we have discussed frustrated magnetism and emergent magnetic phenomena of Ln^{3+} in the pyrochlore lattice within non-magnetic B site ion. Comparing to the aforementioned insulating pyrochlore oxides dominated by the exchange interaction only between Ln^{3+}, rare-earth pyrochlore iridates are such a system in which the interplay between Ln^{3+} and Ir^{4+} cannot be ignored any more. Furthermore, the sublattice of Ir^{4+} itself also exhibits novel states due to the strong spin-orbit coupling (SOC) of the $5d$ electrons.

2.4.1. Spin-orbit interaction in 5d transition metal compounds

Spin-orbit coupling (SOC) is a relativistic effect that provides an interaction between the orbital angular momentum and electron spin in atoms, $\mathcal{H}_{SO} = \lambda_{SO}\hat{L} \cdot \hat{S}$, and is usually considered to be a small perturbation in the discussion of electronic states. Since the strength of SOC, λ_{SO}, is proportionally to Z^4, where Z is the atomic number, SOC can play a significant role in heavy elements. For example, for the $4f$ electrons in rare-earth atoms, instead of the electron spin S, the total angular momentum number J becomes an object to discuss in magnetism, as introduced in CEF subsection.

Table 2.4.1 Comparison of the Coulomb interaction (U) and spin-orbit coupling (λ_{SO}) for various transition metal oxides [108].

	U	λ_{SO}
3d (Cu, Co, Fe…)	4-7 eV	0-0.01 eV
4d (Mo, Ru, Rh…)	1-4 eV	0.01-0.1 eV
5d (Os, Re, Ir…)	0.1-2 eV	0.1-1 eV

Transition-metal oxides with partially filled 4d and 5d shells exhibit an intricate interplay of charge, spin and orbital degrees of freedom arising from a delicate balance of electronic correlations, spin-orbit coupling, and crystal-field effects [109]. Changing from 3d to 5d in the periodic table, the electron correlation energy decreases as the radial expansion of the orbitals allows for the electrons to be further apart while in the same orbital, thereby reducing the electronic Coulomb repulsion U. However, simultaneously, the SOC increases dramatically, and is comparable to the Coulomb interaction for 5d series, as shown in Table 2.4.1. The above discussion could be described by considering a generic model Hamiltonian:

$$\mathcal{H} = \sum_{i,j,\alpha\beta} t_{ij,\alpha\beta} \hat{c}_{i\alpha}^{\dagger} \hat{c}_{j\beta} + h.c. + \lambda_{\mathrm{SO}} \sum_{i} \hat{L}_i \cdot \hat{S}_i + U \sum_{i,\alpha} n_{i\alpha}(n_{i\alpha} - 1) \qquad (2.4.1)$$

where $\hat{c}_{i\alpha}$ is the annihilation operator for an electron in orbital α at site i, $n_{i\alpha} = \hat{c}_{i\alpha}^{\dagger} \hat{c}_{i\alpha}$ is the corresponding occupation number, t is the hopping amplitude, λ_{SO} is the atomic SOC entangling spin $\hat{S}_i$ and angular momentum $\hat{L}_i$, and U is the Hubbard repulsion potential. A schematic phase diagram, a rough guide of the novel type of quantum phases, is drawn in terms of the relative strength of the Coulomb interaction U/t and the SOC λ_{SO}/t by Witczak-Krempa *et al.* [3].
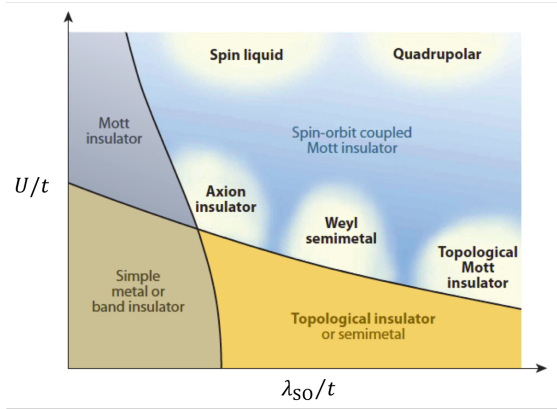
Figure 2.4.1 Sketch of a generic phase diagram based on Eq. (2.4.1). (taken from ref [3])

In the region, where the SOC is negligible, the simple metal could become so-called Mott insulator caused by the strong Coulomb repulsion U (electronic correlation), which can be understood according to the Hubbard model [110,111]. In the weakly correlated regime but relatively strong SOC, topology is found to play a crucial role in these system, and has led to the discovery of the topological band insulator [112,113] and subsequently its metallic analogue Weyl semimetal [114,115]. Upon increasing electronic correlations in the regime with relatively strong SOC, spin-orbit coupled Mott insulators with unusual local moments

can emerge, meanwhile their collective behavior gives rise to unconventional types of magnetism including the formation of quadrupolar correlations or the spin liquid states [116,117].
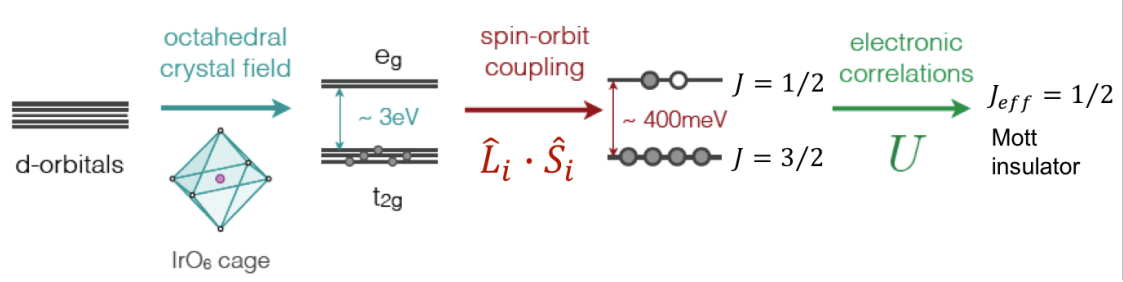
Figure 2.4.2 Formation of the novel effective $J_{eff} = 1/2$ states due to strong spin-orbit coupling in Sr_2IrO_4. (taken from ref [2]).

One of the examples due to the effects of these interactions is the 5d transition metal oxide, iridates. The Ir^{4+} has 5 electrons in the 5d orbital. As shown in Figure 2.4.2, with the octahedral CEF effect, the manifold of 5d orbital will split into two groups, the low-lying triplet t_{2g} and higher energy doublet e_g states when considering only spin degeneracy. This puts the five electrons with a total spin moment $S = 1/2$ into the t_{2g} state with an effective orbital moment $L = 1$. The strong spin-orbit coupling then further lifts the degenerate t_{2g} state, and results in a system with a fully filled band $J = 3/2$ (quartet) and a half-filled band $J = 1/2$ (doublet). The gap between two J bands is proportional to the strength of SOC, $\sim \lambda_{SO}/2$ [109]. The reduced bandwidth of the latter then allows for the opening of a Mott gap even for the relatively moderate electronic correlations U in 5d (and 4d) compounds. This novel $J_{eff} = 1/2$ state was first observed experimentally in the perovskite iridate Sr_2IrO_4 by using resonant x-ray absorption [2,118]. Neutron diffraction on single-crystal Sr_2IrO_4 reveals an ordered moment of 0.208(3) μ_B/Ir, agreeing with the theoretical prediction [119].

For the compounds pyrochlore iridates series, which exhibit metal-insulator transition (MIT) at sufficiently low temperature [120,121] (Figure 2.4.3 (b)), the novel effective $J_{eff} = 1/2$ state of Ir^{4+} is also expected. Taken into account the electron correlation, i.e. Hubbard potential U, novel topological phases may also emerge in this system [109]. As shown in Figure 2.4.3 (a), besides the insulating and metallic states for large and small values of U respectively, a topological phase known as the Weyl semimetal state, in which the bands touch at the Fermi level with linear dispersion through a node termed as Weyl point appearing in pairs with opposite chirality [115,122], is possible for intermediate values of U, when the AIAO magnetic order of Ir^{4+} breaks the time-reversal symmetry (TRS) [114,123,124].
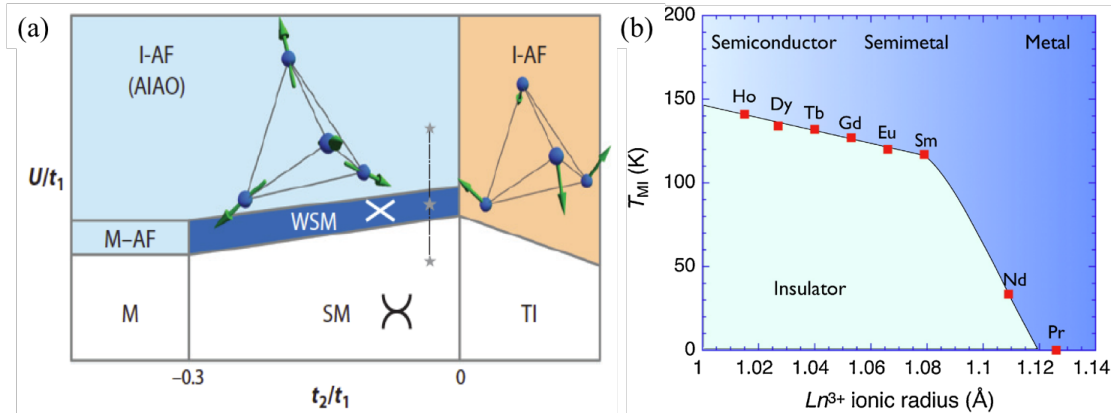
Figure 2.4.3 (a) Sketch of the predicted phase diagram for pyrochlore iridates. I: insulator, M: metal, TI: topological insulator, SM: semimetal, WSM: Weyl-semimetal. (taken from ref [3,114]) (b) Phase diagram of the pyrochlore iridates $Ln_2Ir_2O_7$ based on transport and magnetization measurements. (taken from ref. [121])

The nature of the AIAO order of Ir^{4+} in the magnetic insulator phase has attracted considerable interests in the community. For the pyrochlore iridates compounds with MIT, magnetization measurements display a clear bifurcation between the zero-field cooled and field-cooled DC susceptibilities at T_{MI}, indicating a magnetic phase transition. As this feature appears to be relatively independent of whether or not the Ln^{3+} is magnetic or not, it has been suggested that this feature is caused by the magnetic ordering of the Ir^{4+} sublattice alone [120,121,125]. Muon-spin relaxation measurement has been performed on Eu-[126], Nd-[127], Yb- [128], and Y- [128] pyrochlore iridates. A well-defined muon-procession frequency continuously rises below TMI, indicating a long-range order with commensurate structure. Recent investigations of Eu- [129] and Sm- [130] pyrochlore iridates by resonant X-ray scattering have confirmed that the ordered state of Ir^{4+} is the AIAO configuration. Some have argued in the literatures that the AIAO order of Ir^{4+} could be observed in $Nd_2Ir_2O_7$ based on a subtle comparison of the intensity ratio of magnetic peaks in neutron powder diffraction patterns [131,132]. Unfortunately, a direct observation of the ordered state of Ir^{4+}, for instance in $Y_2Ir_2O_7$, via neutron scattering has not been achieved so far mainly due to a combination of the small magnetic moment of Ir^{4+} and the strong neutron absorption of iridium [133].

2.4.2. Interactions between Ln^{3+} and Ir^{4+} in pyrochlore iridates

Now we turn our attention to the interactions between the Ln^{3+} and Ir^{4+}. As discussed in the previous subsections, the f-electrons can carry a net magnetic moment in a Kramers (Ln =

Nd, Dy, Sm, Gd, and Yb) doublet or a non-Kramers doublet (Pr, Tb, Ho). Given that the strength of the magnetic exchange interaction between Ln^{3+} in pyrochlore oxides is around 1 K, any possible magnetic order of Ln^{3+} is expected to occur at low temperatures, e.g. below 10 K. Thus, if the Ir^{4+} ions order magnetically at high temperature, the rare-earth magnetic moment may feel an effective *molecular magnetic field* generated by the ordered moment of the surrounding Ir^{4+}. Such a molecular field is expected to be along the local $\langle 1\ 1\ 1 \rangle$ direction, as the in-plane components of the magnetic moments on a hexagon of 6 surrounding Ir^{4+} ions in the AIAO configuration are cancelled out, and only the out-of-plane components are retained at the Ln^{3+} position. Thus, such a molecular field may polarize the spin of Ln^{3+} and lead to the AIAO magnetic long-range order of Ln^{3+} for the ions with easy-axis anisotropy, or may suppress the XY order behaviors for the ions with easy-plane anisotropy. As shown in Figure 2.4.4 (a), magnetic Bragg peaks were observed in the neutron powder diffraction of $Tb_2Ir_2O_7$, indicating the long-range order of Tb^{3+} [134]. As the temperature decreases, the ordered moment of Tb^{3+} increases without any sign for saturation. This behavior is interpreted as the induced ordering [131,134]. For the easy-plane single-ion anisotropic Er^{3+} and Yb^{3+}, there is no indication of any long-range magnetic order down to 0.2 K, which will be discussed in Chapter 4.
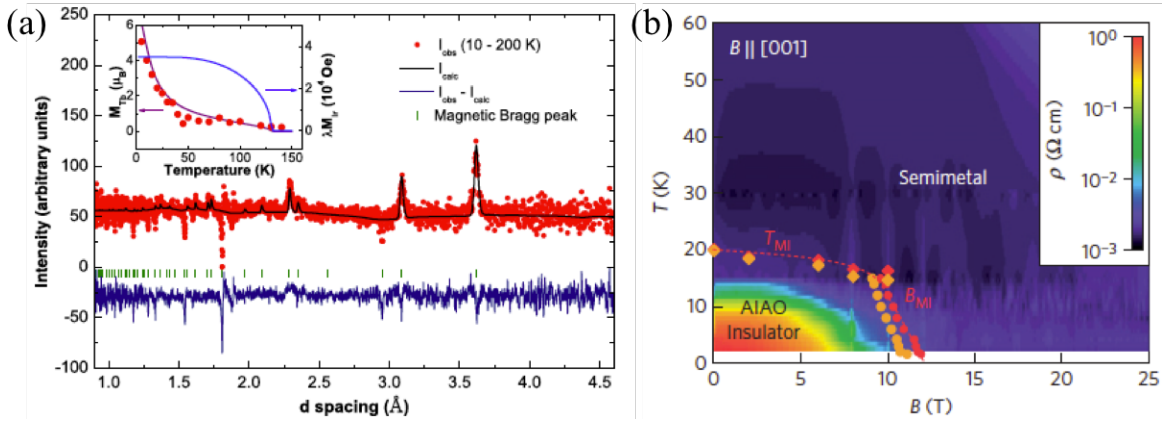
Figure 2.4.4 (a) Magnetic component of neutron powder diffraction of $Tb_2Ir_2O_7$, the insert shows the temperature dependence of the ordered moment of Tb^{3+}. (taken from ref [134]) (b) Temperature-field phase diagram for $Nd_2Ir_2O_7$ under a magnetic field along the [0 0 1] direction. (taken from ref. [135])

In the non-metallic or insulating region in the phase diagram in Figure 2.4.3 (b), e.g. for Ln^{3+} ions with smaller ionic radii, the exchange coupling between the rare-earth and Ir spins is expected to be relatively weak due to the localized nature of $4f$ electrons, so the influence on the Ir magnetism from the localized rare-earth ions would be negligible. However, in the

semi-metal region, e.g. for $Nd_2Ir_2O_7$ and $Pr_2Ir_2O_7$, the magnetic coupling between rare-earth and Ir may be nontrivial and can induce various intriguing phases [136]. For instance, theoretical work has suggested that such a coupling in the form of *f-d* exchange interaction may in turn help to stabilize the Weyl semimetal and axion insulator phases in $Pr_2Ir_2O_7$ [137]. Another example is $Nd_2Ir_2O_7$, which exhibit induced magnetic order with AIAO configuration below T_{MI} [128,131]. A large magnetoresistance was observed in the polycrystalline samples, implying that the electronic states are strongly coupled to the magnetic properties of the compounds [138]. Further investigations of magneto-transport on single crystal samples under applied magnetic fields also support this scenario [135,139]. As shown in Figure 2.4.4 (b), the quantum metal-insulator transition can be achieved by applying magnetic fields along the [0 0 1] direction. This can be understood as follows: when the magnetic field along [0 0 1] direction is applied, the AIAO magnetic configuration of Nd^{3+} can be changed to the 2I2O configuration; therefore, the effective molecular field coming from the 2I2O magnetic configuration of Nd^{3+} may suppress the AIAO magnetic state of Ir^{4+}. Meanwhile, the associated insulating behavior is suppressed and a semi-metallic state arises. This fact indicates that the magnetic-field induced switching of the 4f moment configuration of Nd^{3+} may strongly modify the topological nature of the 5d band structure of Ir.

To conclude, the pyrochlore iridates can provide a fascinating platform for the study of the exotic quantum states and emergent phenomena in a combination of frustration, SOC, and band topology. The coexistence and competition of these interactions may result in an incredibly rich number of interesting or novel ground states that may be tuned by any one of these effects. Furthermore, it has been demonstrated that the application of moderate external magnetic fields can be used to efficiently tune the ground states, thus opening a new avenue for future information technology.

Chapter 3. Experimental Techniques

3.1. Sample preparation

In the experimental condensed matter physics investigation, sample preparation is always the first step to start the program. Samples of high quality are essential for the experimental investigations so that the intrinsic physical signatures can be obtained to compare with the theoretical models. Poor-quality samples are often so 'dirty' that complicated situations may arise from the influences of defect, distortion, off-stoichiometry and so on. On the other hand, a 'dirty' sample sometimes may give us surprises, for example, in the discovery of the iron-based superconductors [140]. The pyrochlore compounds introduced in the previous chapter are oxides, which by nature are ceramic materials. Due to the high melting points of most oxide starting materials, they cannot be simply melted or deposited like intermetallic compounds. Rather, these compounds can be fabricated through high-temperature solid-state reactions that occur between the starting materials at high temperatures for days to form the desired phase.

3.1.1. Solid-states reaction [141]

Solid-state reaction is the most widely used method for the preparation of polycrystalline phases of inorganic solids from a mixture of solid-state starting materials. The advantage of this method is the wide availability of starting materials and the low cost for a bunch of sample preparations. Here we will give an example of A_2O_3(solid) + BO_2(solid) $\rightarrow$ $A_2B_2O_7$(solid, pyrochlore type) to illustrate in detail the mechanism and characteristics of a solid-state synthetic reaction, as well as the procedures for sample preparation.

As shown in Figure 3.1.1, under certain high-temperature conditions, the reaction can proceed at the crystal boundaries of A_2O_3 and BO_2 crystallites and form a product layer of pyrochlore type $A_2B_2O_7$. The first stage of this reaction is to form nuclei of $A_2B_2O_7$ crystallites at the crystal lattice of reactants, or in adjacent to their boundary. The nucleation reaction is very difficult because the nuclei are from different reactants and are different in structure. Therefore, nucleation needs to go through structural rearrangement, including

breaking the cation-anion bonds of reactant molecules, releasing, diffusing and repositioning of A^{3+} and B^{4+} ions in the crystal lattice. The whole process can be achieved at high temperatures, thus leading to the formation of nucleus. Similarly, the growth of nucleus is also not easy. A^{3+} and B^{4+} ions in the reactants need to mobilize through two boundaries (Figure 3.1.1 (a)) and to grow on the nucleus to thicken the product layer. It is obvious that the controlling step of the reaction is the diffusion of A^{3+} and B^{4+} ions, which is favored by increasing the temperature, and so is the reaction. On the other hand, the reaction rate decreases with the thickening of the product layer. As we know the diffusion of ions is mainly driven by their concentration gradient. The diffusion rate at certain temperature will decrease when the concentration gradient becomes smooth due to the thickening of the product layer. Creating fresh reaction surface by regrinding the mixtures is necessary to obtain high efficiency of sample preparation.
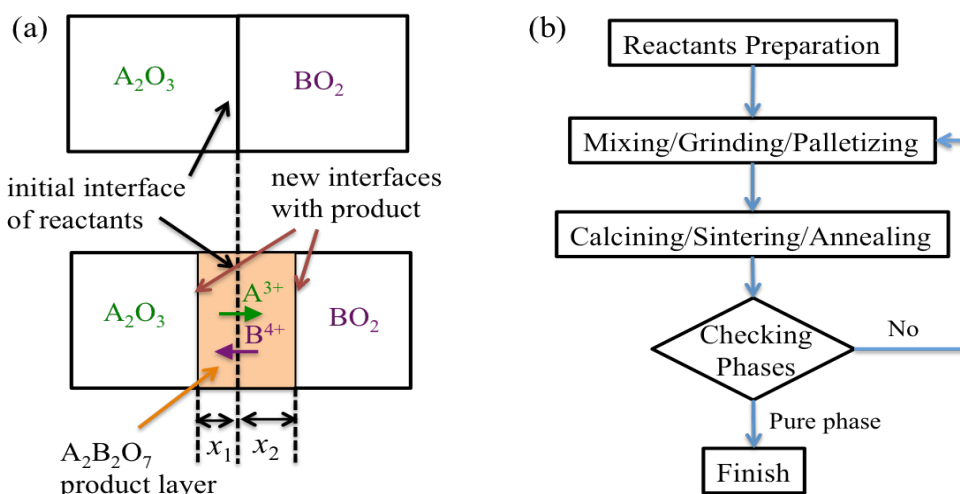
Figure 3.1.1 (a) Schematic diagram of the solid-state reaction mechanism. (b) Typical process routine of sample preparation by solid-state reaction.

In summary, three main factors influence the rate of solid-state reaction: (1) the surface and contacting areas of the reactants; (2) the nucleation rate of the product; and (3) the ionic diffusion rate at the phase boundaries and particularly through the product layer.

The complicated process of solid-state reaction can be simply illustrated as follows (Figure 3.1.1 (b)). (1) The starting materials have to be selected carefully according to the target product and reaction routine. One of the principles is that the elements of the starting materials and the product should be of similar ionic valences. Otherwise additional equipment or process has to be applied. The preheating process is necessary for most of reactants to expulse the absorbed water before weighing the starting materials. Sometimes

the phases of starting materials are also checked beforehand by X-ray powder diffraction (XRPD) to track the reaction routine. Afterwards, a few grams of starting materials will be weighed according to the reaction equation. The loss of reactants during the reaction has to be take into account. (2) The prepared starting materials or reactants will be mixed together for further reaction. As discussed above, one way to improve the reaction rate is to modify the surface area and the contacting area of the reactants. Thus the long-time crushing, milling and pressing steps for the mixture are necessary. Sometimes in order to obtain the reactants with high specific surface area and high surface activity, various additional chemical routes, such as sol-gel method, have to be used. (3) The palletized mixture is then placed in furnace to react at high temperature. Sometimes the mixture is pre-heated at a lower temperature for pre-reaction and nucleation of the new phase, known as the calcining process. Then, a higher temperature is used for further reaction and growth of nucleus of target, known more generically as the sintering process. After calcining and sintering processes, the product may still contain inhomogeneous phases, oxygen vacancies and internal strains. To minimize the possible defects in the product, the sample can be heated up to a certain temperature and stay for a few hours, and then slowly cool down to room temperature, sometimes in a specific atmosphere, which is called the *annealing* process. (4) During the sintering process, the phase analysis of the products has to be performed repeatedly, for example by using XRPD. The controlling step of the reaction – ion diffusion through the phases – is influenced by many factors (such as temperature, thickness of the new phases). Therefore, the composition and the structure of the product from this type of reaction are usually nonstoichiometric and heterogeneous. Several cycles of grinding and sintering processes are necessary to obtain the targeted phase, for instance, in which the impurity phases should no longer be detectable by XRPD.

3.1.2. Preparation of pyrochlore iridates

In general, the pyrochlore structure is favored when the ratio of ionic radii of the A and B cations (written as r_A/r_B) is greater than 1.46 [25]. With $r_A/r_B < 1.46$, the defected-fluorite structure tends to form. It has been well established that the rare earth iridates "227" generally form a pyrochlore structure from Praseodymium to Lutetium, as well as Yttrium [120,121,125,142]. In the literature, IrO_2 and rare earth oxides (Pr_6O_{11}, Tb_4O_7 and Ln_2O_3 for others) were used as the starting materials. The molar ratio of Ln/Ir was chosen to be 1:1.1 after taking into account the evaporation of Ir during the sintering process. After grinding the starting materials together, the mixtures were pelletized and sealed into a Pt tube. Then, they were heated at 1150 to 1250 ^{o}C for a few days in a vacuum silica tube, with several

29

intermediate grindings and supplements of the reactant IrO_2. However, IrO_2 is more expensive than Ir metal, and tends to decompose into IrO_3(gas) and Ir metal(solid) above 950 ^{o}C. A high sintering temperature means relatively lower usage of IrO_2. The amount of IrO_2 loss during sample preparation is non-negligible if we use the above method to prepare several grams of samples of each pyrochlore iridate for neutron scattering experiments. Using metallic Ir as the starting material and a lower sintering temperature may be the way to better control the cost of sample preparation.

In order to control the cost of sample preparation of pyrochlore iridates, we optimized the parameters of the fabrication processes by synthesizing $Pr_2Ir_2O_7$ under different conditions. The Pr_6O_{11} powder and Ir metal powder were used as the starting materials with the molar ratio of Pr/Ir is at 1:1.05. Then, the starting materials around 0.7 grams in total were mixed and grinded in a ball-milling machine. The mixture was pressed into pellets and sintered in a tube furnace in different atmosphere as given in Table 3.1.1. Several intermediate regrindings were employed about every 20 hours in the sintering process, and XRPD was employed to check the sample phases regularly. No additional Ir or IrO_2 was added during regrinding.

Table 3.1.1 $Pr_2Ir_2O_7$ preparation under different conditions

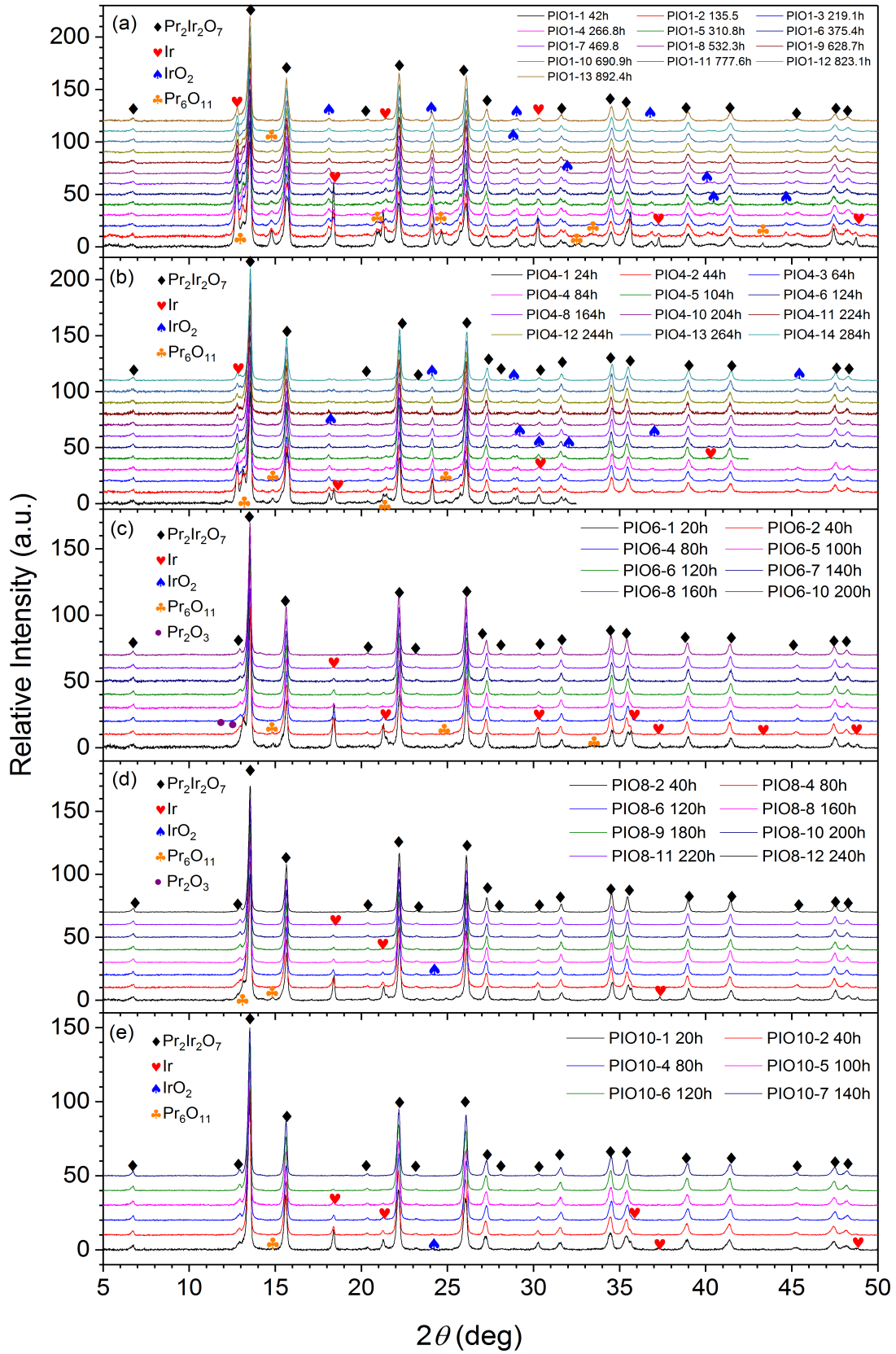| Batch	Temperature (^{o}C)	Atmosphere	Grinding	Flux
PIO1	950	Air	Reactants only	-
PIO4	1050	Oxygen	Reactants only	-
PIO6	1050	Air	Reactants only	-
PIO8	1050	Air	With alcohol	-
PIO10	1050	Air	With alcohol	KF

Figure 3.1.2 The evolution of various phases during the sintering process of the $Pr_2Ir_2O_7$ preparation under different conditions.

Figure 3.1.2 shows the evolution of various phases during sintering of the $Pr_2Ir_2O_7$ preparation of the selected batches. The experimental conditions of the different batches are listed in Table 3.1.1. For the batch PIO1 sintered at 950 ^{o}C for one month, there were still impurity phases in the sample. Other batches sintered at 1050 ^{o}C can give rise to the pure phase of $Pr_2Ir_2O_7$ after sintering for the maximum of 14 days. It is clear that the sintering temperature plays an important role because it significantly influences the reaction rate by increasing the overall diffusion rate. Pure O_2 atmosphere does not help the production of the pure $Pr_2Ir_2O_7$ phases, see for instance, the batch PIO4 in comparison with PIO6. There are always small amounts of IrO_2 in the sample, which was not included in the starting materials. Due to the enhancement of the reaction rate for $Ir + O_2 \rightarrow IrO_3$ in pure O_2, the further decomposition of IrO_3 to IrO_2 and Ir will take place, thus resulting in the residual IrO_2 and Ir metal in the sample. One could also promote the production of $Pr_2Ir_2O_7$ by improving the surfaces of reactants particles. The batch PIO8 was grinded with alcohol. The usage of alcohol during grinding can avoid the powder adhesions with the surface of the balls and inner wall of the jar, which often happens during dry grinding. Grinding with alcohol can also improve the homogeneity of particle size of the reactants. The batch PIO10 was prepared by a new flux method using KF as flux which is used for single crystal growth of $Pr_2Ir_2O_7$ and $Eu_2Ir_2O_7$ [143]. KF melts above 858 ^{o}C. It will form a liquid interface surrounding the reactants and dissolve the reactants. The reaction in the liquid interfaces is faster than that in solid interfaces by direct contact of particles. With seven days of sintering, we obtained the pure phase of $Pr_2Ir_2O_7$, which is the fastest batch we ever obtained. The small amount of KF will be evaporated during sintering and the residual KF becomes negligible. According to the above experiments, we have optimized the recipe for the preparation of $Pr_2Ir_2O_7$ as follows. The starting materials were Pr_6O_{11} and Ir metal with the molar ratio of Pr/Ir at 1:1.05. Then, they were mixed and grinded with alcohol and KF (around 1% of the mixture's mass) in a ball-milling machine for half hour. After pelletizing using an isostatic pressurizer, the pellets were sintered at 1050 ^{o}C in air. Regular regrinding process was employed with the period of 20-36 hours sintering. This process was repeated until the sample became single-phase within the detection limit of XRPD (e.g. a few percent). Finally, the sample was annealed in air with a cooling rate of 100 ^{o}C/hour from 1050 ^{o}C to room temperature to minimize the defect in the sample. This recipe was also applied to the preparation of other pyrochlore iridates compounds.

3.1.3. Preparation of pyrochlore hafnates

It has been established that the pyroclore structure can also be formed from La to Tb in rare earth hafnates compounds in "227" phases. The defect fluorite structure will be favored for Ln cations smaller than Gd [30]. We have thus synthesized the $La_2Hf_2O_7$, $Pr_2Hf_2O_7$ and $Nd_2Hf_2O_7$ powders. Comparing to the preparation of pyrochlore iridates, the synthesis of pyrochlore hafnates is quite simple but requires higher sintering temperature above 1400 ^{o}C. All reagents were obtained from Chempur with purities generally better than 99.99%. Reagents were preheated at 1000 ^{o}C overnight before use. The mixtures were prepared by finely mixing stoichiometric amounts of HfO_2 and rare earth oxides (La_2O_3, Pr_6O_{11}, Nd_2O_3), and then heating to 1250 ^{o}C for 24 h. The products were then ground into fine powders with alcohol, pressed into pellets, and heated to 1450 ^{o}C for 72 h. This process was repeated until a single phase was obtained by checking with XRPD. Finally, all samples were annealed in oxygen from 1200 ^{o}C to room temperature with a cooling rate 100 ^{o}C/h to minimize the sample defects.

3.2. Sample characterization

The sample characterizations include the measurements of laboratory X-ray powder diffraction (XRPD), DC magnetization and heat capacity (HC).

3.2.1. X-ray powder diffraction (XRPD)

X-ray powder diffraction (XRPD) is a fast and non-destructive powerful method for qualitatively and quantitatively analyzing the phases and crystal structure of polycrystalline samples. During the sample preparation discussed above, the laboratory XRPD was frequently used to verify the phases of the sample. The diffraction process is described by the well-known Bragg's law (as shown in Figure 3.2.1), given by:

$$2d_{hkl}sin\theta = n\lambda \tag{3.2.1}$$

where λ is the wavelength of the used radiation, d_{hkl} is the distance between the parallel lattice planes with Miller indices (hkl), θ is the angle between the incident (or diffracted) beam and the relevant lattice planes; n is an integer, referred to as the order of the diffraction, and is often unity.

When Bragg's law is satisfied for a given wavelength λ, x-ray beams scattered from successive planes in the crystal will superimpose coherently at the certain angle θ. Meanwhile an intensity maximum can be recorded in the detector (see Figure 3.2.1 (a)). One can measure the intensity of the scattered beam as a function of the scattering angle 2θ, which is called the diffraction pattern. Since the diffraction pattern corresponds to the phases of

matter, e.g. the crystal structure, it can be treated as the fingerprint of matters to simply verify the phases. A full-profile refinement of XRPD pattern such as the Rietveld method can provide more detailed crystallographic information of the sample.
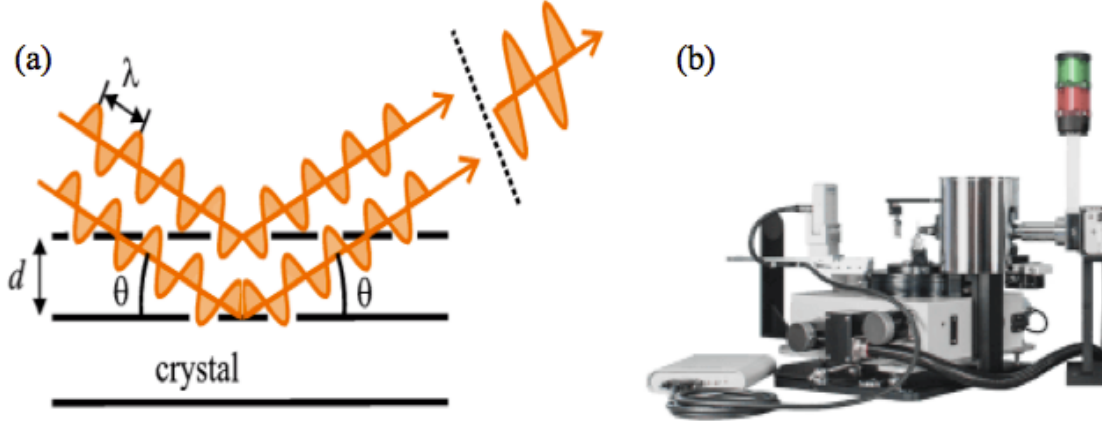
Figure 3.2.1 (a) Illustration of Bragg's law and (b) photo of a STEO XRPD instrument.

3.2.2. Magnetization and MPMS

Magnetization measurements have been performed with Quantum Design MPMS (Magnetic Property Measurement System, see Figure 3.2.2 (a)) at JCNS-2, Forschungzentrum Juelich and at IFP, Karlsruhe Institute of Technology. This magnetometer gives access to a magnetic field range from -7.0 to 7.0 Tesla, and a temperature from 2 to 300 K based on the ^{4}He cryostat. The DC magnetization curve $M(H)$ and the bulk magnetic susceptibility $\chi(T)$ can be obtained.

The core component of MPMS is a SQUID (Superconducting Quantum Interference Device) sensor, which consists of two superconductors separated by thin insulating layers to form two parallel Josephson Junctions. Figure 3.2.2 (c) shows a schematic view of SQUID. The Josephson effect can maintain a current with a zero voltage through the tunneling of Cooper pairs below the superconducting critical current I_c. The Josephson junction's current is enslaved to I_c for a static magnetic flux. For a variation of the magnetic flux inside the loop, a sinusoidal screening current appears in the superconducting ring with a period equal to the number of quantum flux changes, and thus the period of the variation of the voltage at the Josephson junction can be related with one flux quantum,

$$\Phi_0 = \frac{2\pi\hbar}{2e} = 2.0678{\times}10^{-15} \; tesla \cdot m^2 \tag{3.2.2}$$

where $\hbar$ is the reduced Plank constant and e is the elementary charge. By careful design of the electronics, very small amounts of magnetic flux can lead to large changes in the detected current. The sample magnetic moment can be determined down to the order to 10^{-8} emu (10^{-11} J/T).
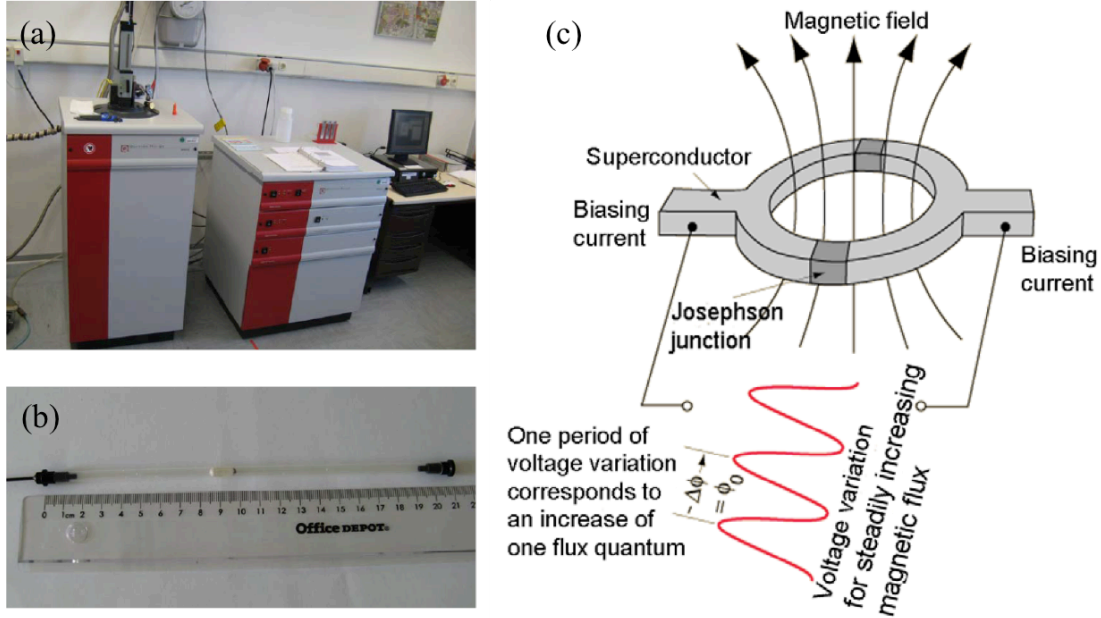
Figure 3.2.2 (a) Picture of Quantum Design MPMS system, (b) prepared sample mounted to MPMS sample, (c) schematic view of the SQUID sensor.

In this thesis, the sample was sealed in a gelatin capsule, and then attached to a non-magnetic rod via a plastic straw and passed through sets of superconducting coils at a frequency of a few Hz. Figure 3.2.2 (b) shows an example of mounted sample ready for MPMS measurement. It should be noted that the DC susceptibility in this thesis is obtained by $\chi = M/H$, where M is the measured magnetization and H is the small applied magnetic field during measurement. For purpose of exploring the effect of external magnetic field on the magnetic ground state, samples were cooled to base temperature $\sim$ 1.8 K in two conditions: with no applied field (zero-field cooled (ZFC)) and in a finite field (field cooled (FC)). In all measurements, samples were first zero-field-cooled, then a magnetic field around $\sim$ 1 kOe was applied and the magnetization of sample was measured while slowly warmed up to above 300 K. The sample is then field-cooled under the applied field and measured during the warming process again in case of the existence of a significant thermal hysteresis around a transition.

3.2.3. Heat capacity and PPMS

The heat capacity (or specific heat) measurements have been performed on a Quantum Design PPMS (Physical Property Measurement System) at JCNS-2, Forschungzentrum Juelich. With the combination of standard liquid ^{4}He cryostat and ^{3}He-^{4}He dilution insert the heat capacity can be measured in the temperature range from 50 mK to 300 K. The system is kept adiabatic supported by a secondary vacuum to ensure no heat losses by exchange gas. The resolution is 10 nJ/K at 2 K. The available maximum magnetic field is 9 Tesla.

Figure 3.2.3 Photography of Quantum Design PPMS equipped with a dilution insert for low temperature heat capacity measurement. The dilution insert components are marked.

The heat capacity is defined as the ratio of the amount of heat, δQ, required to raise the temperature of a material by a unit of temperature:

$$c_x = \lim_{\delta T \to 0} \left(\frac{\delta Q}{\delta T} \right)_x \tag{3.2.3}$$

where x denotes the constraint which can be imposed, such as a constant pressure (p) or constant volume (V). The specific heat C_p is the heat capacity divided by the number of moles of the sample since the heat capacity is an extensive quantity. Note that the difference of measured specific heat in the constant volume or pressure is negligible due to the low compressibility of the solid at low temperature [144].

For heat capacity measurement, PPMS takes the thermal-relaxation method, which measures the response of the sample after a heat perturbation. A flat-plate-shaped sample with a smooth surface was mounted on the micro-calorimeter platform (the puck shown in the left of Figure 3.2.4) linked by four threads with thermal conductance K_p to the cryostat

(Bath). Apiezon N grease was used to increase the thermal conductivity between the micro-calorimeter platform and the sample. The puck with an appropriate amount of the grease has to be measured separately and subtracted from the raw data of the sample measurements to obtain the absolute heat capacity of the sample.
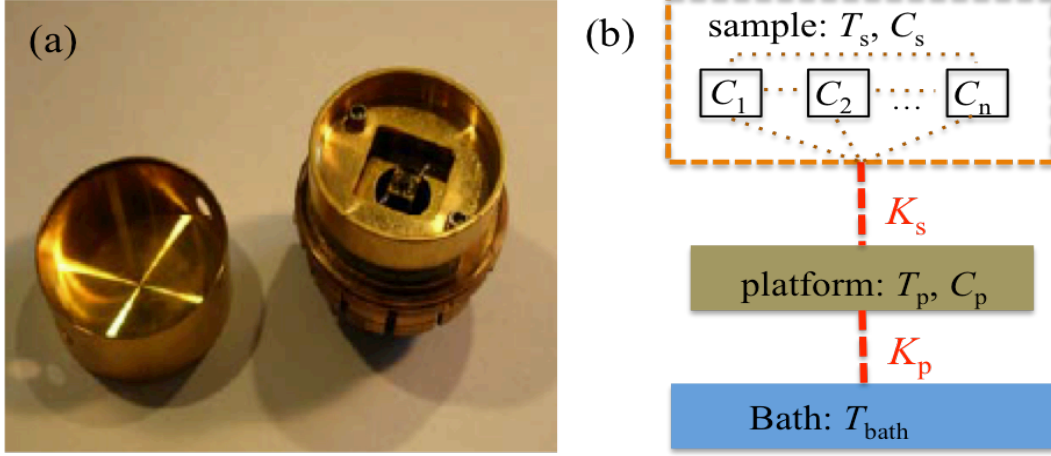
Figure 3.2.4 (a): Picture of the heat capacity puck for standard cryostat. (b): Schematic illustration of the method of thermal relaxation to measure the heat capacity on PPMS.

Figure 3.2.4 (b) shows a simplified experimental setup scheme of the thermal-relaxation method. The T_{bath}, T_p and T_s denote the temperature of the cryostat, the platform and sample with grease, respectively. The K_p and K_s are the thermal conductance between the cryostat (Bath) and the platform, and between the platform and the sample, respectively. $P(t)$ is the heating power as a function of time. The effect of heat flowing between the platform and the sample, and the effect of heat flow between the sample platform and puck can be simulated by a two-tau model.

$$C_p \frac{dT_p}{dt} = P(t) - K_p\big(T_p(t) - T_{bath}\big) + K_s\big(T_s(t) - T_p(t)\big)$$

$$C_s \frac{dT_s}{dt} = -K_s\big(T_s(t) - T_p(t)\big)$$

(3.2.4)

When heat power $P(t)$ is applied to increase the sample temperature from T_0 to $T_0 + \Delta T_1$ at a time $t_f \rightarrow \infty$. The sample temperature can be expressed as:

$$T_s(t) = T_0 + \Delta T_1 \left(1 - \exp\left(-\frac{t}{\tau_1}\right)\right)$$

(3.2.5)

where $\Delta T_1 = P/K_p$ and $\tau_1 = (C_p + C_s)/K_p$ is the relaxation time. Then, cutting the heating power at a time t', the sample temperature relaxes down to the temperature set point from $T_s(t') = T_0 + \Delta T_2$ to T_0:

$$T_s(t) = T_0 + \Delta T_2 \exp\left(-(t - t')/\tau_1\right) \tag{3.2.6}$$

Thus fitting the rising and cooling temperature curves as a single exponential function gives access to the specific heat of the sample. As shown in Figure 3.2.5 (a), the Heat Capacity software of PPMS can automatically fit the temperature relaxation data with the two-tau model and give the heat capacity value of the sample.

However, a problem occurs frequently for non-metallic and pressed powder samples in the temperature range below 1 K. As shown in Figure 3.2.5 (b), the relaxation temperature exhibits an initial rapid drop that is non-exponential in shape, followed by a single, slow exponential one, because the parasitic resistance is internal to the sample itself. This is called the distributed τ_2 effect [145]. The simple two-tau model (two separated single exponential function fitting) can no longer describe the temperature relaxation very well. Multiple exponential terms have to be considered in the function Eq. (3.2.5) and Eq. (3.2.6) to simulate the thermal relaxation between different intra parts of sample C_1, C_2 … C_n. And the measurement time of temperature is required to be long enough to reach the thermal equilibrium. Unfortunately, the Heat Capacity software of PPMS is not suitable to perform multiple-exponential fit. Thus, the data points with sample thermo-coupling below 80% cannot be trusted and have been deleted in our results.
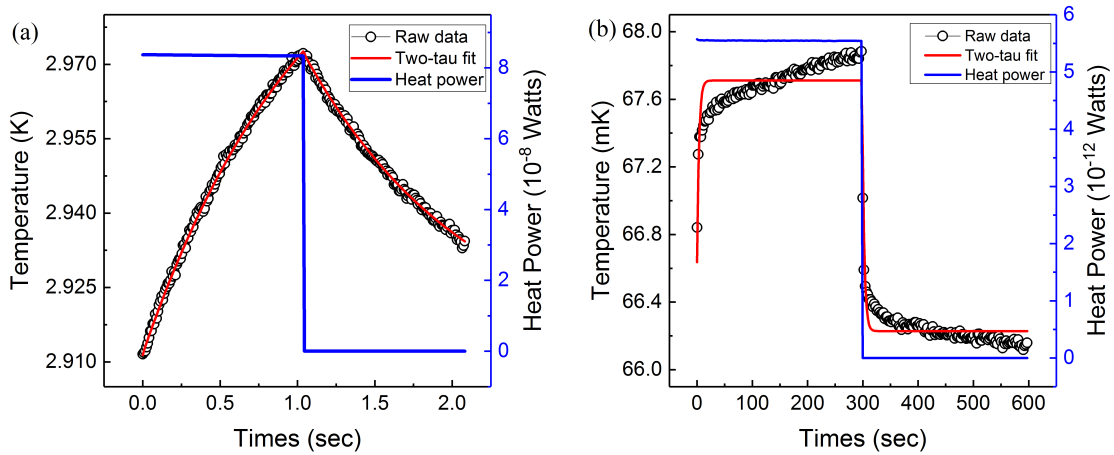
Figure 3.2.5 (a) Two-tau model fitting of the sample temperature. Raw data are displayed by black circles. The blue line is the heat pulse. Red line is a fit using Eq. (3.2.5) and Eq. (3.2.6). (b) Unsuccessful two-tau fitting of the temperature curve due to the distributed τ_2 effect at extremely low temperatures.

3.3. Neutron scattering

Neutrons are charge-neutral particles that carry a nuclear spin 1/2 with a magnetic moment of $\mu = -1.91\,\mu_N$ (μ_N is the nuclear magneton). The weak interaction between neutrons and

charge particles of electrons and protons leads to a large penetration depth of neutrons in matter. The neutrons can interact with the magnetic fields due to the unpaired electrons in materials and the nuclear potential of atomic nucleus. Both interaction strengths are comparable in regards to their scattering probability. The kinetic energy of neutrons associated the de Broglie wavelength λ is given by:

$$E = k_B T = \frac{mv^2}{2} = \frac{h^2}{2m\lambda^2} = \frac{81.81}{\lambda^2} \tag{3.3.1}$$

where $h = 2\pi\hbar$ denotes the Planck constant and v is the velocity of neutron in km/s, energy E is in meV, temperature T in K, λ in Å. Thus $E[\text{meV}] = 81.81/\left(\lambda[\text{Å}]\right)^2$ With typical wavelengths of thermal and cold neutrons from 1 Å to 6 Å, they approximately match the lattice d-spacing of materials and their associated kinetic energies E from 82 to 2 meV also match the energy scales of the elementary excitations in condensed matters [146]. These properties of the neutron allow us to study the static and dynamic properties of materials on atomic scale via scattering methods. This subsection is dedicated to introduction of neutron scattering and three neutron scattering techniques used in this thesis.
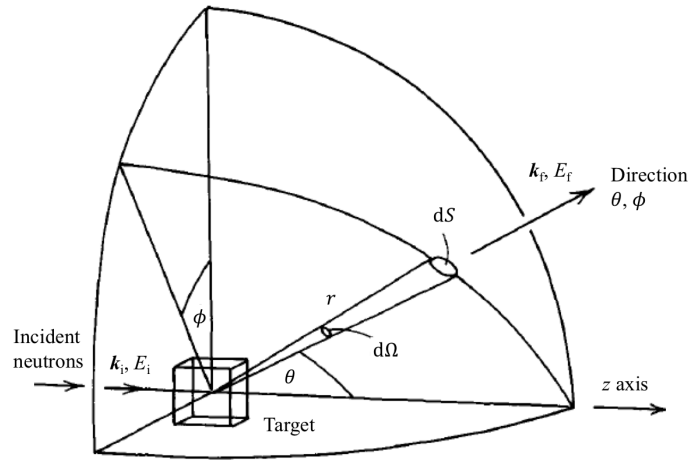
Figure 3.3.1 Geometry for a scattering experiment (taken from [147]).

3.3.1. Introduction to neutron scattering

For an incident beam of neutrons with energy E_i, one can obtain the scattered neutrons with various energies E_f in a small solid angle $d\Omega$ with various directions (θ, ϕ), as shown in Figure 3.3.1. If the incident flux is Φ, the partial differential cross section is defined as:

$$\frac{d^2\sigma}{d\Omega dE_f} = \frac{\text{number of neutrons scattered per second into } d\Omega \text{ with energy between } E_f \text{ and } E_f + dE_f}{\Phi d\Omega dE_f} \tag{3.3.2}$$

The theoretical expressions for the partial differential cross section can be obtained from Fermi's Golden Rule:

$$\frac{d^2\sigma}{d\Omega d\omega} = \left(\frac{m}{2\pi\hbar^2}\right)^2 \frac{k_f}{k_i} \sum_{\alpha_f,\sigma_f} \sum_{\alpha_i,\sigma_i} p_{\alpha_i} p_{\sigma_i} \left|\langle k_f, \sigma_f, \alpha_f | \hat{U} | k_i, \sigma_i, \alpha_i \rangle\right|^2$$

$$\times \delta(\hbar\omega + E_{\alpha i} - E_{\alpha f})$$

(3.3.3)

where k_i and k_f are the incident and the outgoing wavevectors of neutrons with spin states σ_i and σ_f, respectively, and p_{σ_i} is the polarization probability. $|\alpha_i\rangle$ denotes the initial state of the sample, with energy $E_{\alpha i}$ and thermal population factor p_{α_i}, and its final state is $|\alpha_f\rangle$. The δ-function describes the law of energy conservation. $\hat{U}$ is the interaction operator between neutron and the sample, which depends on the specific scattering process. There are two main interaction processes of neutrons with matters, i.e. the nuclear and the magnetic interaction. The major task in the evaluation of the neutron cross-section is the calculation of the transition matrix element in Eq. (3.3.3).

For nuclear scattering, the nuclear potential is well approximated by Fermi pseudopotential:

$$\hat{U} = \frac{2\pi\hbar^2}{m} \sum_j b_j \delta(r - \hat{r}_j)$$

(3.3.4)

where r_j is the position of the jth scattering nuclei in the sample and b_j is the corresponding scattering length with magnitude of the order 10^{-12} cm. Within the plane wave description of neutron, one can evaluate the transition matrix element by inserting Eq. (3.3.4) into Eq. (3.3.3). Thus, we obtain the final cross-section formula:

$$\frac{d^2\sigma}{d\Omega d\omega} = \frac{k_f}{k_i} \frac{1}{2\pi\hbar} \sum_{j,j'} b_j b_{j'} \int_{-\infty}^{+\infty} \langle e^{-iQ\cdot\hat{r}_{j'}(0)} e^{-iQ\cdot\hat{r}_j(t)} \rangle e^{-i\omega t} dt$$

(3.3.5)

within $Q = k_i - k_f$ is the scattering vector. For coherent scattering in Bravais lattice, one can simply write above expression as

$$\frac{d^2\sigma}{d\Omega d\omega} = \frac{k_f}{k_i} \frac{\sigma_{coh}}{4\pi} N S(Q, \omega)$$

(3.3.6)

where $\sigma_{coh} = 4\pi b^2$ is the total coherent cross section. $S(Q, \omega)$ is the dynamic structure factor and is given by

$$S(Q, \omega) = \frac{1}{2\pi\hbar N} \sum_{j,j'} \int_{-\infty}^{+\infty} \langle e^{-iQ\cdot\hat{r}_{j'}(0)} e^{-iQ\cdot\hat{r}_j(t)} \rangle e^{-i\omega t} dt$$

(3.3.7)

N is the number of nuclei and t is time. The angle brackets $\langle \cdots \rangle$ denotes the average over initial states. The dynamic structure factor (also called scattering law or scattering function)

$S(\boldsymbol{Q}, \omega)$ depends on the momentum and the energy transferred from neutron to the sample, but not on absolute values of $\boldsymbol{k}_i$ and $\boldsymbol{k}_f$. It contains information on both the positions and motions of the atoms. The goal of most neutron scattering experiments is to measure $S(\boldsymbol{Q}, \omega)$ and thereby to determine the microscopic properties of the system under investigation.

For the case of magnetic scattering by the interaction of a neutron with the magnetic field $\boldsymbol{H}$ due to unpaired electrons in the sample, the operator is given by:

$$\widehat{U} = \widehat{\boldsymbol{\mu}} \cdot \boldsymbol{H} = -\gamma \mu_N \widehat{\boldsymbol{\sigma}} \cdot \boldsymbol{H}$$

$$\boldsymbol{H} = \nabla \times \left(\frac{-2\mu_B \hat{s}}{|\boldsymbol{r}|^3} \right) - \frac{e}{c} \frac{v_e \times \boldsymbol{r}}{|\boldsymbol{r}|^3} \tag{3.3.8}$$

where $\gamma = -1.913$ is the gyromagnetic ratio, $\widehat{\boldsymbol{\mu}}$ is the magnetic moment operator of the neutron, $\widehat{\boldsymbol{\sigma}}$ is a Pauli spin operator. The magnetic field $\boldsymbol{H}$ is given by considering a single electron moving with velocity v_e, $\boldsymbol{r}$ is the distance from the electron to the point at which the field is measured. $\hat{s}$ is the spin operator of electron and μ_B is the Bohr magneton. After the procedure evaluating the transition matrix element in Eq. (3.3.3) for the case of unpolarized neutrons, identical magnetic ions with localized electrons, and spin-only scattering, we obtain the following master formula:

$$\frac{d^2\sigma}{d\Omega d\omega} = \frac{k_f}{k_i} (\gamma r_0)^2 \left(\frac{g_J}{2} f(|\boldsymbol{Q}|) e^{-W(\boldsymbol{Q})} \right)^2 \sum_{\alpha, \beta} \left(\delta_{\alpha\beta} - \frac{Q_\alpha Q_\beta}{Q^2} \right) S^{\alpha\beta}(\boldsymbol{Q}, \omega) \tag{3.3.9}$$

where, $r_0 = 0.2818 \times 10^{-12}$ cm is the classical radius of the electron, g_J is the Lande factor, $f(|\boldsymbol{Q}|)$ is the dimensionless magnetic form factor defined as the Fourier transform of the normalized spin density associated with the magnetic ions, $e^{-W(\boldsymbol{Q})}$ is the Debye-Waller factor due to thermal movements of the magnetic ions. The polarization factor $\left(\delta_{\alpha\beta} - \frac{Q_\alpha Q_\beta}{Q^2} \right)$ implies that neutrons can only couple to the magnetic moments or spin fluctuations perpendicular to the scattering vector $\boldsymbol{Q}$.

The magnetic neutron scattering can originate either from collective excitations like spin waves or from single particle excitations like crystal-filed excitations. For the case of collective excitations of spin system ($j \neq j'$), the dynamic magnetic structure factor $S^{\alpha\beta}(\boldsymbol{Q}, \omega)$ is the Fourier transform of the magnetic pair correlation function:

$$S^{\alpha\beta}(\boldsymbol{Q}, \omega) = \frac{1}{2\pi\hbar} \sum_{j,j'} \int_{-\infty}^{+\infty} e^{i\boldsymbol{Q} \cdot (\hat{r}_j - \hat{r}_{j'})} \langle \hat{S}_j^\alpha(0) \hat{S}_{j'}^\beta(t) \rangle e^{-i\omega t} dt \tag{3.3.10}$$

where $\langle \hat{S}_j^\alpha(0) \hat{S}_{j'}^\beta(t) \rangle$ is the thermal average of the time-dependent spin operators. It corresponds to the van Hove pair correlation function describing the magnetic correlation between spins.

For the case of single-ion excitations, e.g. transition between different crystal-field states $\Gamma_n \to \Gamma_m$, the magnetic scattering law $S^{\alpha\beta}(\boldsymbol{Q}, \omega)$ reduces to

$$S^{\alpha\beta}(\boldsymbol{Q}, \omega) = N p_n \langle \Gamma_n | \hat{J}_\alpha | \Gamma_m \rangle \langle \Gamma_m | \hat{J}_\beta | \Gamma_n \rangle \delta(\hbar\omega + E_n - E_m) \quad (3.3.11)$$

where N is the total number of the magnetic ions and p_n is the Boltzmann population factor of the initial state $|\Gamma_n\rangle$. For experiments on polycrystalline material, the cross section Eq. (3.3.9) has to be averaged in $\boldsymbol{Q}$ space:

$$\frac{d^2\sigma}{d\Omega d\omega} = \frac{k_f}{k_i}(\gamma r_0)^2 \left(\frac{g}{2} f(|\boldsymbol{Q}|)e^{-W(\boldsymbol{Q})}\right)^2 p_n \langle \Gamma_m | \hat{J}_\perp | \Gamma_n \rangle^2 \delta(\hbar\omega + E_n - E_m) \quad (3.3.12)$$

where $\hat{J}_\perp = \hat{J} - \frac{\hat{J}\cdot\boldsymbol{Q}}{Q^2}\boldsymbol{Q}$ is the component of the total angular momentum perpendicular to the scattering vector $\boldsymbol{Q}$, and

$$\langle \Gamma_m | \hat{J}_\perp | \Gamma_n \rangle^2 = \frac{2}{3}\sum_\alpha \langle \Gamma_m | \hat{J}_\alpha | \Gamma_n \rangle^2 \quad (3.3.13)$$

These matrix elements could be obtained according to the local symmetry analysis and Steven operators equivalence. Since crystal-field excitation is a single-ion property, its inelastic neutron scattering signal is usually dispersionless and the intensity decreases with Q according to $f^2(|\boldsymbol{Q}|)$.

In inelastic neutron scattering experiments the energy transfer can be positive or negative, corresponding to neutron energy-loss and energy-gain processes, respectively. An important property of the scattering function is the principle of detailed balance:

$$S(-\boldsymbol{Q}, -\omega) = e^{-\hbar\omega/k_B T}S(\boldsymbol{Q}, \omega) \quad (3.3.14)$$

where k_B is Boltzmann's constant, T is the temperature, with ω is assumed to be positive. This property indicates the fact that the probability of a transition in the sample depends on the statistical weight factor for the initial state, which will be lower for excitation annihilation than for excitation creation [148].

3.3.2. Neutron powder diffraction

The technique to determine atoms and spins arrangement in real space is known as neutron diffraction or elastic neutron scattering ($k_f = k_i$) which measures the single-differential cross section $d\sigma/d\Omega = \int_{-\infty}^{+\infty}(d^2\sigma/d\Omega d\omega)\, d(\hbar\omega)$. For the case of nuclear scattering from periodically arranged atoms (in a crystal), it can be decomposed into two contributions: (1) the incoherent elastic scattering is isotropic and yields a constant background, (2) the coherent elastic scattering provides information about the mutual arrangement of the atoms

and magnetic moments. The coherent scattering from lattice with more than one atom per unit cell obeys Bragg's law Eq. (3.2.1) and its cross-section can be written as:

$$\frac{d\sigma}{d\Omega}\bigg|_{coh} = N_{nuc} \frac{(2\pi)^3}{v_0} \sum_{\tau} |F_{nuc}(\boldsymbol{\tau})|^2 \delta(\boldsymbol{Q} - \boldsymbol{\tau}) \tag{3.3.15}$$

with the so-called unit-cell nuclear structure factor

$$F_{nuc}(\boldsymbol{\tau}) = \sum_j \overline{b}_j \exp(i\boldsymbol{\tau} \cdot \boldsymbol{r}_j) \exp(-W_j(\boldsymbol{\tau})) \tag{3.3.16}$$

where, N_{nuc} denotes the number of unit cells, v_0 is the volume of the unit cell, $\boldsymbol{r}_i$ is the position vector of the j$^{\text{th}}$ atom in the unit cell, $\overline{b}_j = \sigma^j_{coh}/4\pi$ is the associated atom's scattering length. $\boldsymbol{\tau}$ represents the reciprocal lattice vector. The δ-function implies the diffraction condition that the strong reflections can be observed when the scattering vector $\boldsymbol{Q}$ equals to the reciprocal lattice vector $\boldsymbol{\tau}$ of the sample. The Debye-Waller factor $\exp(-W_j(\boldsymbol{\tau}))$ describes the thermal movements of the atomic positions. Thus, (1) one can obtain the information about the size and the form of the unit cell by examining the scattering angles 2θ at which Bragg reflections occur; (2) the atoms positions in unit cell can be obtained by analyzing the intensities of the Bragg reflections through the structure factor; (3) the atomic displacements can be obtained by studying the $\boldsymbol{Q}$-dependence of the Debye-Waller factor.

For the case of magnetic elastic scattering from a periodic magnetic structure, the nuclear structure factor $F_{nuc}(\boldsymbol{\tau})$ has to be replaced by the magnetic vector structure factor as shown in Appendix D. For example, considering only one type of magnetic ion ordered with a magnetic propagation wavevector $\mathbf{k}_{mag}$, its magnetic moment can be expanded in a Fourier series:

$$\boldsymbol{m}_j = \sum_{\mathbf{k}_{mag}} \boldsymbol{m}^{\mathbf{k}_{mag}} \exp(-i\mathbf{k}_{mag} \cdot \boldsymbol{r}_j) \tag{3.3.17}$$

Therefore, the elastic magnetic scattering cross section is given by:

$$\frac{d\sigma}{d\Omega}\bigg|_{mag} = N_{mag} \frac{(2\pi)^3}{v_{mag}} \sum_{\boldsymbol{\tau},\mathbf{k}_{mag}} \left|F^{\perp}_{mag}(\boldsymbol{Q})\right|^2 \delta(\boldsymbol{Q} - \boldsymbol{\tau} - \mathbf{k}_{mag}) \tag{3.3.18}$$

The magnetic vector structure factor is

$$\boldsymbol{F}_{mag}(\boldsymbol{Q}) = p \sum_j f_j(Q) \boldsymbol{m}_j \exp(i\boldsymbol{Q} \cdot \boldsymbol{r}_j) \exp(-W_j(\boldsymbol{Q})) \tag{3.3.19}$$

$$F^{\perp}_{mag}(\boldsymbol{Q}) = \widehat{\boldsymbol{Q}} \times (F_{mag}(\boldsymbol{Q}) \times \widehat{\boldsymbol{Q}})$$

where N_{mag} is the number of magnetic cells and v_{mag} their volume. $p = \frac{\gamma r_0}{2} = 0.2695\times$
10^{-12}cm is the magnetic scattering length, given in Bohr magnetons μ_B. Referring to the δ-function, if the magnetic propagation wavevector $\mathbf{k}_{mag} = (0\ 0\ 0)$, the magnetic Bragg peaks locate at the positions on the nuclear ones, otherwise, satellite peaks appear at the positions $\boldsymbol{Q} = \boldsymbol{\tau} + \mathbf{k}_{mag}$.

As shown in Figure 3.3.2 (a), a powder or polycrystalline sample always contains some crystallites which are properly oriented to fulfill the Bragg reflection condition (Eq.(3.2.1)). Thus, all the Bragg reflections can be observed in one scattering plane in a powder diffraction experiment. The measurement procedure is equivalent to the Debye-Scherrer method. The scattered neutron intensity is recorded as function of the detector angle 2θ. The observed intensities can be described as follow:

$$I_i = bg(\theta_i) + Sm_{hkl}|F_{hkl}|^2 L(\theta_i)G(\theta_i - \theta_{hkl}) \tag{3.3.20}$$

The first term is the background of the diffraction pattern, S is the scale factor. m_{hkl} denotes the multiplicity of the Bragg reflection $(h\ k\ l)$, $L(\theta_i) = 1/(\sin\theta\sin 2\theta)$ is the so-called Lorentz factor which is tremendously enhanced at small scattering angles θ. $G(\theta_i)$ is the peak shape function describing the instrumental resolution effects and the peak broadening due to the grain size and internal strain effects of the sample, and the linewidth varies as a function of 2θ.

The powder diffraction patterns are often treated by performing the Rietveld method, which is based on the minimization of the weighted sum of the squared differences between the observed and the calculated intensities I_i^{cal} and I_i^{obs}, respectively:

$$\chi^2 = \sum_i \omega_i \left(I_i^{obs} - I_i^{cal}\right)^2 \tag{3.3.21}$$

with $\omega_i = 1/\sigma_i^2$, where σ_i^2 is the variance of the observation I_i^{obs}. The summation runs over the N_p experimental points. With this method, one can get access to the crystallographic information of the sample, such as the lattice constants, the atomic positions, the atomic displacement parameters and the magnetic structure for magnetic materials.

In this thesis, the neutron powder diffraction experiments were performed on SPODI [149] at MLZ and on HRPT [150] at PSI. The diffractometer SPODI is equipped with the monochromator consisting of Ge single crystals. The orientation (5 5 1) was used to obtain incident neutrons of wavelength 1.549 Å. The detector system consists of 80 ^{3}He position sensitive detector tubes (vertical direction) with fixed collimators located in front of each detector. The multi-detector of SPODI covers a scattering angle of 160$^{\rm o}$. Since each detector

covers 2°, the data collection was performed via stepwise positioning of the detector system to obtain a diffraction pattern of desired stepwidth, for example 40 steps for stepwidth 0.05^o. The standard samples, such as Vanadium and $Na_2Ca_3Al_2F_{14}$ (NAC, space group $I2_13$) powders, should be measured in advance to make detector efficiency correction and scattering angle correction for the collimator-detector pairs. Two-dimensional raw data was obtained as a function of detector height and scattering angle for each detector, which allowed a rapid check for sample crystallinity, alignment and possible preferred orientation effects. The conventional diffraction patterns $I(2\theta)$ were derived from the two-dimensional raw data by integration along the Debye-Scherrer rings (see Figure 3.3.2 (a)). The instrument layout of HRPT is similar to that of SPODI. High Q-resolution mode of HRPT was used in the measurements. The incident neutron wavelength was selected as 1.5 Å. The fine powder sample was loaded in a Vanadium or Copper can and measured at several temperatures. The analysis of powder diffraction patterns and the corresponding refinement of the structural parameters was carried out with the aid of program FULLPROF [151].
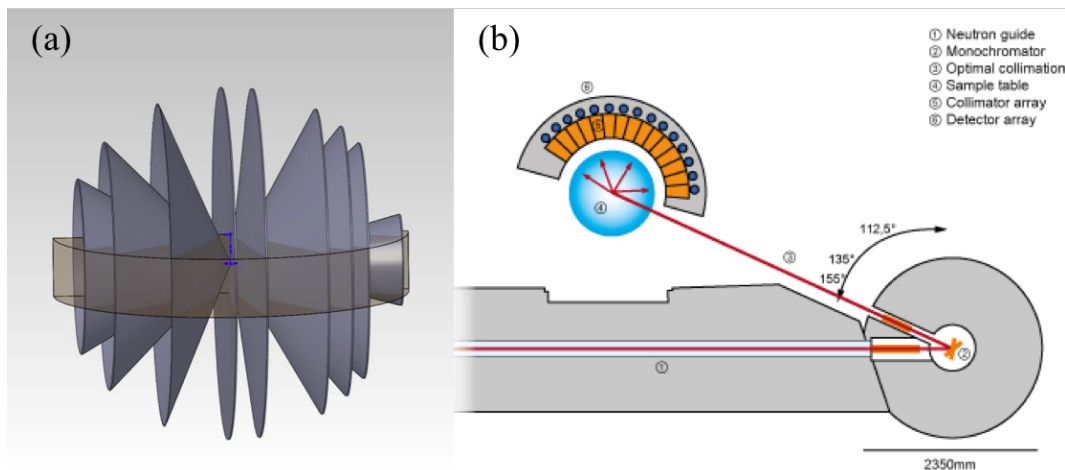
Figure 3.3.2 (a) Debye-Scherrer cones of neutron scattered from a polycrystalline sample are detected in the scattering plane. (b) Illustration of the SPODI diffractometers.

3.3.3. Neutron time-of-flight spectroscopy

To study the excitations of the sample, not only the scattering vector Q but also the energy transfer of neutrons has to be measured, called inelastic neutron scattering (INS), which measures the partial differential cross section $d^2\sigma/d\Omega dE$. According to Eq. (3.2.1), energies of the neutrons can be determined by measuring the flight time t of a neutron in a given flight path L, $E = mv^2/2 = m(L/t)^2/2$, known as time-of-flight technique [152].

Time-of-flight spectrometers are usually equipped with large detector banks, covering a wide scattering angle range. An incident neutron of energy E_i and wavevector k_i is scattered in the detector direction 2θ with a final energy E_f and wavevector k_f. The intensities collected at the detectors represent the raw data of the form $I(2\theta, t)$, which can be transformed to the scattering law $S(\boldsymbol{Q}, \omega)$ as follows:

$$Q = \frac{m}{\hbar} L \sqrt{\frac{t^2 + t_i^2 - 2t_i t \cos(2\theta)}{t_i^2 t^2}}$$

$$\omega(t) = \frac{m}{2\hbar} L^2 \frac{t^2 - t_i^2}{t_i^2 t^2}$$

(3.3.22)

where t_i and t are the flight time of the incident neutrons and the neutrons scattered from the sample to the detector located at scattering angle 2θ, respectively.
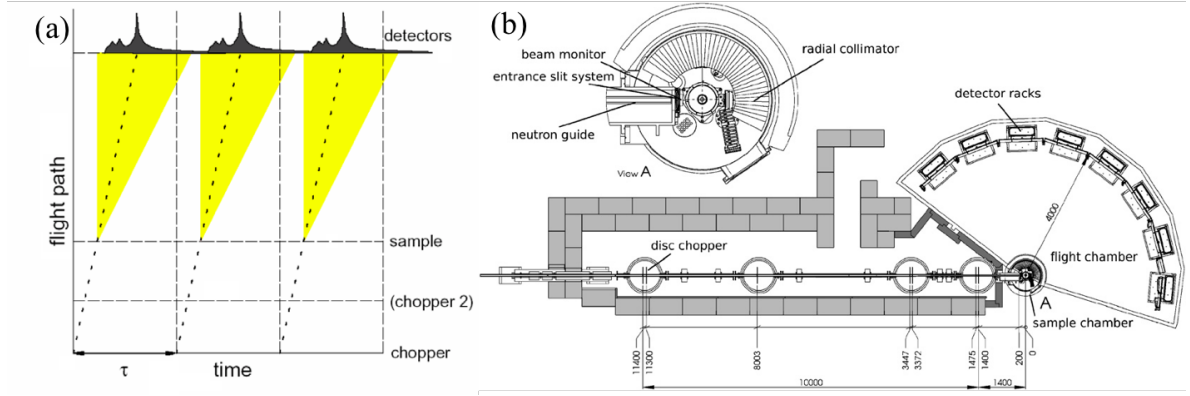
Figure 3.3.3 (a) Phase-space diagrams of direct time-of-flight technique, (b) Schematic view of the TOFTOF spectrometer.

Several time-of-flight spectrometers were employed in this thesis including the IN4 at ILL and MERLIN at ISIS for the investigation of the crystal field transition, and IN6 at ILL, LET at ISIS and TOFTOF at MLZ for the magnetic excitations of the pyrochlore compounds. Here, we give a short description of the typical time-of-flight spectrometer TOFTOF. The TOFTOF spectrometer is a multi-disc chopper time-of flight spectrometer for cold neutrons [153]. The neutrons with wavelength longer than 1.38 Å are guided to the primary spectrometer. Seven high speed neutron chopper discs in the primary spectrometer are used to select short monochromatic neutron pulses from the continuous neutron beam. Then, the neutron pulses pass through the slit system and the primary beam monitor, and hit the sample in the sample chamber equipped with sample environment like a cryostat. The scattered neutrons enter the flight chamber and travel to the detectors. The flight chamber is filled with

argon to avoid undesired scattering by air molecules. The 1000 ^{3}He tube detectors are adjusted tangentially to the intersection lines of the Debye-Scherrer cones with the surface of a virtual sphere with a radius of 4 m around the center of the sample. The detector system covers a scattering angle 2θ range from 7.5 to 140°. The time-of-flight of neutron from the sample to detector is measured by recording the detection time. The final scattering law $S(Q, \omega)$ can be transformed from the raw data in the software Mantid following the standard routine. Benefit from the multi-disc chopper system, the accessible dynamic range and the energy resolution (from 5 μeV to 5 meV) of TOFTOF can be changed conveniently by changing the chopper frequencies from 1000 to 22 000 rpm.

3.3.4. The XYZ neutron polarization analysis

The interaction of the magnetic moment of the neutron with the studied system involves not only the scattering of neutrons from one momentum state to another, but also the neutron spin-dependent terms in the neutron scattering cross-section. The spin-dependent terms give rise to interesting polarization effects and provide additional details about the studied system. Polarized neutrons are often used for determining magnetic correlations, for distinguishing between collective and single-particle excitations (for example, coherent and incoherent scattering processes), and for high-resolution spectroscopy (neutron spin-echo). The scattering theory of polarized neutrons has been completed more than forty years ago [154,155]. In this thesis, one often used polarized neutron scattering technique is the so-called *xyz*-difference method [156], allowing a simultaneous and unambiguous determination of the nuclear, magnetic and nuclear spin-incoherent scattering cross sections as a function of scattering vector and energy transfer. Here, we only discuss the diffraction case.

The spin-dependent scattering cross sections for an *xyz*-polarization analysis measurement are expressed as follows [157]:

$$\frac{d\sigma}{d\Omega}\bigg|_x^{nsf} = \frac{1}{2}\sin^2\alpha \frac{d\sigma}{d\Omega}\bigg|_{mag} + \frac{1}{3}\frac{d\sigma}{d\Omega}\bigg|_{si} + \frac{d\sigma}{d\Omega}\bigg|_{nuc} \tag{3.3.23}$$

$$\frac{d\sigma}{d\Omega}\bigg|_x^{sf} = \frac{1}{2}(\cos^2\alpha + 1)\frac{d\sigma}{d\Omega}\bigg|_{mag} + \frac{2}{3}\frac{d\sigma}{d\Omega}\bigg|_{si} \tag{3.3.24}$$

$$\frac{d\sigma}{d\Omega}\bigg|_y^{nsf} = \frac{1}{2}\cos^2\alpha \frac{d\sigma}{d\Omega}\bigg|_{mag} + \frac{1}{3}\frac{d\sigma}{d\Omega}\bigg|_{si} + \frac{d\sigma}{d\Omega}\bigg|_{nuc} \tag{3.3.25}$$

$$\frac{d\sigma}{d\Omega}\bigg|_y^{sf} = \frac{1}{2}(\sin^2\alpha + 1)\frac{d\sigma}{d\Omega}\bigg|_{mag} + \frac{2}{3}\frac{d\sigma}{d\Omega}\bigg|_{si} \tag{3.3.26}$$

$$\left.\frac{d\sigma}{d\Omega}\right|_z^{nsf} = \frac{1}{2}\left.\frac{d\sigma}{d\Omega}\right|_{mag} + \frac{1}{3}\left.\frac{d\sigma}{d\Omega}\right|_{si} + \left.\frac{d\sigma}{d\Omega}\right|_{nuc} \tag{3.3.27}$$

$$\left.\frac{d\sigma}{d\Omega}\right|_z^{sf} = \frac{1}{2}\left.\frac{d\sigma}{d\Omega}\right|_{mag} + \frac{2}{3}\left.\frac{d\sigma}{d\Omega}\right|_{si} \tag{3.3.28}$$

where the x, y and z subscripts denote the direction of the incident polarization of neutrons, and the *nsf* and *sf* superscripts refer to the non-spin-flip and the spin-flip cross sections, respectively, and the subscript *nuc, mag, si* imply nuclear (and the isotope incoherent), magnetic and spin-incoherent contributions. The so-called "Schärpf angle" α is the angle between the scattering vector and the x axis.

From the above *xyz* equations for the measured cross sections, one can easily obtain the magnetic cross section independently calculated in two ways:

$$\left.\frac{d\sigma}{d\Omega}\right|_{mag} = 2\left.\frac{d\sigma}{d\Omega}\right|_x^{sf} + 2\left.\frac{d\sigma}{d\Omega}\right|_y^{sf} - 4\left.\frac{d\sigma}{d\Omega}\right|_z^{sf}$$

$$\left.\frac{d\sigma}{d\Omega}\right|_{mag} = 4\left.\frac{d\sigma}{d\Omega}\right|_z^{nsf} - 2\left.\frac{d\sigma}{d\Omega}\right|_x^{nsf} - 2\left.\frac{d\sigma}{d\Omega}\right|_y^{nsf} \tag{3.3.29}$$

The nuclear and the spin-incoherent cross sections can be obtained as follow:

$$\left.\frac{d\sigma}{d\Omega}\right|_{nuc} = \frac{1}{6}\left[2\left.\frac{d\sigma}{d\Omega}\right|^{Tnsf} - \left.\frac{d\sigma}{d\Omega}\right|^{Tsf}\right]$$

$$\left.\frac{d\sigma}{d\Omega}\right|_{si} = \frac{1}{6}\left.\frac{d\sigma}{d\Omega}\right|^{Tsf} - \left.\frac{d\sigma}{d\Omega}\right|_{mag} \tag{3.3.30}$$

where $Tnsf$ and Tsf denote the total non-spin-flip and the total spin-flip cross sections, respectively. It should be noted that the xyz-difference method of polarized neutron scattering cannot separate the nuclear coherent and isotope-incoherent contributions. The xyz-difference method of polarization analysis can be used to study the antiferromagnetic structure with the propagation vector $\mathbf{k} = (0\ 0\ 0)$, in which the magnetic peaks locate at the positions of nuclear Bragg peaks and are difficult to be identified with unpolarized neutron scattering. Furthermore, this method is extremely useful for the studies of frustrated magnets, in which the spins often exhibit short-range order leading to the absence of magnetic Bragg peaks. The associated diffuse magnetic scattering signal is usually very weak that is drowned out by background for unpolarized neutron scattering. With the help of polarization analysis, the pure magnetic contribution can be identified and distinguished from other contribution. Thus the magnetic signal-to-background ratio is improved. The diffuse magnetic scattering, even for small magnetic moment system, can be observed by xyz-difference method of neutron polarization analysis.

The polarized neutron scattering measurement in this thesis was performed on the instrument DNS at MLZ. DNS is a cold polarized neutron time-of-flight spectrometer with multi-detector. The incident neutrons with the wavelength ranging from 2.4 to 6 Å can be selected by the double-focusing PG(002) monochrmator and the high-order reflected neutrons are rejected by the velocity selector. In order to perform time-of-flight spectroscopy, a double-chopper system is equipped between the monochromator and the sample position. A polarizer using m = 3 Schärpf bender-type focusing supermirrors, consisting of one type of magnetic layers with aligned magnetization and non-magnetic layers with varying thickness, is placed behind the velocity selector for the spin-up polarized neutrons passing through. Then, a π-flipper is used to reverse the neutron polarization from spin-up to spin-down. The sample position is surrounded by a set of coils, so-called XYZ-coils, which can generate three orthogonal magnetic guide fields with x, y, and z direction for the desired neutron polarizations. The scattered neutron can be recorded by 24 detectors combined with a polarization analyzer in front of each detector. The xyz-polarization is defined with the axis x parallel to averaged Q, with the axes y and z perpendicular to the averaged Q pointing in- and out-of the scattering plane respectively (as shown in Figure 3.3.4 (a)). By controlling the π-flipper and the XYZ-coil, one can measure the six channels of the scattering cross section (Eq. (3.3.23) - (3.3.28)) of the sample. Before the measurements, standard samples are measured: vanadium for detector efficiency normalization, NiCr for flipping ratio calibration and empty cell for background subtraction have to be performed. Then, the nuclear coherent scattering, the magnetic scattering and the spin-incoherent scattering can be separated from the corrected data of the sample according to Eq. (3.3.29) and Eq. (3.3.30).
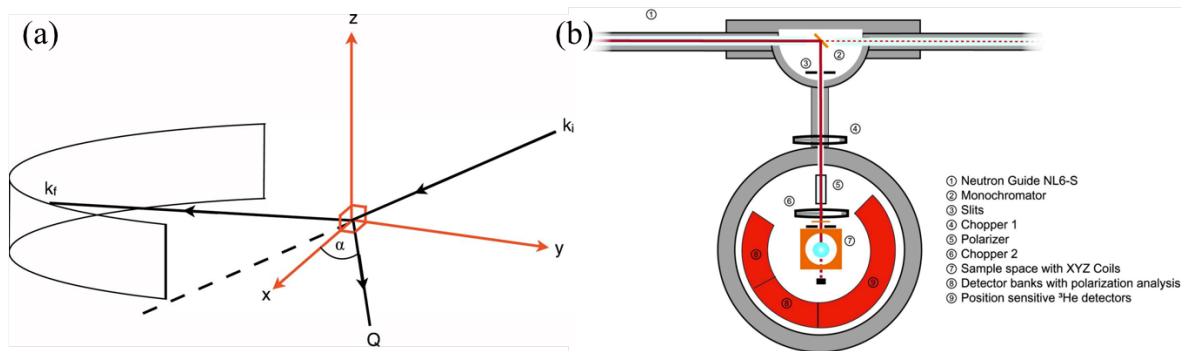

Figure 3.3.4 (a) The geometry of an xyz-polarization analysis experiment, (b) The schematic layout of the DNS spectrometer.

Chapter 4. Phase Diagram of the Rare-earth Magnetic Ground-States in Pyrochlore Iridates

4.1. Introduction

As discussed in Chapter 2, the combination of frustration, SOC and band topology puts the pyrochlore iridates at the intersection of many of the recent developments in condensed matter physics [3]. Early macroscopic measurements have indicated that the electric and magnetic properties depend strongly on the radius of the rare-earth. While the largest member $Pr_2Ir_2O_7$ remains metallic down to the sub-Kelvin temperature [158], other compounds with smaller Ln^{3+} ions enter a magnetic insulator phase at a certain temperature, T_{MI}, which becomes lower for larger ionic sizes of the rare-earth elements [120,121,142]. An AIAO order of the Ir sublattice below T_{MI} has been evidenced in several members via μSR and RXS [126,130,159]. However, neutron scattering, a powerful microscopic technique for magnetism, has failed to determine the magnetic structure of the Ir^{4+} sublattice mainly due to a combination of the strong neutron absorption of iridium and the small magnetic moment of Ir^{4+} [133]. On the other hand, the magnetic scattering signal of some of the Ln^{3+} moments is still detectable if the neutron scattering experiments of iridates are well-designed. Therefore, benefiting from the strong interaction between Ln^{3+} and Ir^{4+}, the study of Ln^{3+} via neutron scattering may shed light on the understanding of the magnetism of the Ir^{4+} sublattice. Additionally, the behavior of the localized 4f electrons in Ln^{3+} may lead to interesting phenomena when the A-B site interaction occurs.

Up to now, only a few investigations of pyrochlore iridates by means of neutron powder diffraction (NPD) have been reported. The AIAO long-range magnetic order of Ln^{3+} was observed in $Nd_2Ir_2O_7$[131,132], $Tb_2Ir_2O_7$ [134] and $Ho_2Ir_2O_7$ [160]. The temperature dependence of the intensity of magnetic Bragg peaks (proportional to the squared ordered moment of Ln^{3+}) exhibited an unusual behavior that the intensity increased slowly below T_{MI} and sharply on further lowering the temperature without any sign of saturation. Based on the assumption of the AIAO order of Ir^{4+}, the induced ordering model, in which a *molecular magnetic field*, B_{mf}^{Ir}, was generated by the ordered moment of Ir^{4+}, was proposed to account for the temperature dependence of Ln^{3+} ordering [134,160]. Meanwhile, such a molecular

magnetic field might split the doublet of the CEF ground-state of Ln^{3+}, which could be observed in inelastic neutron scattering (INS). However, only one triple-axis spectrometer measurement on $Nd_2Ir_2O_7$ powder sample reported that a gapped inelastic scattering signal with slight dispersion centered around 1.2 meV was observed. The INS studies on other compounds are still missing. Additionally, the ordered moment of Ln^{3+} is only 1/3 or 1/2 of the total magnetic moment of Ln^{3+} under CEF. The behavior of disordered magnetic moment is still poorly understood due to the lack of studies on spin dynamics, for example via INS. On the other hand, based on the same AIAO magnetic long-range structure of Nd^{3+}, two NPD experiments gave different ordered moment, 2.3(4) μ_B at 0.7 K [131] and 1.27(1) μ_B at 1.8 K [132]. The possible reason is that the extraction of magnetic diffraction patterns between two different temperatures results leads to a significant error since the magnetic Bragg peaks are on the top of nuclear Bragg peaks for AIAO magnetic structure. Therefore, it is also worthwhile to addressing the controversial observations of $Nd_2Ir_2O_7$.

This chapter will focus on the series of compounds which exhibit a metal-insulator transition (MIT) at finite temperature (from 33 K for $Nd_2Ir_2O_7$ (NIO) to above 100 K for $Tb_2Ir_2O_7$ (TIO), $Dy_2Ir_2O_7$ (DIO), $Ho_2Ir_2O_7$ (HIO), $Er_2Ir_2O_7$ (EIO), $Yb_2Ir_2O_7$ (YbIO)). By using the neutron powder diffraction, magnetic susceptibility, specific heat, polarized neutron scattering and inelastic neutron scattering, we systematically investigated the properties, magnetic structure and magnetic excitations below T_{MI}. Finally, a phase diagram including the rare-earth magnetic ground state is established.

4.2. Experimental details

Polycrystalline samples of $Ln_2Ir_2O_7$ (Ln = Nd, Tb, Dy, Ho, Er and Yb) were synthesized by solid state reaction. Starting from the mixture of rare-earth oxides (99.99% Ln_2O_3 for Ln = Nd, Dy, Ho, Er and Yb; 99.99% for Pr_2O_{11}; 99.99% for Tb_4O_7) and metal Iridium (99.99%), with molar ratio 1:1.05 of Ln to Ir, the samples were prepared by a new flux method using KF as flux. The mixture was pressed into pellets, placed in alumina crucible and sintered at 1050 -1100 ^{o}C in air for 7 days with several intermediate grinding and pelletizing steps. The reference compound $Y_2Ir_2O_7$ (YIO) was also prepared by the same way and used to estimate the phonon contribution in the heat capacity. The phases of the sample were regularly checked during synthesis by room temperature x-ray powder diffraction (XRD) using the laboratory-based diffractometer (STOE, Mo-$K_{\alpha 1}$) with a monochromator. The magnetic susceptibility measurement was performed by using a Quantum Design magnetic properties measurement system (MPMS) equipped with a superconducting quantum interference device

(SQUID) magnetometer. The heat capacity of the pelletized samples was measured down to 50 mK using a Quantum Design physical properties measurement system (PPMS) equipped with a dilution refrigerator.

The neutron powder diffraction (NPD) measurements were carried out using the powder neutron diffractometer SPODI at the Heinz Maier-Leibnitz Zentrum (MLZ), Garching, Germany. The XRPD and NPD data were refined using the package FULLPROF suite. The diffuse neutron scattering with xyz-polarization analysis was performed on the diffuse neutron scattering spectrometer (DNS) at MLZ, operated by Juelich Centre for Neutron Science (JCNS). The powder sample around two grams was sealed in a hollow cylinder copper can with optimized thickness to reduce neutron absorption. A dilution refrigerator was used to achieve the lowest temperature of 0.1 K. An incident neutron beam of wavelength $\lambda = 4.2$ Å was used for the experiments. The inelastic neutron scattering (INS) measurement was performed on the time-of-flight spectrometer TOFTOF at MLZ. The incident neutron beam of wavelengths of $\lambda = 5.0$ and 5.5 Å were chosen to cover a large enough dynamic range and maintain a reasonable energy resolution.

4.3. Results and discussion

4.3.1. Neutron powder diffraction

The room temperature NPD patterns of Ln$_2$Ir$_2$O$_7$ (Ln = Nd, Tb, Dy, Ho, Er, Yb) are presented in Figure 4.3.1 and Figure 4.3.2. All patterns have been Rietveld refined with the cubic pyrochlore structure (space group $Fd\bar{3}m$, Ln at the 16d (1/2, 1/2, 1/2), Ir at 16c (0, 0, 0), O at 48f (x, 1/8, 1/8) and O' at 8b (3/8, 3/8, 3/8)). During refinement, the copper peaks from the sample holder have been excluded. As marked by orange arrows in the middle pattern of Figure 4.3.1, the contamination of impurity phases around 2-3 % was found in TIO. The broadened Bragg peaks imply the existence of internal strain, most likely due to inhomogeneity of samples.

Table 4.3.1 Selected crystallographic information obtained from Rietveld refinement of the NPD.

Ln	Pr	Nd	Tb	Dy	Ho	Er	Yb
a (Å)	10.4086(1)	10.3891(3)	10.1267(4)	10.2198(5)	10.1931(3)	10.1674(3)	10.1248(3)
48f x	0.3306(1)	0.3316(1)	0.3347(5)	0.3379(5)	0.3380(3)	0.3386(3)	0.3412(3)
Ln-O (Å)	2.5487(6)	2.5362(6)	2.4810(40)	2.4510(40)	2.4440(30)	2.4340(30)	2.4060(30)
Ln-O' (Å)	2.2535(0)	2.2476(1)	2.2154(1)	2.2127(1)	2.2069(1)	2.2013(1)	2.1921(1)
Ir-O (Å)	2.0221(4)	2.0202(4)	2.0166(18)	2.0180(30)	2.0128(14)	2.0105(14)	2.0140(14)
Ir-O-Ir (°)	131.00(4)	130.57(5)	128.80(30)	127.10(30)	127.07(16)	126.76(16)	126.42(16)
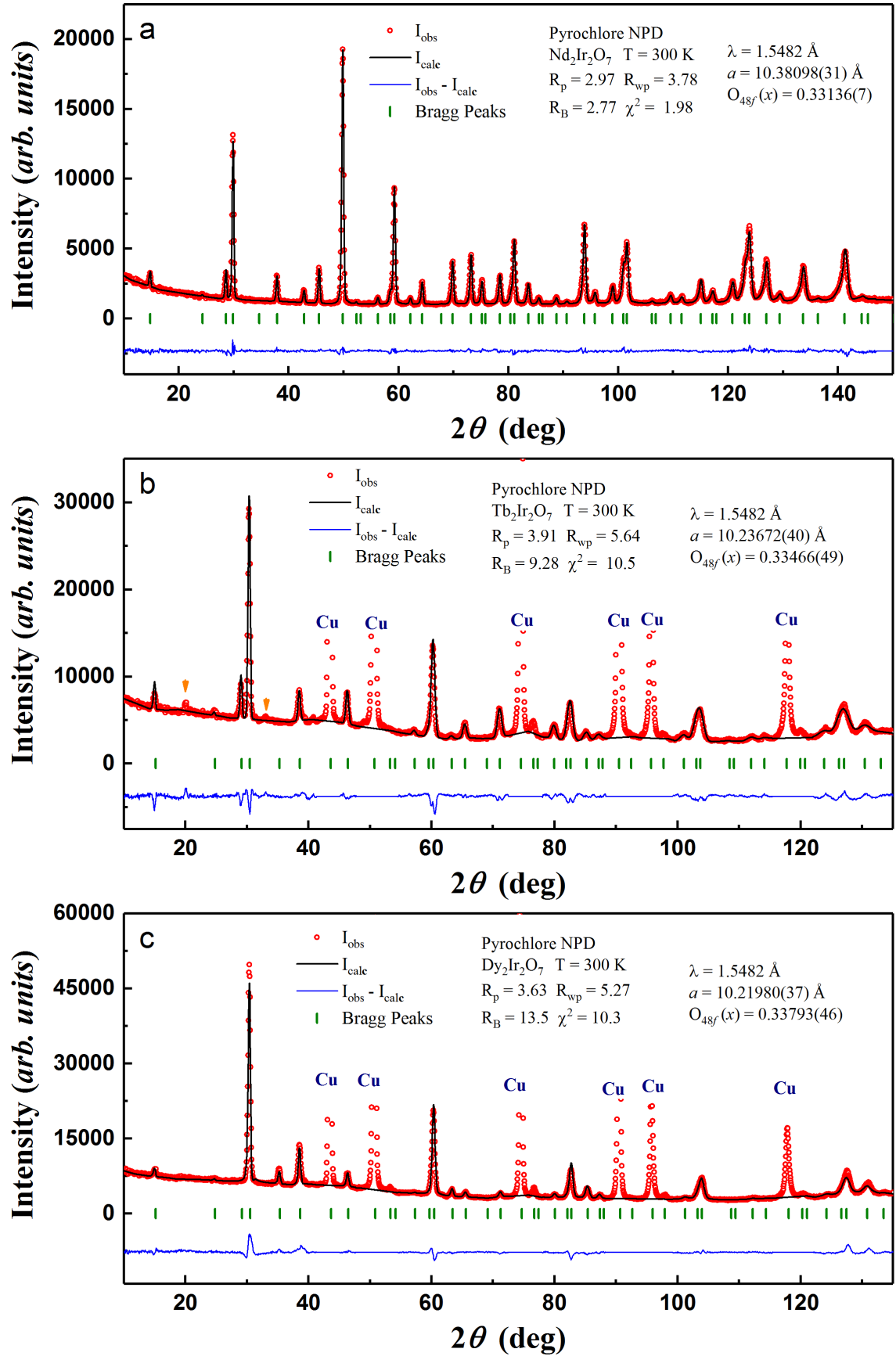
Figure 4.3.1 Neutron powder diffraction (NPD) patterns for Nd$_2$Ir$_2$O$_7$ (top), Tb$_2$Ir$_2$O$_7$ (middle) and Dy$_2$Ir$_2$O$_7$ (bottom) at 300 K, as well as their Rietveld refinement with pyrochlore structure. The copper peaks from container have been excluded.

Figure 4.3.2 Neutron powder diffraction (NPD) patterns for $Ho_2Ir_2O_7$ (top), $Er_2Ir_2O_7$ (middle) and $Yb_2Ir_2O_7$ (bottom) at 300 K, as well as their Rietveld refinement with pyrochlore structure. The copper peaks from container have been excluded.
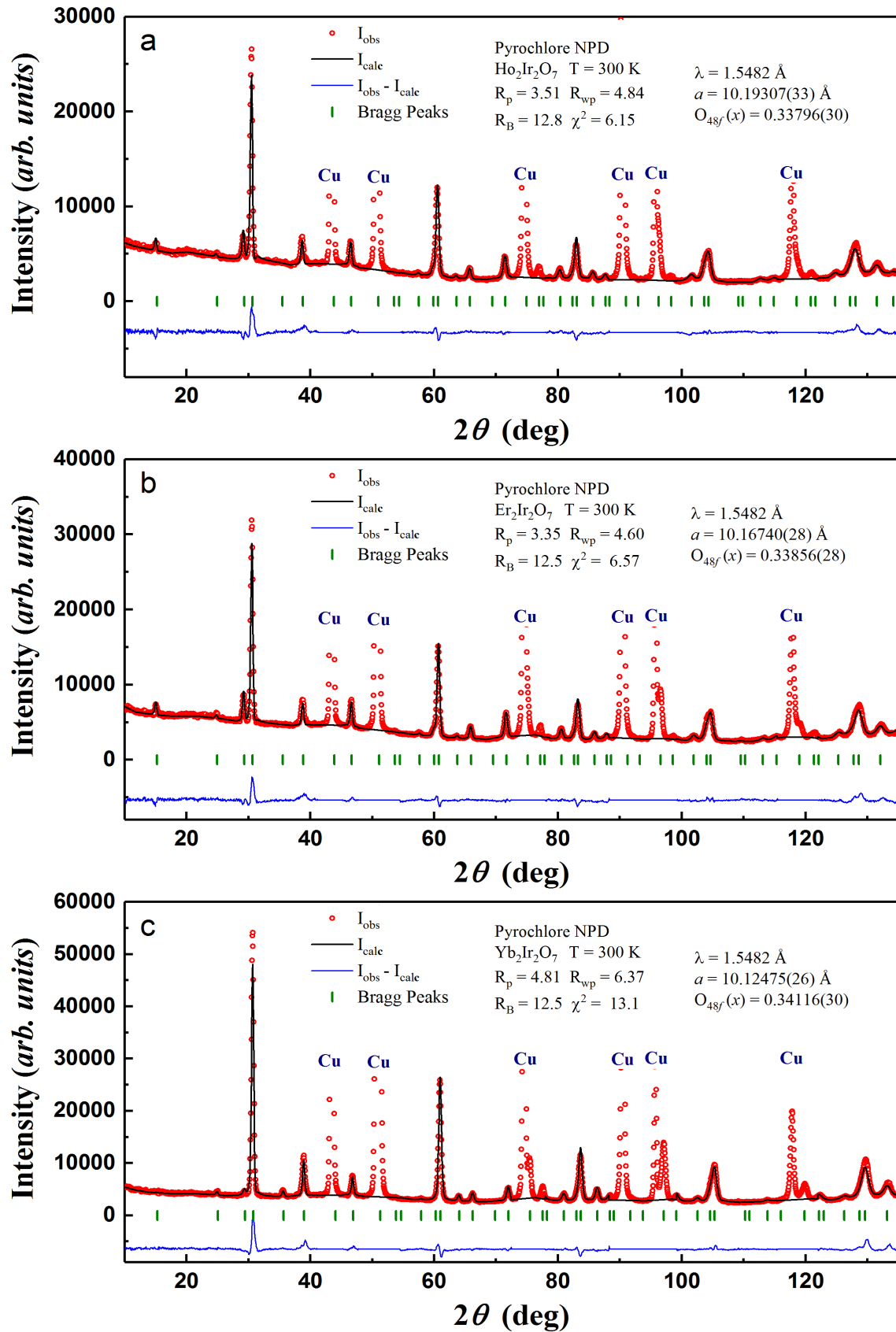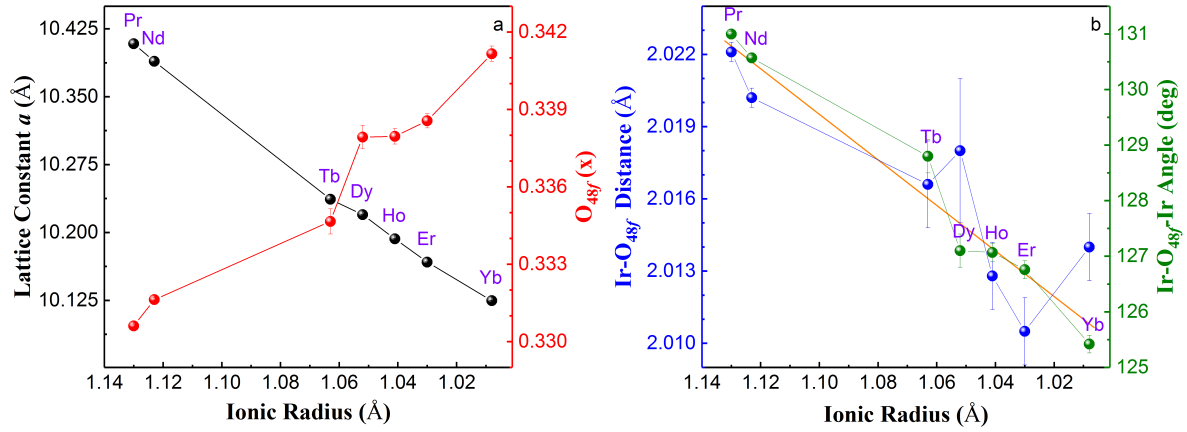
Figure 4.3.3 (a) The cubic lattice constant *a* and 48*f* oxygen *x*-parameter, (b) the Ir-O distance and the Ir-O-Ir angle as function of the rare-earth ion radius as determined from Rietveld refinement of NPD. The orange line is a guide to the eye.

A summary of the results obtained from the Rietveld refinements is given in Table 4.3.1, showing the same variation of the parameters in other series of pyrochlore compounds [30,161]. The dependence of the cubic lattice constant *a* and the 48*f* oxygen coordinate *x*-parameter on the ionic radius of the Ln cation is shown in Figure 4.3.3 (a). A nearly linear decrease in the lattice constant of pyrochlore, *a*, is observed as the lanthanoid cation radius decreases. The 48*f* *x*-parameter of the iridate pyrochlores shows a nearly linear increase from Pr$_2$Ir$_2$O$_7$ (0.331) to Yb$_2$Ir$_2$O$_7$ (0.341). The smaller 48*f* *x*-parameter compared to the value for the ideal fluorite phase (0.375) [25] implies that the pyrochlore phase of Ln$_2$Ir$_2$O$_7$ is stable. On the other hand, $x > 5/16 = 0.3125$ indicates that the oxygen octahedron environment of Ir^{4+} is compressed along the [1 1 1] directions, the so-called trigonal distortion, as the threefold rotational symmetries are preserved. Early electronic band structure calculation associates the trigonal distortion to the variation of T_{MI} with different Ln^{3+}: larger Ln^{3+} ions lead to a decreased trigonal compression of the octahedral, which increases the Ir-O orbital overlap and thus improves the hopping of Ir electrons [162]. As shown in Figure 4.3.3 (b), despite the Ir-O distance becoming slightly larger with increasing of Ln^{3+} ionic radius, the Ir-O-Ir angle increases from 125.5° to 131°, implying a trend of perfect oxygen octahedron formation and facilitating the Ir-O orbital overlap [109].

4.3.2. DC magnetization

For all 6 compounds, the zero-field cooled (ZFC) and field-cooled (FC) magnetization was measured in an applied field of 50 − 1000 Oe (see left panels in Figure 4.3.4 and Figure

4.3.5). As summarized in Table 4.3.2, the ZFC and FC curves separate at a certain temperature from 33 K for NIO to 143 K for YbIO, which is an indicator of the T_{MI} being associated with Ir^{4+} ordering [121,126,127,129,130]. The variation of T_{MI} with different Ln^{3+} is consistent with previous structure analysis, a large Ln^{3+} refers to lower T_{MI}. The bifurcation of the ZFC-FC magnetization originates probably from either glass-like behavior due to the defect, such as the stuffing defect [163] or substitution of Ir^{5+}/Ir^{4+} [164], or the presence of magnetic domains at 180° in the AIAO long range order [134,165,166]. Both ZFC and FC magnetization increase down to 2 K for all compounds. Below T_{MI}, the FC magnetization remains above the ZFC one for NIO, HIO, EIO and YbIO. Crossing of the ZFC and FC curves of TIO and DIO can be observed, meanwhile the FC curves of these two compounds exhibit saturation tendency below 6 K and 3 K, for TIO and DIO, respectively. This could be attributed to the saturation of magnetic long-range ordering of Tb^{3+} and Dy^{3+}, which will be discussed below. The bifurcation temperature of ZFC-FC magnetizations is also a characteristic of sample quality. For example, the stoichiometric sample of NIO shows the transition temperature around 30-36 K [121,131,132], while non-stoichiometric sample has different transition temperature ~110 K [167,168]. The ZFC-FC behaviors and T_{MI} of our samples are consistent with previous results reported for this family, implying good sample quality [120,121,142].

Table 4.3.2 The bifurcation temperature T_{MI} of ZFC and FC magnetization curves and Curie-Weiss fitting parameters for $Ln_2Ir_2O_7$. The μ_{free} is the paramagnetic moment of free Ln^{3+} ions.

Ln	Nd	Tb	Dy	Ho	Er	Yb
T_{MI} (K)	33	127	125	135	142	143
χ_0 (10^{-4} emu/Oe/mole)	7.5	3.0	1.0	4.7	109.1	11.5
θ_{CW} (K)	-18.6	-13.2	-10.2	2.67	-7.5	-45.5
μ_{eff} (μ_B)	3.14	9.85	10.96	11.53	9.48	4.34
μ_{free} (μ_B)	3.52	9.72	10.65	10.61	9.58	4.54
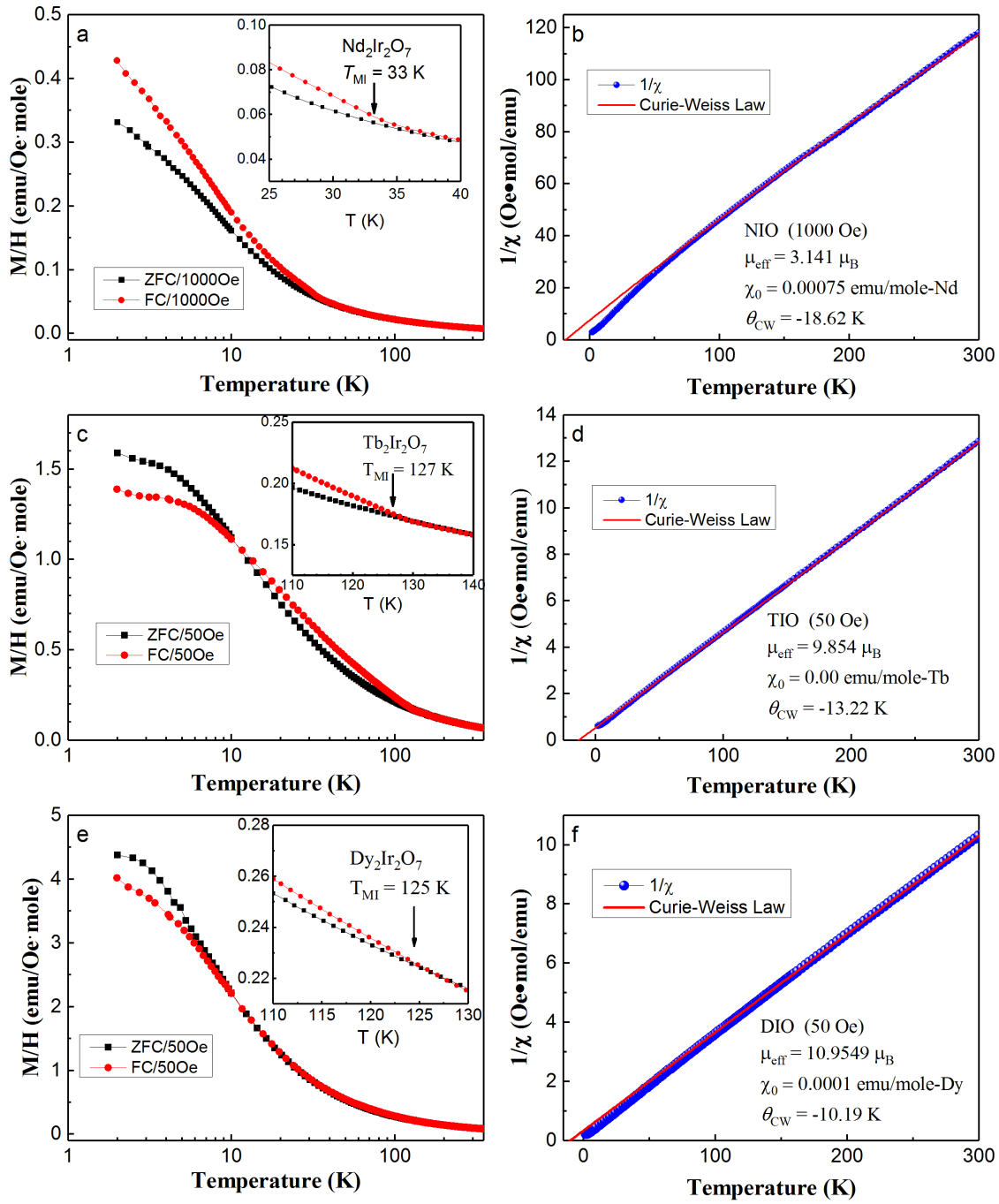
Figure 4.3.4 DC magnetic susceptibility *M/H* (left panels) and inverse susceptibility (right panels) versus temperature for Nd$_2$Ir$_2$O$_7$ (top panels), Tb$_2$Ir$_2$O$_7$ (middle panels) and Dy$_2$Ir$_2$O$_7$ (bottom panels). The inserts of left panel show the detail of the bifurcation of ZFC and FC curves. The solid line in right panels represent the fits of the Curie-Weiss law.
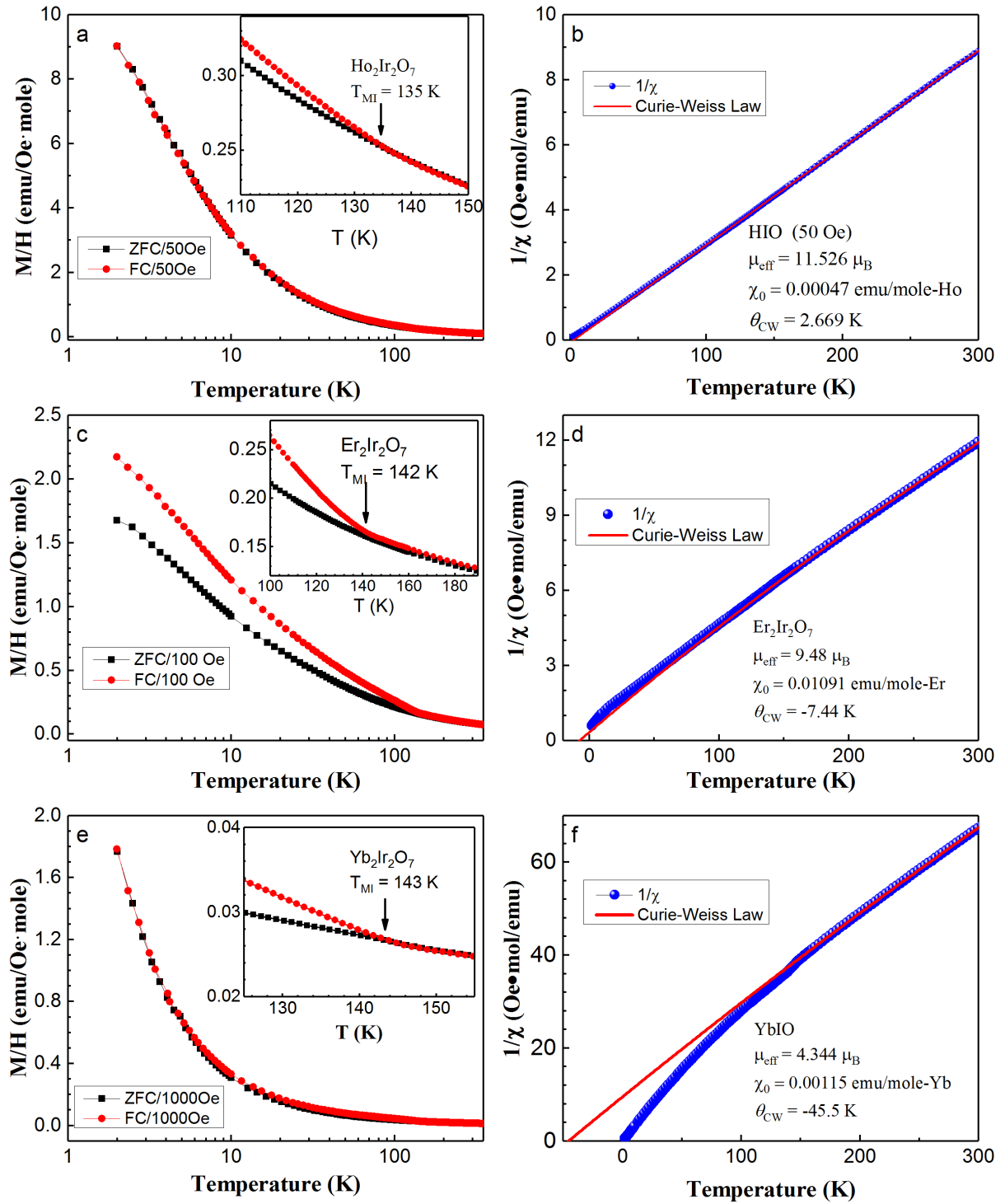
Figure 4.3.5 DC magnetic susceptibility *M/H* (left panels) and inverse susceptibility (right panels) versus temperature for $Ho_2Ir_2O_7$ (top panels), $Er_2Ir_2O_7$ (middle panels) and $Yb_2Ir_2O_7$ (bottom panels). The inserts of left panel show the detail of the bifurcation of ZFC and FC curves. The solid line in right panels represent the fits of the Curie-Weiss law.

The Curie-Weiss (CW) law fitting was performed to the ZFC magnetization curve according to the formula:

$$\chi(T) = \chi_0 + \frac{C}{T - \theta_{\text{CW}}}, \quad C = N_A \mu_{eff}^2 / 3k_B \tag{4.3.1}$$

where N_A is the Avogadro number and k_B is the Boltzmann constant, θ_{CW} is the Curie-Weiss temperature, μ_{eff} is the effective moment in unit μ_{B}, the temperature-independent term χ_0 is accounting for the Van-Vleck effect. The fitting was performed from 150 K to 300 K where the Ir moment is still in the paramagnetic state. The CW law fit and the inverse susceptibility as function of temperature are shown in the right panels of Figure 4.3.4 and Figure 4.3.5. It is clear that the inverse susceptibility obeys the CW law at high temperature. At low temperature, the divergence between the measured inverse susceptibility and CW law implies that the magnetic correlations between ions start playing a role. Especially for YbIO, the divergence takes place just at T_{MI}, indicating the strong magnetic correlation in this system. The parameters obtained by fitting are summarized in Table 4.3.2. The magnetic moment of Ir^{4+} could be ignored due to its small size [133]. The obtained effective magnetic moments μ_{eff} agree with the expectation for Ln^{3+} ions, indicating the localized nature of the trivalent rare-earth ions. Except for HIO, the negative CW temperatures θ_{CW} imply antiferromagnetic coupling between Ln^{3+} moment with high coupling strength, because all amplitudes of θ_{CW} in pyrochlore iridates are larger than that in their counterpart compounds, such as titanates, stagnates, or hafnates. More interestingly, some of them even changes the sign. For example, Dy^{3+} in Ln$_2$B$_2$O$_7$ (B = Ti, Sn) is known to yield positive $\theta_{CW} = 1$ K due to the strong ferromagnetic coupling of dipole-dipole interaction between Dy^{3+} [169], but a negative $\theta_{CW} = -10.2$ K for the antiferromagnetic coupling is obtained in Dy$_2$Ir$_2$O$_7$. This difference suggests the involvement of the magnetic sublattice of Ir strongly affects the interaction between the rare-earth moments. The constant term χ_0 of Van Vleck susceptibility are comparable to that of their system compounds. Our results are consistent with previous report [142].

4.3.3. Specific heat

With the dilution refrigerator, we measured the specific heat of these series compounds Ln$_2$Ir$_2$O$_7$ down to 50 mK. In order to obtain the pure magnetic specific heat and corresponding magnetic entropy, the obtained raw data C_{exp} was treated in the same way as discussed in the next two chapters and Appendix A. The phonon contribution C_{latt} was estimated by the nonmagnetic sample Y$_2$Ir$_2$O$_7$ based on the Debye model [170]. The crystal electric field contribution C_{CEF} was calculated as follow:

$$C_{Sch} = \frac{R}{Z^2} \left[Z \sum_{i=1}^{n} \left(\frac{\varepsilon_i}{k_B T}\right)^2 e^{\left(-\frac{\varepsilon_i}{k_B T}\right)} - \left\{ \sum_{i=1}^{n} \varepsilon_i e^{\left(-\frac{\varepsilon_i}{k_B T}\right)} \right\}^2 \right] \tag{4.3.2}$$

where $Z = \sum_{i=1}^{n} e^{(-\varepsilon_i/k_B T)}$ is the partition function of the system, ε_i is the CEF scheme of Ln^{3+} taken from other pyrochlore compounds. Below 10 K, the C_{CEF} in NIO, DIO, HIO, EIO and YbIO could be ignored due to higher energy of the first excitation level of CEF, while the specific heat of TIO still has a huge CEF contribution due to the lower lying excitation levels. Since the C_{CEF} represents the thermal population of CEF levels of Ln^{3+}, the above analysis suggests that the Ln^{3+} (Ln = Nd, Dy, Ho, Er and Yb) in iridates could be treated as pseudospins below 10 K. The nuclear contribution due to hyperfine splitting of the nuclear spin is subtracted by $C_{nuc} \propto T^{-2}$ with the constraint of zero magnetic specific heat at lowest temperature [171]. In fact, the C_{nuc} in NIO, DIO, EIO and YbIO could be ignored (see details in Appendix A). The conduction electron contribution was ignored due to the poor electrical conductivity of these compounds. The corresponding entropy $S_{mag}(T)$ is obtained by integrating C_{mag}/T over the investigated temperature range, where $C_{mag} = C_{exp} - C_{latt} - C_{CEF} - C_{nuc}$ is the obtained magnetic specific heat. The obtained C_{mag} and $S_{mag}(T)$ of the aforementioned compounds (except HIO due to huge C_{nuc} below 3 K), together with the classical spin-ice (CSI) compound $Dy_2Ti_2O_7$ as reference, are presented in Figure 4.3.6. The contributions of different terms and origin data for each sample could be found in the appendix A. In the right panels of Figure 4.3.6, the magnetic entropy of the paramagnetic state for spin-1/2 system, $S_{PM} = R ln2$ (black line), and residual entropy of CSI, $S_{CSI} = R/2 ln(3/2)$ (red line), [31] are also given.

Table 4.3.3 The temperature of the magnetic specific heat hump maximum T_h for different rare-earth ions. The CSI compound $Dy_2Ti_2O_7$ exhibits a similar hump with maximum at 1.2 K. $\Delta_C = T_h/0.42/11.6$ is the excitation level associated to T_h, based on the two-level assumption.

Ln^{3+}	Nd	Tb	Dy	Er	Yb
T_h (K)	5.0	3.0	3.0	1.5	2.3
Δ_C (meV)	1.03	0.62	0.62	0.31	0.47

Turn to the specific heat anomaly associated to the AIAO ordering of Ir^{4+}. As shown in the insert of Figure 4.3.6 (b), NIO displays such an anomaly around 33 K, which is in excellent agreement with the previous magnetization result, $T_{MI} = 33$ K. Unfortunately, the

anomaly in other compounds with $T_{MI} > 120$ K was not observed, possibly due to the weak signal compared to the huge phonon and CEF contributions above 100 K.
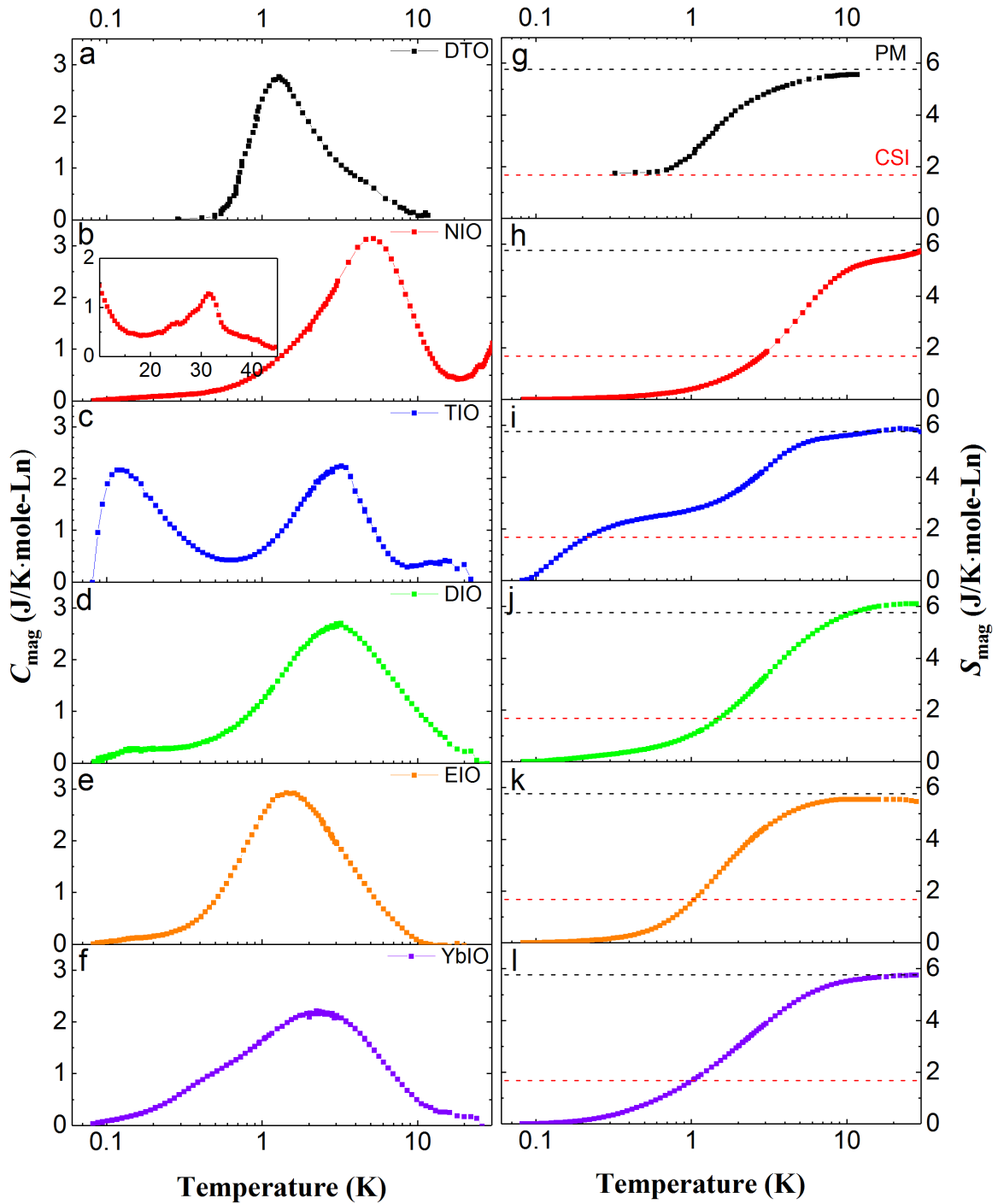
Figure 4.3.6 The obtained magnetic specific-heat C_{mag} (left panel) and the corresponding magnetic entropy $S_{mag}(T)$ (right panel) of the pyrochlore iridates. (a) and (g) show the C_{mag} and $S_{mag}(T)$ of the CSI compound Dy₂Ti₂O₇ as reference.

As shown in the left panel of Figure 4.3.6, no sharp anomaly associated with magnetic order of Ln³⁺ could be observed, however, the obtained C_{mag} of Ln₂Ir₂O₇ (Ln = Pr, Nd, Tb,

Dy, Er, Yb) universally reveals a broad hump with the maximum at the temperature T_h, which is listed in Table 4.3.3. The broad peak in NIO was explained as the Schottky anomaly of a two levels system with energy splitting $\Delta = 1.12$ meV, possibly due to the CEF ground-state splitting of Nd^{3+} [121]. As discussed in Chapter 2, the CEF ground-state of Ln^{3+}, either Kramers or non-Kramers ions, in pyrochlore is doublet. If the ordered Ir^{4+} generates a *molecular-magnetic field* at Ln^{3+}, the doublet of CEF should be split. Then, based on the two-level model of the Schottky anomaly (Eq. (4.3.2)) in the specific heat, one could observe a broad peak with maximum at $T_h = 0.42\, \Delta_C * 11.6$ [172], where Δ_C is the splitting energy, 11.6 is used to transform units from meV to K. Following this scenario, the estimated energy of the CEF ground-state splitting of Ln^{3+}, Δ_C, are shown in Table 4.3.3. However, this Δ_C is absent in most of INS measurements of $Ln_2Ir_2O_7$, as discussed below. On the other hand, the hump is also an indicator of the development of magnetic short-range ordering in frustrated magnets. As shown in Figure 4.3.6 (a), the CSI compound $Dy_2Ti_2O_7$ displays a specific heat hump at 1.2 K associating the magnetic short-range order with 2I2O configuration [64]. As a result, the system exhibits a residual magnetic entropy, the so-called Paul entropy (shown in Figure 4.3.6 (g)). The magnetic entropy S_{mag} corresponding to the hump of $Ln_2Ir_2O_7$ were calculated and shown in the right panel of Figure 4.3.6. The S_{mag} of $Ln_2Ir_2O_7$ approximates to the ideal value S_{PM} for a paramagnetic state with $S = 1/2$ at 25 K. If the doublet splitting of the CEF ground-state exists, the calculated entropy S_{mag} should be larger than that of the S_{PM}. This fact strongly suggests that the hump of C_{mag} at T_h is mainly originating from the existence of an unknown short-range spin ordering. Furthermore, the T_h of $Ln_2Ir_2O_7$ is larger than that of DTO, implying the exchange interaction strength in $Ln_2Ir_2O_7$ is enhanced due to the involvement of Ir^{4+}. The different results of pyrochlore iridates compared to their counterpart compounds indicate that the nature of the rare-earth ion physics in pyrochlore structure is strongly tuned by the magnetic ion Ir^{4+} with $5d^5$. This may lead to novel ground states of spin system and exotic magnetic excitations.

4.3.4. Polarized neutron diffraction

The polarized neutron scattering measurements were performed on DNS down to 0.5 K for He3 insert and 0.2 K for dilution insert. Benefiting from the xyz-polarization analysis on DNS, one can separate the nuclear coherent scattering, magnetic scattering and spin-incoherent scattering contributions of the sample at the same temperature. This may reduce the error of the extracted magnetic signal in unpolarized neutron diffraction. In this

subsection, the iridates will be discussed according to the single-ion anisotropy of rare-earth ions Ln^{3+}.

A. Easy-axis anisotropy case (NIO, TIO, DIO and HIO)

As discussed in Chapter 2, the rare-earth ions Nd^{3+}, Tb^{3+}, Dy^{3+} and Ho^{3+} in pyrochlore often exhibit single-ion anisotropy with easy-axis along the local $\langle 1\,1\,1 \rangle$ direction due to CEF. Here we discuss NIO with lower $T_{MI} = 33$ K at first, then focus on the compounds TIO, DIO and HIO with T_{MI} above 120 K.
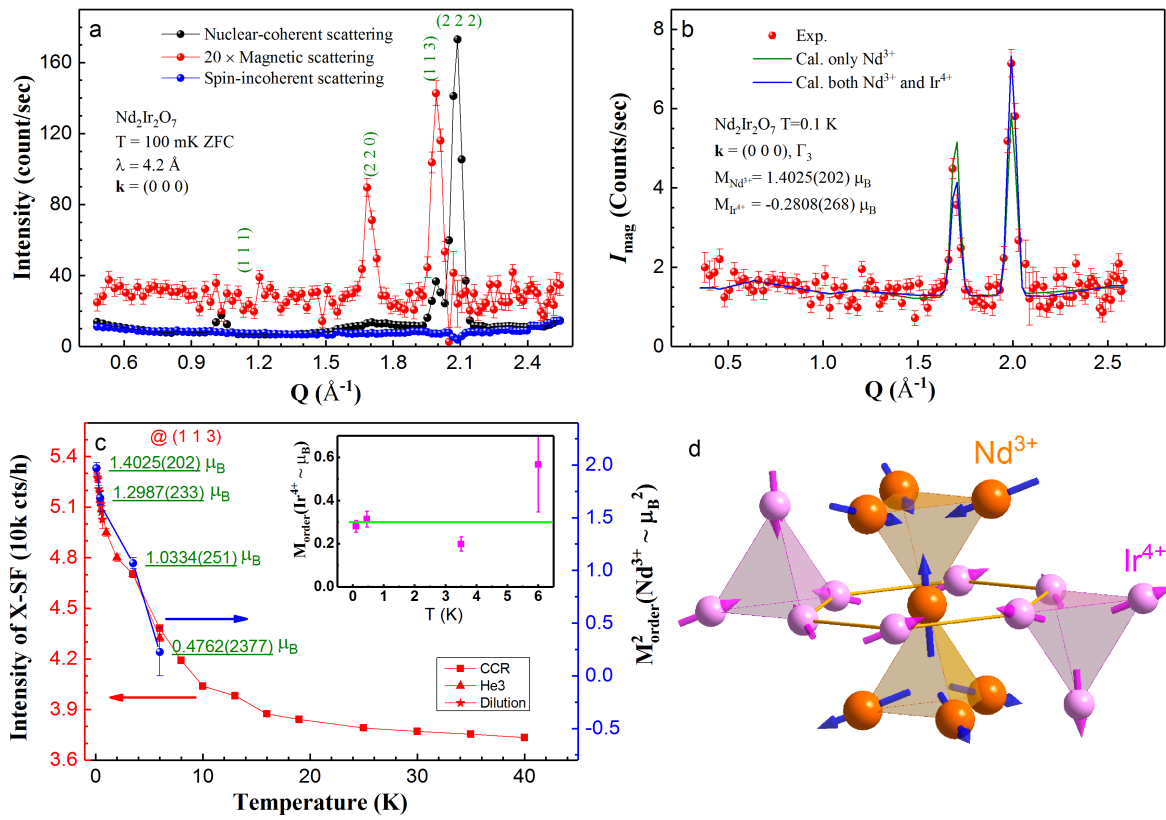
Figure 4.3.7 (a) Nuclear coherent scattering, spin incoherent scattering and magnetic scattering of $Nd_2Ir_2O_7$ at 0.1 K. (b) Refinement of magnetic scattering with the magnetic structure shown in (d). (c) Temperature dependence of the intensity of the neutron x-spin-flip (X-SF) channel at peak (1 1 3) (red and left axe), as well as the ordered moment of Nd^{3+} (blue and right axe). The green numbers indicate the ordered moment of Nd^{3+} obtained from Rietveld refinement. The ordered moment of Ir^{4+} is shown in the insert of (c).

Figure 4.3.7 (a) shows the nuclear coherent, spin-incoherent and magnetic scattering contributions of $Nd_2Ir_2O_7$ at 0.1 K. Besides the constant spin-incoherent scattering intensity and several nuclear Bragg peaks in the nuclear coherent component, two magnetic Bragg

peaks located at $Q = 1.68$ and 1.98 Å^{-1}, corresponding to (2 2 0) and (1 1 3) are observed in the magnetic component. The intensity of the magnetic Bragg peak (1 1 3) is slightly higher than that of (2 2 0). This observation is consistent with the previous report on the unpolarized NPD [131,132].

In order to solve the magnetic structure, we employ the symmetry analysis by BASIREPS and Rietveld refinement by Fullprof [151]. All the magnetic peaks can be indexed by a propagation vector $\mathbf{k} = (0\ 0\ 0)$. For the space group $Fd\bar{3}m$ with $\mathbf{k} = (0\ 0\ 0)$, the magnetic representation of Nd (16d) and Ir (16c) can be reduced into four nonzero irreducible representations (IRs) of the little group:

$$\Gamma_{mag} = 1\Gamma_3^1 + 1\Gamma_5^2 + 1\Gamma_7^3 + 2\Gamma_9^3 \qquad (4.3.3)$$

The detailed simulation of the neutron powder diffraction pattern of magnetic scattering is presented in Appendix B. The absence of the magnetic Bragg peaks (1 1 1) and (2 0 0) allow us to reduce the IRs to Γ_3 , in which the spins are arranged with AIAO configuration in the unit of tetrahedra. During refinement, the overall scale factor and lattice parameter are obtained from the nuclear coherent scattering pattern. As shown in Figure 4.3.7 (b), we use two models to refine the magnetic scattering pattern: (1) only considering the Nd^{3+} is AIAO ordered (green solid line) and (2) both Nd^{3+} and Ir^{4+} are AIAO ordered (blue line). According to the simulations, the magnetic peak (2 2 0) is comparable to the (1 1 3) in the case of the first model (green curve in Figure 4.3.7 (b)), however, the magnetic peak (2 2 0) becomes weaker than the (1 1 3) if both Nd^{3+} and Ir^{4+} are considered (blue curve in Figure 4.3.7 (b)). A much worse agreement ($\chi^2 = 2.827$) is obtained for the AIAO model only considered Nd^{3+}. A good refinement ($\chi^2 = 1.754$) is obtained for the second model with ordered moments of Nd^{3+} 1.4025(202) μ_B and of Ir^{4+} 0.2808(268) μ_B at 0.1 K. The obtained ordered moment of Nd^{3+} is in agreement with Guo's result 1.27 μ_B at 1.8 K [132], but not Tomiyasu's result 2.3 μ_B at 0.7 K [131] possibly due to its poor statistics. The ordered moment of Ir^{4+} is consistent with the $J_{eff} = 1/2$ state prediction and the experimental results of Sr$_2$IrO$_4$ with 0.208 μ_B/Ir^{4+} [119].

The obtained magnetic structure is shown in Figure 4.3.7(d). Both Nd^{3+} and Ir^{4+} exhibit AIAO configuration, in which each Nd^{3+} is surrounded by six Ir^{4+} ions forming a hexagon. The six magnetic moments of Ir^{4+} on a hexagon cancel out the in-plane components and retain the out-of-plane component with a net moment $M_{Ir}^{eff} = 6 \times M_{Ir}/3$ on the Nd^{3+} site. The net moment M_{Ir}^{eff} is parallel to the ordered moment of Nd^{3+}, indicating a ferromagnetic coupling between Nd^{3+} and Ir^{4+}. As shown in Figure 4.3.7(c), the magnetic peak (1 1 3), mainly contributed by the ordered moment of Nd^{3+}, displays an unusual temperature

dependence. On cooling, the peak intensity starts to increase significantly below 20 K and does not saturate down to 0.1 K. This behavior could be understood by the induced ordering model discussed below.
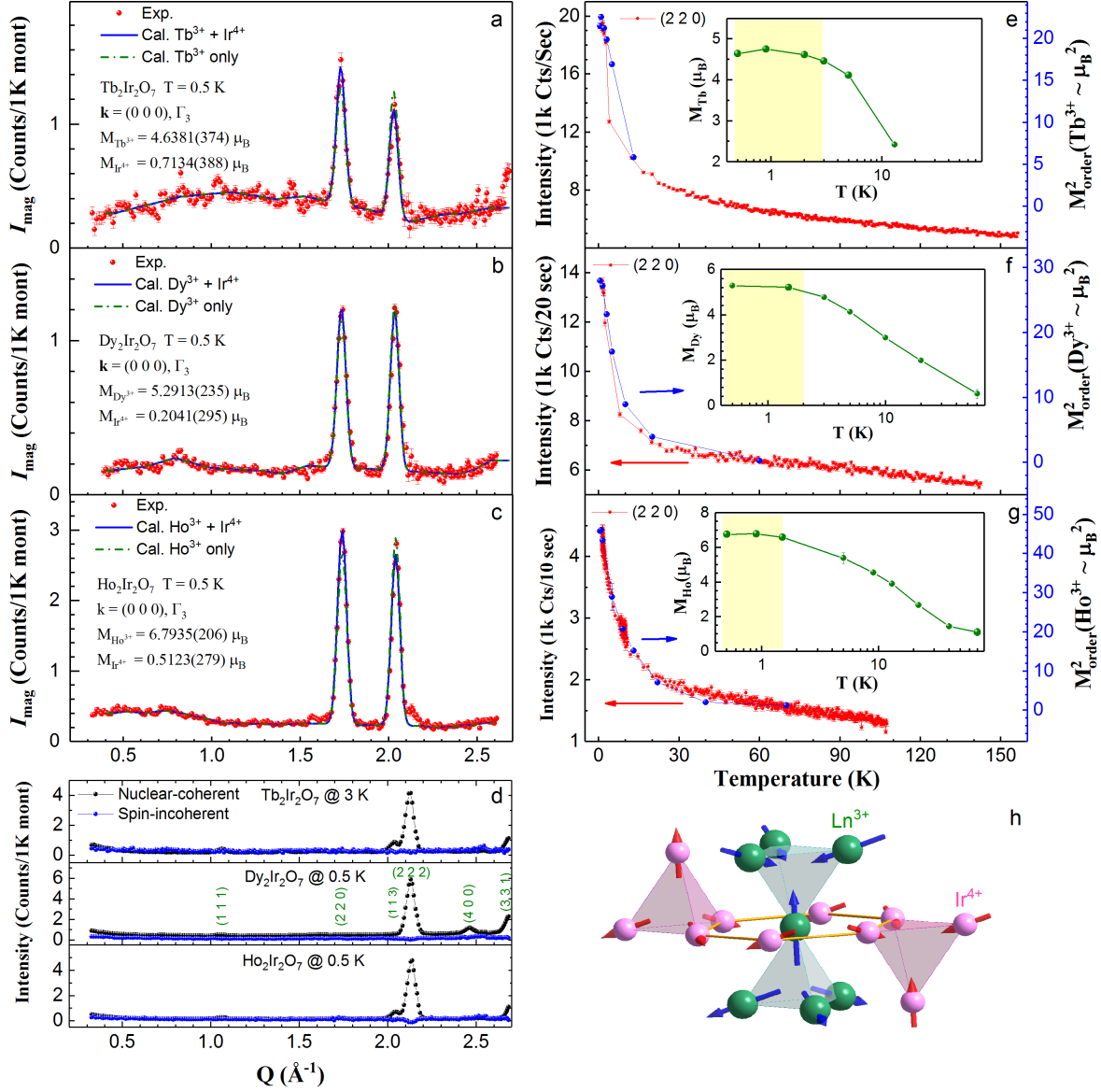
Figure 4.3.8 (a-c) The experimental and calculated magnetic scattering of TIO, DIO and HIO at 0.5 K. (d) The nuclear-coherent and spin-incoherent scattering of the three compounds. (e-g) Temperature dependence of the magnetic peak (2 2 0) intensity of TIO, DIO and HIO. Insert: the temperature dependence of the ordered moment of Ln^{3+} obtained by magnetic structure refinement. (h) The magnetic structure of these three compounds. Note: 1000 monitor counts (1K mont) corresponds to 0.035 sec during DNS measurement.

As shown in Figure 4.3.8 (a-c), the presence of magnetic peaks (2 2 0) and (1 1 3) indicates that TIO, DIO and HIO order in AIAO configuration, similar to NIO. In contrast to NIO, the magnetic peak (2 2 0) of these three compounds is slightly higher than peak (1 1 3). The NIO

magnetic structure refinement strategy was applied to these three compounds. The model considering two magnetic sublattices with Ln^{3+} and Ir^{4+} results a good agreement of refinement, as shown with the solid line in Figure 4.3.8 (a-c). The obtained ordered moment of Ln^{3+} and Ir^{4+} is present in Table 4.3.4, in which the ordered moments of Ln^{3+} in TIO and HIO agree to the recent unpolarized NPD results [134,160]. The obtained M_{Ir} from TIO and HIO is larger than that from NIO and DIO, which is possibly caused by the uncertainty of the *xyz*-polarization separation on strong nuclear Bragg peaks (1 1 3) in TIO and HIO. In Figure 4.3.8 (e-g), the temperature dependence of the magnetic peak (2 2 0) of these three compounds shows unusual behavior like NIO. The difference is that the ordered moment of Ln^{3+} (Tb, Dy, Ho) starts to saturate around 2 K, implying the interaction between Ln^{3+} plays a role. The dominating interaction at this temperature is possibly the dipole-dipole interaction due to the large magnetic moment of Tb^{3+}, Dy^{3+} and Ho^{3+} [31].

Table 4.3.4 The ordered moment of Ln^{3+} and Ir^{4+} obtained by the refinement with AIAO configuration of both two sublattices. The negative sign of the Ir^{4+} moment refers the relative parallel arrangement to M_{Ln}. μ_{eff} is the effective magnetic moment obtained from the CW fitting of the susceptibility in higher temperature range. μ_{CEF} is the reduced magnetic moment due to CEF adopted from Chapter 2.

Ln^{3+}	Nd (0.1 K)	Tb (0.5 K)	Dy (0.5 K)	Ho (0.5 K)
M_{Ir} (μ_B)	-0.2808(268)	0.7134(388)	0.2041(295)	0.5123(279)
M_{Ln} (μ_B)	1.4025(202)	4.6381(374)	5.2913(235)	6.7935(206)
μ_{eff} (μ_B)	3.35	9.85	10.96	10.44
μ_{CEF} (μ_B)	2.65	5.35	9.8	9.8

Although both sublattice Ln^{3+} and Ir^{4+} display AIAO magnetic structure in the unit of tetrahedra, their relative arrangement is antiferromagnetic, meaning the net magnetic moment M_{Ir}^{eff} is antiparallel to the Ln^{3+} moment. This is determined by the relative intensity ratio of the magnetic peaks (2 2 0) and (1 1 3). A higher magnetic peak intensity of (2 2 0) associates to the relatively antiparallel arrangement between Ln^{3+} and Ir^{4+}, while the higher magnetic peak intensity of (1 1 3) corresponds to the relatively parallel case, such as in NIO. This result is not only observed in our polarized NPD experiment, but also in the reported unpolarized NPD of $Ln_2Ir_2O_7$. For instance, the extracted magnetic diffraction pattern of NIO displays a higher (1 1 3) peak [132], while the recently reported unpolarized NPD of TIO and HIO reveals a higher (2 2 0) peak [134,160]. However, the relative arrangement of Ln^{3+} and Ir^{4+} has not been noticed by the authors. On the other hand, all of the ordered moments of Ln^{3+} at

lowest temperature is smaller than that of the μ_{eff} and μ_{CEF}, implying the persistence of strong magnetic moment fluctuation at that temperature.

B. Easy-plane anisotropy case (EIO and YbIO)

Due to the CEF, the magnetic moments of Er^{3+} and Yb^{3+} in pyrochlore have a strong easy-plane component, so-called easy-plane or XY anisotropy. The nuclear coherent and magnetic scattering of Er$_2$Ir$_2$O$_7$ at 0.5 K is presented in the left panel of Figure 4.3.9. Besides several nuclear Bragg peaks observed in the nuclear coherent scattering pattern, a broad peak centered at Q = 1.16 Å^{-1} appears in the magnetic scattering contribution. This response is typical for a diffuse scattering, where spin correlations extend over a few interatomic distances. Such magnetic diffuse scattering has been observed in Er$_2$Sn$_2$O$_7$ at 1.5 K [41]. Assume the Er$_2$Ir$_2$O$_7$ is antiferromagnet with XY single-ion anisotropy (as Er^{3+} presented in other pyrochlore compounds), we could model the magnetic ground state in Er$_2$Ir$_2$O$_7$ by considering finite size magnetic domains (to account for the peak broadening) chosen among the symmetry allowed patterns for a **k** = (0 0 0) propagation vector.
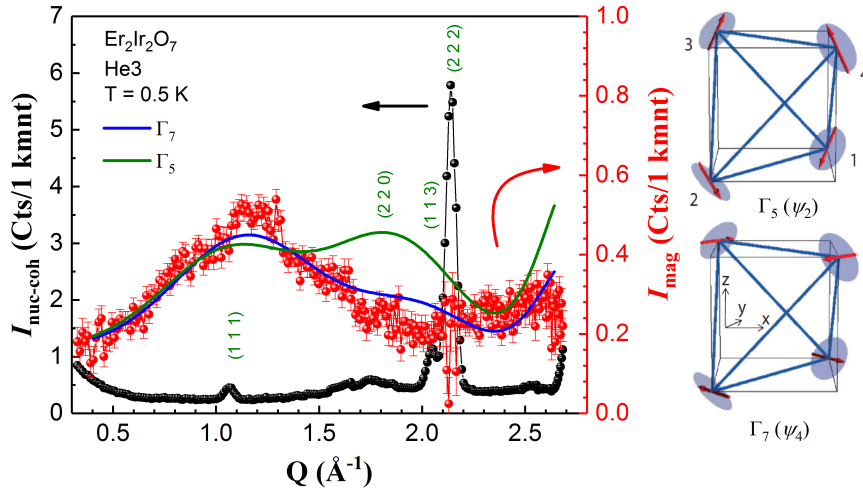
Figure 4.3.9 *Left*: Nuclear coherent scattering and magnetic scattering of Er$_2$Ir$_2$O$_7$ at 0.5 K. The solid lines are the result of a Rietveld fit assuming either the $\psi_{2,3} - \Gamma_5$ (green line) or the $\psi_{4,5,6} - \Gamma_7$ (blue line) structure. *Right*: Magnetic configurations ψ_2 and ψ_4 predicted by the symmetry analysis for the k = (0 0 0) propagation vector. The Γ_7 irreducible representation is associated to the Palmer-Chalker state. Note: 1000 monitor counts (1K mont) corresponds to 0.035 sec during DNS measurement.

According to the symmetry analysis in Appendix B, the XY anisotropy is minimized only for (1) linear combinations of the two basis vectors ψ_2 and ψ_3 which transform according to Γ_5; and (2) a discrete set of basis vectors $\psi_{4,5,6}$ which transform according to Γ_7. The ground

state of $Er_2Ti_2O_7$ corresponds to ψ_2 [99], while the Palmer-Chalker states (PC) (spins are pairwise anti-parallel, and collinear with an edge of the tetrahedron) corresponds to $\psi_{4,5,6}$ [40]. As shown in appendix B, the powder measurements cannot distinguish between the basis vectors of either Γ_5 or Γ_7. However, for a given representation, the relative intensities of the (1 1 1) and (2 2 0) peaks are fixed. The choice between Γ_5 and Γ_7 IRs is thus unambiguous.

We can simply simulate the magnetic diffuse magnetic scattering by following Ref [41]. As done in the ordered iridates, we fitted the crystalline structure in the nuclear coherent scattering patterns to determine the overall scaling factor and the lattice parameters. Employing these values and assuming a given ψ sets, the two remaining parameters of the proposed model are the amplitude of Er^{3+} moment and the coherence length of the magnetic domains, which determines the width of the diffuse magnetic scattering peaks. As shown in the left panel of Figure 4.3.9, a good refinement is obtained with the vectors $\psi_{4,5,6}$ of Γ_7, with an Er^{3+} moment of 5.032 μ_B at 0.5 K and a coherence length of about 7.9 Å. A much worse agreement is obtained with the vectors $\psi_{2,3}$ of Γ_5. The results strongly suggest that the Er^{3+} in $Er_2Ir_2O_7$ is short-range ordered as Palmer-Chalker configuration at 0.5 K. Additionally, the estimated moment 5.032 μ_B of Er^{3+} is smaller than that of 9.5 μ_B for the free ion, implying that the strong fluctuation exists at 0.5 K.
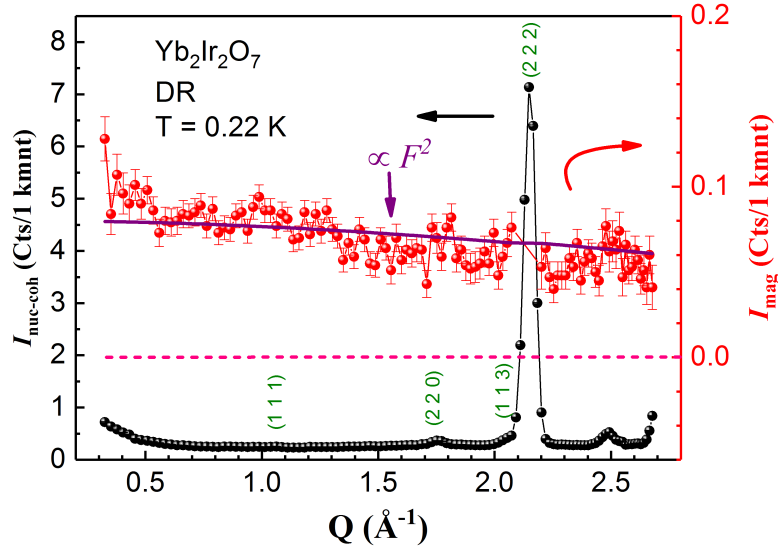

Figure 4.3.10 Nuclear coherent scattering and magnetic scattering of $Yb_2Ir_2O_7$ at 0.22 K. The purple solid line is proportional to the squared magnetic form factor of Yb^{3+}, representing the Q dependence of magnetic scattering in the paramagnetic state.

Figure 4.3.10 shows the nuclear coherent and magnetic components from Yb$_2$Ir$_2$O$_7$ at 0.22 K. No magnetic Bragg peaks associated with magnetic long-range order are observed in the magnetic scattering pattern. The intensity of magnetic scattering decays with Q, however, slightly faster than that of the paramagnetic state following the squared magnetic form factor of Yb^{3+} (purple solid line). This is possibly caused by the ferromagnetic correlation of Yb^{3+} that leads to the nearly collinear order of Yb$_2$Ti$_2$O$_7$ and splayed ferromagnetic order of Yb$_2$Sn$_2$O$_7$ below 0.28 K and 0.15 K, respectively [39,94]. According to the absence of the specific heat anomaly of YbIO below 0.22 K, the YbIO would not undergo a phase transition to some kind of magnetic long-range order like other Yb-based pyrochlore. Further investigations at low temperature is still necessary to refine this statement.

The above discussion has presented that the magnetic long-range order of Ln^{3+} emerges in the system in which rare-earth ions exhibit easy-axis anisotropy, but is absent in the system with strong planar spin anisotropy of Ln^{3+}. The molecular-magnetic field model was proposed to explain this result and the unusual temperature dependence of the order parameter [134]. As shown in Figure 4.3.7 (d), each six first-neighbor Ir^{4+} of Ln^{3+} form a hexagon plaquette, where Ln^{3+} is at the center. The AIAO arrangement of Ir sublattice yields a net moment M$_{Ir}^{eff}$ perpendicular to the hexagon plane (parallel to local $\langle 1\ 1\ 1\rangle$ direction). The M$_{Ir}^{eff}$ then could generate a *molecular-magnetic field*, $B_{mf}^{Ir} \propto$ M$_{Ir}^{eff}$ on the Ln^{3+} site. Therefore, for the Ln^{3+} with easy-axis anisotropy, i.e. Nd^{3+}, Tb^{3+}, Dy^{3+} and Ho^{3+}, such a molecular field B_{mf} can easily polarize the spin of Ln^{3+} to form AIAO long-range order according to the symmetry. On the contrary, the B_{mf}^{Ir} cannot induce any long-range order of Ln^{3+} along local $\langle 1\ 1\ 1\rangle$ direction in EIO and YbIO due to the strong easy plane anisotropy of Er^{3+} and Yb^{3+}, and even suppress their easy-plane ordering like in other Er- and Yb- based pyrpchlore compounds. For this reason, no magnetic Bragg peaks associated to magnetic long-range order are observed in the magnetic scattering of EIO and YbIO at very low temperature.

The temperature dependence of the order parameter in NIO, TIO, DIO and HIO is thus the so-called induced ordering. The induced ordering behavior often occurs in a two magnetic sublattice system with different coupling strength in each magnetic sublattice. For example, in the iron-based superconductor SmFeAsO, the magnetic moments of d and f electrons cannot naturally order at the same temperature due to the different magnetic coupling strength of the Fe and Sm sublattice, as revealed by resonance X-ray scattering [173]. When the d electrons of Fe order magnetically at 110 K, the Sm magnetic structure grows mainly below 50 K and accelerates significantly with further cooling due to the exchange field between Sm

and Fe. In $Ln_2Ir_2O_7$ (Ln = Nd, Tb, Dy and Ho), the magnetic ordering of Ir^{4+} is expected to occur at $T_{MI} \sim 33\text{-}145$ K, the exchange interaction in Ln sublattice is around 1 K. Therefore, the magnetic moment of Ln^{3+} would show the induced ordering behavior in the range from ~ 1 K to T_{MI}. The induced ordering of Ln^{3+} can be described by the Hamiltonian: $\mathcal{H} = \mathcal{H}_{CEF} + \mathcal{H}_{Ln\text{-}Ir}$, where $\mathcal{H}_{CEF}$ is the CEF Hamiltonian (Eq 2.2.3) and $\mathcal{H}_{Ln\text{-}Ir} = B_{mf}^{Ir} g_J \mu_B \vec{J}$ is the Ln-Ir magnetic coupling by the Ir^{4+} molecular field B_{mf}. The Ln^{3+} magnetic moment is then calculated as $\vec{M}_{Ln} = g_J \mu_B \mathrm{Tr}\big[\vec{J}\exp(-\beta\mathcal{H})\big]$ [134]. As discussed in Chapter 2, the CEF ground-state of Ln^{3+} in pyrochlore exhibits Kramers or non-Kramers doublet due to the local point symmetry D_{3d}. For the ions with a well-isolated ground-state doublet, only the ground-state doublet is appreciably populated at low temperature. Then one can simplify the aforementioned Hamiltonian to the splitting of the ground-state doublet. The ordered moment is [174]:

$$M_{Ln}(\mathrm{T}) = M_0 \tanh\left(\frac{\Delta_Z}{2k_B \mathrm{T}}\right) \tag{4.3.4}$$

where M_0 is the effective moment of Ln^{3+}, k_B is the Boltzmann constant and $\Delta_Z = 2g_J \mu_B J B_{mf}^{Ir}$ is the Zeeman splitting of the ground-state doublet by B_{mf}^{Ir}. For a pseudospin-1/2 system [175]:

$$\Delta_Z = \mu_B \sqrt{\left(g_{\parallel} B_{mf,\parallel}^{Ir}\right)^2 + \left(g_{\perp} B_{mf,\perp}^{Ir}\right)^2} \tag{4.3.5}$$

where $g_{\parallel}$ and $g_{\perp}$ are the anisotropy g tensor components along and perpendicular to the local $\langle 1\,1\,1 \rangle$ axis, $B_{mf,\parallel}^{Ir}$ and $B_{mf,\perp}^{Ir}$ are the corresponding projection of the molecular field B_{mf}^{Ir}. Since the AIAO ordered Ir sublattice only yields a net moment M_{Ir}^{eff} along the local $\langle 1\,1\,1 \rangle$ direction on the Ln site,

$$B_{mf,\parallel}^{Ir} = B_{mf}^{Ir} = \lambda \mathrm{M}_{Ir}^{eff} , \; B_{mf,\perp}^{Ir} = 0$$
$$\Delta_Z = \mu_B g_{\parallel} B_{mf}^{Ir} \tag{4.3.6}$$

Figure 4.3.11 shows the temperature dependence of the ordered moment of Ho^{3+} and Dy^{3+} obtained from the magnetic structure refinement. The solid lines represent the fitting of the induced ordering model in the temperature range $5-80$ K, where the ordered moment of Ir^{4+} is stable and the interaction of the Ln sublattice is negligible. The fitting yields the effective moment M_0 as 4.6975(3443) and 6.0049(3101) μ_B for Dy^{3+} and Ho^{3+}, respectively. The obtained M_0 is quite close to the saturated ordered moment obtained from the magnetic structure refinement, implying only part of the Ln^{3+} magnetic moment could be polarized by the B_{mf}^{Ir}. Indeed, the non-zero diffuse magnetic scattering of DIO and HIO at 0.5 K (in Figure

4.3.8) strongly suggests the existence of the disordered moment. The fitting gives rise to the Zeeman splitting of the ground-state doublet, Δ_Z, 1.3662(2547) and 1.2057 (1295) meV for Dy^{3+} and Ho^{3+}, respectively. According to Eq. (4.3.6), the corresponding effective molecular field of Ir^{4+}, B_{mf}^{Ir}, is around 1.1336(1259) T, which is close to the reported estimation [134,160]. Assuming the same B_{mf}^{Ir} for other pyrochlore iridates at low temperature, according to the g tensor (Table 2.2.2) one can roughly estimate the Zeeman splitting $\Delta_Z =$ 0.3447 meV for NIO, 0.7021 meV for TIO, 0.2559 meV for EIO and 0.1260 meV for YbIO (as listed in Table 4.3.5). However, the estimated Zeeman splitting Δ_Z does not match the energy level Δ_C obtained from the magnetic specific heat C_{mag} in the previous subsection. It is worth to examine the possible Zeeman splitting of the Ln^{3+} ground-state doublet via inelastic neutron scattering. In addition, the molecular field model could not explain the relative arrangement of magnetic moments between Ln^{3+} and Ir^{4+}, that are the effective ferromagnetic arrangement in NIO and the antiferromagnetic arrangement in TIO, DIO and HIO.
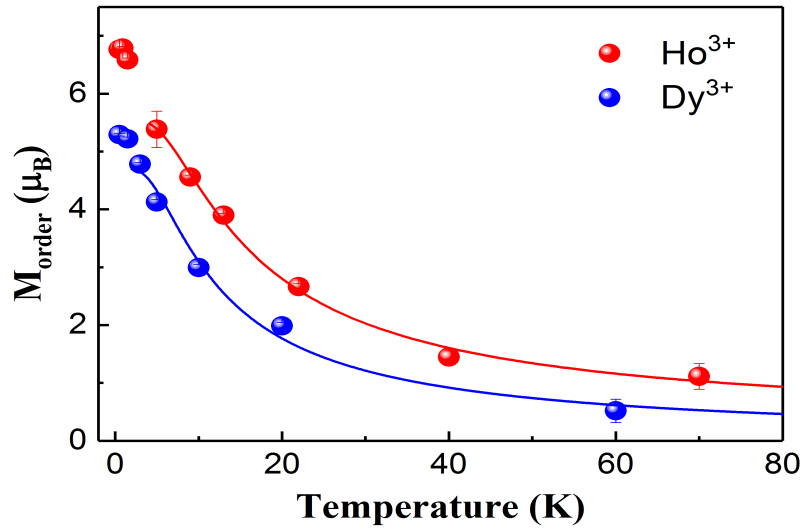
Figure 4.3.11 The temperature dependence of the ordered moment of Ho^{3+} and Dy^{3+} in HIO and DIO. The solid lines represent the induced ordering behavior.

Table 4.3.5 Predicted Zeeman splitting Δ_Z of the CEF ground-state doublet of Ln^{3+} according the induced ordering model.

Ln^{3+}	Nd	Tb	Dy	Ho	Er	Yb
Δ_Z (meV)	0.3447	0.7021	1.3662	1.2057	0.2559	0.1260

4.3.5. Inelastic neutron scattering

In order to observe the possible Zeeman splitting of the Ln^{3+} ground-state doublet in $Ln_2Ir_2O_7$, we performed systematic INS measurements of this compound series on TOFTOF at 3.5 K. The incident neutron energies 3.27 meV for NIO, TIO, DIO and HIO and 2.70 meV for EIO and YbIO give rise to the measurable dynamic range up to 2.5 meV and the energy resolution around 0.15 meV and 0.06 meV, respectively, which are good enough to observe the possible Zeeman splitting of Ln^{3+} estimated in previous subsections. Data sets were collected at 3.5 K, where the ordered moment of Ir^{4+} is assumed to be stable. The raw data was reduced to $I(Q,E)$ format in a standard routine taken into account the neutron absorption of iridium.

As shown in Figure 4.3.12, there is no clear gapped sharp excitation corresponding to the splitting of the Dy^{3+}, Ho^{3+} and Yb^{3+} ground doublet, except a strong broaden quasielastic signal associated to collective spin behaviors. The gapped excitations could be observed around 1.20 meV, 0.5 meV and 0.35 meV in NIO, TIO and EIO, respectively. However, these modes appear slightly dispersive and none of them exhibit the characteristic Q dependence of the CEF excitation which follows the squared magnetic form factor of the Ln^3, as plotted in Figure 4.3.13. Although, some of the lower lying CEF excitations of Tb^{3+} and Er^{3+} in pyrochlore at low temperature may show weak dispersion due to the strong exchange interactions [37,176,177]. This fact strongly suggests that these modes possibly belong to the collective spin excitations of Ln^{3+}.
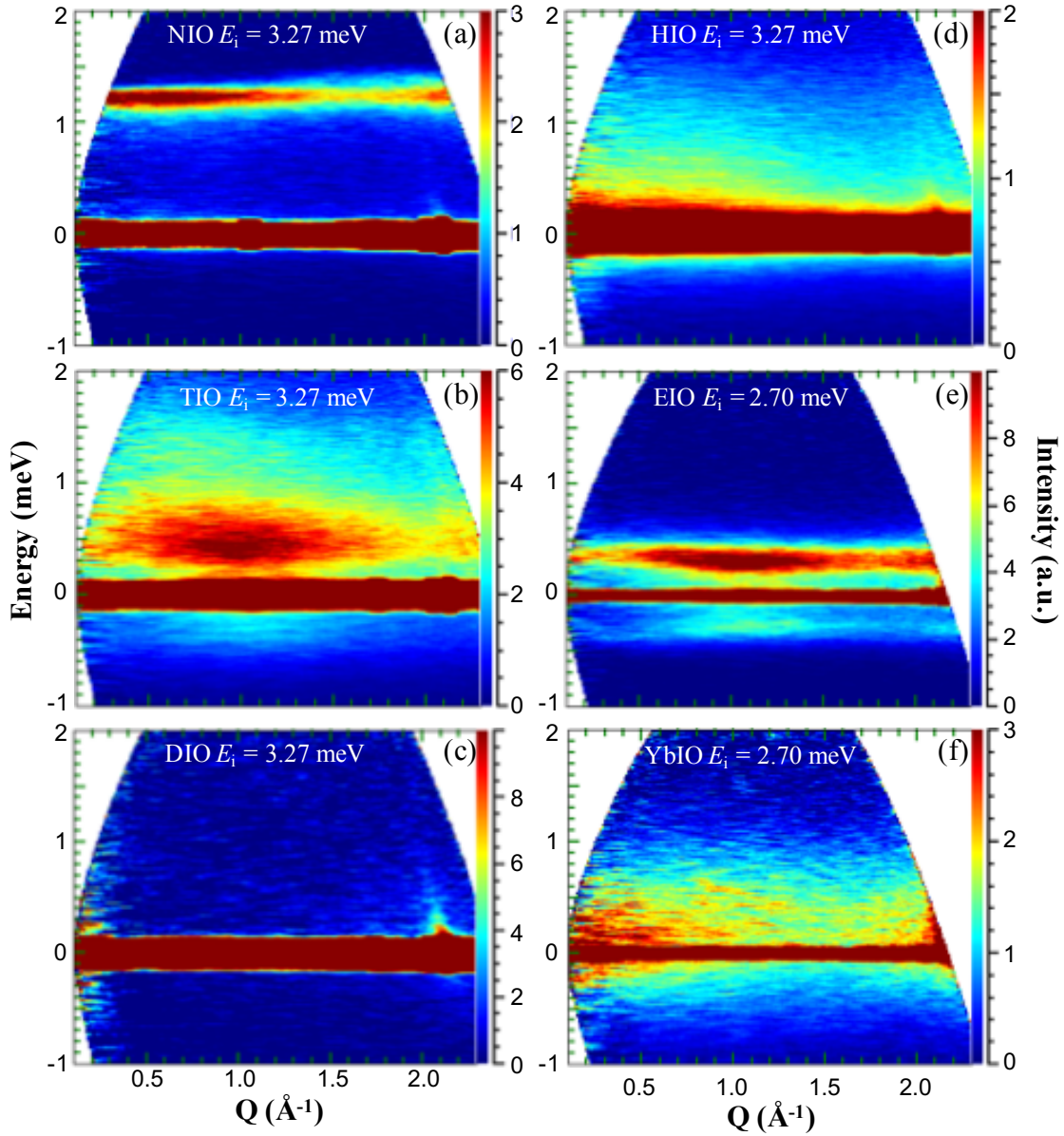
Figure 4.3.12 Inelastic neutron scattering measurements with an incident energy of E_i = 3.27 meV (IRF ~ 0.15 meV) for NIO, TIO, DIO and HIO and E_i = 2.70 meV (IRF ~ 0.06 meV) for EIO and YbIO at 3.5 K. The color-bar represents the intensity in arbitrary unit.

As see in Figure 4.3.12 (a), beside the flat mode around 1.2 meV, another dispersive mode appears from the (1 1 1) peak, agreeing with previous report [131]. The intensity of this excitation illustrated in Figure 4.3.13 (a) shows a dipolar-spin-ice characteristic with a maximum intensity around Q = 0.5 Å^{-1} and a minimal intensity at Q = 1.5 Å^{-1} [67]. In fact, the similar excitation has been observed in other Nd-based pyrochlore compounds in their AIAO state due to the 'dipolar-octupolar' nature of the Kramers Nd^{3+} doublet [44]. For example, INS measurement on Nd$_2$Zr$_2$O$_7$ (NZO) show a spin-ice characteristic flat mode at 0.07 meV (T_N = 285 mK) [178], while Nd$_2$Hf$_2$O$_7$ (NHO) exhibits the flat excitation at 0.1

meV (T_N = 535 mK, Chapter 6). The difference of the mode in NIO is the excitation energy is 10 times larger than that in NZO and NHO. The possible reason to lift the mode to such higher energy could be attributed to the molecular field B_{mf}^{Ir} and the RKKY interaction in NIO, since NIO is a semimetal, while NZO and NHO are perfect insulator. The absence of the splitting of the ground doublet in our INS experiment implies that the exchange strength between Ln^{3+} and Ir^{4+} should be smaller than the best energy resolution ~ 0.06 meV. Thus, the RKKY interaction would dominate the system. Indeed, a recent band structure measurement has observed the quadratic band touching near the Fermi level in NIO [179]. This band structure may provide conduction electron to mediate the magnetic interaction between Nd^{3+}. Therefore, the simple molecular field model of Ln-Ir is not suitable to understand the above phenomena. A complex model considering the detail of the *f-d* exchange is expected. The process of understanding the INS data of other pyrochlore iridates is still ongoing.
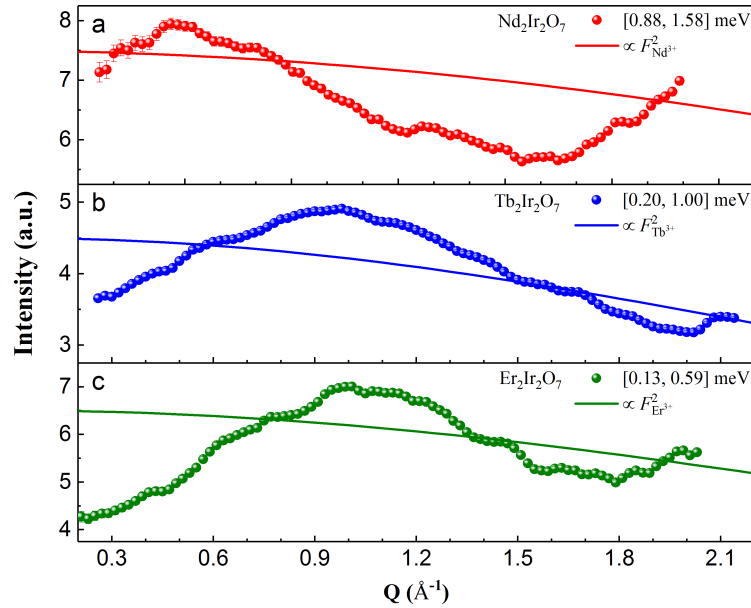
Figure 4.3.13 Q dependence of the intensity of the gapped excitation of NIO, TIO and EIO integrated over the energy interval indicated in the figure in Figure 4.3.12 (a, b, e). The solid line is proportional to the squared magnetic form factor of Ln^{3+} (Nd, Tb and Er). A CEF excitation of Ln^{3+} should follows the solid lines.

4.4. Conclusion

The rare-earth pyrochlore iridates $Ln_2Ir_2O_7$ (Ln = Nd, Tb, Dy, Ho, Er, Yb) with metal-to-insulator transition have been systematically investigated by means of neutron powder diffraction, dc-magnetization, specific heat, polarized neutron scattering and inelastic

neutron scattering. While the 48f oxygen x-parameter decreases with increasing Ln ionic radius, the cubic lattice constant a, the Ir-O bond length and the O-Ir-O angle systematically increase, supporting the theoretical band structure calculation of the metal-to-nonmetal transition of Ln$_2$Ir$_2$O$_7$. The ZFC-FC magnetization curves of Ln$_2$Ir$_2$O$_7$ bifurcate at T_{MI} for Ln = Nd, Tb, Dy, Ho, Er and Yb with T_{MI} = 33, 127, 125, 135, 142 and 143 K, suggesting a magnetic transition at T_{MI}. Except for HIO with a positive CW temperature, other compounds reveal a negative CW temperature indicating the antiferromagnetic coupling between Ln^{3+}. A specific heat anomaly associated with the magnetic transition T_{MI} in NIO is observed at 33 K, supporting AIAO ordering of the Ir sublattice. All compounds exhibit a broad hump in the obtained magnetic specific heat, C_{mag}, at 5.0, 3.0, 3.0, 1.5 and 2.3 K for Ln = Nd, Tb, Dy, Er and Yb. The calculation of the corresponding entropy strongly suggests the hump of C_{mag} corresponds to the development of the magnetic short-range ordering of Ln^{3+}. With polarized neutron diffraction, the magnetic ground-state phase diagram of Ln$_2$Ir$_2$O$_7$ is created, as shown in Figure 4.4.1. For the planar anisotropic ions, Ln = Er and Yb, the observed diffuse magnetic scattering indicates the short-range ordered state of Er^{3+} and Yb^{3+}. The ions with easy-axis single-ion anisotropy, Ln = Nd, Tb, Dy and Ho, the Ln^{3+} exhibit a magnetic long-range order state with AIAO configuration. A molecular magnetic field, B_{mf}^{Ir}, generated by AIAO ordered Ir^{4+} was introduced to account for the magnetic state phase diagram and the unusual ordering behavior of NIO, TIO, DIO and HIO. The estimated strength of B_{mf}^{Ir} is around 1.1336(1259) T, yielding a possible Zeeman splitting of the CEF ground doublet of Ln^{3+}. Unfortunately, the absence of the ground doublet splitting in the INS measurements does not support the molecular field scenario. A more complex model involving the RKKY interaction and considering the f-d exchange in detail is needed.
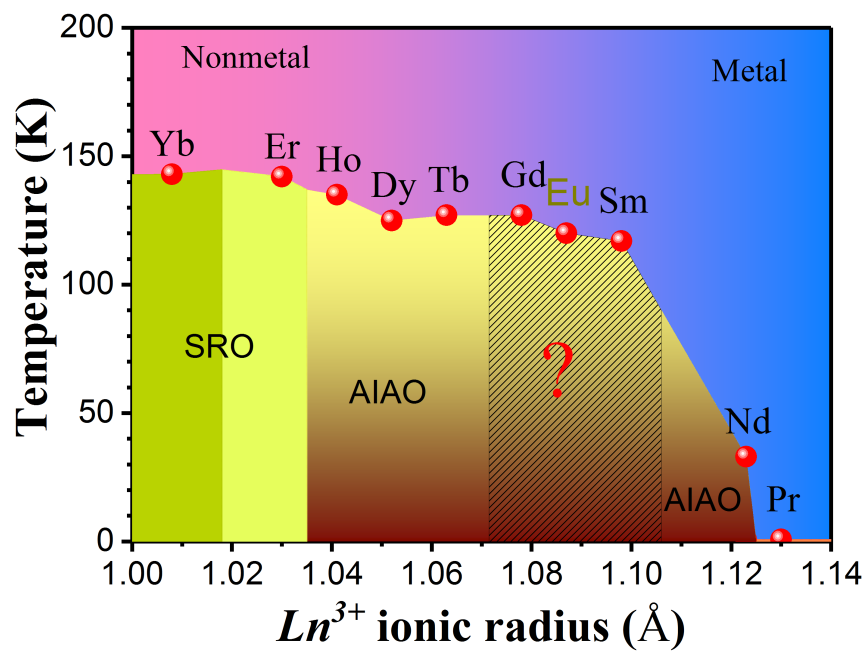
Figure 4.4.1 Phase diagram of the Ln^{3+} magnetic states in $Ln_2Ir_2O_7$.

Chapter 5. Long-range Spin-Ice Order and Magnetic Excitations in Metallic Pyrochlore $Pr_2Ir_2O_7$

5.1. Introduction

As discussed in the previous chapters, one can experimentally realize the physics of the quantum spin ice by reducing the dipolar interaction and enhancing quantum fluctuations. The Pr-based pyrochlore compounds, $Pr_2B_2O_7$ (with B = Sn, Zr, Hf and Ir) are such candidates. The first three are insulators, while $Pr_2Ir_2O_7$ is a metal. The dipolar interaction strength is estimated around 0.13 K [95], almost 10 times smaller than that of classical spin ice (CSI) compounds DTO and HTO. Their crystal field scheme suggests that the moments are Ising-like, along the local $\langle 1\,1\,1 \rangle$ axis, with a non-Kramers doublet ground-state that could be described by effective spin-1/2 [33,180]. The quantum fluctuation could be enhanced by incorporation of the quadrupolar degrees of freedom [42,86,181] or random transverse fields due to the slight site disorder [45,182]. Indeed, significant spin fluctuations, which are absent in CSI, were observed experimentally in the insulator compounds [95-97,183,184]. However, the QSI phase has not been unambiguously confirmed in the Pr-227 insulating compounds up to now.

Due to strong spin-orbit coupling (SOC) and strong electron-electron interactions, novel states may emerge in the metallic pyrochlore iridate $Pr_2Ir_2O_7$. A recent ARPES (angle-resolved photoemission) experiment on a single crystal sample provides strong evidence for a quadratic band-touching dispersion in the semi-metallic paramagnetic phase [185]. However, the magnetic properties of metallic $Pr_2Ir_2O_7$ are strongly sample dependent. Early measurements focused on the single crystal sample, which is believed to be stoichiometric, grown by flux method [143]. Neither the specific heat, nor the DC magnetization show any sign of long-range ordering transition down to a field-cooled and zero field-cooled bifurcation temperature $T_f = 1.2\,\text{K}$, where the moments partially freeze [186]. More interestingly, Hall-effect measurements in the single crystal reveal a $\ln T$ temperature dependent Hall resistivity and a zero-field anomalous Hall effect in the temperature range $0.3\,\text{K} < T < 1.5\,\text{K}$ [187-189]. This has been interpreted as evidence of chiral spin liquid, in which the chirality of the Pr^{3+} moment configurations in one tetrahedral is the order parameter.

Spin-ice type physics for the Pr moments has also been inferred. The origins for these phenomena have been suggested by several theoretical works, including ordinary and exotic RKKY interactions, quadrupolar ordering, etc [190-193]. Early Muon-spin relaxation (μSR) measurements in a powder sample suggest a non-magnetic Pr^{3+} ground state, against the CEF analysis [194-196]. A reason is that the muons reside in the sample, leading to the splitting of the non-Kramers ground state of Pr^{3+}, and the effect is enhanced by the hyperfine interaction of nuclear magnetization at low temperature [197]. This means that the μSR results for disordered Pr-pyrochlore are unreliable. On the other hand, the transport properties of the "stuffed" $Pr_2(Ir_{2-y}Pr_y)O_{7-y/2}$ suggests a phase transition around 0.8 K [158,198], which is further confirmed by powder neutron diffraction as a "two-in-two-out" (2I2O) long-range magnetic order transition with an ordered moment of 1.73 μ_B/Pr [199]. The author argued that the 2I2O order of Pr^{3+} is unstable based on the estimated correlation time of a few nanoseconds for the Pr^{3+} $4f$ moment, which is expected to be identified by neutron spin echo experiment. It should be noted that the phase transition does not change the metallic nature of the stuffed $Pr_2(Ir_{2-y}Pr_y)O_{7-y/2}$ [198].

Motivated by the fascinating physics and the controversial results of the metallic pyrochlore $Pr_2Ir_2O_7$, we have synthesized high-quality powder samples at a relatively low temperature using an optimized synthesis recipe (see Chapter 3). According to our combined Rietveld refinements of XRPD and NPD, the stuffing level y is determined to be less than 0.02. The sample exhibits a negative Curie-Weiss temperature and undergoes an 2I2O long-range order transition at 0.76 K as determined by specific heat and polarized neutron scattering. A gapped exotic magnetic excitation was observed by inelastic neutron scattering. By employing the sum rule, we found that the total magnetic (i.e. fluctuating plus ordered) magnetic moment of Pr^{3+} is conserved through the transition, and is consistent to that obtained from the CEF analysis.

5.2. Experimental details

A polycrystalline $Pr_2Ir_2O_7$ sample was synthesized by solid state reaction starting from a mixture of powder Pr_7O_{11} (99.99%) and metal Iridium (99.99%), with molar ratio 1:1.05 of Pr-to-Ir, and by a new flux method using KF as flux. Then, the mixture was pressed into pellets, placed in an alumina crucible and sintered at 1050 ^{o}C in air for 7 days with several intermediate grindings and pelletizings. The nonmagnetic reference compound $Y_2Ir_2O_7$ was also prepared by the same method and used to estimate the phonon contribution for the heat

capacity. The phases of the sample were regularly checked during synthesis by room temperature powder x-ray diffraction (XRD) using a laboratory-based diffractometer (STOE, Mo-$K_{\alpha 1}$) with monochromator. Magnetic susceptibility was measured using a Quantum Design magnetic properties measurement system (MPMS) superconducting quantum interference device (SQUID) magnetometer. The heat capacity of the pelletized sample was measured down to 70 mK using a Quantum Design physical properties measurement system (PPMS).

Neutron diffraction measurements were carried out using the SPODI powder neutron diffractometer at the Heinz Maier-Leibnitz Zentrum (MLZ), Garching, Germany. The xyz-polarization analysis (XYZ-PA) was performed on the diffuse neutron scattering spectrometer (DNS) at MLZ, operated by the Juelich Centre for Neutron Science (JCNS). Around two grams powder sample were sealed in a hollow cylinder copper can with optimized thickness to reduce neutron absorption. A dilution refrigerator was used to achieve the lowest temperature of 0.1 K. An incident neutron beam of wavelength λ = 4.52 Å was used for the experiments, and the data were collected for 20 hours at each temperature. The XRPD and NPD data were refined using the package FULLPROF suite.

Inelastic neutron scattering measurements with thermal and cold neutrons were performed on the direct geometry time-of-flight spectrometers MERLIN at ISIS, LET at ISIS and TOFTOF at MLZ, respectively. On MERLIN, the sample was measured with three incident energies E_i = 65.7, 116 and 150 meV at 5 K by using a standard 'Orange' cryostat. With a dilution refrigerator, the collective magnetic excitation was measured on LET with the incident neutron beam of multi-E_i = 0.60, 0.90, 1.40 and 2.68 meV, and on TOFTOF with the incident neutron beam of E_i = 2.27 meV in the temperature range from 50 mK to 25 K. The raw data were reduced to $I_{raw}(Q,E)$ following standard procedures with the self-attenuation correction according to the sample absorption cross section and geometry. These measurements were carried out using the same sample as measured on DNS.

5.3. Results and discussion

5.3.1. Sample quality determination

Rietveld refinement was performed using Fullprof on the combined XRPD and NPD patterns to determine the crystallographic structure of the sample, as well as the sample quality [151]. The refinement is performed based on the stuffed pyrochlore model, Pr$_2$(Ir$_{2-y}$Pr$_y$)O$_{7-y/2}$. Within the face-centered cubic (fcc) space group $Fd\bar{3}m$, the 16d site is fully occupied by Pr,

the $16c$ site is dominated by Ir with small mixing of Pr, and oxygen vacancies were equally assigned to the two sites $48f$ and $8b$ according to the electric balance of the compounds. Both XRPD and NPD patterns were taken at room temperature ~ 300 K. Figure 5.3.1 shows the Rietveld refinement result of NPD and XRPD with stoichiometric model ($y = 0$). Both patterns have good agreement to theoretical calculation with $\chi^2 = 5.86$ and 2.31 for NPD and XRPD, respectively. As shown in Table 5.3.1, the lattice constant of our sample is estimated to be 10.40863(5) Å, slightly larger than 10.396(15) Å for single crystal [143], but smaller than 10.672(1) Å of the stuffed polycrystalline sample [199]. The lattice constant of our sample is also smaller than that of 10.6728 Å for $Pr_2Hf_2O_7$ [180], 10.7 Å for $Pr_2Zr_2O_7$ [96,200] and 10.6004(1) Å for $Pr_2Sn_2O_7$ [62], which is consistent with the fact that the ionic radius of Ir^{4+} is smaller than that of Hf^{4+}, Zr^{4+} and Sn^{4+}. The parameter of the oxygen position at $48f$ is $x = 0.33061(3)$, which is close to 0.33299(2) for single crystal sample. The comparison of different PIO samples suggests that our sample has no significant defects. In order to obtain the stuffing level, we performed a joint XRPD and NPD refinement as a function of parameter y. The Rietveld refinement agreement factors are plotted in the insert of Figure 5.3.1. It is clear that the agreement factors increase as y increases, indicating poor agreement with the stuffed pyrochlore model. The stuffing level y in our sample is then less than 0.02, which is the limit of the joint refinement of XRPD and NPD. It has to be noticed that the Bragg peaks in both patterns are slightly broadened, implying the existence of internal strain in the sample.

Table 5.3.1 Comparison of the lattice parameters a and x-parameter of the $48f$ oxygen position for various $Pr_2Ir_2O_7$ (PIO) samples and other Pr pyrochlore oxides.

	Lattice a (Å)	O_{48f} (x)	Stuffing y	T (K)	Ref
Ours PIO	10.40863(5)	0.33061(3)	<0.02	300	-
Single crystal PIO	10.396(15)	0.3299(2)	-	298	[143]
Powder PIO	10.406(5)	-	<0.2	300	[198]
Stuffed PIO	10.672(1)	-	0.4	2	[199]
$Pr_2Hf_2O_7$	10.6728(1)	0.3351(4)	<0.01	300	[180]
$Pr_2Zr_2O_7$	~10.7	~0.334	<0.01	300	[96,200]
$Pr_2Sn_2O_7$	10.6004(1)	0.33148(5)	-	300	[62,95,161]
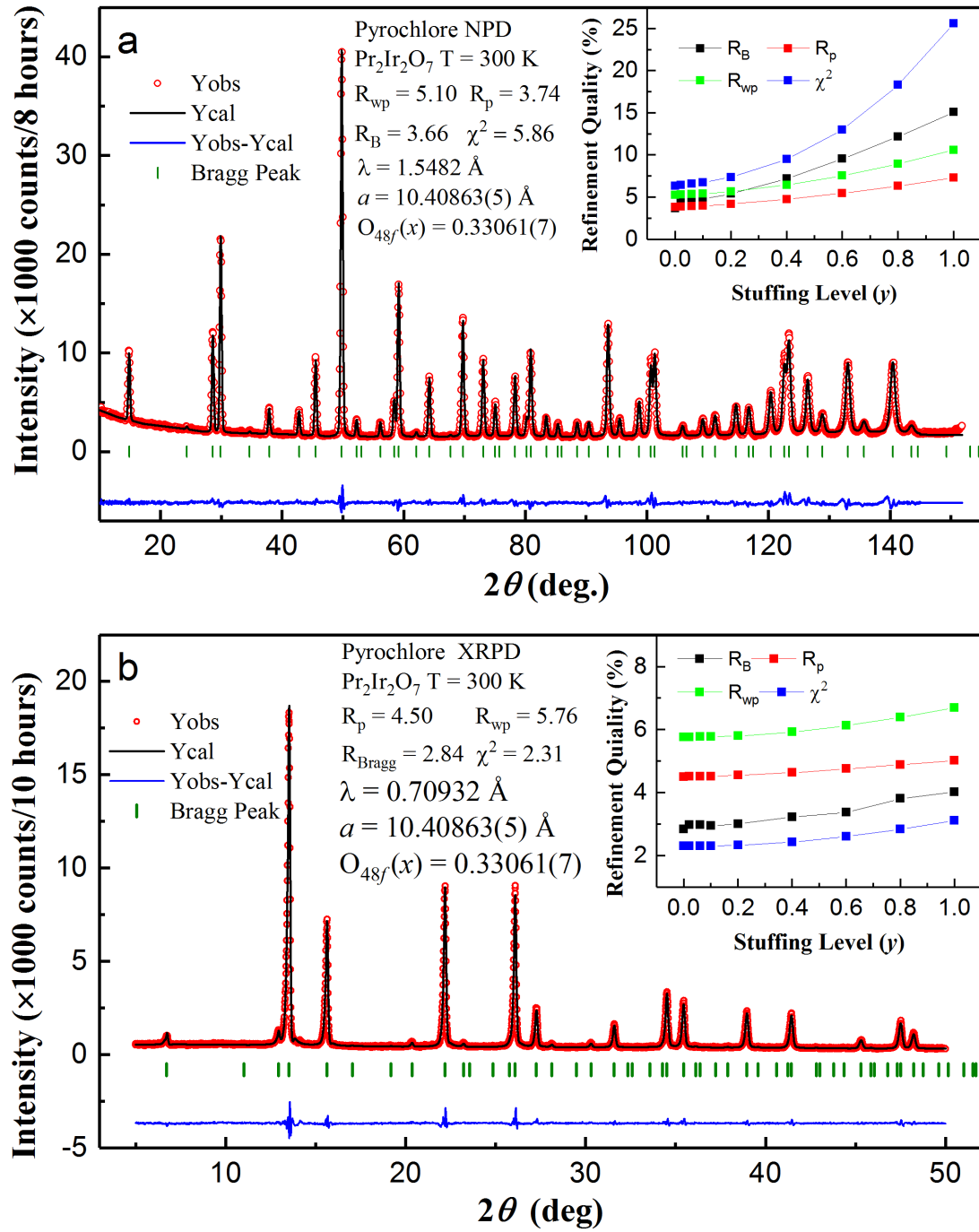
Figure 5.3.1 Experimental (Yobs), calculated (Ycal) and difference (Yobs-Ycal) neutron powder diffraction (NPD, upper panel) and X-ray powder diffraction (XRPD lower panel) patterns obtained at room temperature (~300 K) with the Rietveld refinement of pyrochlore structure. The green short lines indicate the position of the Bragg peaks. Insert shows the agreement factors as function of the stuffing level y in the refined model Pr$_2$(Ir$_{2-y}$Pr$_y$)O$_{7-y/2}$ with pyrochlore structure.

5.3.2. Bulk magnetization

Figure 5.3.2 (a) shows the field-cooled (FC) and zero-field-cooled (ZFC) DC magnetic susceptibility χ versus temperature measured in a field of $H = 0.1$ T. No anomalies or

thermal hysteresis, corresponding to the transitions to a long-range order or spin-glass in ZFC and FC $\chi(T)$ are observed down to 2 K. The insert of Figure 5.3.2 (a) shows the inverse susceptibility of $Pr_2Ir_2O_7$, as well as the Curie-Weiss (CW) fitting. As we will discuss in the crystal electric field (CEF) section, the first-excited CEF level of Pr^{3+} in $Pr_2Ir_2O_7$ is at 13 meV, roughly corresponding to about 150 K, therefore the thermal population of CEF will influence the CW fitting above 50 K. On the other hand, below 10 K, PIO enters the Kondo regime in which the localized magnetic moment is partially screened by the conduction electron [186]. Thus, the temperature range of the CW analysis was chosen from 15 to 40 K. A temperature-independent term χ_0 was included in the CW analysis to account for the Van Vleck effect [196]:

$$\chi(T) = \chi_0 + \frac{C}{T - \theta_{CW}}, \quad C = N_A \mu_{eff}^2 / 3k_B \tag{5.3.1}$$

where N_A is the Avogadro number and k_B is the Boltzmann constant. The fitting gives a negative Weiss temperature θ_{CW} = -1.811(31) K and μ_{eff} = 2.846(3) μ_B/Pr with Van Vleck contribution χ_0 = 0.00064(4) emu/mol-Pr. The negative CW temperature implies a weak antiferromagnetic (AF) coupling among Pr ions. The AF CW temperature is common for different PIO sample, most likely due to the RKKY interactions of the $4f$ moments [186], however, our sample shows the smallest absolute value of the Weiss temperature, compared to -20 K for single crystal [186,196] and -6 K for the polycrystalline sample [198]. The disagreement may be due to a different fitting temperature range that was used in other samples, i.e. up to 200 K, where the CEF effect can no longer be ignored. The temperature-independent constant, χ_0 is comparable to other PIO samples, as well as the effective magnetic moment, which is reduced to ~ 2.846(3) μ_B/Pr due to the CEF effect (see the discussion in the CEF section). As shown in Table 5.3.2, the metallic Pr-pyrochlore PIO exhibits a similar effective magnetic moment compared with its insulator counterparts. However, the CW temperature value of PIO is larger than that of other Pr-pyrochlore, implying a stronger magnetic interaction between Pr^{3+} moments. This can be attributed to the smaller lattice constant and the RKKY interaction assisted by the conduction electrons [190,201].

Table 5.3.2 Comparison of Curie-Weiss analysis of various $Pr_2Ir_2O_7$ and Pr pyrochlore oxides.

	θ_{CW} (K)	$\mu_{eff}(\mu_B)$	χ_0 (emu/mole-Pr)	T-range (K)	ref
Present sample	-1.811(31)	2.846(3)	0.00064(4)	15-40	-
Single crystal	-20	3.06	0.00125	100-350	[196]
Powder	-6	2.8	0.003	>100	[198]
$Pr_2Hf_2O_7$	0.06 or 0.40	2.54	0.005	12-25 or 1-4	[97,180]
$Pr_2Zr_2O_7$	-0.55 or -0.8	2.47	-	4-10	[181,200]
$Pr_2Sn_2O_7$	0.23	2.67	-	3-20	[62,95]
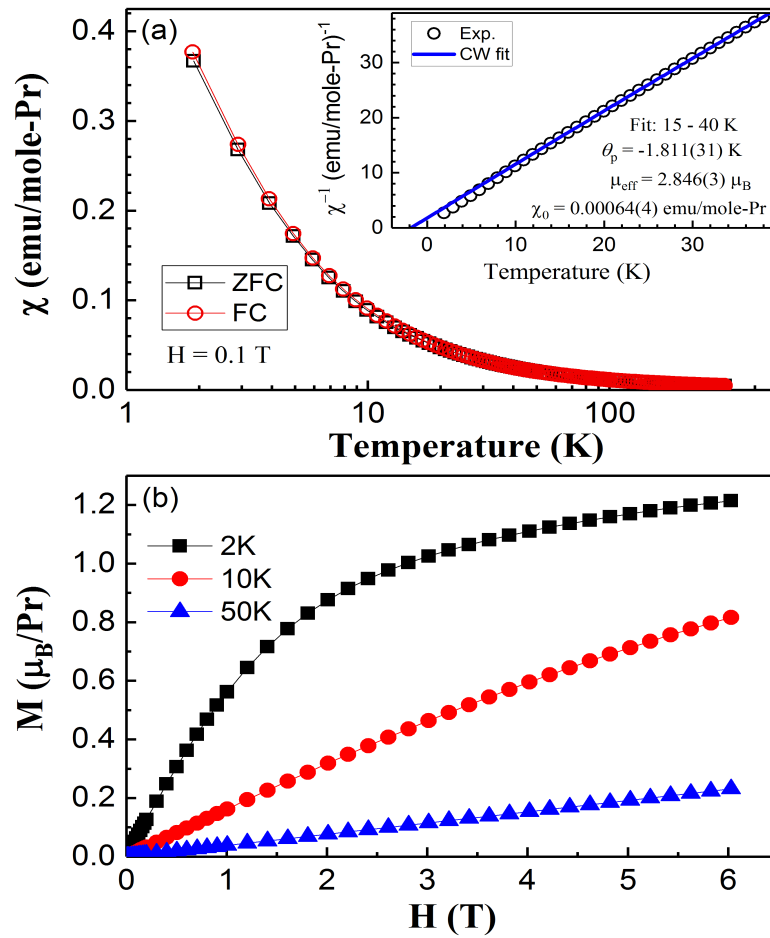
Figure 5.3.2 (a) Temperature dependence of susceptibility χ of polycrystalline sample $Pr_2Ir_2O_7$, measured from 2 to 300 K in an applied field $H = 0.1$ T. Insert: temperature dependence of inverse susceptibility χ^{-1} with the fit of Curie-Weiss law in the range 15 to 40 K (blue line). (b) Isothermal magnetization curves from 0 to 6 T at 2, 10 and 50 K.

Figure 5.3.2 (b) shows the isothermal magnetization curves $M(H)$ of $Pr_2Ir_2O_7$ at T = 2, 10 and 50 K. The $M(H)$ curve at 2K exhibits a saturation tendency with a magnetization value of M ~ 1.20 μ_B/Nd at 6 T, which is much smaller than the theoretical saturation magnetization

$M_s = g_J J \mu_B = 3.58 \, \mu_B/Pr$ for free Pr^{3+} ion. The strongly reduced value of M_s can be attributed to the strong Ising anisotropy and the reduction of the Pr^{3+} moment due to the CEF effect (see the CEF section). For a pyrochlore lattice with local [1 1 1] Ising anisotropy, the saturation magnetizations M_s at high fields for the three crystallographic directions [100], [110], and [111] are given by $g_{eff} J_{eff} \mu_B (1/\sqrt{3})$ for (two-in-two-out), $g_{eff} J_{eff} \mu_B (\sqrt{2/3} \times 2)/4$ for (two-in-two-out) and $g_{eff} J_{eff} \mu_B (1 + 1/3 \times 3)/4$ for (three-in-one-out), respectively [202]. Then the powder averaged M_s value should be $\langle M_s \rangle = \left(6M_{[100]} + 12M_{[110]} + 8M_{[111]}\right)/26 = 0.4755 \times g_{eff} J_{eff} \mu_B$, where the weight factors 6, 12 and 8 are the number of equivalent directions for [100], [110] and [111] [4]. As we show below $g_{eff} J_{eff} \mu_B = 2.283 \, \mu_B/Pr$ in the CEF section, the powder averaged saturation magnetization thus becomes $\langle M_s \rangle = 1.085 \, \mu_B$. The measured $M_s = 1.20 \, \mu_B$ at 2 K and 6 T is slightly bigger than the expected value. With increasing T, the linear regime of $M(H)$ extends over a large field range, although at a more gradual rate.

5.3.3. Specific heat

The specific heat $C(T)$ of $Pr_2Ir_2O_7$ in the temperature range from 80 mK to 40 K under zero magnetic field is shown in Figure 5.3.3. On cooling, the specific heat shows a characteristic broad hump as in spin ice with maximum around 2 K. A sharp peak appears at $T_{order} \sim 0.8$ K, with a characteristic λ-shape indicating a bulk phase transition associated with the ordering of the Pr^{3+} moments. At lower temperatures, another peak in the specific heat is observed around 0.15 K. This was explained as a [141]Pr nuclear Schottky anomaly associated with the hyperfine field B_{hf} due to the ordered Pr^{3+} ionic moments [203]. However, the explanation is not suitable for our case because the nuclear Schottky anomaly is much broader than the peak at 0.15 K.
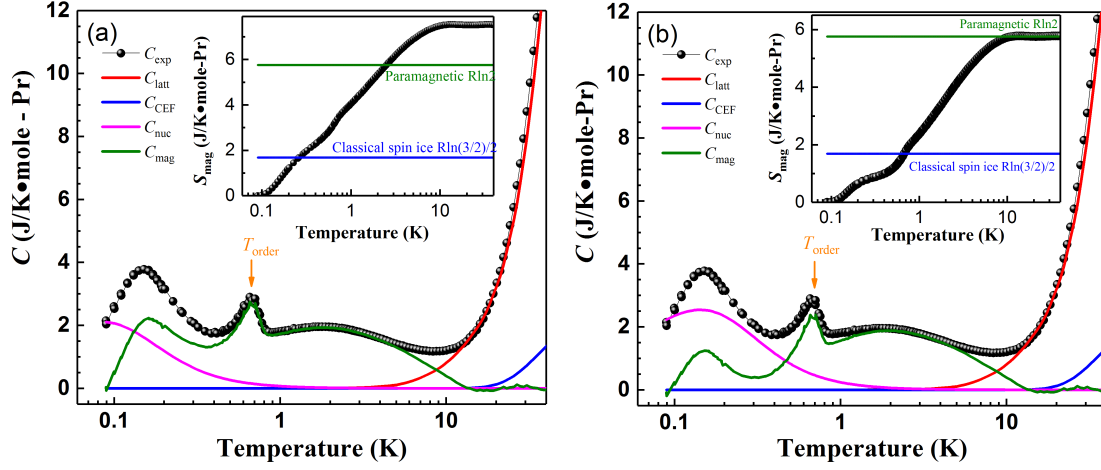
Figure 5.3.3 Temperature dependence of the specific heat and corresponding magnetic entropy S_{mag} (insert) of Pr$_2$Ir$_2$O$_7$ in zero field. (a) and (b) display the situations due to different estimation of the nuclear Schottky anomaly. See detail in main text.

One can obtain the pure magnetic specific heat of electron spins $C_{Mag}(T)$ and estimate the magnetic entropy S_{mag} by subtracting the lattice contribution (phonon), C_{latt}, the crystal electric field (CEF) states contribution, C_{CEF}, and the nuclear contribution C_{Nuc}. The phonon contribution to the specific heat is estimated by appropriately scaling the measured specific heat of the nonmagnetic isostructural compound Y$_2$Ir$_2$O$_7$ as described in Appendix (red solid line). The Schottky anomaly of CEF states was calculated by

$$C_{Sch} = \frac{R}{Z^2}\left[Z \sum_{i=1}^{n} \left(\frac{\varepsilon_i}{k_B T}\right)^2 e^{\left(-\frac{\varepsilon_i}{k_B T}\right)} - \left\{\sum_{i=1}^{n} \varepsilon_i e^{\left(-\frac{\varepsilon_i}{k_B T}\right)}\right\}^2 \right] \tag{5.3.2}$$

where $Z = \sum_{i=1}^{n} e^{(-\varepsilon_i/k_B T)}$ is the partition function of the system, in which the CEF scheme of Pr^{3+} in Pr$_2$Ir$_2$O$_7$ is based on the inelastic neutron scattering analysis in the next subsection. It is clear that the CEF contribution (blue solid line in Figure 5.3.3) becomes significant above 20 K. For the nuclear contribution C_{Nuc}, both quadrupole and hyperfine splitting of the nuclear levels of ^{141}Pr may play a role. Here, we only consider the hyperfine splitting of nuclear levels since the quadrupole moment of ^{141}Pr is too small (0.0589 barn) to be relevant in the temperature range of our measurements [204]. The nuclear specific heat of the split level of ^{141}Pr nuclear is expressed as follow [96,203]:

$$C_N = N_A k_B \frac{\alpha^2}{4I^2}\left[\frac{1}{sinh^2(\alpha/2I)} - \frac{(2I+1)^2}{sinh^2((2I+1)\alpha/2I)}\right] \tag{5.3.3}$$

$$\alpha = A_{hf}\left(\mu_{hyp}^{Pr}/g_J\right)I/k_B T$$

where N_A and k_B are Avogadro's number and Boltzmann's constant, respectively. $I = 5/2$ and A_{hf} = 0.078 T [205,206] are the nuclear spin and hyperfine coupling constant for ^{141}Pr.

g_J=4/5 and μ_{hyp}^{Pr} are Lande's g_J factor and the magnetic moment of Pr^{3+}. However, the standard calculation of C_N based on Eq. (5.3.3) with ordered moment μ_{hyp}^{Pr}= 1.508 μ_B gives a large value of the nuclear Schottky peak, which is inconsistent with the data. One has to introduce a dimensionless factor f, representing the reduction of the amplitude of the nuclear hyperfine Schottky anomaly, which is caused by the 4f moment fluctuations of the rare-earth ions [207]. This could be understood if the correlation time of the fluctuations of the magnetic moment is of the order of or less than the spin-lattice relaxation time [207]. The practice expression for the nuclear hyperfine specific heat is $C_{nuc} = f \times C_N$.

   The practical separation of various contributions to specific heat is shown in Figure 5.3.3. Two methods were considered for estimating C_{nuc}. In the left panel of Figure 5.3.3, the only constraint is that the specific heat value must be positive after C_{nuc} subtraction, where C_{nuc} is calculated with ordered moment μ_{hyp}^{Pr}= 1.508 μ_B and f = 0.3. However, the corresponding entropy at 20 K is larger than $Rln(2)$ per spin, which is the magnetic entropy of the paramagnetic state for a spin-1/2 system. In the right panel of Figure 5.3.3, two constraints were applied: after the subtraction of non-magnetic contributions, the entropy at 20 K should be the value of $Rln(2)$ and the magnetic specific heat $C_{Mag}(T)$ should be positive. The best fit is obtained with μ_{hyp}^{Pr}= 2.62 μ_B and f=0.36. No matter which method we used to subtract the nuclear specific heat C_{nuc}, it seems that a peak around 0.15 K always appears in C_{Mag}, implying additional unknown contribution. This anomaly at 0.15 K was also observed in the disordered single crystal sample [203]. The obtained magnetic entropy reveals a plateau above 10 K, representing the paramagnetic state. Then, it drops to be close to the Pauling entropy $(R/2) ln(3/2)$ above the transition temperature 0.8 K, indicating the formation of two-in-two-out (2I2O) spin-ice configuration. During the phase transition, the magnetic entropy is partially released and exhibits a plateau until 0.15 K. Finally, it reaches to zero at about 80 mK.

5.3.4. Crystal electric field excitations

In order to determine the Crystal Electric Field (CEF) induced level scheme and single-ion anisotropy, an inelastic neutron scattering experiment of polycrystalline sample was performed on the time-of-flight spectrometer MERLIN at the ISIS spallation source. Around 0.88 g of powder samples were spread uniformly on a thin wrapper of aluminum foil in a cylindrical geometry with height 42 mm and diameter 40 mm, then, mounted into a closed-cycle refrigerator. Spectra were recorded with incident neutron energies E_i = 38, 69, 100 and

170 meV at temperatures T = 5 K. The raw data were reduced to $I(Q, E)$ format following the standard procedures.
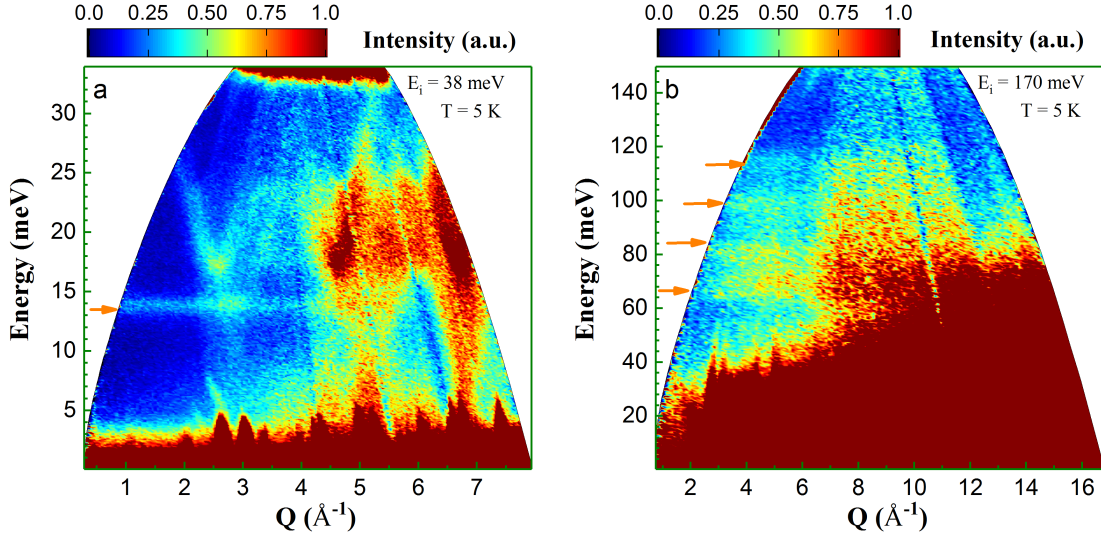
Figure 5.3.4 Inelastic neutron spectra of polycrystalline Pr$_2$Ir$_2$O$_7$ as a function of scattering vector Q. The spectra were recorded with an incident energy E_i = 38 meV (left panel) and 170 meV (right panel). The CEF transitions, marked by orange arrows, are the bands of scattering observed at low Q whose intensities decrease with Q. The strong scattering at large Q is from phonons.

Figure 5.3.4 shows the normalized scattering cross section $I(Q, E)$ of Pr$_2$Ir$_2$O$_7$ measured with incident energies of 38 and 170 meV at 5 K. The strong signal around E = 0 is from elastic scattering, and the gradual increase in intensity with increasing Q is caused by the scattering from phonons. The CEF transitions cause the weak dispersionless bands of scattering at low Q and their intensity follows the squared magnetic form factor $f^2(Q)$ of Pr^{3+}. One CEF level around 14 meV can be identified with E_i = 38 meV, as well as four CEF levels from 65 to 115 meV with E_i = 170 meV, in agreement with the previous work [196], and similar to the observation in Pr$_2$Sn$_2$O$_7$ [33], Pr$_2$Zr$_2$O$_7$ [96] and Pr$_2$Hf$_2$O$_7$ [97,180]. To minimize contributions from phonon scattering, only data in the low-Q regime were used. The main panel of Figure 5.3.5 shows energy spectra integrated over a small range of scattering angles ϕ from 8° to 15°. In order to obtain the CEF transition energies and integrated intensities, Gaussian profiles with polynomial backgrounds were used to fit the observed data. The results of the fitting are listed in Table 5.3.3, in which the integrated intensities are recorded relatively with respect to the strongest peak. The integrated intensities have been corrected according to the neutron transmission ratio at the corresponding energy.

The obtained CEF peak positions and intensities thus were subsequently used to refine the CEF parameters.
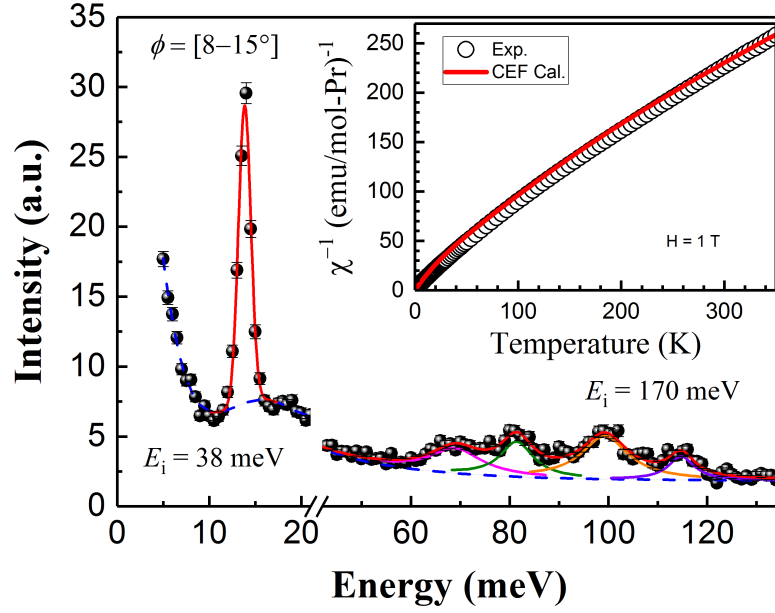
Figure 5.3.5 Crystal electric field analysis of inelastic neutron scattering and susceptibility. Main panel: neutron-scattering intensity $S(\langle\phi\rangle, E)$ as function of energy transfer, obtained by combining T = 5 K data for two incident beam energies: E_i = 38 and 170 meV. The blue dashed line denoted fitted polynomial backgrounds. The red solid line is the calculated best fit of peaks. Insert: Temperature dependence of the inverse magnetic susceptibility. The red solid line in the insert was calculated using the CEF parameters obtained from the analysis of inelastic neutron scattering data.

In the absence of the CEF interaction, the ground state of Pr^{3+} with $4f^2$ configuration, governed by Hund's rules, is $^3H_4$ (L=5, S=1, J=4) with ninefold degeneracy. The crystal field acting on the Pr ions in $Pr_2Ir_2O_7$ has point symmetry D_{3d}, with the local 3-fold rotation axis parallel to the local [1 1 1] directions of the crystal lattice. The ground state $^3H_4$ then splits into three doublets and three singlets, designated by the symmetry decompositions $3\Gamma_3^+ + 2\Gamma_1^+ + \Gamma_2^+$ in the irreducible representations of D_{3d}. With the quantization axes along the local [1 1 1] axis, the CEF Hamiltonian takes the form:

$$\widehat{\mathcal{H}}_{CEF} = B_0^2 C_0^2 + B_0^4 C_0^4 + B_3^4 (C_{-3}^4 - C_3^4) + B_0^6 C_0^6 + B_3^6 (C_{-3}^6 - C_3^6)$$
$$+ B_6^6 (C_{-6}^6 - C_6^6) \tag{5.3.4}$$

where B_q^k denotes the crystal-field parameters and C_q^k are the components of the tensor operator. We diagonalized $\widehat{\mathcal{H}}_{CEF}$ within the set of 91 intermediate coupling basis states of the f^2 configuration of Pr^{3+}, using the program SPECTRE [208]. The measured neutron-scattering cross section for the single-ion magnetic transitions was discussed in Chapter 3.

The CEF parameters in Pr$_2$Sn$_2$O$_7$ [33] were used as the starting parameter for the least-square fitting algorithm in which the experimental uncertainties in the energies and relative intensities of the peaks were used as reciprocal weights. The refinement reaches $\chi^2 = 3.2093$, where is χ^2 the standard normalized goodness-of-fit parameter.

Table 5.3.3. Observed and calculated crystal-field transition energies (E) and integrated intensity (I) of Pr$_2$Ir$_2$O$_7$ at 5 K. The intensity is relative with respect to the highest peak observed. D indicates the degeneracy. The best-fit CEF parameters used for the calculations are $B_0^2 = 32.43$ meV, $B_0^4 = 410.3$ meV, $B_3^4 = 253.8$ meV, $B_0^6 = 184.0$ meV, $B_3^6 = -140.8$ meV and $B_6^6 = 237.7$ meV. The refinement reaches the standard normalized goodness-of-fit parameter $\chi^2 = 3.2093$. Note: the intensity of the first observed excitation at 13.8 meV was not used for the CEF fitting.

Level	D	E_{obs} (meV)	E_{cal} (meV)	I_{obs}	I_{cal}
Γ_3^+	2	0	0	-	-
Γ_1^+	1	13.8(5)	14.1	-	-
Γ_3^+	2	68.9(7)	68.15	0.51(10)	0.47
Γ_1^+	1	81.4(7)	83.0	0.49(8)	0.25
Γ_3^+	2	99.3(1.0)	101.3	1.00	1.00
Γ_2^+	1	114.7(1.5)	113.87	0.36(7)	0.28

Table 5.3.3 gives the best-fit CEF parameters together with the calculated energies and relative intensities of the calculated levels. The calculated values of energies are seen to agree well with the observations. However, the observed intensities are not in good agreement with the predictions of the model due to the strong neutron absorption and the contamination of the phonon scattering. The accuracy of the CEF parameters could be improved by taking the INS data with a specially designed sample holder and performing precise neutron absorption corrections [209].

The CEF level scheme of Pr$_2$Ir$_2$O$_7$ is found to be very similar to that of other Pr-based pyrochlore compounds [33,97,180]. The CEF analysis of INS data reveals that the ground state of Pr^{3+} is a non-Kramers doublet, well separated from first excited singlet at 14 meV. The ground state doublet wave function (symmetry Γ_3^+) can be written in terms of the $\left|^{2S+1}L_J, M_J\right\rangle$ basis as follow:

$$\left|\pm\right\rangle = 0.807\left|^3H_4, \pm 4\right\rangle \pm 0.534\left|^3H_4, \pm 1\right\rangle - 0.164\left|^3H_4, \mp 2\right\rangle$$
$$+ 0.135\left|^1G_4, \pm 4\right\rangle \pm 0.090\left|^1G_4, \pm 1\right\rangle \qquad (5.3.5)$$
$$\mp 0.044\left|^3H_5, \pm 4\right\rangle \pm 0.060\left|^3H_5, \mp 2\right\rangle$$

We note the significant admixture of terms $\left| {}^3H_4, M_J = \pm 4 \right\rangle$ with $\left| {}^3H_4, M_J \neq \pm 4 \right\rangle$, as well as with ${}^1G_4$ and ${}^3H_5$, in the ground state. The ground-state wave function gives the magnetic moment of 2.283 μ_B/Pr with $g_{zz} \approx 4.566$ and $g_{xy} \approx 0$. The reduced magnetic moment is smaller than the effective moment of 2.846 μ_B obtained from the CW analysis of magnetic susceptibility. This difference could be attributed to the Kondo effect, since the INS measurement for the reconstruction of CEF was performed at 5 K, which is in the Kondo regime of the metallic Kondo lattice. The localized magnetic moment of Pr^{3+} is partially screened by the conduction electrons, thus becomes smaller than that obtained from the CW fitting at higher temperature. The CEF parameters obtained from the analysis of INS data are able to reproduce the powder DC susceptibility as shown in the insert of Figure 5.3.5. A very good agreement between the experimental data and the calculation supports the obtained CEF states and parameters. The calculated anisotropy in the susceptibility is $\chi_\parallel / \chi_\perp \approx 25.3$ at T = 10 K, where $\chi_\parallel$ and $\chi_\perp$ are the susceptibilities parallel and perpendicular to the $\langle 111 \rangle$ quantization axis of the crystal field. Additionally, the transverse part of the susceptibility is purely Van-Vleck type, and so the ratio $\chi_\parallel / \chi_\perp$ tends to infinity as the temperature approaches zero. Furthermore, if we ignore the higher order terms, the non-Kramers doublet ground state of Pr^{3+} in $Pr_2Ir_2O_7$ consists of a dominant $\left| {}^3H_4, \pm 4 \right\rangle$ and a significant admixture of $\left| {}^3H_4, \pm 1 \right\rangle$ and $\left| {}^3H_4, \mp 2 \right\rangle$. Projection to this doublet allows us to reconstruct the set of Pauli matrices of a pseudospin-1/2, $\boldsymbol{\tau} = \left(\tau^{x'}, \tau^{y'}, \tau^{z'} \right)$. The z components $\tau^{z'}$ describe the Ising dipolar magnetic moments pointing along the local [1 1 1] axis and the x and y components $\{ \tau^x, \tau^y \}$ carry a quadrupole moment [181,191]. Thus, the magnetic moment of Pr^{3+} in $Pr_2Ir_2O_7$ can be treated as the effective spin-1/2 system with strong Ising anisotropy.

5.3.5. Magnetic ordering and diffuse magnetic scattering

As shown in its specific heat data, $Pr_2Ir_2O_7$ undergoes a phase transition around 0.8 K. We use polarized neutron scattering to investigate the new phase below the transition temperature. Figure 5.3.6 shows the nuclear coherent (blue spheres) and magnetic (red spheres) components of the total scattering from $Pr_2Ir_2O_7$ at 87 mK by means of *xyz*-polarization analysis (XYZ-PA) on DNS. The nuclear Bragg peaks (1 1 1), (1 1 3) and (2 2 2) can be observed in the nuclear coherent scattering in the Q range. Satellite Bragg peaks at Q = 0.55, 0.82, 1.32 and 1.45 Å^{-1} were observed in the magnetic scattering component, indicating the long-range order of the Pr^{3+} moments. They can be indexed using a magnetic propagation wavevector $\mathbf{k} = (0\ 0\ 1)$ in reciprocal lattice units of the $Fd\bar{3}m$ space group. The

corresponding Miller indices of the magnetic peaks are marked above the peaks in Figure 5.3.6. The same result was also observed in stuffed Pr$_{2.4}$Ir$_{1.6}$O$_{7-\delta}$ [199].
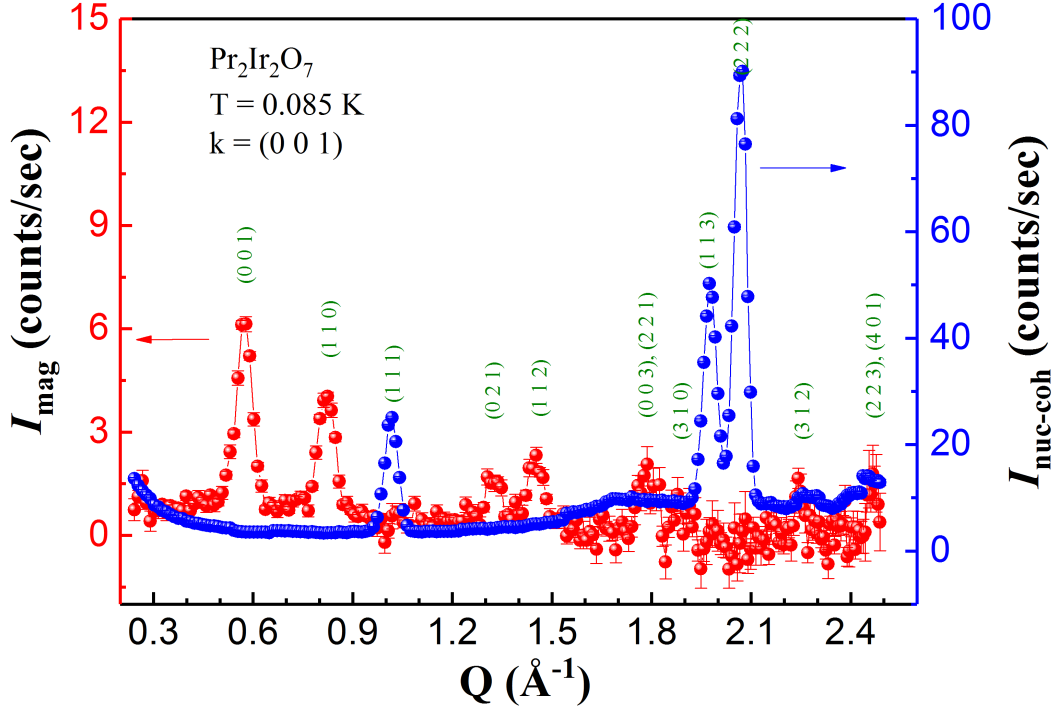
Figure 5.3.6 Nuclear coherent scattering (blue spheres to right y-axis) and magnetic scattering (red spheres to left y-axis) of Pr$_2$Ir$_2$O$_7$ at 87 mK, obtained by XYZ-PA on DNS.

In order to solve the magnetic structure, irreducible representations (IRs) and their basis vectors are calculated by using the BASIREPS program [151]. In the space group $Fd\bar{3}m$ with a propagation wave vector $\mathbf{k} = (0\ 0\ 1)$, the decomposition of the magnetic representation for Pr site (1/2, 1/2, 1/2) is

$$\Gamma_{mag} = 1\Gamma_1^2 + 2\Gamma_2^4 + 1\Gamma_3^2 + 2\Gamma_4^4 \tag{5.3.6}$$

the multiply factors represent the number of the times of the IRs occurs, the dimensionality and the order of IR are denoted as superscript and subscript in Eq. (5.3.6). All possible models of the magnetic structure can be obtained by the combination of the basis vector of the IRs. We found that only the combination of bases vectors of ψ_3 and ψ_4 in IR Γ_2 are suitable for this case, with the magnetic peaks present at (0 0 1), (1 1 0), (0 2 1) and (1 1 2). Considering a constraint of the Ising single-ion anisotropy in the [1 1 1] direction for Pr^{3+} moments, the magnetic structure is a long-range ordered spin-ice configuration, in which each tetrahedron has two spins pointing in (2-in) and two spins pointing away (2-out) from its center (right panel of Figure 5.3.7). Since the XYZ-PA separates the nuclear coherent scattering and magnetic scattering of the sample at the same temperature, we can obtain the scale factor and

the crystallographic parameters from the nuclear coherent scattering, then refine the ordered magnetic moment of Pr^{3+} in the magnetic scattering. The refinement of magnetic scattering of PIO at 87 mK for above model is shown in the left panel of Figure 5.3.7, with an ordered magnetic moment of m_{ord}= 1.508(25) μ_B/Pr. The ordered moment of Pr is smaller than 1.71(1) μ_B/Pr of the stuffed sample $Pr_{2.4}Ir_{1.6}O_{7-\delta}$ [199].
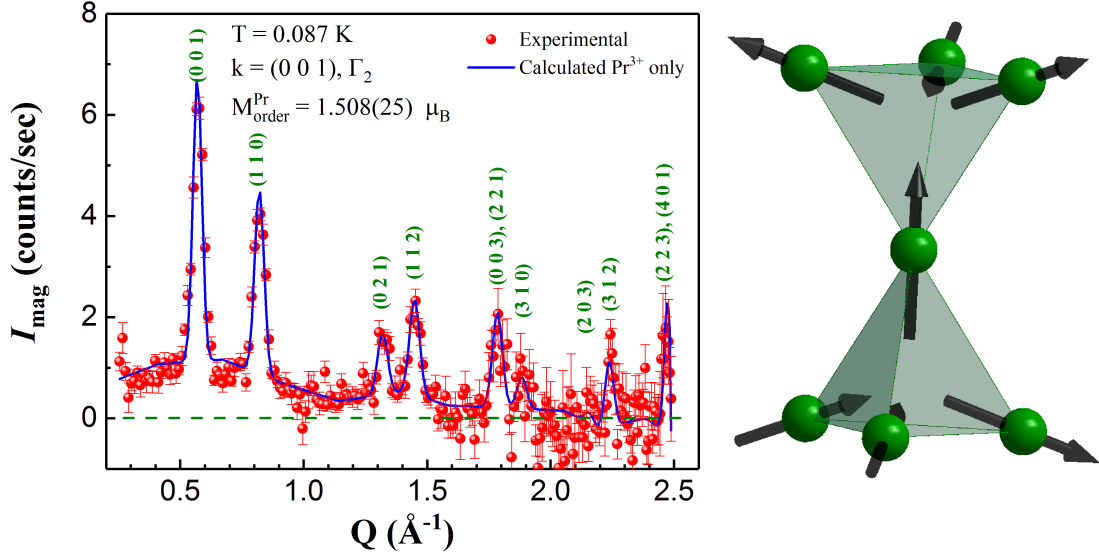
Figure 5.3.7 Refinement of the magnetic scattering of $Pr_2Ir_2O_7$ at 87 mK (*left*) and the corresponding "2-In-2-Out" (2I2O) long-range magnetic order model (*right*).

This ordered state with 2I2O configurations was predicted in the dipolar spin-ice model (DSI) [65] and the Heisenberg spins model on the pyrochlore lattice [54]. Both models take the strong dipole-dipole interaction into account due to the large magnetic moment of Ho^{3+}, Dy^{3+} and Gd^{3+}. However, considering the CEF reduced magnetic moment of Pr^{3+} in $Pr_2Ir_2O_7$, the nearest-neighbor dipole-dipole interaction strength $D_{nn} = \frac{5}{3}\frac{\mu_0}{4\pi}\frac{\mu^2}{r_{nn}^3} \approx 0.11$ K (where $r_{nn} = a_{latt}\sqrt{2}/4$) is ten times smaller than that of Dy^{3+} and Ho^{3+}. Thus, one can ignore the dipole-dipole interaction in Pr-based pyrochlore system in the studied temperature range. In metallic $Pr_2Ir_2O_7$, magnetic coupling between the localized Pr^{3+} moments can be mediated by conduction electrons. This is the so-called RKKY interaction. Early studies of Monte Carlo simulation on a simple RKKY exchange interaction Hamiltonian within classical isotropic spin have predicted the co-existence of the **k** = (0 0 1) 2I2O long-range ordered phase and the negative CW temperature depending on the parameter k_F representing the Fermi wavevector [190]. However, due to the quadratic band touching near the Fermi energy of the Ir conduction electrons, a small amount of sample defects, such as oxygen and Ir off-

stoichiometry, may shift the Fermi energy and thus modify the RKKY interaction between the Pr^{3+} local moments [210]. As a result, different samples may exhibit 2I2O long-rang order or disorder states [186,199]. In our sample, a possible source of sample defects is the internal strain, since the stuffing level of our sample is less than 0.02, much smaller than that previously reported [199]. For the metallic Pr$_2$Ir$_2$O$_7$, the non-Kramers doublet could be described as the pseudospin $\left(\tau^{x'}, \tau^{y'}, \tau^{z'}\right)$. The pseudospin component $\tau^{z'}$ along the local $\langle 1\,1\,1 \rangle$ axis carries a magnetic dipole moment and can be coupled to the conduction electron spin density, while the components $\tau^{x',y'}$ perpendicular to the local $\langle 1\,1\,1 \rangle$ axis carry a quadrupole moment and can be coupled to the electron charge density [137]. A phase diagram of the pseudospin ground-state has been established according to the above consideration [201].
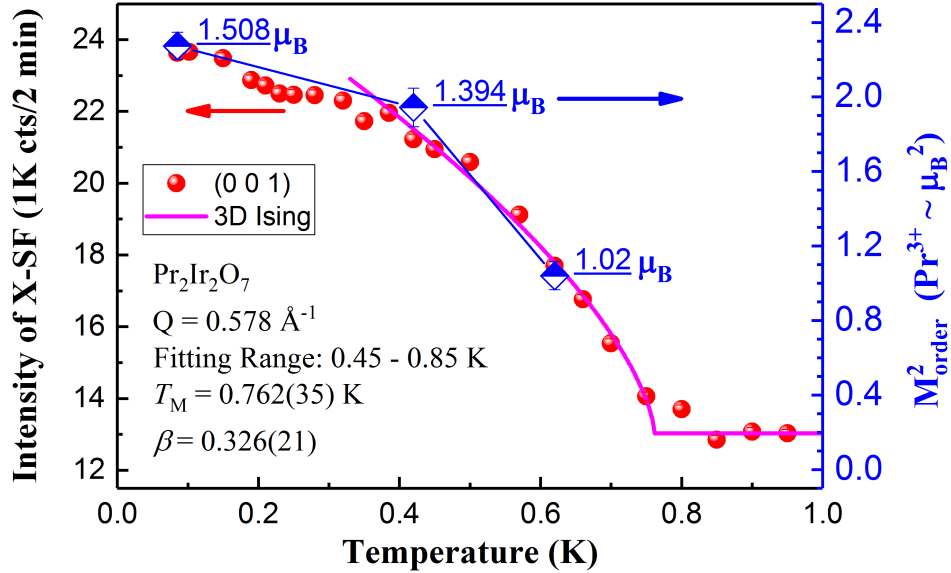
Figure 5.3.8 Temperature dependence of the peak (0 0 1) intensity of the neutron x-spin-flip (x-SF) channel. The pink curve is the fit of a power-law function for the ordering parameter $m_{ord} \propto \sqrt{I_{mag}}$. The blue curve corresponds the squared ordered moment m_{order}^2 obtained from Rietveld refinement at different temperature (right axis).

The temperature dependence of the intensity of the spin-flip (SF) scattering with x polarization was measured at the magnetic peak (0 0 1) position from 0.1 to 0.95 K, as shown in Figure 5.3.8. Since $\sigma_x^{SF} = 1/2\,\sigma_{mag} + 2/3\,\sigma_{spin-inc}$ in powder samples, the variation of the intensity of x-SF channel is proportional to the squared ordered moment, because the spin incoherent scattering of the sample is usually temperature independent. A modified power law, which assume the background corrected intensity of x-SF is proportional to the ordered moment, $I = I_0 (1 - T/T_N)^{2\beta} + bg$, was applied to fit the magnetic ordering behavior from

0.45 to 0.85 K. The fit is shown by the pink solid curve in Figure 5.3.8, and gives $T_M = 0.762(35)$ K and $\beta = 0.326(21)$, which, within the error bar, is close to the expected critical exponent 0.33 for a three-dimensional Ising system [6]. The $T_M = 0.762(35)$ is consistent with the specific heat anomaly around 0.8 K discussed above. Comparing with the stuffed sample with the ordering temperature $T_M = 0.93(1)$ K [199], the magnetic transition temperature in our sample is lower.

The ordered-state magnetic moment of Pr^{3+}, $m_{ord} = 1.508(25)$ μ_B/Pr, at 87 mK is strongly reduced compared to the magnetic moment 3.56 μ_B /Pr for free Pr^{3+} ions ($\mu_{eff} = g_J\sqrt{J(J+1)}, J = 4, g_J = 4/5$ for Pr^{3+}), as well as the effective moment $\mu_{CEF} = 2.275$ μ_B/Pr due to CEF effect. The reduction of the ordered moment implies the presence of strong quantum fluctuations. As shown in Figure 5.3.7, it is remarkable that a non-negligible background exists in the magnetic scattering component, beside the magnetic Bragg peaks for the long-range magnetic order at 87 mK. The non-negligible magnetic scattering background indicates possible presence of diffuse magnetic scattering, which could be elastic or inelastic scattering. The elastic magnetic scattering data taken from DNS is actually energy-integrated within the energy transfer window of DNS, up to 70-80% of the incident neutron energy at $81.81/\lambda^2 = 4$ meV for $\lambda = 4.52$ Å, i.e. about 3 meV. If the overall energy scale of the magnetic excitations in the system is smaller than 3 meV, which is the case for $Pr_2Ir_2O_7$ (as will be demonstrated in next subsection), the magnetic scattering result of DNS would also include contributions from the fluctuating magnetic moments. One can estimate the total fluctuating magnetic moment from the diffuse magnetic scattering, after calibrating the intensity of magnetic scattering to absolute unit barn/sr/Pr.
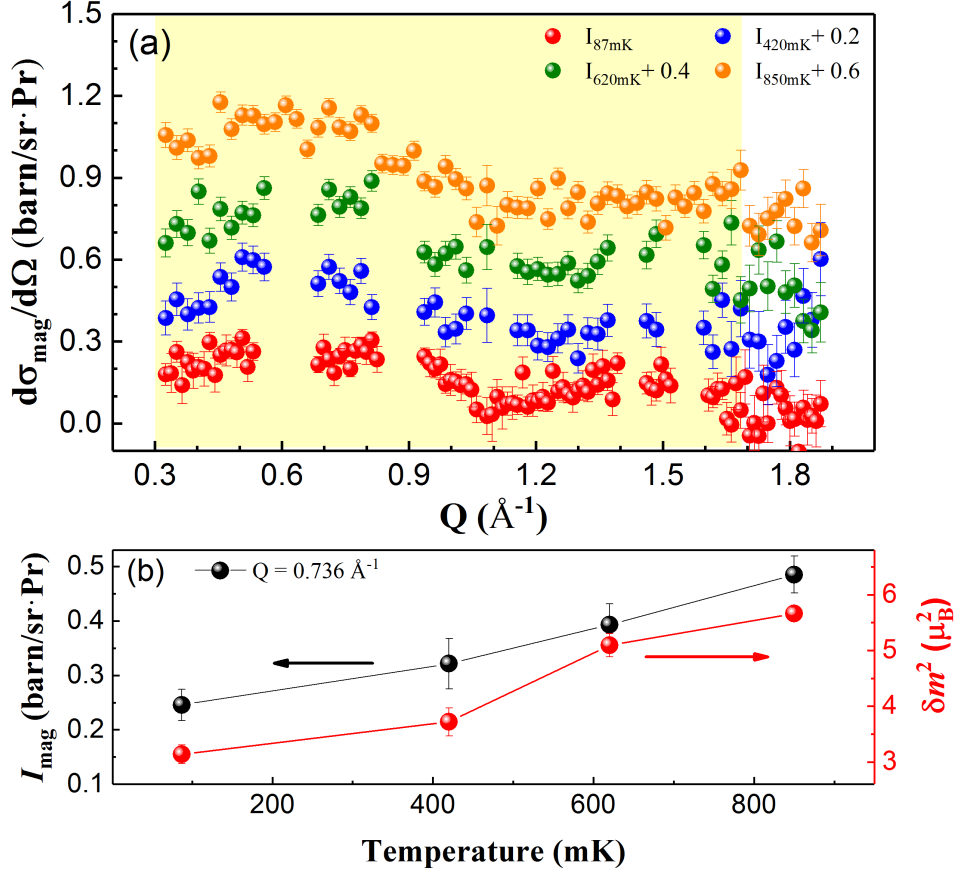
Figure 5.3.9 (a)The magnetic diffuse scattering of Pr$_2$Ir$_2$O$_7$ at different temperature. The magnetic Bragg peaks due to 2I2O long-range order have been excluded. The intensity at 420, 620 and 850 mK are displaced vertically by 0.2, 0.4 and 0.6 barn/sr/Pr, respectively. (b) Temperature dependence of the magnetic scattering intensity at 0.736 Å^{-1}, and the disordered moment square calculated according to the magnetic diffuse scattering.

Figure 5.3.9 (a) shows the diffuse magnetic scattering of Pr$_2$Ir$_2$O$_7$ at different temperature. The intensity of magnetic scattering has been normalized to the absolute cross section, barn/sr/Pr, by the nuclear Bragg peaks according to the formula (see the detail in Appendix C):

$$\frac{d\sigma_{mag}}{d\Omega} = \frac{I_{mag}^{exp}}{I_{peaks}^{exp}} \times \frac{d\sigma_{peak}}{d\Omega} \tag{5.3.7}$$

where $\frac{d\sigma_{peak}}{d\Omega}$ is the nuclear Bragg peak scattering cross section for powder sample [211], I_{peaks}^{exp} is the Q integrated intensity of nuclear Bragg peaks from nuclear coherent scattering, and I_{mag}^{exp} is the magnetic scattering patterns. This normalization method gives rise to a systemic error of 13% [212]. The magnetic Bragg peaks associated with 2I2O magnetic order at 87, 420, 620 mK have been excluded. The differential cross section of magnetic scattering at 420, 620 and 850 mK are shifted vertically by 0.2, 0.4, and 0.6, respectively. Above the

2I2O transition, the magnetic scattering at 850 mK only displays a spin-ice like modulation, where two broad humps are observed at 0.6 and 1.5 Å^{-1} in the measured Q range [67]. On cooling, the magnetic Bragg peaks appears and their intensity increases due to the development of the 2I2O ordering. However, the diffuse magnetic scattering can always be observed. The diffuse magnetic scattering at 620, 420 and 85 mK has similar modulation as observed at 850 mK. This indicates that the disordered magnetic moment may exhibit a spin-ice correlation beside the 2I2O long-range order. Furthermore, with decreasing temperature the intensity of magnetic diffuse scattering decreases from 0.49 to 0.25 barn/sr/Pr at $Q =$ 0.736 Å^{-1}, as shown in Figure 5.3.9 (b), while the ordered moment increases, as shown in Figure 5.3.8.

Table 5.3.4 Ordered and disordered magnetic moment of Pr^{3+} in Pr$_2$Ir$_2$O$_7$ at different temperature. The ordered moment was obtained from the refinement of the 2I2O magnetic structure, while the disordered moment was calculated from the magnetic diffuse scattering. See the detail in main text. The total magnetic moment m_{tot}^2 is nearly temperature independent, within the systemic error.

Moment (μ_B^2)	87 mK	420 mK	620 mK	850 mK	3.5 K
$\langle m \rangle^2$	2.274(74)	1.943(103)	1.041(76)	-	-
δm^2	3.135(168)	3.718(253)	5.094(207)	5.660(115)	5.115(146)
m_{tot}^2	5.409(184)	5.661(273)	6.135(221)	5.660(115)	5.115(146)

The opposite temperature dependence of the magnetic Bragg peaks and the diffuse magnetic scattering intensity implies the possibility of the conservation of the total moment in this system during measurement. One can directly obtain the disordered magnetic moment according to [213]:

$$\delta m^2 = \mu_B^2 \frac{\iint Q^2 6I(Q,E)/|r_0 f(Q)|^2 dQdE}{\int Q^2 dQ} \tag{5.3.8}$$

where $r_0 = 0.539 \times 10^{-12}$ cm and $I(Q,E) = d\sigma_{mag}^2/d\Omega dE$ is the double differential cross section. Given the energy-integral mode employed at DNS, it can be inferred that the magnetic scattering data are already approximately energy-integrated. The Q integration range was chosen from 0.3 to 1.7 Å^{-1} that covers the whole Brillion Zone (BZ). The temperature dependence of the disordered magnetic moment obtained from the diffuse magnetic scattering is shown in Figure 5.3.9 (b). The disordered moment decreases from 5.660(115) μ_B^2 at 850 mK to 3.135(168) μ_B^2 at 87 mK. The disordered moment δm^2 and the ordered moment $\langle m \rangle^2$ are listed in Table 5.3.4, as well as the total moment m_{tot}^2. The total

moment m_{tot}^2 is nearly temperature independent within the error bar (considering the systemic error and standard derivation). The average value of the total moment m_{tot}^2 is around 5.6 μ_B^2, which is smaller than 12.8 μ_B^2 for free Pr^{3+} (with $g_J = 4/5$, $J = 4$), but approximately same as 5.2 μ_B^2 obtained from the CEF result. This result strongly suggests that the total magnetic moment of Pr^{3+} in Pr$_2$Ir$_2$O$_7$ is conserved, and its reduced value is due to CEF.

5.3.6. Magnetic excitations
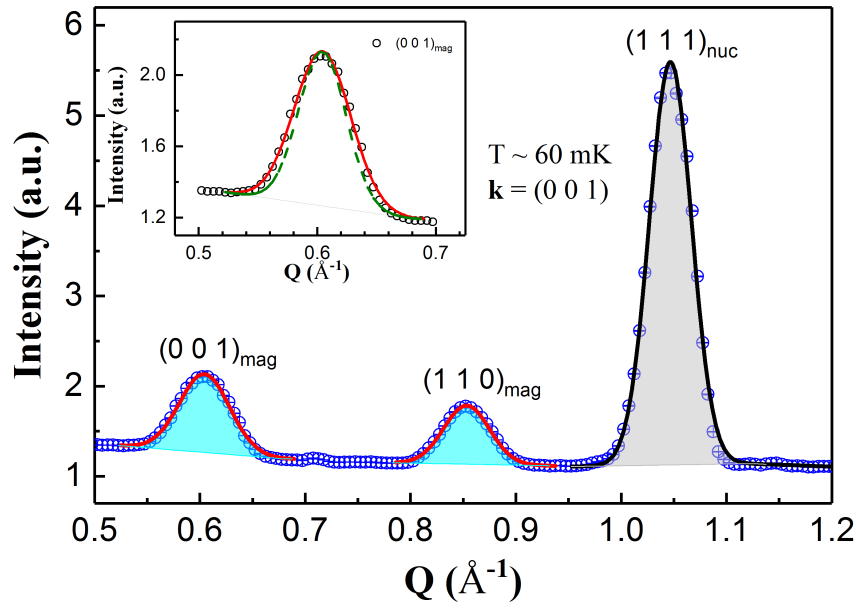
Figure 5.3.10. The diffraction pattern of Pr$_2$Ir$_2$O$_7$ at 60 mK, obtained by energy integration of $I_{raw}(Q, E)$ from -0.3 to 0.3 meV at each Q with $\Delta Q = 0.005$ Å^{-1}. Insert: profile of magnetic peak (0 0 1). Red solid line is the Gaussian fit of the peak, green dashed line is the Gaussian profile with (1 1 1) peak width.

We now turn to the low-energy magnetic excitations of Pr$_2$Ir$_2$O$_7$, studied by cold neutron inelastic scattering. Figure 5.3.10 shows the diffraction pattern at 60 mK obtained by integrating the spectrums in the energy range from -0.3 to 0.3 meV, which is large enough to include all the elastic component (see in Figure 5.3.11). The peak at $Q = 1.05$ Å^{-1} is a pure nuclear Bragg peak, which can be used to perform the absolute unit calibration. Additionally, there are two magnetic peaks (0 0 1) and (1 1 0) at $Q = 0.61$ Å^{-1} and 0.85 Å^{-1}, respectively. It has been noticed that the magnetic Bragg peaks are broader than the nuclear Bragg peaks in the stuffing sample [199]. Similarly, as shown in the insert of Figure 5.3.10, the magnetic Bragg peak (0 0 1) is also slightly broader than the nuclear peak (1 1 1) in our sample.

However, the real resolution function (FWHM *vs* Q or 2θ) of the diffraction pattern obtained from $I_{raw}(Q, E)$ is unknown, and high-resolution neutron powder diffraction measurements are necessary to clarify this. The refinement of the diffraction patterns shown in Figure 5.3.10 yields an ordered moment 1.703(41) μ_B/Pr in $Pr_2Ir_2O_7$ at 60 mK.
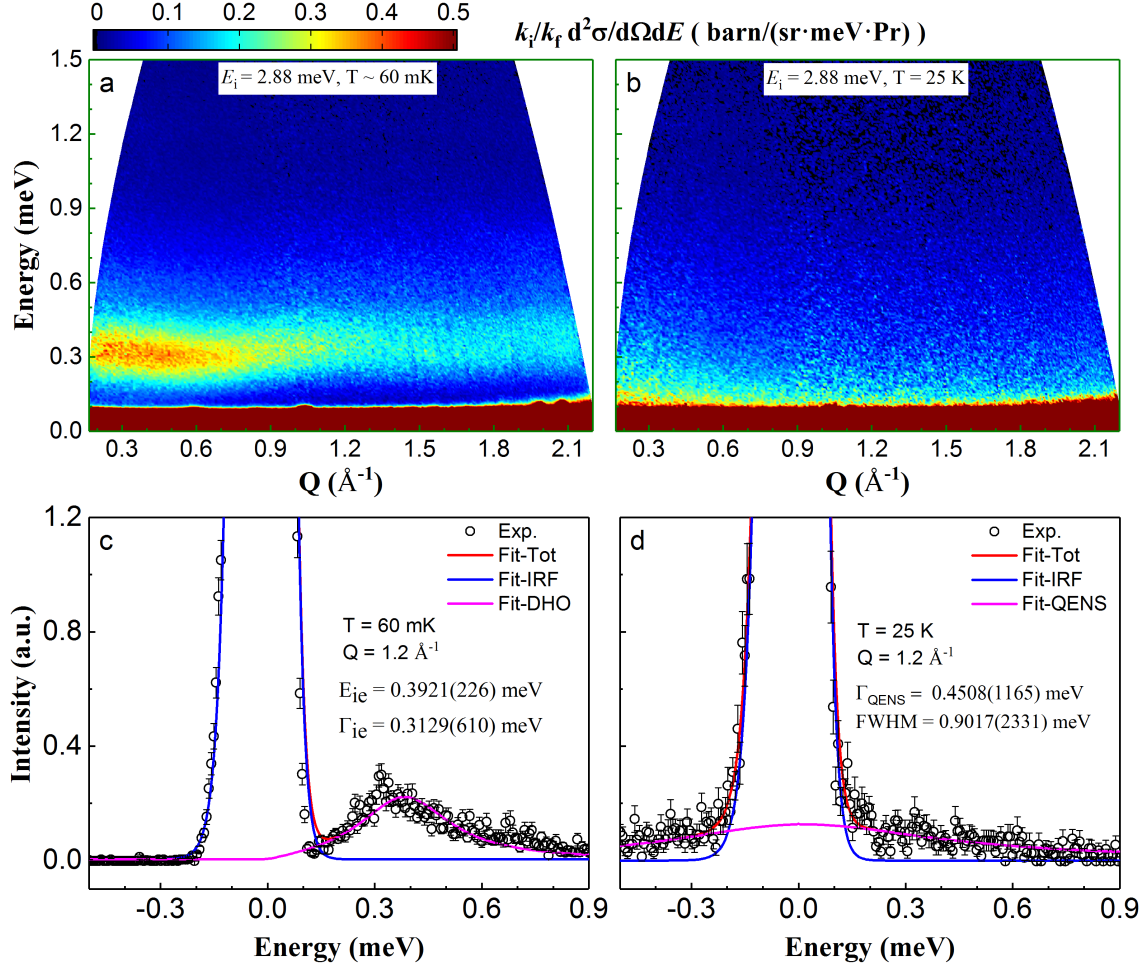
Figure 5.3.11 Neutron scattering spectrum of polycrystalline $Pr_2Ir_2O_7$ at 60 mK (a) and 25 K (b), measured on LET with E_i = 2.88 meV. The intensity has been normalized to barn/sr/meV/Pr by the nuclear peak (1 1 1). Inelastic spectra of $Pr_2Ir_2O_7$ for constant Q = 1.2 Å^{-1} with ΔQ = 0.02 Å^{-1} at 60 mK and 25 K are presented in (c) and (d), respectively. Open circles are experimental data. Red, blue and pink solid lines are the total profile, elastic, inelastic, and quasielastic component, respectively, of the fitting.

Figure 5.3.11 (a) and (b) provide an overview of the neutron spectrum recorded at T = 60 mK and 25 K with E_i = 2.88 meV. The intensity $I(Q, E) = k_i/k_f \ (d^2\sigma/d\Omega dE)$ has been normalized to absolute units (barn/sr/meV/Pr) using the integrated intensity of the nuclear Bragg peak (1 1 1) [211]. This produces an overall scale accuracy of 10%. At T = 25 K, it displays a typical paramagnetic response, as shown in Figure 5.3.11 (b), in which strong

quasielastic scattering could be observed at low Q. At T = 60 mK, a broad low-energy response centered around 0.35 meV could be observed. Since it appears below the phase transition, it should be a purely magnetic contribution. Turning now to the energy dependence of the response, we carry out fits of the spectra to following function:

$$I(Q,E) = A \cdot IRF(Q,E) + \frac{B}{1 - \exp(-E/k_B T)} \frac{E\Gamma_{QENS}}{E^2 + \Gamma_{QENS}^2}$$
$$+ \frac{1}{1 - \exp(-E/k_B T)} \sum_i \frac{C_i E \Gamma_i}{(E^2 - E_i^2)^2 + (E\Gamma_i)^2}$$

(5.3.9)

where the first term represents the elastic component of Gaussian profile with FWHM ~ 0.13 meV, the second term represents the quasielastic magnetic component with FWHM = $2\Gamma_{QENS}$ and the third terms represent several inelastic magnetic components (A, B and C_i are constants, Γ_i is the FWHM of different inelastic scattering components at inelastic peaks $E_i^{ie} = \pm\sqrt{E_i^2 - (\Gamma_i/2)^2}$). The expression for inelastic component is equivalent to the Lorentzian profile which is often used to fit the magnetic inelastic scattering.

The fitting results at constant $Q = 1.2$ Å^{-1} are illustrated in Figure 5.3.11 (c) and (d) for temperature at 60 mK and 25 K, respectively. At T = 25 K, the paramagnetic state of the system can be expressed as the combination of elastic component and quasielastic component with FWHM = 901.7 μeV, corresponding to the relaxation time $\tau(ns) = 1.31/\text{FWHM}(\mu eV)$ = 0.00145 ns which is significantly faster than 1-10^{-1} ms for the classical spin ice compounds [214,215]. At T = 60 mK, the fitting yields the accurate excitation 0.39 meV with a linewidth 0.313 meV, which is broader than the instrumental resolution, suggesting possible dispersive excitations. Indeed, the slightly dispersive nature of the excitation could be observed in Figure 5.3.11 (a). To clarify the dispersion of the excitation at 60 mK, we applied the fit discussed above to the whole spectrum. The excitation energy E_{ie} and the linewidth Γ_{ie} are subtracted and plotted as a function of Q, as shown in Figure 5.3.12 (a). The linewidth Γ_{ie} slightly increases at large Q. The excitation energy of the inelastic component exhibits a Q dependence. As Q increases, the excitation shifts to lower energy and reaches a minimum round $Q = 0.6$ Å^{-1} if Q increases further, the excitation shifts to higher energy.

A discrete excitation was also observed at low temperature in other Pr-based pyrochlore [95-97]. For example, the INS measurement on single crystal Pr$_2$Zr$_2$O$_7$ shows a broad low energy response whose structure factor is similar to the specific pattern observed in classical spin ice [181]. However, the observed excitation in our sample does not follow the structure factor of either the classical spin ice or the paramagnetic magnetic state. Figure 5.3.12 (b)

shows the energy integrated inelastic components $I(Q)$ which is related to the powder-averaged dynamical spin correlation function $S(Q)$. The energy integration is performed from 0.15 to 1.2meV. The purple line is proportional to the magnetic form factor square of Pr^{3+} representing the paramagnetic state, while the red line is proportional to the magnetic structure factor of the classical spin ice [78]. It is clear that the Q dependence of the excitation is completely different to the classical spin ice. Interestingly, our experimental result is very similar to the observation in $Tb_{2.005}Ti_{1.995}O_{7+y}$ [216,217]. That excitation can be described in terms of pseudospin waves in the planar antiferropseudospin (PAF) and planar ferropseudospin (PF) phases in which the quadrupolar degree of freedom $(\tau^{x'}, \tau^{y'})$ play a role and impact the dynamic of the magnetic dipolar component τ^z [218]. Indeed, the CEF ground-state of both Pr^{3+} and Tb^{3+} in pyrochlore are non-Kramers doublet. The CEF ground doublet could be described as the pseudospin $(\tau^{x'}, \tau^{y'}, \tau^{z'})$, which $\tau^{z'}$ along the local $\langle 1\,1\,1 \rangle$ direction carries a magnetic dipole moment and $\tau^{x'}$ and $\tau^{y'}$ in the plane perpendicular to the local $\langle 1\,1\,1 \rangle$ direction carry a quadrupole moment. Instead of the quadrupole order in $Tb_{2.005}Ti_{1.995}O_{7+y}$, $Pr_2Ir_2O_7$ exhibits the dipole moment ordering of the pseudospin component $\tau^{z'}$. The effect of the quadrupolar degree of freedom has been proposed to explain the INS result of $Pr_2Zr_2O_7$ [181]. Possibly this needs to be taken into account in this case.
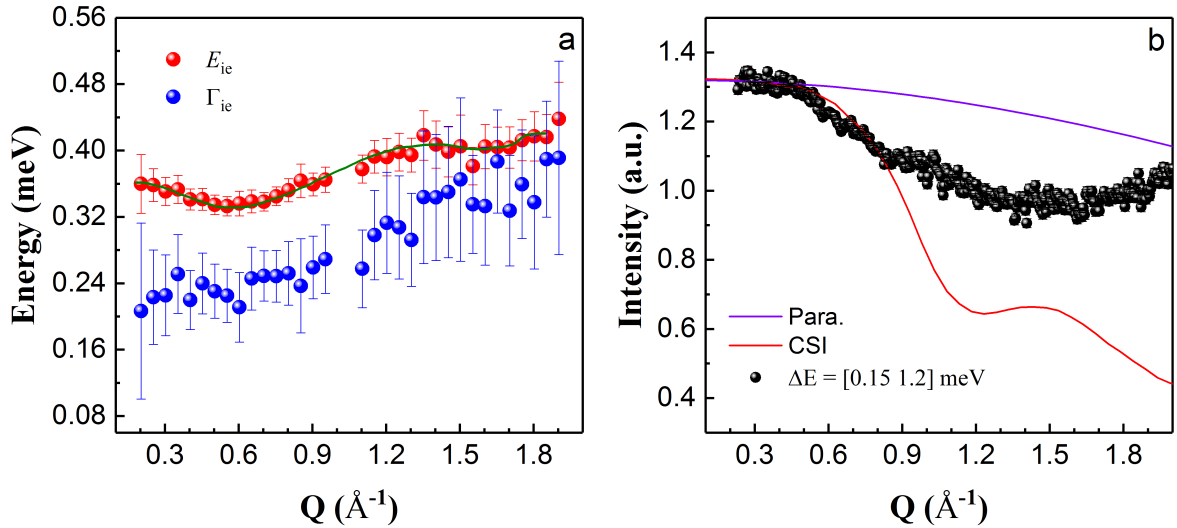
Figure 5.3.12 (a) Q dependence of the linewidth Γ_{ie} and excitation energy E_{ie} of the inelastic component obtained by the fit to the INS spectrum at T = 60 mK. The green line is guide to eye. (b) E integrated INS intensity as function of wave vector transfer $I(Q)$ at 60 mK. The purple solid line is proportional to the squared magnetic form factor of Pr^{3+} representing paramagnetic state.

One can also calculate the fluctuating moment to check the possibility of the existence of disordered static magnetic moments according the sum rule. The excitation-associated magnetic moment is around $\delta m^2 = 3.639(80)\,\mu_B^2$, calculated according to Eq. (5.3.8). Considering the ordered moment $\langle m \rangle^2 = 2.786(150)\,\mu_B^2$, the total magnetic moment is $6.4025(170)\,\mu_B^2$, which is close to the CEF moment $5.212\,\mu_B^2$. Taking into account the systemic error and contamination of the elastic component, the total magnetic moment sum rule is satisfied. This is in excellent agreement with the neutron polarization analysis on DNS. That signifies that there is no disordered static moment in Pr$_2$Ir$_2$O$_7$ at 60 mK.
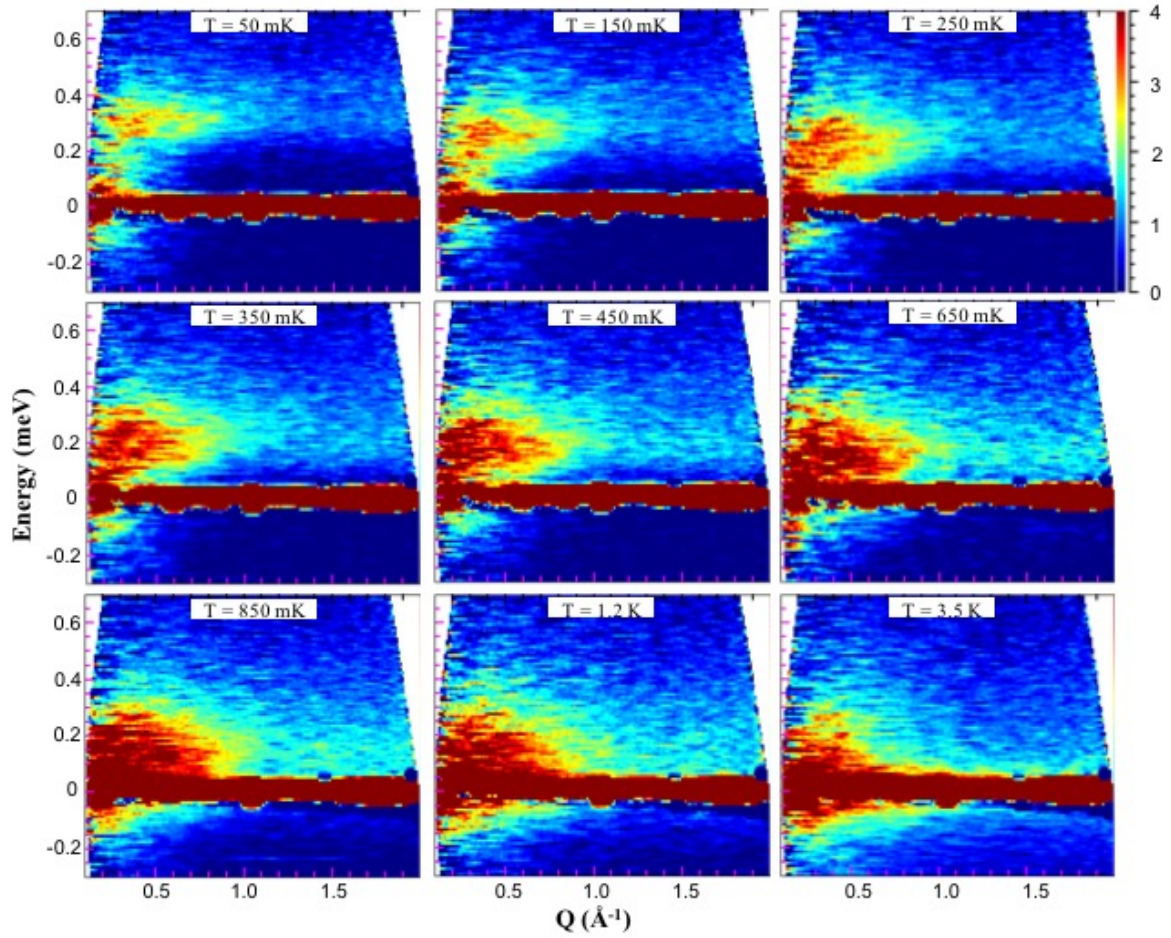
Figure 5.3.13 Temperature dependence of the $I_{raw}(Q, W)$ of the powder Pr$_2$Ir$_2$O$_7$.

The thermal evolution of the spectrum was measured on TOFTOF at MLZ. The color contour plots of the inelastic neutron scattering are presented in Figure 5.3.13. The strong quasielastic signal at low Q and low energy is due to the contaminations of the direct beam and the excitations from a small amount of Helium exchange gas used in the top-loading closed cycle cryostat (CCR) (see Appendix Figure E.1). With the instrument resolution as

good as ~ 0.04 meV, the gapped excitation could be clearly observed at 50 mK. When increasing the temperature, the mode persists up to 1.2 K, far above the 2I2O antiferromagnetic transition (T_{order} = 0.762 K). At 3.5 K, the strong magnetic quasielastic scattering is observed. The temperature dependence of the spectrum at constant Q = 1.2 Å^{-1} as well as the fits of Eq. (5.3.9) are shown in Figure 5.3.14 (a). With decreasing temperature, there is only a loss of spectral weight at lower energies, while the spectral weight at high energies is nearly unaffected. The excitation energy E_{ie} and the linewidth Γ_{ie} are subtracted and plotted as a function of temperature, as shown in Figure 5.3.14 (b). The linewidth Γ_{ie} of the mode increases with increasing temperature due to the enhanced thermal fluctuation. However, the excitation energy E_{ie} exhibits an unusual temperature dependence, as guided by the blue line. The excitation energy E_{ie} roughly stays constant above 2I2O phase transition temperature, but gradually moves to higher energies when further cooling to low temperature. This behavior of E_{ie} may suggest that the exchange interaction between Pr^{3+} is enhanced when the 2I2O magnetic ordering occurs. The dominating exchange interaction between Pr^{3+} in the metallic Pr$_2$Ir$_2$O$_7$ is the RKKY interaction that strongly depends on the band structure of this material. One of possibilities is that the 2I2O magnetic order of Pr^{3+} may affect conduction electrons and modify the Fermi level, since the Fermi energy is very close to the quadratic band touching [185, 210, 219]. As a result, the RKKY interaction is enhanced as the 2I2O order evolves during cooling. Clearly, further experimental and theoretical works are need to clarify this.
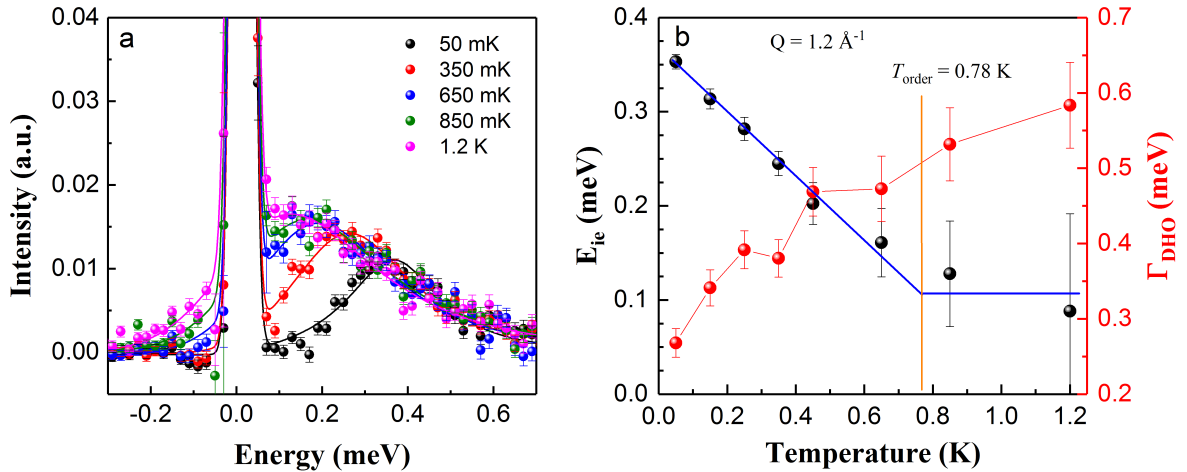

Figure 5.3.14 (a) Representative spectra carried out at Q = 1.2 Å^{-1}. The lines are fits according to Eq. (5.3.9), showing a strong mode at energy E_{ie} . (b) Temperature dependence of the gap position E_{ie} and the line width Γ_{DHO} of the excitation.

5.4. Conclusion

In this chapter, the metallic pyrochlore compound Pr$_2$Ir$_2$O$_7$ has been studied comprehensively via both macroscopic and neutron scattering techniques. Pr$_2$Ir$_2$O$_7$ crystallizes in the $Fd\bar{3}m$ crystallographic structure with a cubic lattice constant a = 10.40863(5) Å at room temperature. The combined Reitveld refinement of XRPD and NPD patterns suggests that the stuffing level of Pr-to-Ir site in the powder sample should be less than 0.02, however, the broadening of the diffraction peaks implies the existence of the internal strain. No bifurcation of the ZFC and FC magnetization was found above 2 K. The Curie-Weiss fitting of the DC susceptibility gives a negative CW temperature, implying an antiferromagnetic effective interaction. Due to the CEF effect, Pr^{3+} is a well isolated non-Kramers doublet with a reduced magnetic moment of 2.283 μ_B/Pr below 20 K. The magnetic moment displays strong easy-axis anisotropy along the local $\langle 1\,1\,1 \rangle$ direction. The CEF ground state doublet can be projected as the pseudospin $\left(\tau^{x'}, \tau^{y'}, \tau^{z'} \right)$, which is a dipole moment and quadrupole moment combination. Pr$_2$Ir$_2$O$_7$ exhibit a second phase transition indicated by a heat capacity anomaly at 0.76 K and determined by polarized neutron diffraction as a transition from the paramagnetic state to the 2I2O magnetic long-range order of Pr^{3+}. However, the ordered moment of Pr^{3+} is around 1.7 μ_B below 0.1 K, which is smaller than the expected moment in CEF. The missing moment is found fluctuating and forms a gapped excitation around 0.35 meV as observed by INS. The reason for the mode is possibly due to the quadrupole interactions between the pseudospins. The excitation energy exhibits unusual thermal evolution in the 2I2O ordered state. With decreasing temperature, the gapped excitation moves to high energies and becomes sharper, implying the strengthening of the exchange interaction. One possible scenario is that this may be caused by the strong interplay between the 2I2O order of Pr^{3+} and the conduction electron of Ir^{4+} due to the sensitivity of the quadratic band touching close to the Fermi energy. Further theoretical investigation is necessary to understand the above experimental results for Pr$_2$Ir$_2$O$_7$.

Chapter 6. All-In-All-Out Magnetic Order and Magnetic Excitations in Pyrochlore Nd₂Hf₂O₇

6.1. Introduction

In previous chapters, I have discussed the pyrochlore iridates $Ln_2Ir_2O_7$, in which both rare earth ions Ln^{3+} and transition metal ions Ir^{4+} are magnetic. The non-negligible interplay between Ln and Ir in pyrochlore iridates leads to the relevant complexity of the system. In order to study the properties of rare earth ions in pyrochlore lattice, one can replace the Ir^{4+} by Hf^{4+}, which is also a $5d$ transition metal but non-magnetic ($5d^0$). As introduced in the background of this thesis, the rare earth compounds of hafnate-227 form the pyroclore structure from La to Tb. This chapter will focus on $Nd_2Hf_2O_7$ (NHO), which is a counterpart of $Nd_2Ir_2O_7$.

The Nd-based pyrochlore compounds stand out as a fascinating system, and intense investigations are undergoing. The CEF ground doublet of Nd^{3+} in pyrochlore is a Kramers doublet called a "dipolar-octupolar" (DO) doublet (if $J = 9/2$ or $15/2$, and the CEF is dominated by the parameter $B_2^0 < 0$ in Eq 2.2.3). The ground doublet thus could be represented as a pseudospin-1/2, in which two components of the effective pseudospin operator (z and x) behave like a dipole under space-group symmetry transformation, whereas the third component (y) behaves like an octupolar tersor [44, 220]. In the case of the large-U limit of localized electrons, where the degrees of freedom are the pseudospin-1/2 moments $\tau_i^{u'}$ ($u' = x', y', z'$), the most general symmetry allowed nearest-neighbor exchange is $H_{ex}^{DO} = \sum_{\langle i,j \rangle} \left[\mathcal{J}_x \tau_i^{x'} \tau_j^{x'} + \mathcal{J}_y \tau_i^{y'} \tau_j^{y'} + \mathcal{J}_z \tau_i^{z'} \tau_j^{z'} + \mathcal{J}_{x,z} (\tau_i^{x'} \tau_j^{z'} + \tau_i^{z'} \tau_j^{x'}) \right]$, where the sum is over nearest-neighbor bonds. Employing a rotation by an angle θ in the (x', z') plane, the term $\mathcal{J}_{x,z}$ can be eliminated and it leaves us with the "diagonal" "XYZ" Hamiltonian for the new pseudospin components $\tilde{\tau}_i^{\tilde{u}}$ ($\tilde{u} = \tilde{x}, \tilde{y}, \tilde{z}$) [44, 221]:

$$H_{XYZ}^{DO} = \sum_{\langle i,j \rangle} \left[\tilde{\mathcal{J}}_x \tilde{\tau}_i^{\tilde{x}} \tilde{\tau}_j^{\tilde{x}} + \tilde{\mathcal{J}}_y \tilde{\tau}_i^{\tilde{y}} \tilde{\tau}_j^{\tilde{y}} + \tilde{\mathcal{J}}_z \tilde{\tau}_i^{\tilde{z}} \tilde{\tau}_j^{\tilde{z}} \right] \tag{6.1.1}$$

Based on the three parameters $\tilde{\mathcal{J}}_{x,y,z}$, a rich theoretical phase diagram was established (see Figure 6.1.1) [44]: besides the ordered phases like the AIAO configuration where dipoles

point along the local axis toward or outward the centers of tetrahedron, an antiferro-octupolar (AFO) phase appears along with two distinct quantum spin-ice (QSI) phases dubbed as *dipolar*-QSI and *octupolar*-QSI [44]. Indeed, the AIAO antiferromagnetic order has been found in a few of the Nd-based pyrochlores, as listed in Table 6.1.1. However, below 0.1 K, all the Nd^{3+} ordered magnetic moments are smaller than the one for free ion (3.35 μ_B) and also for the CEF reduced value (2.45 μ_B). This fact implies the persistence of the fluctuating magnetic moment due to quantum effects of the pseudospin $\tilde{\tau}_i^{\tilde{u}}$.
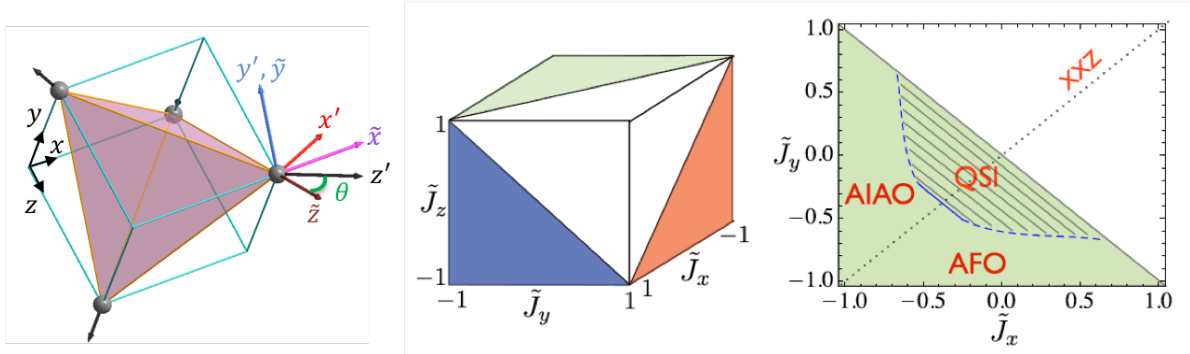
Figure 6.1.1 Coordinate systems and the phase diagram based on the "XYZ" model (taken from ref [44]). "XXZ" refers to the XXZ model in Chapter 2. AIAO, QSI and AFO represent the phases of "all-in-all-out" dipoles order, quantum spin ice, and antiferro-octupolar order, respectively.

Table 6.1.1 Summary of the AIAO ordered Nd-based pyrochlore, as well as the lattice constant a and Curie-Weiss temperature θ_p . (Nd$_2$Ir$_2$O$_7$ has no clear ordering temperature.)

	a (Å)	θ_p (K)	T_N (K)	M_{order} (μ_B)	Ref.
Nd$_2$Ir$_2$O$_7$	10.3809(3)	-18.62	<20K	1.4025(202)	Chapter 4, [131,132]
Nd$_2$Sn$_2$O$_7$	10.568(3)	-0.32	0.91	1.708(3)	[222]
Nd$_2$Zr$_2$O$_7$	10.6735	0.124(2)	0.3	1.26(2)	[34,223,224]
Nd$_2$Hf$_2$O$_7$	10.6389	0.135(43)	0.535(5)	1.415(13)	present, [225]

Recently, the investigation of the spin dynamics of Nd$_2$Zr$_2$O$_7$ by inelastic neutron scattering shows that a flat magnetic excitation mode centered at 0.07 meV, coexists with the AIAO long-range order below $T_N \sim 0.3$ K, and persists up to 0.6 K [178]. This flat mode exhibits a pinch point pattern characteristic of the magnetic Coulomb phase. The observation was interpreted as the *magnetic moment fragmentation* proposed by Brooks-Bartlett *et al.* [178,226]. The fragmentation scenario is based on the classical spin ice model. As shown in

Figure 6.1.2, the magnetic density mapped from crystallized single charged monopole, which presents "three-in-one-out" (or "one-in-three-out", 3I1O) configuration, can fragment into two parts under Helmholtz decomposition:

$$\boldsymbol{M} = \boldsymbol{M}_m + \boldsymbol{M}_d = \nabla\psi + \nabla\times\boldsymbol{A} \qquad (6.1.2)$$

where $\boldsymbol{M}_m = \nabla\psi$ is "divergence full", corresponding to the AIAO order and $\boldsymbol{M}_d = \nabla\times\boldsymbol{A}$ is "divergence free", and gives rise to the pinch-point correlations associated with the fluctuating Coulomb phase [60, 66, 78, 227]. However, the observed cusp in the susceptibility at the AFM phase transition does not agree with the above classical fragmentation scenario in which the susceptibility would appear to be featureless [224]. Benton further point out the quantum origins of the observed moment fragmentation based on the XYZ model [221]. I would like to remind that the flat like band excitation has also been observed in $Nd_2Ir_2O_7$ below 30 K, but it was interpreted as a CEF ground doublet splitting due to the Zeeman effect of the *molecular magnetic field, B_{mf}^{Ir}*, generated by ordered Ir^{4+} [131]. Thus, it is desired to study another Nd-based pyrochlore, e.g. $Nd_2Hf_2O_7$.
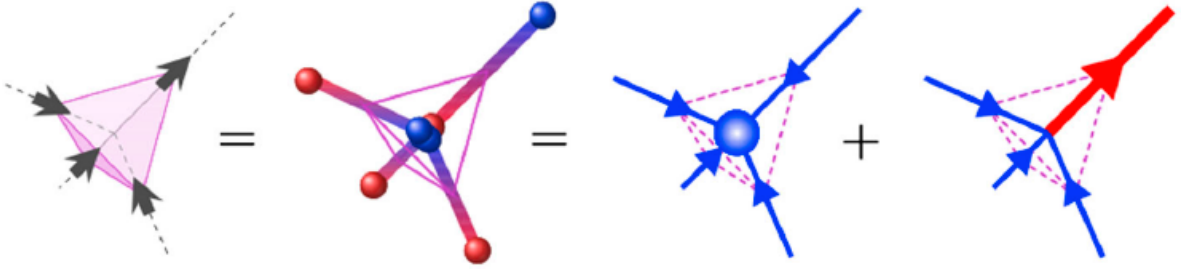
Figure 6.1.2 Illustration of the classical moment fragmentation: the 3I1O spin configuration (left) with its dumbel model (middle) could be decomposed into a static magnetic charge modelling the AIAO long-range order and a fluctuating dipolar field showing monopole dynamics via Helmholtz mechanism (taken from ref [226]).

The properties of $Nd_2Hf_2O_7$ have been studied by neutron scattering and μSR [225, 228, 229]. However, Anand observed unusual saturation behavior of the ordered moment, which cannot to be explained. On the other hand, more information below 2 K, such as the specific heat anomaly associated to the phase transition and the observation of the collective magnetic excitation are still missing. In this chapter, we systematically investigate the magnetic properties of $Nd_2Hf_2O_7$ by means of DC magnetization, specific heat, polarized neutron scattering and inelastic neutron scattering. The total moment sum rule of the magnetic neutron scattering was employed to examine the moment fragmentation scenario. The linear spin wave theory (LSWT) based on XYZ model can account for the low temperature magnetic excitations, as well as the excitation above T_N.

6.2. Experimental details

A polycrystalline Nd$_2$Hf$_2$O$_7$ sample was synthesized by solid state route via firing the stoichiometric mixture of Nd$_2$O$_3$ (99.99%) and HfO$_2$ (99.99%) in an alumina crucible at 1550 ^{o}C in air for 7 days with several intermediate grindings and pelletizing. Then, the pellets were ground into fine powder and annealed for two days in pure O$_2$ flow at 1000 ^{o}C. The nonmagnetic reference compound La$_2$Hf$_2$O$_7$ was also prepared by the same method and used to estimate the phonon contribution to the heat capacity. The quality of the sample was checked at room temperature by x-ray powder diffraction (XRPD) using the laboratory-based diffractometer (STOE, Mo-$K_{\alpha 1}$) with monochromator. The magnetic susceptibility measurement was performed using a Quantum Design magnetic properties measurement system (MPMS) superconducting quantum interference device (SQUID) magnetometer. The heat capacity of the pelletized sample was measured down to 70 mK using a Quantum Design physical properties measurement system (PPMS) with a dilution refrigerator.

The neutron powder diffraction (NPD) measurements were carried out using the powder neutron diffractometer SPODI at the Heinz Maier-Leibnitz Zentrum (MLZ), Garching, Germany. The xyz neutron polarization analysis was performed on the diffuse neutron scattering spectrometer DNS at MLZ, operated by the Juelich Centre for Neutron Science (JCNS). Around two grams of the powder sample were sealed in a hollow cylinder copper can with optimized thickness ~ 1.25 mm to reduce neutron absorption. A dilution refrigerator was used to achieve the lowest temperature of 0.1 K. An incident neutron beam of wavelength λ = 4.2 Å was used for the experiments. At each one of the temperatures, data were collected for 15 hours. The XRPD and NPD data were refined using the package FULLPROF suite.

The inelastic neutron scattering (INS) measurements with thermal and cold neutrons were performed, respectively, at the direct geometry time-of-flight spectrometers IN4 and IN6 at the Institute Laue Langevin (ILL), Grenoble, France. Both measurements were carried out using the same sample measured at DNS. On IN4, the sample was measured with three incident energies E_i = 65.7, 116 and 150 meV at 2, 50, 100 K by using a standard 'Orange' cryostat. On IN6, an incident neutron beam of wavelength λ = 5.12 Å was used for the experiments at the temperatures 0.056, 0.6 and 15 K achieved using a dilution refrigerator. All obtained INS raw data is converted to $I(Q, E)$ format in the standard routine with self-attenuation correction according to the sample absorption.

6.3. Results and discussion

6.3.1. Sample quality determination

During the sample synthesis processes, the XRPD was employed regularly to exam the sample quality, such as phases purity and evolution phases. The process stops when the contents of impurity phases reach levels below the detectable limit of XRPD. Besides, since the frustrated magnets such as pyrochlores stand on the subtle balance among the competing interactions, a slight defect of the sample may drive the system to different phases. For example, in the pyrochlore $Yb_2Ti_2O_7$ the "stuffing" defect, when a small amount Yb occupies the 16c site of Ti, leads to the variation of the delicate magnetic ground state of $Yb_2Ti_2O_7$. One can determine the stuffing level employing the Rietveld refinement of powder diffraction [230].

The Fullprof software was employed to perform the Rietveld refinement of the crystallographic structure [151]. The neutron coherent scattering length b_c of Nd and Hf are so similar (7.69 fm for Nd and 7.77 fm for Hf) that the contrast of Nd and Hf is lost in the structure refinement of NPD. The joint refinement of XRPD and NPD has to been performed. The refined structure model was the stuffed pyrochlore model, $Nd_2(Hf_{2-y}Nd_y)O_{7-y/2}$. Within the face-centered cubic (fcc) space group $Fd\bar{3}m$, the 16d site is fully occupied by Nd, the 16c site is dominated by Hf with a slight mixing of Nd, and oxygen vacancies were assigned to the two sites 48f and 8b according to the electric balance of the compounds. Both XRPD and NPD patterns were taken at room temperature ~ 300 K. Figure 6.3.1 shows the Rietveld refinement result of XRPD and NPD with $y = 0$, i.e. of the stoichiometric pyrochlore model. Both patterns have good agreement with theoretical calculation with $\chi^2 = 4.28$ and 1.52 for XRPD and NPD, respectively. As shown in Table 6.3.1, the cubic lattice constant a of the sample is 10.6459(2) Å, which is close to the previous reported value of 10.6389(1) Å [225], smaller than the value $a = 10.6735(7)$ Å of $Nd_2Zr_2O_7$ [34], and bigger than the value $a = 10.568(3)$ Å of $Nd_2Sn_2O_7$ [222]. The x-parameter of the 48f oxygen position is 0.33395(9) which is in agreement with the reported values of 0.3340(5) for $Nd_2Hf_2O_7$ [225], 0.3356(2) for $Nd_2Zr_2O_7$ [34], and 0.33250(8) for $Nd_2Sn_2O_7$ [34]. The x-parameter is smaller than the value 0.375, expected for a perfect cubic oxygen environment about the 16d site. That implies a distorted feature of the oxygen octahedra, which is important for the Nd^{3+} CEF excitations and single-ion anisotropy discussed below. In order to obtain the possible stuffing level, we performed the joint XRPD and NPD refinement as function of y. The Rietveld refinement agreement factors as function of the stuffing level are plotted in Figure 6.3.2. It is clear that

the agreement factors increase when y increases, which implies a poor agreement with the model. We conclude that the stuffing level y in this sample should be less than 0.02, which is the limit of accuracy of the joint refinement of XRPD and NPD. The anisotropic displacement parameters are listed in the Table 6.3.2. The value of the parameters is comparable with other published results for pyrochlore compounds [230].

Table 6.3.1 Comparison of the lattice parameters a and 48f oxygen position x at 300 K for different Nd pyrochlore.

	Nd$_2$Hf$_2$O$_7$ (this work)	Nd$_2$Hf$_2$O$_7$	Nd$_2$Zr$_2$O$_7$	Nd$_2$Sn$_2$O$_7$	Nd$_2$Ir$_2$O$_7$ (this work)
Lattice a Å	10.6459(2)	10.6389(1)	10.6735(7)	10.568(3)	10.3809(3)
O$_{48f}$ (x)	0.33395(9)	0.3340(5)	0.3356(2)	0.33250(8)	0.33136(7)
Stuffing y	< 0.02	-	<0.005	0.013	-
Ref	-	[225]	[34]	[222]	Chapter 4

Table 6.3.2 Anisotropic displacement parameters (ADPs) $U \times 10^{-4}$ Å^2 obtained for stoichiometric model Nd$_2$Hf$_2$O$_7$. The results are obtained from the refinement of NPD at 300 K.

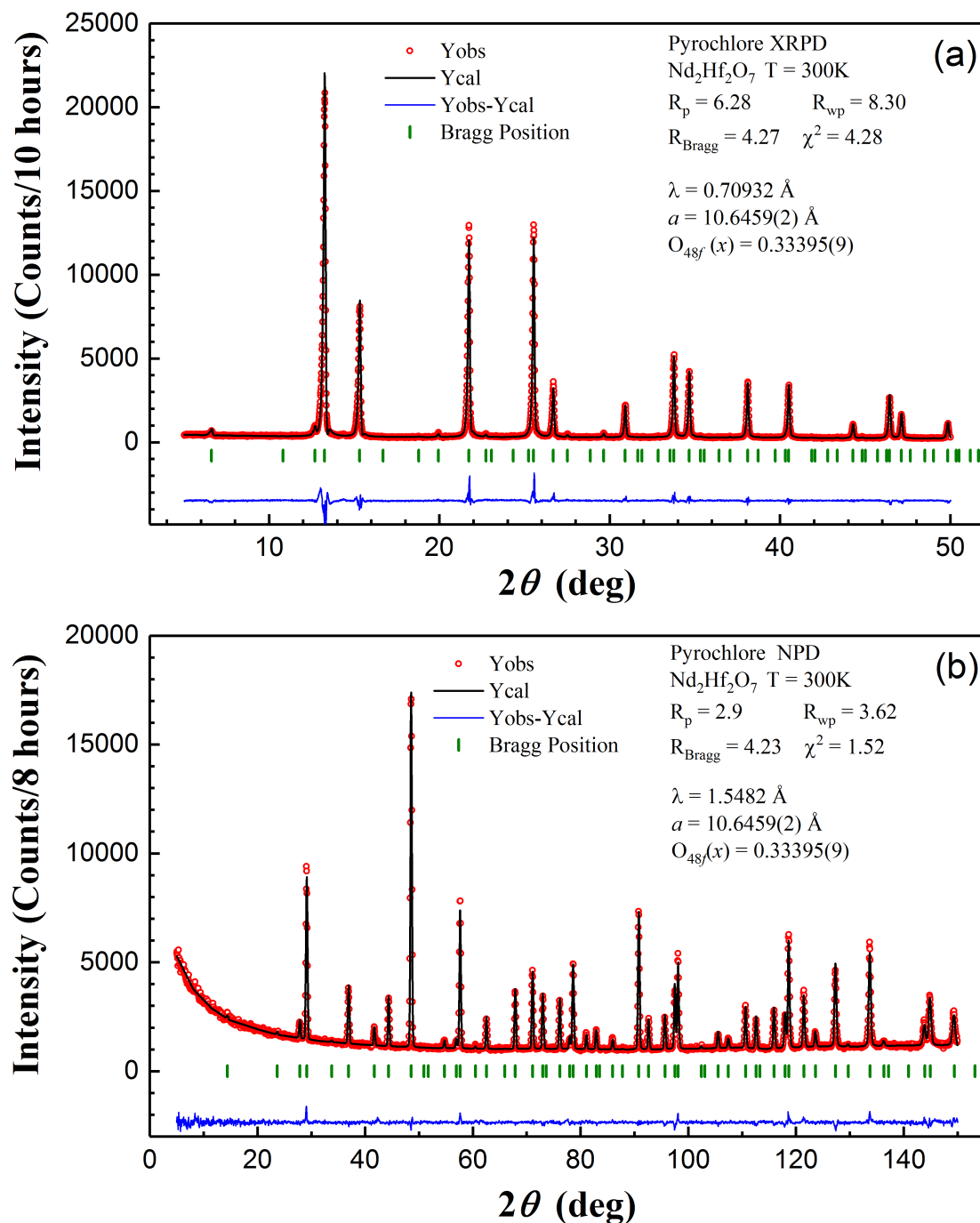|	U_{11}	U_{22}	U_{33}	U_{12}	U_{13}	U_{23}
Nd (16d)	6.7(4)			-0.8(4)		
Hf (16c)	7.0(4)			1.0(4)		
O (48f)	15.1(5)	9.9(4)		-		4.2(5)
O (8b)	11.6(10)			-		

Figure 6.3.1 Experimental (Yobs), calculated (Ycal) and difference (Yobs-Ycal) X-ray powder diffraction (XRPD) (a) and neutron powder diffraction (NPD) (b) patterns obtained at room temperature (~300 K) with the Rietveld refinement of pyrochlore structure. The green short lines indicate the position of the Bragg peaks.
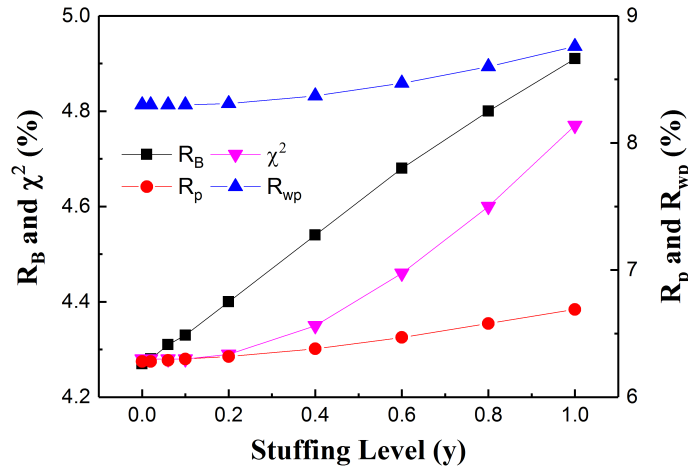
Figure 6.3.2 The joint refinement agreement factors as function of the stuffing level y in the refined model Nd$_2$(Hf$_{2-y}$Nd$_y$)O$_{7-y/2}$ within the pyrochlore structure. The refinement agreement factors R_B and χ^2 are read from the left axis, while R_P and R_{wp} are read from the right axis.

6.3.2. Bulk Magnetization

Field-cooled (FC) and zero-field-cooled (ZFC) DC magnetic susceptibility χ versus temperature measured in a field of $H = 0.1$ T are shown in Figure 6.3.3 (a), No anomalies and thermal hysteresis between ZFC and FC in $\chi(T)$ are observed down to 2 K, in agreement with the reported results of Nd$_2$Hf$_2$O$_7$ [225], Nd$_2$Zr$_2$O$_7$ [34,223] and Nd$_2$Sn$_2$O$_7$ [222]. Attempts to fit the temperature-dependence of the reciprocal magnetic susceptibility reveal that the $\chi^{-1}(T)$ data do not obey a Curie-Weiss (CW) law in the temperature range $2 - 350$ K. As we will discuss in the crystal electric field (CEF) section, the first-excited CEF level of Nd^{3+} in Nd$_2$Hf$_2$O$_7$ is at 23meV, situated at about 270 K. Therefore the thermal population of the CEF will influence the CW fitting above 100 K. To minimize the effects of short-range magnetic correlations (at T<10K, discussion in the heat capacity result) and CEF on the estimation of the CW temperature θ_p and the effective moment μ_{eff} of the atomic ground state, the $\chi(T)$ data were fitted in the temperature range 10 K < T < 30 K. Firstly, the linear fitting was performed to the curve of χ^{-1} (T) according to the CW law:

$$\chi(T) = \frac{C}{T - \theta_{CW}}, \quad C = N_A \mu_{eff}^2 / 3k_B \qquad (6.3.1)$$

Where N_A is the Avogadro number and k_B is the Boltzmann constant. The fitting gives a negative CW temperature of $\theta_{CW} =$ -1.62(10) K and the effective moment of $\mu_{eff} =$ 2.83(4) μ_B/Nd (μ_B is the Bohr magneton). More precise fitting of the CW law for rare earth compounds should involve a temperature-independent term χ_0 accounting for the Van Vleck paramagnetism contribution. The CW law can be modified as follows:

$$\chi(T) = \chi_0 + \frac{C}{T - \theta_p}, \quad C = N_A \mu_{eff}^2 / 3k_B \qquad (6.3.2)$$

The fitting of Eq. (4.3.1) yields a negative CW temperature θ_p = -0.135(43) K and μ_{eff} = 2.626(7) μ_B/Nd with Van Vleck contribution χ_0 = 0.0034(2) emu/mol-Nd. The negative CW temperature would imply a weak antiferromagnetic coupling among Nd spins. Although the obtained results are slightly different compared to the reported result with positive value θ_p = +0.24 K in ref [225], the negative θ_p is consistent with the AIAO magnetic long-range order of Nd^{3+} in the picture of CSI model [65]. The obtained μ_{eff} = 2.626(7) μ_B/Nd is much lower than the theoretical moment of 3.62 μ_B/Nd for free Nd^{3+} ions ($\mu_{eff} = g_J\sqrt{J(J+1)}$, $J = 9/2$, $g_J = 8/11$ for Nd^{3+}), however, it is comparable with the result obtained from CEF analysis via INS.
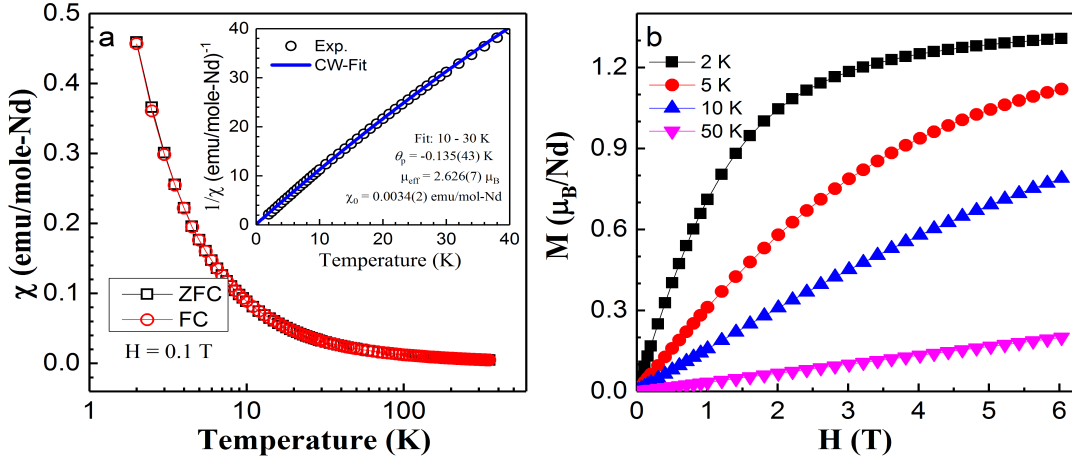
Figure 6.3.3 (a) Temperature dependence of susceptibility χ of polycrystalline sample $Nd_2Hf_2O_7$, measured from 2 to 300 K in an applied field H = 0.1 T. Insert: temperature dependence of inverse susceptibility χ^{-1} with the fit of Curie-Weiss law in the range 10 to 30 K (blue line). (b) Isothermal magnetization curves from 0 to 6 T at 2, 5, 10 and 50 K.

Figure 6.3.3 (b) shows the isothermal magnetization curves $M(H)$ of $Nd_2Hf_2O_7$ at T = 2, 5, 10 and 50 K. The $M(H)$ curve at 2 K shows a saturation tendency with a magnetization value of $M \sim 1.30$ μ_B/Nd at 6 T, which is much lower than the theoretical saturation magnetization $M_s = g_J J \mu_B = 3.27$ μ_B/Nd for free Nd^{3+} ion. The strongly reduced value of M_s can be attributed to the strong Ising anisotropy and the reduction of the Nd^{3+} moment due to the CEF effect. For a pyrochlore lattice with local $\langle 1\,1\,1 \rangle$ Ising anisotropy, the saturated magnetizations M_s at high fields along the three crystallographic directions [100], [110], and [111] are given by $g_{eff}J_{eff}\mu_B(1/\sqrt{3})$ [2I2O spin structure], $g_{eff}J_{eff}\mu_B(\sqrt{2/3} \times 2)/4$ [one-in-

one-out, two free] and g$_{eff}$J$_{eff}$μ$_B$(1 + 1/3×3)/4 [3Ī1O], respectively [202]. Then the powder averaged M_s value should be $< M_s > = \left(6M_{[100]} + 12M_{[110]} + 8M_{[111]}\right)/26 = 0.4755 \times g_{eff}J_{eff}\mu_B$, where the weighting factors 6, 12 and 8 are the number of equivalent [100], [110] and [111] directions [34]. According to the CEF reduced moment $\mu_{CEF} = 2.45\,\mu_B$, the powder averaged saturation magnetization $\langle M_s \rangle = 1.16\,\mu_B$/Nd. The measured $M_s = 1.30\,\mu_B$ at 2 K and 6 T is slightly bigger than the expected value. With increasing temperature, the linear regime of $M(H)$ extends over a large field range, although at a more gradual rate.

6.3.3. Heat capacity

Figure 6.3.4 (a) illustrates the specific heat $C(T)$ of Nd$_2$Hf$_2$O$_7$ in the temperature range from 80 mK to 30 K under zero magnetic field. It is clear that the $C(T)$ data plotted in a semi-logarithmic scale exhibits a sharp λ-shaped peak at $T_N \sim 0.5$ K, what provides the evidence for the occurrence of a second-order phase transition, corresponding to the transition of AIAO antiferromagnetic long-range order of Nd^{3+} (see the subsection 6.3.5 and the reference [225].

   In order to obtain pure magnetic specific heat of electronic spins $C_{mag}(T)$ and estimate the magnetic entropy S_{mag}, the lattice contribution (phonon), C_{latt}, the CEF contribution, C_{CEF}, and the nuclear contribution C_{nuc} have to been subtracted from the raw data C_{exp}. The detail of the data treatment can be found in previous chapters and Appendix A. Here, the C_{latt} is estimated by appropriately scaling the measured specific heat of the nonmagnetic isostructural compound La$_2$Hf$_2$O$_7$ (red line in Figure 6.3.4 (a)). The Schottky anomaly of CEF, C_{CEF}, (blue line in Figure 6.3.4 (a)) is nearly zero below 30 K because the first CEF excited state is around 23 meV corresponding energy range 270 K. The measured specific heat C_{xp} shows an upward trend below 0.15 K, which can be attributed to the nuclear hyperfine split of the isotope ^{143}Nd and ^{145}Nd due to the magnetic order. This can be approached by $C_{nuc} \propto T^{-2}$ with a constraint of zero magnetic specific heat at lowest temperature point.
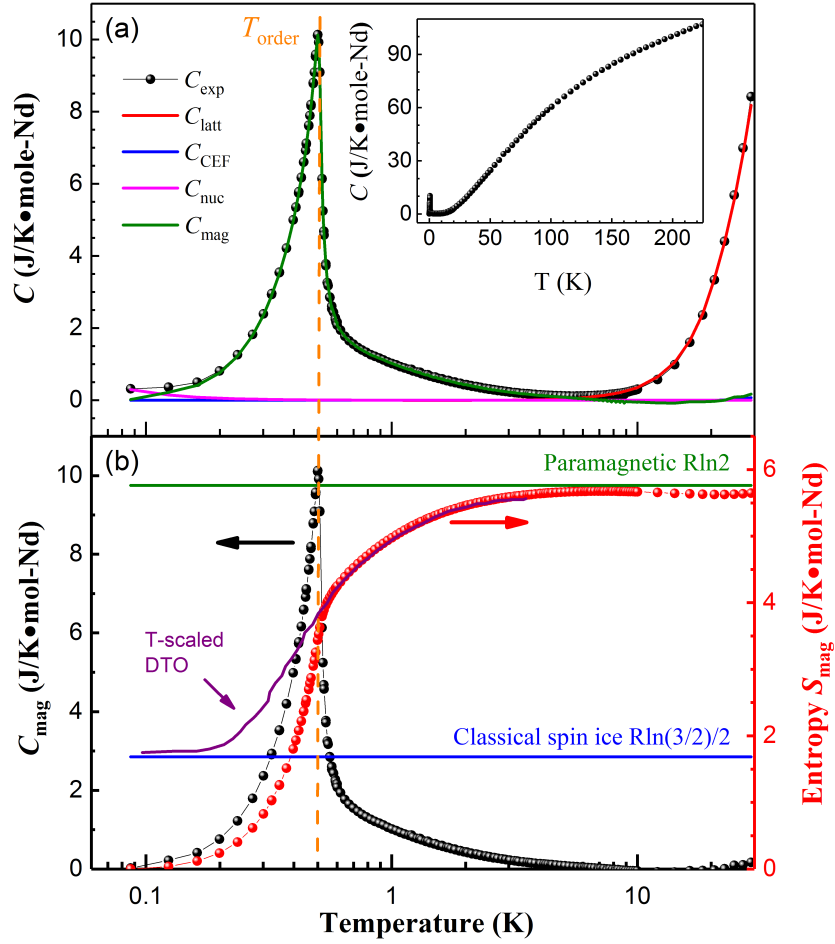
Figure 6.3.4 (a) Temperature dependence of the specific heat $C(T)$ of $Nd_2Hf_2O_7$, within different contributions: measured data (black spheres), lattice (phonon) contribution (red solid line), crystal electric field Schottky anomaly (blue solid line), nuclear h.f.s. contribution (magenta solid line), and magnetic contribution (green solid line). (b) The obtained magnetic specific heat $C_{mag}(T)$ (black spheres) and the corresponding magnetic entropy $S_{mag}(T)$ (red spheres). The green and blue line represent the S_{mag} for the paramagnetic state of a spin-1/2 system and the residual entropy of CSI. The S_{mag} of the CSI $Dy_2Ti_2O_7$ is scaled in temperature to match the magnetic entropy $S_{mag}(T)$ of $Nd_2Hf_2O_7$ (purple solid line).

The magnetic specific heat C_{mag} obtained according to $C_{mag} = C_{exp} - C_{latt} - C_{CEF} - C_{nuc}$ is plotted in Figure 6.3.4 (a) as green line and black spheres in Figure 6.3.4 (b). The corresponding magnetic entropy $S_{mag}(T)$ obtained by integrating C_{mag}/T over the investigated temperature range is plotted in Figure 6.3.4 (b). In the temperature range above 7 K, the entropy reaches a constant value of 5.67 J/(K mol-Nd), which is close to the value of $Rln(2)$ (green line) for the spin-1/2 paramagnetic state. When the temperature decreases, the $S_{mag}(T)$ drops slowly from 8 K to 0.56 K, like in the CSI compound $Dy_2Ti_2O_7$ (the temperature was multiplied a factor of 0.3, and plotted as purple line in Figure 6.3.4 (b)) [61]. It was found that a portion (~28%) of the entropy is released above $T_N = 0.53$ K, which

115

suggests the development short-range spin correlations above the AIAO transition. Unlike the existence of residual entropy $R/2ln(3/2)$ in the CSI compounds Dy- and Ho-based pyrochlore, the magnetic entropy of NHO drops sharply around $T_N \sim 0.5$ K, and it is completely released to zero at 80 mK.

6.3.4. Crystal electric field excitations

Figure 6.3.5 shows the normalized scattering cross section $I(Q, E)$ of powder Nd₂Hf₂O₇ measured with an incident energy of 65.7 and 150 meV at 2 K. The strong signal around $E = 0$ is from elastic neutron scattering, and the gradual increase in intensity with increasing Q is caused by scattering from phonons. The CEF transitions cause the weak dispersionless bands of scattering at low Q. Three CEF levels can be identified at energy transfers near 23.1, 35 and 101 meV, which are similar to the observation in Nd₂Zr₂O₇ [34, 223].
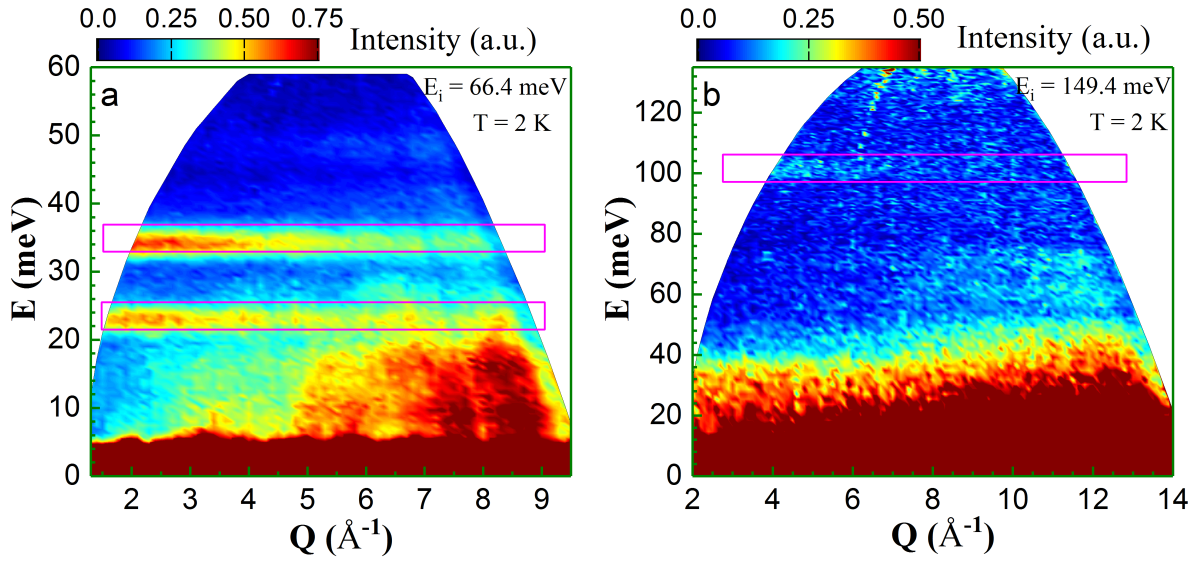
Figure 6.3.5 Inelastic neutron scattering spectra of Nd₂Hf₂O₇ at 2K with (a) E_i= 66.5 meV and (b) E_i= 149.4 meV.

Figure 6.3.6 (a) shows energy spectra integrated over a small range of the wave-vector transfer Q in Figure 6.3.5 (a). The energy spectra integrated in the same Q width at high-Q is used to estimate the nonmagnetic background. $I_{mag}(E) = I_{lowQ}(E) - fac * I_{highQ}(E)$ The scale factor fac is determined $I_{highQ}(E_{bg})/I_{lowQ}(E_{bg})$ where E_{bg} is the energy far away from the excitations. (More precise treatment is that the scale factor should be calculated from the isostructural nonmagnetic reference sample at the same Q positions, for example La₂Hf₂O₇ [97,231]). The high temperature data sets were treated in the same way (see Figure

6.3.6 (b)). When temperature increases, the intensities of the CEF excitations at $E_1 = 23.8(2)$ and $E_2 = 35.0(2)$ meV, corresponding to transitions from the ground to excited states, decrease. Additional excitation around $E_3 = 12.6(2)$ meV becomes visible. The E_3 can be attributed to the intermediated transition between E_1 to E_2, $E_3 \approx E_2 - E_1$, when the $E_2 = 23.1$ meV gets thermally populated at high temperature. The thermal population of CEF levels is also the reason of the weaker intensity of E_1 and E_2 at high temperature.
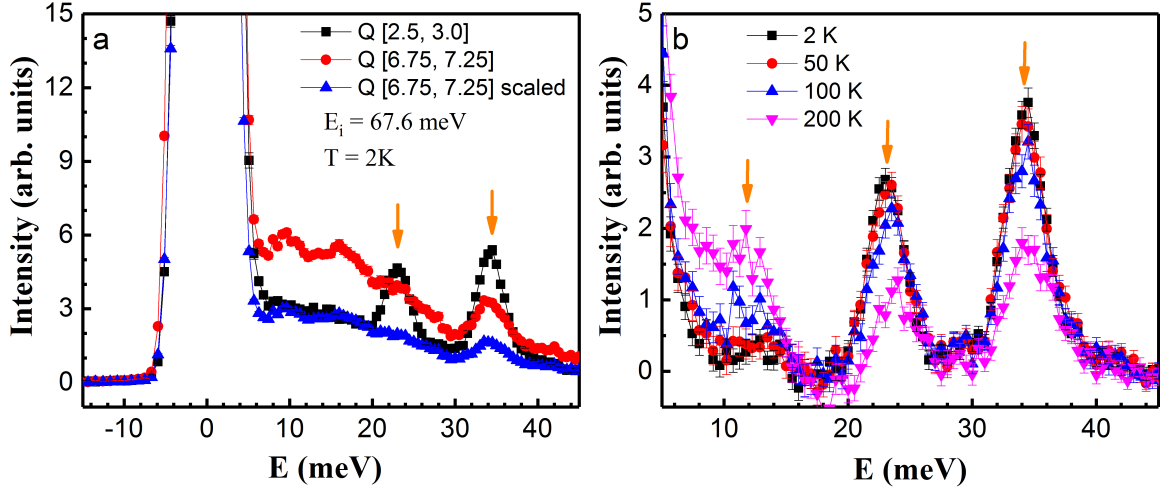
Figure 6.3.6 (a) Energy spectra $S(E)$ of $Nd_2Hf_2O_7$ at $Q = 2.75$ Å^{-1} (black) and 7 Å^{-1} (red) integrated with $\Delta Q = 0.5$ Å^{-1}. The blue curve represents the estimated background. (b) Background subtracted energy spectra $S(E)$ at different temperatures at $Q = 2.75$ Å^{-1}.

For the Nd^{3+} ion, the Hund's-rule ground state (GS) multiplet is $^4I_{9/2}$ and the first excited multiplet is $^4I_{11/2}$. In pyrochlore structure, the eight neighboring oxygen ions create a distorted octahedral with D_{3d} point group in which the local 3-fold rotation axis is along the local [1 1 1] direction of the crystal lattice. The GS ($4f^3$ with $J = 9/2$) will split into five doublets according to Kramers theorem. The integrated intensities respected to the largest peak E_2 at 35 meV, obtained from Gaussian profile fitting, are given in Table 6.3.3. The intensity of peaks $E_4 = 101$ meV was scaled to $Q = 2.75$ Å^{-1} according to the $F^2(Q)$ of Nd^{3+} (see Figure 6.3.7). The energies and intensities of these excitations at 2 K were used to adjust the six parameters of the crystal field Hamiltonian:

$$\mathcal{H}_{CEF} = B_0^2 C_0^2 + B_0^4 C_0^4 + B_3^4(C_{-3}^4 - C_3^4) + B_0^6 C_0^6 + B_3^6(C_{-3}^6 - C_3^6) \\ + B_6^6(C_{-6}^6 - C_6^6)$$

(6.3.3)

where B_q^k denotes the CEF parameters and C_q^k are the components of the tensor operator. Considering the significant J mixing in the crystal-field wave functions due to the

comparable strength of the CEF interaction and the spin-orbit interaction of Pr and Nd ions in other pyrochlore compounds, we therefore diagonalized $\mathcal{H}_{CEF}$ within the set of 98 intermediate coupling basis states of the f^3 configuration of Nd^{3+} using the program SPECTRE [208]. The CEF parameters in Ref. [34] were used as the starting parameter for the least-square fitting. Taken into account the double-differential cross section of CEF (Eq 3.3.12), the refinement of the INS spectra reaches the standard normalized goodness-of-fit parameter $\chi^2 = 0.406$.
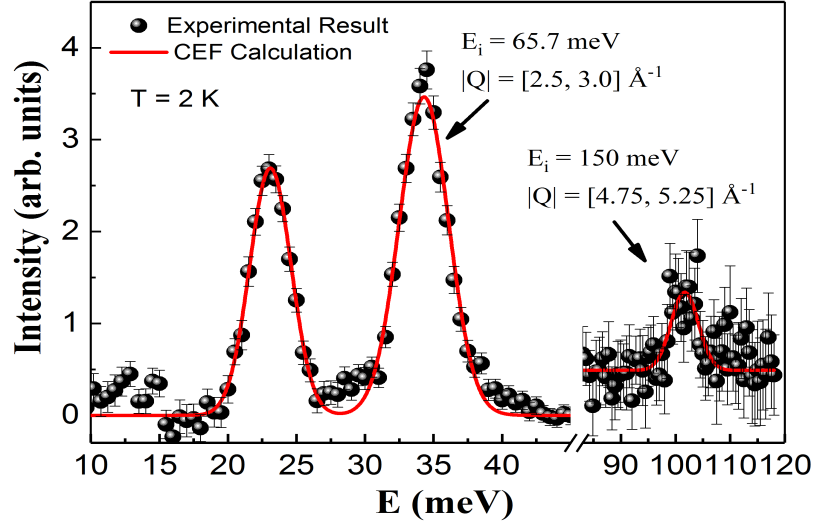
Figure 6.3.7 Fitted inelastic neutron spectra of Nd$_2$Hf$_2$O$_7$ at 2 K. The data for the two lower peaks are from the data set with $E_i = 65.7$ meV integrated over the interval $Q = [2.5 - 3]$ Å^{-1}. The data for the peak at 101 meV are from the data set with $E_i = 150$ meV integrated over the range $Q = [4.75 - 5.25]$ Å^{-1}.

Table 6.3.3 Observed and calculated crystal-field transition energies (E) and integrated intensity (I) within the ground state multiplet $^4I_{9/2}$ of Nd$_2$Hf$_2$O$_7$ at 2 K. The intensity is relative to the highest peak. The refinement reaches the standard normalized goodness-of-fit parameter $\chi^2 = 0.406$.

Levels	E_{obs} (meV)	E_{cal} (meV)	I_{obs}	I_{cal}
Γ_{56}^+	0	0	-	2.53
Γ_4^+	23.1(2)	23.9	0.63(5)	0.68
Γ_{56}^+	34.3(3)	34.3	⎤	0.65
Γ_4^+	35.3(3)	36.0	⎦ 1	0.35
Γ_4^+	101(1)	101.3	0.60(5)	0.63

The CEF parameters obtained from the analysis are $B_0^2 = 31.76$ meV, $B_0^4 = 402.2$ meV, $B_3^4 = 86.24$ meV, $B_0^6 = 146.2$ meV, $B_3^6 = -97.82$ meV and $B_6^6 = 128.5$ meV. As listed in Table 6.3.3, these CEF parameters correspond to five doublets at 0, 23.9, 34.3, 36.0 and 101.3 meV. These parameters are also converted into the Stevens' formalism according the relation $D_k^q = \lambda_{kq}\theta_k B_q^k$ (λ_{kq} and $\theta_k = \alpha_J$, β_J and γ_J listed in Ref. [232]) $D_2^0 = -0.102$ meV, $D_4^0 = -0.0146$ meV, $D_4^3 = -0.0743$ meV, $D_0^6 = -0.00035$ meV, $D_6^3 = 0.00476$ meV and $D_6^6 = -0.00464$ meV. These CEF parameters are comparable with those obtained from $Nd_2Zr_2O_7$ in Ref. [34] and recent NHO result [229]. These parameters indicate that the CEF ground-state of Nd^{3+} in NHO is typical of a dipolar-octupolar doublet, expected when $D_2^0 < 0$ and dominates over the other terms [44]. In NHO the CEF ground doublet wave function (symmetry Γ_{56}^+) could be written in terms of the $\left|^{2S+1}L_J, M_J\right\rangle$ basis as follow:

$$
\begin{aligned}
|\pm\rangle = 0.879\big|\,^4I_{9/2}, \pm 9/2\big\rangle &\mp 0.305\big|\,^4I_{9/2}, \pm 3/2\big\rangle \\
&+ 0.335\big|\,^4I_{9/2}, \mp 3/2\big\rangle \mp 0.114\big|\,^4I_{11/2}, \pm 9/2\big\rangle
\end{aligned}
\tag{6.3.4}
$$

We note the significant admixture of terms $\big|\,^4I_{9/2}, M_J = \pm 9/2\,\big\rangle$ with $\big|\,^4I_{9/2}, M_J \neq 9/2\,\big\rangle$ in the CEF ground doublet as well as a small mixing with $^4I_{11/2}$ leading to the reduction of the Nd^{3+} moment. This CEF ground-doublet gives a magnetic moment $\mu_{CEF} = 2.475(5)\ \mu_B$ with anisotropy g tensor, $g_{\parallel} \approx 4.95$ and $g_{\perp} \approx 0$. The reduced magnetic moment is close to the effective moment μ_{eff} obtained from the CW analysis of the susceptibility and consistent also with the one recently reported in Ref [229], and $Nd_2Zr_2O_7$ in Ref [34]. The CEF parameters obtained from the analysis of INS data are able to reproduce the powder DC susceptibility and the Schottky anomaly in specific heat, as shown in Figure 6.3.8. A very good agreement between the experimental data and the calculation supports the obtained CEF states and parameters. The calculated anisotropy in the susceptibility is $\chi_{\parallel}/\chi_{\perp} \approx 60$ at T = 10 K, where $\chi_{\parallel}$ and $\chi_{\perp}$ are the susceptibilities parallel and perpendicular to the $\langle 111 \rangle$ quantization axis of CEF. The CEF analysis indicates that the Nd^{3+} in NHO can be treated as an effective spin-1/2 system with strong Ising anisotropy
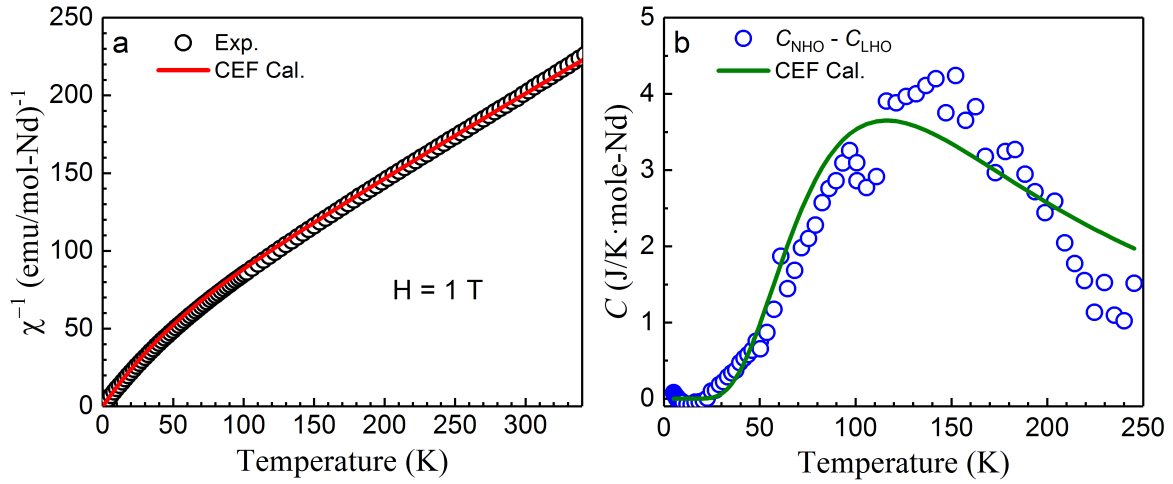
Figure 6.3.8 Comparison of the experimental CEF results of (a) susceptibility and (b) CEF Schottky contribution to specific heat with the calculated result (solid line) according to the CEF parameters obtained from the analysis of INS data.

6.3.5. Magnetic Ordering and diffuse magnetic scattering

The specific heat anomaly of NHO indicates a second phase transition around 0.5 K. Polarized neutron diffraction on DNS was employed to explore the phase of NHO below the transition temperature. Figure 6.3.9 shows the nuclear coherent (black spheres), spin-incoherent (blue spheres) and magnetic (red spheres) components of the total scattering from NHO at 89 mK obtained by means of xyz-polarization analysis (XYZ-PA) at DNS. The spin-incoherent scattering intensity is nearly constant, suggesting a successful separation of the different scattering contributions. The Bragg peaks observed in the nuclear coherent scattering component could be indexed as (1 1 1), (2 2 0), (1 1 3) and (2 2 2). Though the magnetic scattering is very weak as compared to the nuclear coherent scattering, two magnetic peaks located at (2 2 0) and (1 1 3) positions of the nuclear Bragg peaks are clearly observed. The same results have been found in Ref [225] and other Nd-based pyrochlore compounds Nd$_2$Zr$_2$O$_7$ [34,223] and Nd$_2$Sn$_2$O$_7$ [222], implying a similar magnetic structure.
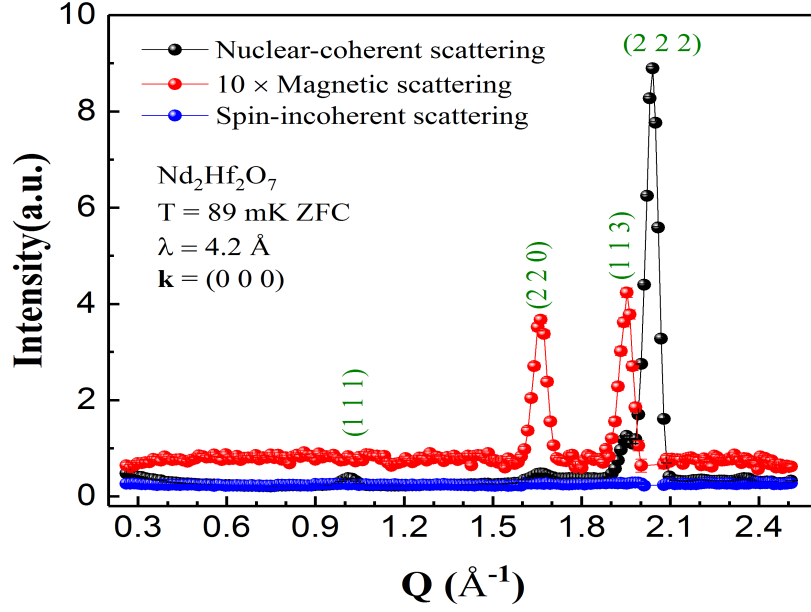
Figure 6.3.9 Nuclear coherent (black spheres), spin-incoherent (blue spheres) and magnetic (red sphere) scattering of $Nd_2Hf_2O_7$ at 89 mK separated by XYZ-PA on DNS. The sample was cooled under zero magnetic field condition.

The magnetic peaks could be indexed in the simple cubic (s.c.) unit cell using a single propagation vector of $\mathbf{k} = (0\ 0\ 0)$. Considering the propagation vector, the representation analysis conducted using the software BASIREPS [151] gives a result that the magnetic representation of Nd (16d) can be reduced into four nonzero irreducible representations (IRs) of the little group:

$$\Gamma_{mag} = 1\Gamma_3^1 + 1\Gamma_5^2 + 1\Gamma_7^3 + 2\Gamma_9^3 \tag{6.3.5}$$

The multiplicative factors represent the number of the times that the IRs occurs, the dimensionality and the order of IRs are denoted as superscript and subscript in Eq. (6.3.5), respectively. All possible models of the magnetic structure can be obtained by the linear combination of the basis vectors of the IRs.

The simulation of the magnetic Bragg peaks based on different combinations of the basis vectors of the IRs can be found in Appendix B. We found that only Γ_3 is suitable for our observation, because magnetic peaks only appear at (2 0 0) and (1 1 3) but are absent at (1 1 1) and (2 0 0). The magnetic structure is comprised of alternating 'all-in' and 'all-out' (AIAO) units of corner-sharing tetrahedra, where each tetrahedron unit consists of four Nd^{3+} magnetic moments at the vertices of the tetrahedron all pointing either toward the center (all-in) or away from the center (all-out) of tetrahedral (see Figure 6.3.10 right panel). Since the XYZ-PA separates the nuclear coherent scattering and magnetic scattering of the sample at the same temperature, we can obtain the scale factor and the crystallographic parameters from

the nuclear coherent scattering component, then refine the ordered magnetic moment of Nd^{3+} in the magnetic scattering. The refinement of the magnetic scattering of NHO at 89 mK for the Γ_3 model is shown in the left panel of Figure 6.3.10, and gives an ordered moment of m_{ord}= 1.415(13) μ_B/Nd.
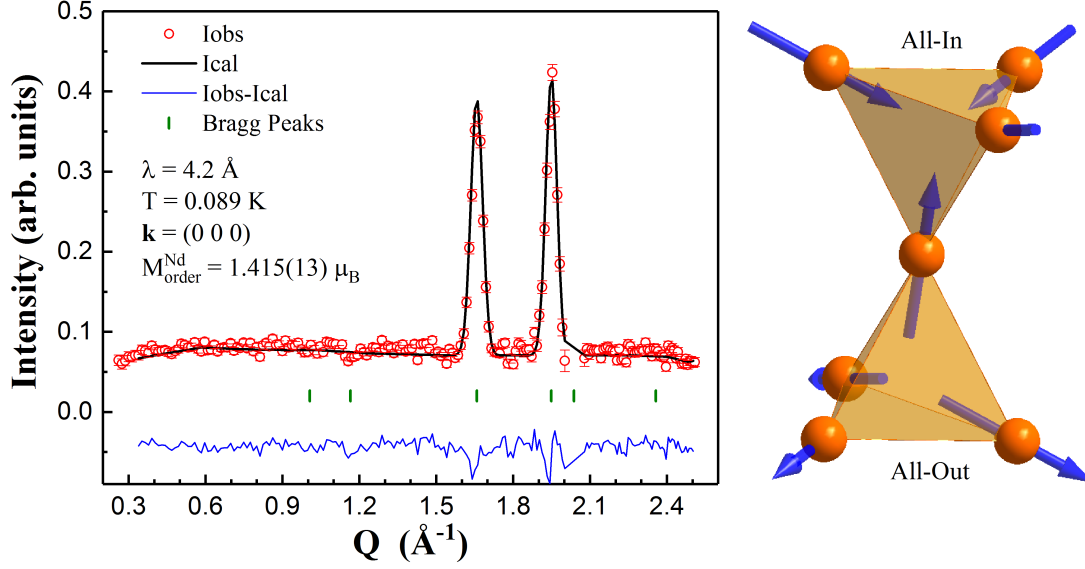
Figure 6.3.10 Refinement of the magnetic scattering of Nd$_2$Hf$_2$O$_7$ at 89 mK (*left*) and corresponding AIAO magnetic structure (*right*).

The temperature dependence of the intensity of the peak (1 1 3) from 0.1 to 0.85 K was traced in spin-flip (SF) and non-spin-flip (NSF) channel with *x* polarization. For the XYZ-PA method of a powder sample, the cross section of x-SF and x-NSF can be expressed as

$$\sigma_x^{SF} = \frac{1}{2}\sigma_{mag} + \frac{2}{3}\sigma_{si},$$

$$\sigma_x^{NSF} = \frac{1}{2}\sigma_{mag} + \frac{1}{3}\sigma_{si} + \sigma_{nu} + \sigma_{ii}$$

(6.3.6)

The subscripts *nc*, *mag*, *si*, and *ii* stand for 'nuclear coherent', 'magnetic', 'spin-incoherent' and 'isotope-incoherent' contributions, respectively. As shown in the inset of Figure 6.3.11, the intensity of x-NSF channel is approximately temperature independent because the nuclear coherent scattering of the Bragg peak dominates the intensity, what also implies no crystallographic structure changes. Since only magnetic scattering and spin incoherent scattering contribute to the x-SF channel, and the spin incoherent scattering is usually temperature independent in this temperature range, the temperature dependence of the x-SF intensity at the magnetic peak position will mirror the magnetic ordering behavior of Nd^{3+}. As illustrated in Figure 6.3.11, the intensity of the x-SF channel increases with the decreasing

of temperature below 0.55 K. A modified power law, which assumes that the background corrected intensity of the x-NSF channel is proportional to the squared moment, $I = I_0(1 - T/T_N)^{2\beta} + bg$, was applied to fit the magnetic ordering behavior from 0.3 to 0.60 K. The fit is plotted as blue solid curve in Figure 6.3.11, and gives $T_N = 0.535(5)$ K and $\beta = 0.308(35)$ which within the error bars is close to the expected critical exponent 0.33 for a three-dimensional Ising system [6].
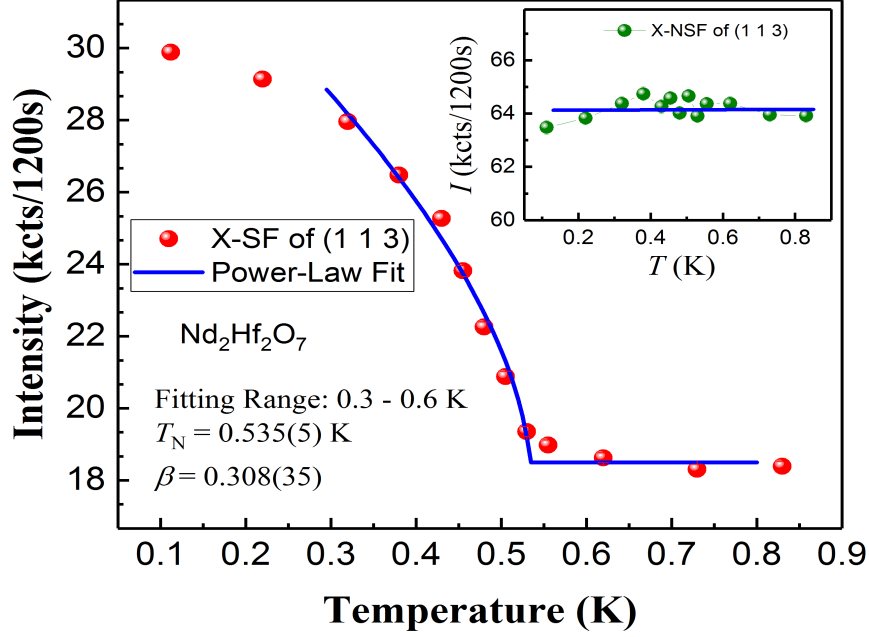
Figure 6.3.11 Temperature dependence of the intensity of the x-SF and x-NSF channels of the peak (1 1 3). The blue curve is the fit of a power-law function as discussed in the text.

Our results for the ordered moment of Nd^{3+} and its temperature behavior are completely different to the reported results [225], where the ordered moment is only 0.62(1) μ_B/Nd and saturates unusually below 0.4 K. The disagreement may be due to the different applied techniques of neutron scattering. For the unpolarized neutron powder diffraction, the non-magnetic contributions, such as nuclear Bragg peaks and incoherent scattering, have to be subtracted based on the data taken at higher temperature above the phase transition. This may introduce a large error for the case with the propagation vector $\mathbf{k} = (0\ 0\ 0)$, since the magnetic peaks are located on top of the nuclear peaks. The situation becomes serious when strong magnetoelastic effect exists. In contrast, the advantage of the polarized neutron scattering with XYZ-PA is that the nuclear coherent, magnetic and spin-incoherent scattering can be separated at the same temperature. The temperature effect of the lattice constant a is minimized. Thus, we think our result is more precise. The obtained ordered moment in this

work is also comparable to the reported 1.708(3) μ_B/Nd at 0.1 K for Nd$_2$Sn$_2$O$_7$ [222] and 1.26(2) μ_B/Nd at 0.1 K for Nd$_2$Zr$_2$O$_7$ [34].
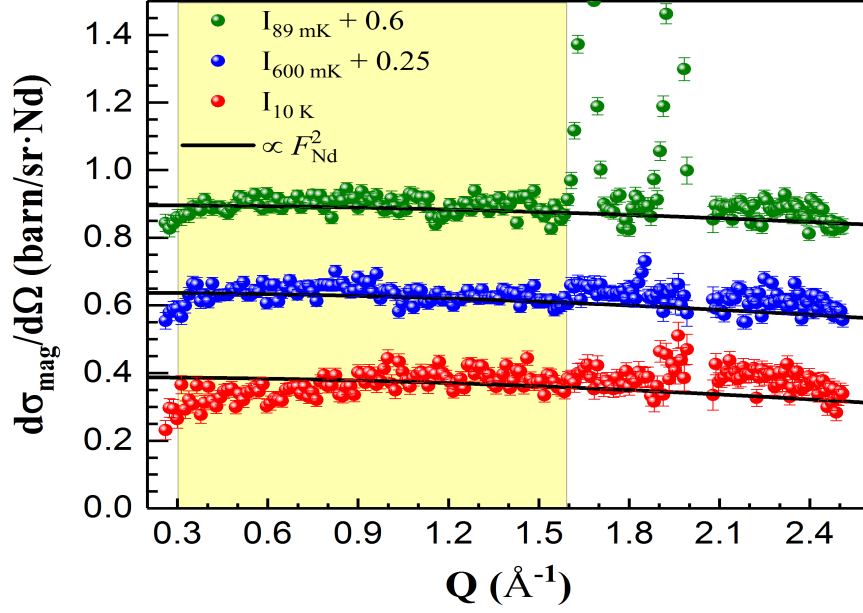
Figure 6.3.12 Temperature dependence of the magnetic diffuse scattering. The value of x- and y- axis corresponds to the data of 10 K. The data at 600 mK and 89 mK are shifed vertically by 0.25 and 0.6 barn/sr/Nd, respectively. The black solid lines are proportional to the squared magnetic form factor of Nd^{3+}.

The ordered-state magnetic moment of Nd^{3+}, m_{ord}= 1.415(13) μ_B/Nd, at 0.089 K is highly reduced compared to the free ion magnetic moment 3.62 μ_B for free Nd^{3+} ions, as well as the $\mu_{CEF} = 2.475$ μ_B for the CEF ground doublet. The reduction of the ordered moment suggests the presence of strong quantum fluctuations. More remarkable, non-negligible diffuse magnetic scattering exists in the magnetic scattering result together with the magnetic Bragg peaks at 89 mK, as shown in Figure 6.3.10. The diffuse magnetic scattering can be elastic or inelastic scattering. If the overall energy scale of the magnetic excitations in the system is smaller than 3 meV, which is true for Nd$_2$Hf$_2$O$_7$ (will be demonstrated by inelastic neutron scattering), the magnetic scattering data of DNS will include the contributions from the fluctuating magnetic moment (see the discussion in Chapter 5). Thus one can estimate the total fluctuating magnetic moment from the diffuse magnetic scattering, after calibrating the intensity of magnetic scattering to absolute units barn/sr/Nd.
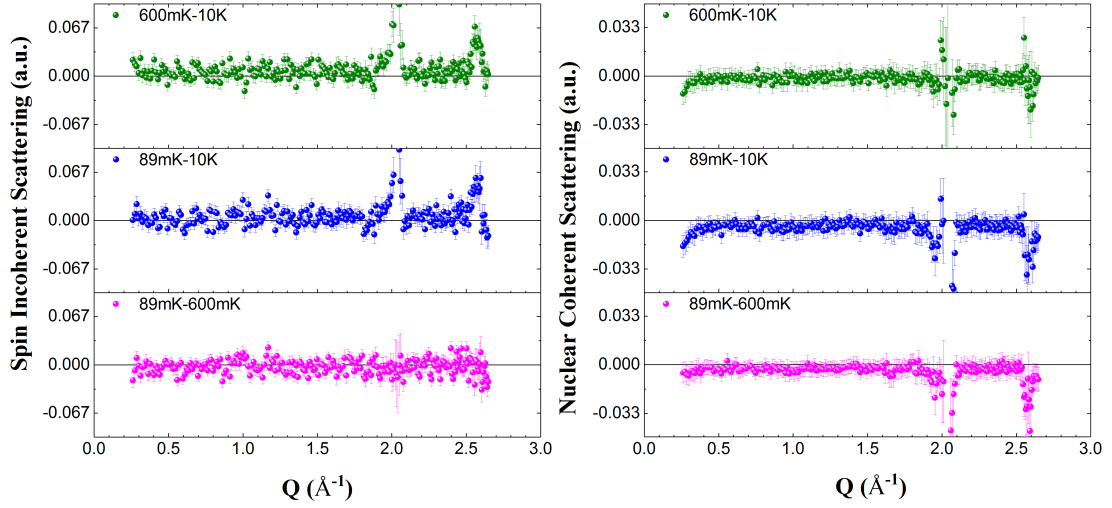
Figure 6.3.13 Difference of the spin-incoherent scattering (*left*) and nuclear coherent scattering (*right*) among 89 mK, 600mK and 10 K. The zero values of the differences indicate no nuclear spin ordering and significantly lattice changing in NHO from 89 mK to 10 K.

Due to the strongly neutron absorption of hafnium, the obtained magnetic scattering intensity has to be normalized to the cross section by the spin-incoherent scattering of NHO, as follow (see detail in Appendix C):

$$\frac{d\sigma_{mag}}{d\Omega} = \frac{I_{mag}}{I_{spin-inc}} \times \frac{\sigma_{spin-inc}^{NHO}}{4\pi} \tag{6.3.7}$$

where I_{mag} and $I_{spin-inc}$ are the measured intensities of the magnetic scattering and the spin-incoherent scattering after XYZ-PA, $\sigma_{spin-inc}^{NHO}$ is the spin-incoherent cross section of $Nd_2Hf_2O_7$, $\sim 9.2 + 2.6 = 11.8$ barn/Nd. The magnetic scattering in the absolute unit barn/sr/Nd is plotted in Figure 6.3.12, where the data at 600 mK and 89 mK are shifted vertically by 0.25 and 0.6 barn/sr/Nd, respectively. The intensities of the diffuse magnetic scattering at 600 mK and 10 K, above long-range order phase transition, are similar around 0.4 barn/sr/Nd at $Q = 0.9$ Å^{-1}, while that at 89 mK is a bit smaller around 0.3 barn/sr/Nd. It makes sense since the ordered magnetic moment at 89 mK does not contribute to the diffuse magnetic scattering. Smaller fluctuating moment compared to that of 600 mK and 10 K implies lower intensity of diffuse magnetic scattering, if the total magnetic moment is constant. Before making a conclusion about the total moment of Nd^{3+}, one has to take into account the introduced error by the changing of the spin-incoherent scattering and nuclear-coherent scattering, due to the nuclear spin ordering and significant lattice changing. Figure 6.3.13 illustrates that these influences could be ignored in the measured temperature range. These facts strongly imply that the total moment is possibly conserved.

According to the magnetic neutron scattering from powder sample, the fluctuating magnetic moment can be obtained by [213, 233, 234]:

$$\delta m^2 = \mu_B^2 \frac{\iint Q^2 6I(Q,E)/|r_0 f(Q)|^2 dQdE}{\int Q^2 dQ} \tag{6.3.8}$$

where $r_0 = 0.539 \times 10^{-12}$ cm and $I(Q,E) = d\sigma_{mag}^2/d\Omega dE$ is the double differential cross section. Since the magnetic scattering data taken from DNS are already approximately energy-integrated, the integration is only performed in the Q range from 0.3 to 1.6 Å^{-1} which covers the whole Brillouin Zone (BZ). As shown in Table 6.3.4, the fluctuating moments obtained are 8.214(31) and 8.217(37) μ_B^2/Nd for 10 K and 600 mK, respectively, while the magnetic diffuse scattering at 89 mK yields the fluctuating moment 6.391(32) μ_B^2/Nd. Consider the ordered moment at 89 mK around 2.003(37) μ_B^2/Nd, one could have total magnetic moment ~ 7.967(69) μ_B^2/Nd at 89 mK, which is close to the fluctuating moment 8.2 μ_B^2/Nd at 600 mK and 10 K. This fact suggests that the total magnetic moment m_{tot}^2 is conserved within the error bar. The average value of m_{tot}^2 is 8.133(87) μ_B^2, which is slightly larger than the result 6.125(25) μ_B^2 obtained from CEF ground doublet. This could be attributed to the higher Hund's state $^4I_{11/2}$ contamination of the CEF ground-doublet, since the μ_{CEF}^2 is obtained only considering the CEF splitting of $^4I_{9/2}$. On the other hand, the total moment conservation also implies that the magnetic excitations, if exist, should below the effective energy-integration upper limit of DNS ~ 3 meV.

Table 6.3.4 Ordered and disordered magnetic moment of Nd^{3+} in Nd₂Hf₂O₇ at different temperatures. The ordered moment was obtained from the refinement of the AIAO magnetic structure, while the disordered moment was calculated from the magnetic diffuse scattering. See the detail in the main text. The total magnetic moment m_{tot}^2 is nearly temperature independent, within the systemic error.

Moment (μ_B^2)	$\langle m \rangle^2$	δm^2	m_{tot}^2	$g^2 J(J+1)$	μ_{CEF}^2
89 mK	2.003(37)	6.391(32)	8.394(49)		
600 mK	-	8.214(37)	8.214(37)	12.39	6.125(25)
10 K	-	8.217(37)	8.217(37)		

6.3.6. Magnetic excitations

Due to the strong neutron absorption of the sample, the intensities of $I(Q,E)$ have to be normalized to the absolute unit (barn/sr/meV/Nd) by the nuclear Bragg peaks as follows. We firstly focus on this method which is also applied in the other chapters. Figure 6.3.14 shows

the three temperature diffraction patterns obtained by energy integration of the pre-reduced $I_{raw}(Q,E)$ spectrum in sufficient range from -0.3 to 0.3 meV (the areas are marked as pink rectangles in Figure 6.3.15). The higher background could be attributed to the large spin-incoherent scattering of the sample, as illustrated on the elastic line of Figure 6.3.15. The diffraction patterns at 600 mK and 10 K are identical, while the Bragg peaks (2 2 0) and (1 1 3) grow at 57 mK due to the AIAO ordering below 530 mK.
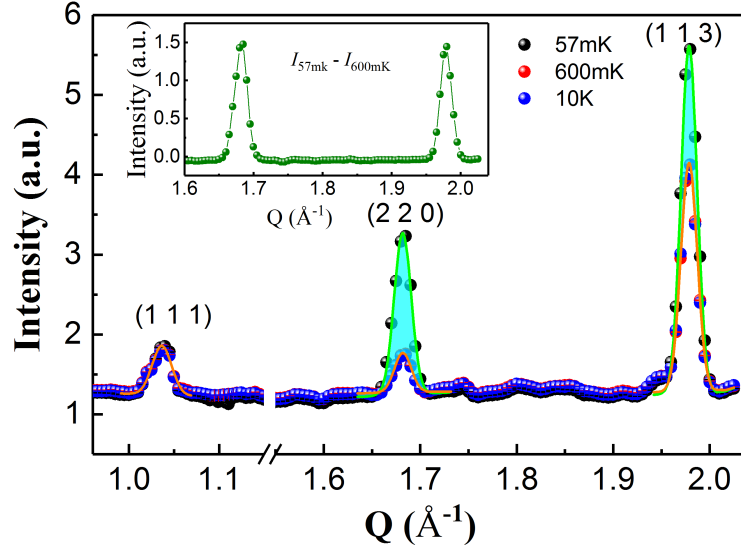
Figure 6.3.14 Diffraction patterns of $Nd_2Hf_2O_7$ at different temperature. The diffraction patterns were obtained by energy integration of $I_{raw}(Q,E)$ from -0.3 to 0.3 meV at each Q with $\Delta Q = 0.005$ Å^{-1} (pink rectangles in Figure 6.3.15).

The normalization factor (or instrument resolution volume [212]) is defined as

$$\text{NCR}_0 = \int I^{obs}(Q-\tau,E)dQdE / I^{cal}(\tau) \tag{6.3.9}$$

where τ denotes the specified Bragg peak, $I^{cal}(\tau)$ and I^{obs}_{bragg} are the Bragg scattering cross sections for a powder sample and the observed intensity of Bragg peak. As shown in Table 6.3.5, the I^{obs}_{bragg} is the integrated intensity obtained by a Gaussian-profile fitting of the Bragg peaks. The $I^{cal}(\tau)$ is calculated according to Appendix C and Ref [211]. The normalization factor $\text{NCR}_0 = 0.5846(323)$ could be obtained by comparing the observed and calculated intensity of the Bragg peak (1 1 1) with pure nuclear contribution. Thus, one can calibrate the inelastic neutron scattering intensity $I(Q,E)$ to the absolute units (barn/sr/meV/Nd) using the follow equation:

$$I(Q,E) = \frac{k_i}{k_f}\frac{d^2\sigma}{d\Omega dE}(Q,E) = \frac{I_{raw}(Q,E)}{\text{NCR}_0} \tag{6.3.10}$$

The ordered moment is thus $m_{\text{ord}} = \sqrt{(I^{obs}_{57mK}(\tau) - I^{obs}_{600mK}(\tau))/(I^{cal}_{mag}(\tau) \cdot NCR_0)} =$ 1.474(12) μ_B, which is consistent with the Rietveld refinement by Fullprof, as well as the result of DNS. The normalization method gives a systemic error 5.1 %.

Table 6.3.5 The measured and calculated Q-integrated intensities of Bragg peaks for Nd$_2$Hf$_2$O$_7$. m indicates the multiplicity of the peak due to powder average. The theoretical intensities of nuclear Bragg peaks I^{cal}_{nuc} are normalized to per Nd atom, while the calculated magnetic intensities I^{cal}_{mag} are normalized to per Nd per μ_B^2.

τ	m	Q	I^{cal}_{nuc}	I^{cal}_{mag}	I^{exp}_{57mK}	I^{exp}_{600mK}	I^{exp}_{10K}
h.k.l		Å^{-1}	barn/Nd	barn/Nd/μ_B^2		a.u.	
1 1 1	8	1.035	0.0269	-	0.0167(5)	0.0150(5)	0.0155(6)
2 2 0	12	1.690	0.0214	0.0252	0.0451(5)	0.0108(5)	0.0114(5)
1 1 3	24	1.981	0.1365	0.0258	0.0910(5)	0.0605(5)	0.0619(5)

An overview of the normalized inelastic neutron scattering $I(Q,E)$ is presented in Figure 6.3.15 (a-c) for the temperatures 57 mK, 600 mK and 10 K. The magnetic scattering can be identified according to its temperature dependence behavior. At T = 57 mK, the asymmetry of the elastic line implies a strong excitation around 0.1 meV, which may become weak at high Q. Another weak dispersive excitation could be found at high Q, which is centered around $E = 0.23$ meV at $Q = 1.82$ Å^{-1}. At 600mK and 10 K, the intensities of both excitations diminish, which confirms that they are magnetic. Although the lower-lying magnetic excitation at 57 mK could not be directly observed in $I(Q,E)$ due to the poor energy resolution of the experiment and strong spin-incoherent scattering of the sample, the spectra at constant $Q = 0.4$ Å^{-1} exhibits a clear shoulder on the positive energy side of the elastic scattering line, as shown in Figure 6.3.16 (a). One way to obtain pure inelastic scattering signal is to subtract the elastic scattering line by fitting the spectrum.

The measured inelastic scattering spectra are the convolution between the resolution function of the instrument (IRF) and the sample response. Here we use a Gaussian function to describe IRF profile. The energy resolution at elastic line, represented by the full-width at half maximum (FWHM), is around 76 µeV obtained from the trial fitting of the vanadium results, which is consistent with results based on the instrument setup at 5.12 Å^{-1}. In the fitting, we neglect the convolution process because the FWHM of the quasielastic components and inelastic components of sample response are larger than the that of IRF.
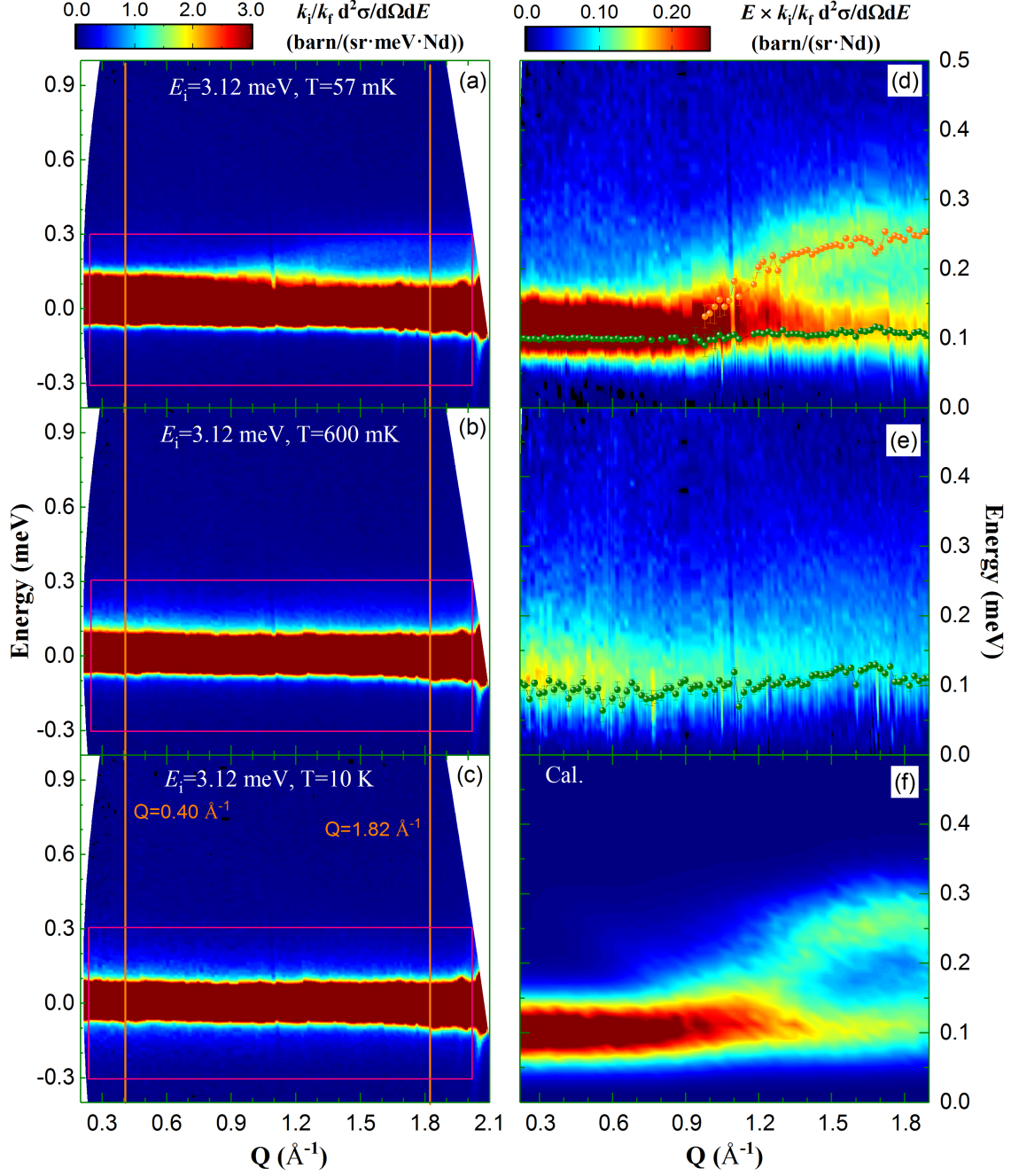
Figure 6.3.15 (*left*) Powder-averaged inelastic neutron scattering cross section $I(Q,E)$ for Nd$_2$Hf$_2$O$_7$ measured at 57 mK (a), 600mK (b) and 10 K (c). The cross section is placed in absolute units by calibrating against the integrated intensity from nuclear Bragg reflections. Pink rectangles indicate the energy integration from -0.3 to 0.3 meV for powder diffraction patterns. (*right*) The spectra $E \times I(Q,E)$ within only inelastic scattering components at 57 mK (d) and 600 mK (e). The elastic lines have been taken out according to the fitting described in the main text. The green and orange spheres indicate the obtained inelastic peak energies. (f) Powder-averaged inelastic scattering $E \times I(Q,E)$ as a function of Q and E, as predicted by LSWT using XYZ model. The unit of the calculated intensities is arbitrary unit. (Note: recently the sample has been re-measured on TOFTOF with a better energy resolution ~ 44 μeV. The updated INS results can be found in Appendix E.)

We carry out fits of the data set to follow function:

$$I(Q,E) = A \cdot IRF(Q,E) + \frac{B}{1 - \exp(-E/k_B T)} \frac{E\Gamma_{QENS}}{E^2 + \Gamma_{QENS}^2}$$

$$+ \frac{1}{1 - \exp(-E/k_B T)} \sum_i \frac{C_i E\Gamma_i}{(E^2 - E_i^2)^2 + (E\Gamma_i)^2}$$

(6.3.11)

where the first term represents the elastic scattering of Gaussian profile with fixed FWHM ~ 76 μeV, the second term represents the quasielastic neutron scattering (QENS) component with FWHM = $2\Gamma_{QENS}$ and the third term represents several inelastic magnetic components (A, B and C_i are constants, Γ_i is the FWHM of different inelastic scattering components at inelastic peak $E_i^{ie} = \pm\sqrt{E_i^2 - (\Gamma_i/2)^2}$) [235]. Typical results of the fitting based on Eq. (6.3.11) to the experiment data are shown in Figure 6.3.16. For data at 57 mK, one inelastic component could describe the spectrum at low Q very well, while two inelastic components have been taken into account at high Q. The Q dependence of the excitation energies obtained from the fitting of whole spectra at 57 mK is plotted as spheres in Figure 6.3.15 (c). The excitation consists of two modes, a dispersionless flat band (green spheres) centered at around 0.1 meV with FWHM 0.07-0.09 meV and a dispersive excitation (orange spheres) above the flat mode, which stems from (1 1 1) peak and reaches a maximum energy of about 0.24 meV at $Q = 1.82$ Å^{-1} with FWHM = 0.116 meV. The similar excitations picture was also observed in the AIAO ordered state of Nd$_2$Zr$_2$O$_7$, in which the flat band exhibits the pinch point patterns of the spin-ice characteristic [178]. For the data at 600 mK above the AIAO ordering, the fitting of a considering only quasielastic scattering model could not converge. Then, the single inelastic scattering component model was applied to fit, as show in Figure 6.3.16 (b) and (e) for the data at $Q = 0.4$ and 1.82 Å^{-1}, respectively. The whole spectra fitting displays an approximately dispersionless band centered around 0.1 meV, as illustrated in Figure 6.3.15(e). The FWHM of the flat band at 600 mK is broader than that at 57 mK. For the data at 10 K, the quasielastic scattering only model is used, as shown in Figure 6.3.16 (c) and (f) for $Q = 0.4$ Å^{-1} and 1.82 Å^{-1}, respectively. The FWHM of QENS is around 0.135 meV, yields a characteristic relaxation time $\tau(ns) = 1.31/FWHM(\mu eV) = 0.0097$ ns, if we ignore the convolution effect of the IRF. The relaxation time τ of Nd$_2$Hf$_2$O$_7$ is extremely faster than 1-10^{-1} ms in the classical spin ice Ho$_2$Ti$_2$O$_7$ [214] and Dy$_2$Ti$_2$O$_7$ [236,237], which implies the existence of stronger spin fluctuation in Nd$_2$Hf$_2$O$_7$ at 10 K.
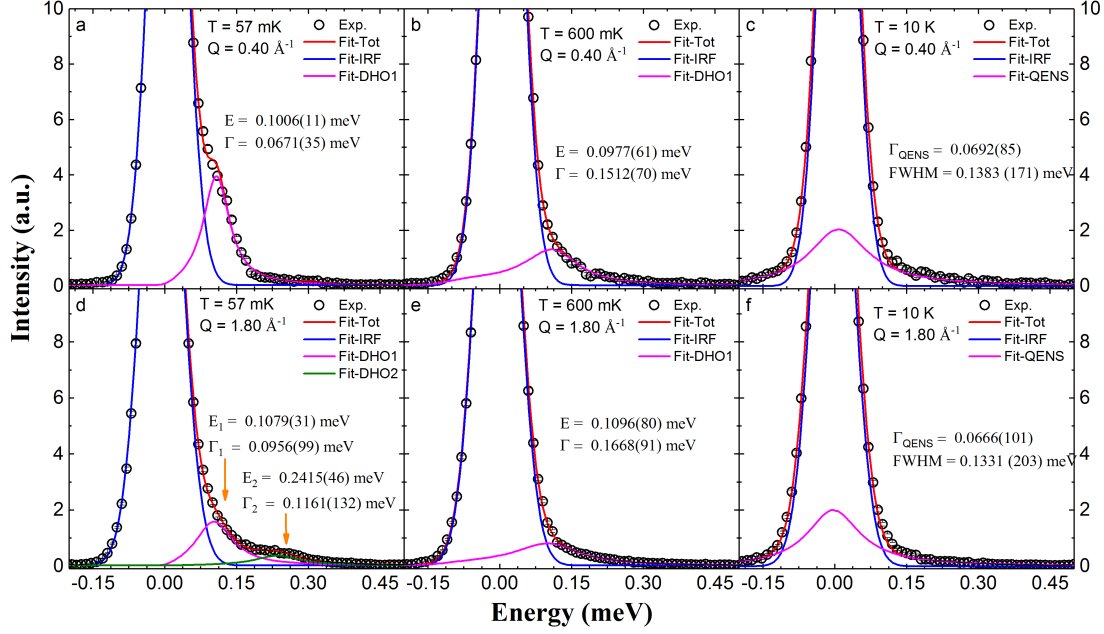
Figure 6.3.16 Inelastic spectra of $Nd_2Hf_2O_7$ for constant wave vector transfer $Q = 0.40$ and 1.80 Å^{-1} with $\Delta Q = 0.02$ Å^{-1} at various temperatures (marked as orange line in Figure 6.3.15). Closed circles are experimental data, solid lines stand for the profiles of different components (IRF labels Gaussian function as elastic scattering at $E = 0$, DHO labels the inelastic scattering signal descript by DHO function and QENS labels the quasielastic scattering descript in the main text.).

Applying the above discussed fitting on the whole spectra at 57 mK and 600 mK, one can separate the elastic and inelastic scattering components. The reconstructed spectra within the inelastic scattering components only is presented in the format $E \times I(Q, E)$ in Figure 6.3.15 (e) and (f) for 57 mK and 600 mK, respectively. Multiplication by energy makes the weaker signals at higher energies more visible. Comparing to the reported results of $Nd_2Zr_2O_7$ [178], this treatment is reliable. (Our recent INS result with a better energy resolution shows the clear flat mode and the dispersive mode excitations, which is in agreement with these analysis. See the results in Appendix E) Figure 6.3.17 (a) shows the energy-dependence of the obtained inelastic components within the wavevector integration range $0.3 < Q < 1.6$ Å^{-1}. The horizontal bar indicates the FWHM of instrument energy resolution. Both data at 57 mK and 600 mK shows a strong peak around 0.1 meV corresponding to the low-lying flat mode, while additional small hump associated to the dispersive mode could be observed around 0.25 meV in the data of 57 mK. Figure 6.3.17 (b) shows the energy integrated inelastic components $I(Q)$, which is related to the powder-averaged dynamical spin correlation function $S(Q)$. The energy integration is performed from 0.03 to 0.5 meV. The $I(Q)$ at 57 mK is in excellent agreement with the predicted spin correlations (purple solid line) based on the LSWT of the XYZ model, Eq. (6.1.1). The intensity of $I(Q)$ at 600 mK, shown as red

circles, is lower than that at 57 mK. Due to the principle of detailed balance in INS, around 22% spectra weight may be lost during energy integration. The re-scaled data of 600 mK (blue circle) shows similar modulation of that at 57 mK, while the intensity is still lower that at 57 mK implying relatively smaller fluctuating magnetic moment.
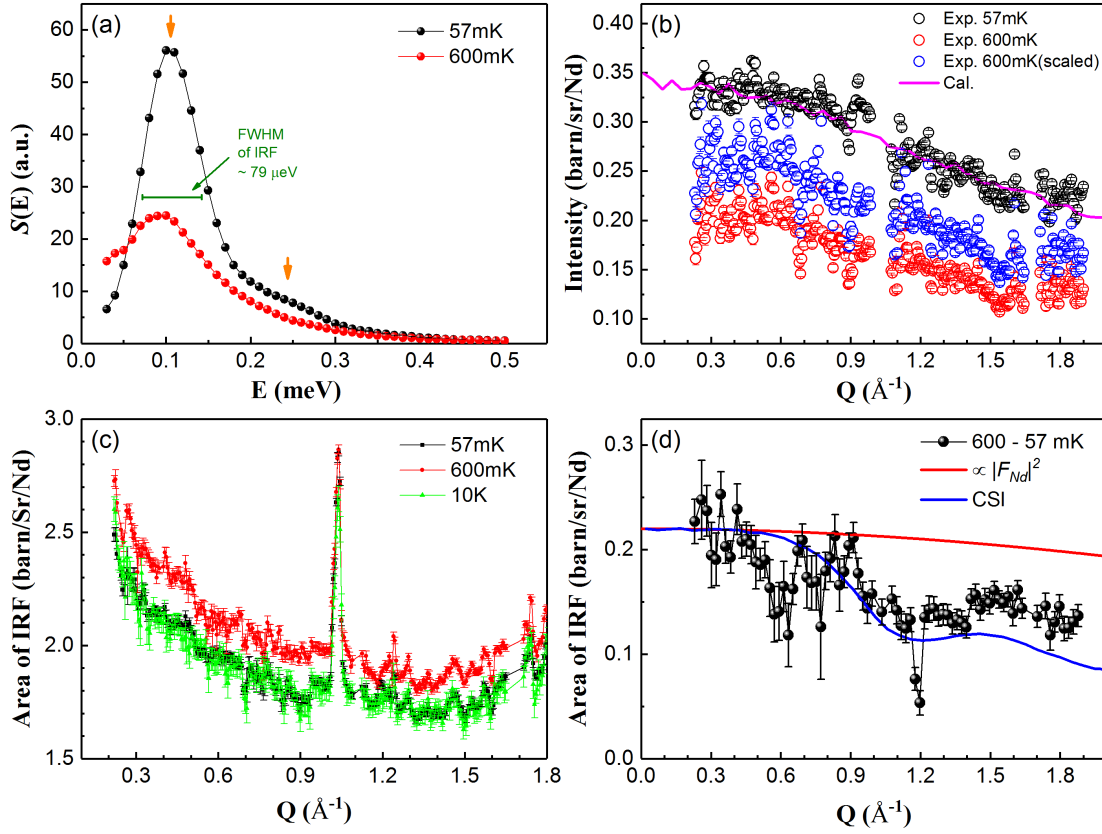
Figure 6.3.17 (a) Q integrated dynamic scattering factor as function of energy transfer $S(E)$. (b) E integrated INS intensity as function of wavevector transfer $I(Q)$. (c) Elastic scattering IRF as function of wavevector transfer Q, and (d) Elastic magnetic scattering at 600 mK, obtained by calculating the difference of $IRF(Q)$ between 600 mK and 57 mK.

According to the discussion in previous subsection, the total magnetic moment of Nd^{3+} below 10 K is conserved to around 8.133(87) μ_B^2. Due to the energy-integration of diffraction, the disordered moments either static or dynamic cannot be clarified from the polarized neutron scattering results. For the INS results, one can examine this by calculating the spectral weight of the excitations, according to Eq. (6.3.8). As shown in Table 6.3.6, the spectral weight of the excitations yields the dynamic magnetic moment $\delta m^2 = 5.794(46)$ μ_B^2 and $4.191(53)$ μ_B^2 for 57 mK and 600 mK, respectively. Considering the AIAO ordered moment $\langle m \rangle^2 = 2.173(52)$ μ_B^2 at 57 mK, the total magnetic moment is about $m_{tot-57mK}^2 = 7.967(69)$ μ_B^2, in good agreement with total moment obtain from DNS result.

However, except for the dynamic moment associated to the excitation, no static moment contributes to magnetic Bragg peaks at 600 mK. It seems some of the magnetic moment is missing at 600 mK. Back to the elastic scattering component in the fitting, Figure 6.3.17 (c) shows the Q dependence of the energy integrated IRF, which is the pure elastic scattering component of the spectra. The intensity of the elastic scattering component at 600 mK is higher than that of 57 mK and 10 K, indicating the existence of the static magnetic moment or unresolved dynamical magnetic moment. The amount of these disordered static moment is around 3.126(274) μ_B^2, and they may exhibit CSI spin correlation, as shown in Figure 6.3.17 (d). Thus, the total magnetic moment at 600 mK is around 7.317(279) μ_B^2, roughly equal to the expected value.

Table 6.3.6. The static (elastic) and dynamic (inelastic) contributions of magnetic moment per Nd at 57 mK and 600 mK. The dynamic moment is obtained by the calculation of the inelastic spectral weight. The static moment at 57 mK is obtained from the magnetic Bragg peaks, while the static moment at 600 mK is obtained from the elastic scattering components $I(Q)$ in Figure 6.3.17 (d) according to Eq. (6.3.8). For free Nd^{3+} ion, $g = 8/11, J = 6$.

Moment (μ_B^2)	Static	Dynamic	Total	$g^2 J(J+1)$	μ_{CEF}^2
57 mK	2.173(52)	5.794(46)	7.967(69)	12.39	6.125(25)
600 mK	3.126(274)	4.191(53)	7.317(279)		

The spin excitations of $Nd_2Hf_2O_7$ could be interpreted using linear spin-wave theory (LSWT) [221] and the the XYZ model Hamiltonian Eq. (6.1.1) [44]. In the AIAO state of the system, the LSWT treatment yields the spin excitation consisting of two degenerate flat bands at energy

$$\Delta_{flat} = \sqrt{\left(3|\tilde{\mathcal{J}}_z| - \tilde{\mathcal{J}}_x\right)\left(3|\tilde{\mathcal{J}}_z| - \tilde{\mathcal{J}}_y\right)} \qquad (6.3.12)$$

and two dispersive bands with upper limit

$$\Delta_{upp} = \sqrt{9\left(|\tilde{\mathcal{J}}_z| + \tilde{\mathcal{J}}_x\right)\left(|\tilde{\mathcal{J}}_z| + \tilde{\mathcal{J}}_y\right)} \qquad (6.3.13)$$

The neutron scattering actually probes the effective magnetization on each site. Within the global pseudospin rotation, the magnetization on each site could be decomposed as:

$$\boldsymbol{m}_i = \mu_B g_\parallel \left(\tilde{\tau}_i^{\tilde{x}} \sin\theta + \tilde{\tau}_i^{\tilde{z}} \cos\theta\right)\hat{z}_i \qquad (6.3.14)$$

where $\hat{z}_i$ is the unit vector along the local $\langle 1\,1\,1 \rangle$ direction and $g_\parallel = 4.95$ is the anisotropy g-factor along $\hat{z}_i$. θ is the rotation angle in (x', z') plane. The pseudospin $\tilde{\tau}_i^{\tilde{z}}$, which is in fact an octupolar degree of freedom, does contribute to the mangetic moment. Thus, the observed

133

magnetic moment is always along the local $\langle 1\,1\,1 \rangle$ direction, regardless of the values of $\tilde{\tau}_i^{\tilde{x}}$ and $\tilde{\tau}_i^{\tilde{z}}$. The magnetic structure factor $S(\boldsymbol{Q}, \omega)$ is accessible to neutron scattering. Eq. (3.3.10) can be expressed in terms of the pseudospin $\tilde{\tau}_i^{\tilde{u}}(\tilde{u} = \tilde{x}, \tilde{z})$:

$$S(\boldsymbol{Q}, \omega) = g_{\parallel}^2 \mu_B^2 \big[\cos^2 \theta \, S^{\tilde{z}\tilde{z}}(\boldsymbol{Q}, \omega) + \cos \theta \sin \theta \, S^{\tilde{x}\tilde{z}}(\boldsymbol{Q}, \omega)$$
$$+ \cos \theta \sin \theta \, S^{\tilde{z}\tilde{x}}(\boldsymbol{Q}, \omega) + \sin^2 \theta \, S^{\tilde{x}\tilde{x}}(\boldsymbol{Q}, \omega)\big] \tag{6.3.15}$$

where

$$S^{\tilde{\alpha}\tilde{\beta}}(\boldsymbol{Q}, \omega) = \int dt e^{-i\omega t} \sum_{i,j=0}^{3} \left(\hat{z}_i \cdot \hat{z}_j \right.$$
$$\left. - \frac{(\hat{z}_i \cdot \boldsymbol{Q})(\hat{z}_j \cdot \boldsymbol{Q})}{Q^2}\right) \langle \tilde{\tau}_i^{\tilde{\alpha}}(-\boldsymbol{Q}, t)\tilde{\tau}_j^{\tilde{\beta}}(\boldsymbol{Q}, t)\rangle \tag{6.3.16}$$

due to the symmetry of Eq. (6.1.1), the mixed terms $S^{\tilde{x}\tilde{z}}(\boldsymbol{Q}, \omega)$ and $S^{\tilde{z}\tilde{x}}(\boldsymbol{Q}, \omega)$ vanish. Only terms $S^{\tilde{z}\tilde{z}}(\boldsymbol{Q}, \omega)$ and $S^{\tilde{x}\tilde{x}}(\boldsymbol{Q}, \omega)$ contribute to the neustron scattering structure factor with weight proportional to $\cos^2 \theta$ and $\sin^2 \theta$, respectively:

$$S(\boldsymbol{Q}, \omega) = g_{\parallel}^2 \mu_B^2 \big[\cos^2 \theta \, S^{\tilde{z}\tilde{z}}(\boldsymbol{Q}, \omega) + \sin^2 \theta \, S^{\tilde{x}\tilde{x}}(\boldsymbol{Q}, \omega)\big] \tag{6.3.17}$$

These two contributions to the structure factor exhibit different behavior as a function of $\boldsymbol{Q}$ and ω. In the ordered state of Nd$_2$Hf$_2$O$_7$, the first term $S^{\tilde{z}\tilde{z}}(\boldsymbol{Q}, \omega)$ associate to the ordered and static correlations of $\boldsymbol{m}_i^{\tilde{z}}$ and gives rise to magnetic Bragg peaks at $\omega = 0$ within the AIAO configuration. The second term $S^{\tilde{x}\tilde{x}}(\boldsymbol{Q}, \omega)$ comes from $\boldsymbol{m}_i^{\tilde{x}}$ and exhibits spin-ice forms with the pinch-point singularities at $\omega = \Delta_{flat}$, as well as the dispersive bands.

Comparing with the experiment results, we obtained the exchange parameters:

$$\tilde{J}_x = 0.096 \text{ meV}; \ \tilde{J}_y = 0.011 \text{ meV}; \ \tilde{J}_z = -0.055 \text{ meV} \tag{6.3.18}$$

The calculated powder-averaged INS is illustrated in Figure 6.3.15 (f), in excellent agreement with the experimental result of Figure 6.3.15 (d) at 57 mK. The energy integrated scattering as a function of Q is shown in the Figure 6.3.17 (b). The theory calculation (pink solid line) has been multiplied by an over scale factor for comparison with the experimental data (black circles). The degree of agreement between theory and experiment is very strong. This fact suggests that $\tilde{J}_x > 0$ favors spin-ice correlations, while $\tilde{J}_z < 0$ prefers to the AIAO order. The above model can also explain the INS observation at 600 mK, above the AIAO ordering transition. At finite temperature $T > T_N$, the system is dominated by the $\tilde{J}_x$ term in Eq. (6.1.1). Thus, Nd$_2$Hf$_2$O$_7$ behaves like a spin-ice with a finite population of thermally excited "monopole". The term $S^{\tilde{z}\tilde{z}}(\boldsymbol{Q}, \omega)$ is mostly dynamic and associated to the gapped monopoles, while $S^{\tilde{x}\tilde{x}}$ is mostly static, exhibits spin-ice correlations. Figure 6.3.17 (d) shows

the elastic scattering at 600 mK, which is similar to the predictions of a spin-ice model with a finite density of thermally excited monopoles [78]. This fact strongly suggests that the magnetic moment fragmentation occurs above the AIAO transition at T_N.

6.4. Conclusion

In this chapter, the 5d pyrochlore insulator $Nd_2Hf_2O_7$ powder has been comprehensively investigated by means of macroscopic and microscopic techniques. $Nd_2Hf_2O_7$ crystallizes in the $Fd\bar{3}m$ crystallographic structure with a cubic lattice constant a = 10.6459(2) Å and the 48f oxygen x-parameter x = 0.33395(9) at room temperature. The combined Reitveld refinement of XRPD and NPD patterns suggests that the stuffing level of Nd-to-Hf site in the powder sample should be less than 0.02. The ZFC and FC DC susceptibilities suggests no magnetic phase transition or spin-glass crossover above 2K. The Curie-Weiss fitting of the gives a negative CW temperature θ_p = -0.135(43), implying an antiferromagnetic effective interaction between Nd^{3+} moments. Due to the CEF, the magnetic moment of Nd^{3+} exhibits strong easy-axis anisotropy (Ising type) along local $\langle 1\ 1\ 1 \rangle$ with a reduce moment μ_{CEF} = 2.475(5) μ_B. The CEF ground state of Nd^{3+} in NHO is a dipolar-octupolar doublet, which could be described as the pseudospin-1/2, $\tau_i^{u'}$ ($u' = x', y', z'$) with the two dipole components of z' and x' and an octupolar component of y'. The anomaly of magnetic specific heat suggests a phase transition at T_N = 0.53 K, while no residual entropy could be observed down to 80 mK. The further studies of the polarized neutron scattering indicate that the phase transition is the magnetic long-range order transition of Nd^{3+} with AIAO configuration. The temperature dependence of the ordered moment displays the 3D Ising ordering behavior. On the other hand, the ordered moment at 89 mK is around 1.415(13) μ_B/Nd, smaller than the expected moment due to CEF. The existence of the diffuse magnetic scattering implies strong moment fluctuation. The quantitative analysis of the total moment sum rule suggests that the total moment is conserved below 10 K, roughly equals to the CEF reduced value. In the ordered state at 57 mK, the excitation consisting of a flat mode around 0.1 meV and a dispersive mode up to 0.23 meV is observed via INS. The flat band still persists at 600 mK above T_N. The summation of the static moment with AIAO order and the dynamic moment associate the magnetic excitations satisfies the total moment sum rule. At 600 mK, a static moment with the spin-ice correlation could be found besides the dynamic moment corresponding to the flat band. The excitation could be understood by the XYZ model of the "dipolar-octupolar" pseudospin-1/2.

Chapter 7. Conclusion and Outlook

In this thesis, a comprehensive study of the pyrochlore compounds $Ln_2B_2O_7$ (B = Ir and Hf) by means of in-house characterizations and neutron scattering have been reported. The focus is on the magnetic order and excitations of Ln^{3+} in the above pyrochlore compounds. This chapter is dedicated to a summary of some important results and discussions of some perspectives of further studies.

7.1. Conclusion

The systematic experimental results described in Chapter 4 provide a unified picture of the magnetic behavior of the pyrochlore iridates that exhibits metal-to-insulator transition. First of all, the predicted AIAO magnetic ordered state of Ir^{4+}, which is one of the prerequisite of the magnetic Weyl semimetal phase, has been confirmed by our polarized neutron scattering experiments in several compounds. Benefitting from the subtle intensity ratio of two magnetic peaks (1 1 3) and (2 2 0) we were able to obtain the AIAO ordered moment around 0.2 μ_B/Ir^{4+} below T_{MI}. Unlike other pyrochlore series, such as titanates, both Ln^{3+} and Ir^{4+} are magnetic in $Ln_2Ir_2O_7$, therefore, the interaction between Ln and Ir can play an important role in dictating the magnetic properties of Ln^{3+} sublattice in pyrochlore lattice. One can simply assume that the AIAO ordered Ir^{4+} ions generate an effective *molecular-magnetic field*, B_{mf}^{Ir}, along the local $\langle 1\ 1\ 1 \rangle$ direction, which acts on the Ln^{3+} sublattice. We found that the magnetic ground state of the Ln^{3+} sublattice strongly depends on the B_{mf}^{Ir} and the Ln^{3+} single-ion anisotropy determined by the CEF in the following manner.

(1) The Ln^{3+} with easy-plane single-ion anisotropy (Ln = Er and Yb) does not order down to the lowest temperature (EIO at 0.5 K and YbIO at 0.22 K) since the B_{mf}^{Ir} may suppress the XY ordering of Er^{3+} and Yb^{3+}. Comparing to other Er- and Yb- based pyrochlores (see Table 2.3.1), these two compounds are the only system which displays XY disorder state at extremely low temperature. They are excellent candidates to study the exotic magnetic excitations in a completely disordered magnetic system.

136

(2) The Ln^{3+} ions with easy-axis anisotropy (Ln = Nd, Tb, Dy and Ho), which is compatible with B_{mf}^{Ir}, exhibits the long-range magnetic ordered ground state with AIAO configuration. Their unusual temperature dependence of the ordered moment thus can be explained as the induced ordering behavior with an estimated field $B_{mf}^{Ir} = 1.1336(1259)$ T.

Furthermore, we found that the ordered moment of Nd^{3+}, Tb^{3+}, Dy^{3+}, and Ho^{3+} at 0.5 K is significantly smaller than the expected CEF reduced moment of Ln^{3+}, suggesting the persistence of strong magnetic fluctuationst. On the other hand, the gapped excitations in several compounds (NIO, EIO, TIO) were observed in inelastic neutron scattering experiments at 3.5 K, which has not been reported in other pyrochlores at such high temperature. Meanwhile, the hump of magnetic specific heat of all pyrochlore iridates moves to higher temperature comparing to that in titanates. These results strongly imply that the involvement of the magnetic Ir^{4+} enhances the quantum fluctuation of Ln^{3+} at high temperature. Our results reveal a way to realize the quantum spin dynamic at higher temperature.

In chapter 5, a comprehensive investigation on the defect-minimized metallic pyrochlore $Pr_2Ir_2O_7$ is presented. A detailed CEF analysis of Pr^{3+} in $Pr_2Ir_2O_7$ was shown based on the inelastic neutron scattering experiment. The result reveals that the Pr^{3+} in PIO exhibits strong easy-axis anisotropy along the local $\langle 1\ 1\ 1 \rangle$ direction with a reduced moment of 2.283 μ_B/Pr below 20 K. With a negative CW temperature, the system undergoes a magnetic transition from paramagnetic state to the 2I2O magnetic long-range order at 0.76 K. Via cold neutron inelastic scattering, we were able to observe the collective magnetic excitation of the 2I2O magnetic structure for the first time. At 60 mK, a broad gapped magnetic excitation with clear dispersion from the magnetic Brillouin Zone center appears around 0.35 meV. Furthermore, the excitation moves to high energies and becomes sharper with cooling below the 2I2O transition. These behaviors may be caused by the strong interplay between the 2I2O order of Pr^{3+} and the conduction electron of Ir^{4+} due to the sensitivity of the quadratic band touching close to the Fermi energy. Additionally, the summation of the ordered moment and the fluctuating moment of Pr^{3+} at 60 mK is in excellent agreement with the expect value of the CEF ground-doublet, suggesting that no static disordered static moment exists.

In Chapter 6, a detailed study of the magnetic ground state of the insulating $Nd_2Hf_2O_7$ is presented. Based on the inelastic neutron scattering experiments, the CEF ground doublet of Nd^{3+} in this compound has been determined as the expected "dipolar-octupolar" doublet with easy-axis single-ion anisotropy and a reduced moment 2.475(5) μ_B/Nd. Indicated by the specific heat anomaly at $T_N = 0.53$ K, the system undergoes a magnetic phase transition from

paramagnetic state to a magnetic long-range order with the AIAO configuration of Nd^{3+} determined by the polarized neutron scattering experiments. Our magnetic structure refinement at 0.09 K provides the more accurate ordered moment 1.415(13) μ_B/Nd that is smaller than the expected moment of the CEF ground doublet. Using inelastic neutron scattering, we observe the magnetic excitations that consists of a flat band mode centered at 0.1 meV, and a dispersive mode up to 0.23 meV. The magnetic excitation feature can be recovered according to the linear spin wave theory based on the XYZ model with $\tilde{J}_x = 0.096$ meV ; $\tilde{J}_y = 0.011$ meV and $\tilde{J}_z = -0.055$ meV . Additionally, our quantitative analysis of the inelastic neutron scattering results reveals that total moment sum rule is satisfied, which means that the summation of the static and dynamic magnetic moment keeps in constant and equals roughly to the expected total magnetic moment of Nd^{3+}. This conclusion provides a strong proof for the quantum magnetic moment fragmentation scenario in the Nd-based pyrochlore [178, 221].

7.2. Outlook

In order to understand the results of $Ln_2Ir_2O_7$, the molecular magnetic field approximation of the Ln-Ir interaction was introduced, however, the expected Zeeman splitting of the CEF ground doublet of Ln^{3+} has not been observed in either specific heat or inelastic neutron scattering. This simple model clearly has its limitations, since it largely ignores the detail of the interaction between Ln^{3+} and Ir^{4+} and the influence of the band structure formed by Ir^{4+} electrons. It has been recently evidenced by several experiments on single crystal samples EIO [238] and NIO [179] that the well documented "metal-to-insulator" transition in $Ln_2Ir_2O_7$ may actually be a metal-to-semimetal transition. Then the RKKY interaction mediated by the conduction electrons of Ir^{4+} may dominate the coupling between Ln^{3+}. Due to the band touching near Fermi surface, the RKKY interaction may exhibit specific temperature dependent behavior and leads to the ordering behavior of Ln^{3+} that looks like the induced ordering. On the other hand, the development of the spin correlations between localized Ln^{3+} electrons may also give a feedback on the band structure of Ir^{4+} electrons via Kondo coupling [137]. This scenario is very complicated, however, may be efficient for a unified explanation of the above experimental results. Moreover, most of the models applied on the Pr-based pyrochlore focus on the insulator case, in which the superexchange interaction between the pseudospin of Pr^{3+} is only taken into account. Theoretical

investigations involving the *f-d* electrons coupling based on metal or semimetal cases are also expected to understand the results of PIO.

The phase diagram of $Ln_2Ir_2O_7$ has shown a metal-semimetal transition between $Pr_2Ir_2O_7$ and $Nd_2Ir_2O_7$ at zero temperature. Meanwhile, the ordered state of Ln^{3+} changes from 2I2O to AIAO magnetic structure for Pr^{3+} and Nd^{3+}, respectively. A quantum criticality, in which the quantum phases transition from the nodal non-Fermi liquid to the AFM Weyl semimetal occurs, has been predicted in this range [136]. Indeed, the resistivity measurements on the series of $(Nd_xPr_{1-x})_2Ir_2O_7$ have revealed a zero-temperature metal-to-semimetal crossover with the critical point $x = 0.8$ [239]. It will be very interesting to investigate the quantum criticality and search for novel phases in this region via neutron scattering.

As discussed in previous chapters, one can realize the quantum spin ice phase by reducing the magnetic moment of Ln^{3+} and enhancing the quantum fluctuation. The Nd-based pyrochlore fulfills these requirements, however, most of the $Nd_2B_2O_7$ shows AIAO magnetic long-range order below 0.4 K. On the other hand, the QSI is also predicted in the phase diagram of the XYZ model for the dipolar-octupolar pseudospin-1/2. Thus, the application of external parameters, such as magnetic field, hydrostatic pressure and chemical pressure, may help to suppress the AIAO ordering and drive the system to the QSI phase. It has been reported recently that the application of the external field along the [1 1 1] axis on $Nd_2Zr_2O_7$ is able to create a dynamic kagome ice state [240]. It is worth to study the influence of the external parameters, such as pressure, magnetic field and chemical doping, on the $Nd_2B_2O_7$ and to search for the possible QSI phase in this system. Besides, the pressure or magnetic field can also be applied on our $Pr_2Ir_2O_7$ powder sample to suppress the 2I2O ordered state and achieve the metallic QSI phase.

Obtaining high-quality single crystal sample of $Ln_2Ir_2O_7$ is still a challenge. Up to now, only for very few compounds like $Pr_2Ir_2O_7$, $Nd_2Ir_2O_7$, $Eu_2Ir_2O_7$ and $Sm_2Ir_2O_7$ single crystals could be grown successfully by the flux method with KF flux. However, the size of these single crystals is around 0.5 mm, and they are too small to perform neutron scattering measurement. Due to the incongruent melting and decomposition of $Ln_2Ir_2O_7$, the floating zone method, which is often used for other pyrochlore compounds, is not suitable to grow crystals for these compounds. One way is to still improve the flux method. For example, replacing KF by other flux, such as KOH, CsCl or the mixture of KF and KOH, may provide a wide temperature range for crystal growth [241]. On the other hand, the vapor transport method maybe another way to achieve the single crystal growth of $Ln_2Ir_2O_7$. For example,

the single crystal of iridates Li_2IrO_3 has been obtained by an unconventional vapor transport method [242]. However, this method has not been used for the iridate-227 phases.

Appendices

A. Specific heat data analysis

Before performing neutron scattering measurements, the specific heat can provide a first insight into the investigated materials. For instance, the structural or the magnetic transition of solids usually induces a λ-shape peak in temperature dependent specific heat $C(T)$. The discrete energy levels, such as the crystal-field levels of magnetic ions in solids, contributes a broad hump in $C(T)$, which is so-called the Schottky anomaly. Additionally, the magnetic excitations in the conventional magnetic ordered compounds cause a power-law temperature dependence in $C(T)$. Moreover, the magnetic entropy S_{mag} obtained from the magnetic specific heat C_{mag} is often used to probe the degeneracy of the magnetic manifolds. This subsection is dedicated for the specific heat analysis to obtain the pure magnetic specific heat C_{mag} and the corresponding magnetic entropy S_{mag}. Then, several practices are presented as the supplement information of the main text.

A.1. Method

As many other physical properties, the specific heat can be defined in terms of other thermodynamic state variables. It can be written as the derivative of either the entropy, S or internal energy, E, as:

$$C_V = \left(\frac{\partial E}{\partial T}\right)_V = T\left(\frac{\partial S}{\partial T}\right)_V \tag{A.1}$$

V denotes the constant volume condition. It should be noted that the specific heat difference between constant pressure and constant volume for a solid sample could be ignored at low temperature. In the practical measurement on PPMS, the specific heat is carried out under the constant pressure condition.

In order to obtain the pure magnetic specific heat C_{mag}, the non-magnetic contributions from the lattice (and the conduction electrons in metal) C_{latt}, the crystal electric field C_{CEF} and the nucleus C_{nuc} have been subtracted from the measured data C_{exp}.

Lattice contribution [172]: At high temperature below melting point, the specific heat of the atomic vibration is expected to obey the classical Dulong-Petit law $C_{latt} = 3nR$, where

n is the number of the atoms per formula unit (f.u.) and R is the molar gas constant. The Dulong-Petit is a simple model, in which the motion of atoms in solid is assumed as a three-dimensional oscillator with the average internal energy $E = 3nRT$, giving rise to a constant specific heat $C_{latt} = \partial E / \partial T = 3nR$. At low temperature, the lattice vibration can be described by the quasi-particle, phonon, in the quantum mechanical treatment. The lattice specific heat is then approached as follows:

$$C_{latt}(T) = 3p_D R \left(\frac{T}{\theta_D}\right)^3 \int_0^{\theta_D/T} \frac{x^4 e^x}{(e^x - 1)^2} dx$$
$$+ R \sum_i p_{Ei} (\frac{T}{\theta_{Ei}})^2 R \frac{exp(\theta_{Ei}/T)}{(exp(\theta_{Ei}/T) - 1)^2} \tag{A.2}$$

The first term is based on Debye model accounting for the acoustic modes of phonons, while the second term is the expression of Einstein model associated to the optical modes of phonons. θ_D and θ_{Ei} are the so-called Debye and Einstein temperature, respectively. p_D and p_{Ei} are the weight factor for different phonon modes contributions. The constrain is $p_D = 3$ and $p_D + \sum_i p_{Ei} = 3n$. Depending on the number of the Einstein term, the Monte-Carlo method or the simulated annealing method is often used for the practical fitting of the experiment data. Instead, a simple estimation of C_{latt} below 100 K is the odd power-law:

$$C_{latt} = \gamma T + \beta T^3 + \delta T^5 \cdots \tag{A.3}$$

where the first term represents the conduction electrons contribution, other high order terms are the approximation of the phonon contribution. Then, the Debye temperature $\theta_D = (12\pi^4 nR/5\beta)^{1/3}$.

If the thermal dynamic of the lattice is out of the focus, the C_{latt} could be simply estimated by the measured data of a suitable nonmagnetic isostructural sample. For example, the measured specific heat C_{LHO} of $La_2Hf_2O_7$, which is a non-magnetic insulator pyrochlore, was used to estimate the C_{latt} of $Nd_2Hf_2O_7$. Before performing subtraction of C_{latt}, the temperature of C_{LHO} has to be re-scaled to [170, 243]:

$$T^* = \frac{T}{(M_{NHO}/M_{LHO})^{1/2}} \tag{A.4}$$

considering only the Debye model, $\theta_D \sim 1/M^{1/2}$, where the M_{NHO} and M_{LHO} are the formula mass of $Nd_2Hf_2O_7$ and $La_2Hf_2O_7$, respectively. Similarly, the specific heat of $Y_2Ir_2O_7$ is selected to estimate the lattice contribution of $Ln_2Ir_2O_7$ (Ln = rare-earth elements).

CEF contribution [172]: The degenerate electronic ground-state of a free ion in crystal is often split into several discrete energy states due to the crystal field interaction or Zeeman effect. These discrete energy states lead to a Schottky anomaly in the specific heat.

Considering a multi-level system in which n discrete states with degeneracies $g_1, g_2, g_3, \cdots g_n$ have energies $\varepsilon_1, \varepsilon_2, \varepsilon_3, \cdots \varepsilon_n$. The probability of the ith level being occupied is governed by the Boltzmann factor. Therefore, the average thermal energy at temperature T is:

$$E = \frac{\sum_{i=1}^{n} \varepsilon_i g_i e^{\left(-\frac{\varepsilon_i}{k_B T}\right)}}{\sum_{i=1}^{n} g_i e^{\left(-\frac{\varepsilon_i}{k_B T}\right)}} \tag{A.5}$$

The specific heat is then obtained by calculating dE/dT, as follow:

$$C_{Sch} = \frac{R}{Z^2} \left[Z \sum_{i=1}^{n} \left(\frac{\varepsilon_i}{k_B T}\right)^2 e^{\left(-\frac{\varepsilon_i}{k_B T}\right)} - \left\{ \sum_{i=1}^{n} \left(\frac{\varepsilon_i}{k_B T}\right) e^{\left(-\frac{\varepsilon_i}{k_B T}\right)} \right\}^2 \right] \tag{A.6}$$

where $Z = \sum_{i=1}^{n} e^{(-\varepsilon_i/k_B T)}$ is the partition function of the system. For a two-level system, the above expression becomes:

$$C_{Sch} = R \left(\frac{\Delta}{k_B T}\right)^2 \frac{(g_0/g_1)e^{\left(\frac{\Delta}{k_B T}\right)}}{\left[1 + (g_0/g_1)e^{\left(\frac{\Delta}{k_B T}\right)}\right]^2} \tag{A.7}$$

where Δ is the energy gap (in the unit meV) between ground state and first excited state. If $g_0 = g_1$, the C_{Sch} is characterized by a broad peak at an intermediate temperature $T_m \cong 0.4 \, \Delta/k_B$.

Nuclear contribution: The interaction between the effective field arising from the localized electrons and the nuclear magnetic moment of the nucleus, and that between the quadrupole moment of the nucleus and the electric field gradient (EFG), are called the hyperfine interactions. The degenerate nuclear state can be lifted by hyperfine interaction, leading to a nuclear Schottky anomaly at low temperature (usually below 2 K for rare-earth ions Ln^{3+}). In this thesis, the concerned temperature range (above 50 mK) only covers the right side of the nuclear specific heat from Ln^{3+}, except Ho^{3+}. Thus, Eq. (A.6) for the nuclear contribution could be simply approximated by the power-law [171]:

$$C_{nuc} \propto T^{-2} \tag{A.8}$$

Finally, one can obtain the magnetic specific heat and the corresponding magnetic entropy as follows:

$$C_{mag} = C_{exp} - C_{latt} - C_{CEF} - C_{nuc}$$

$$S_{mag} = \int_0^T \frac{C_{mag}}{T} dT \tag{A.9}$$
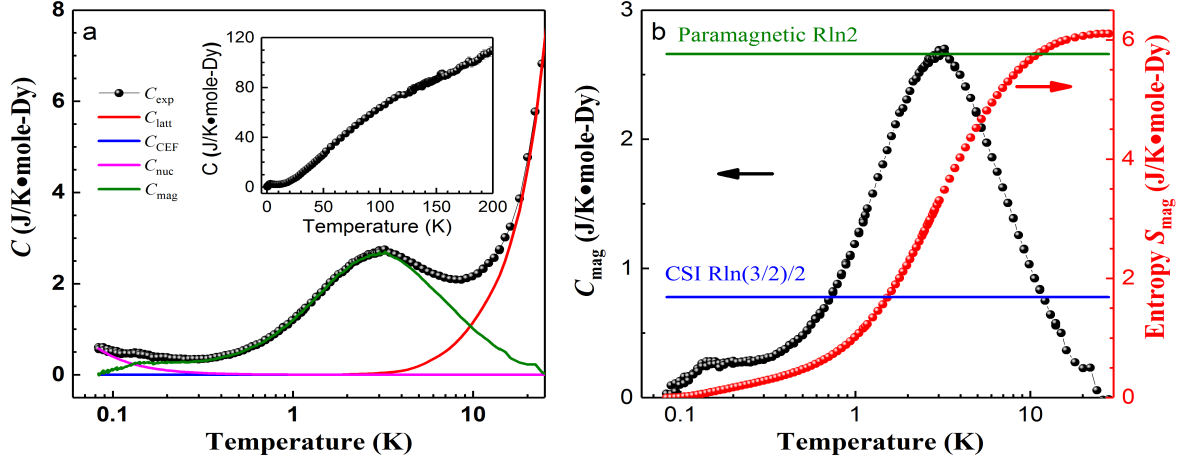
A.2.   Analysis of the low-temperature specific heat of Ln$_2$Ir$_2$O$_7$

The left panels of Appendix Figure A.1-5 show the analysis of the low-temperature specific heat of Ln$_2$Ir$_2$O$_7$ (Ln = Nd, Tb, Dy, Er and Yb). The lattice contribution C_{latt} was estimated according to Eq. (A.4) with Y$_2$Ir$_2$O$_7$ as the reference sample. The nuclear contribution C_{nuc} was fitted based on Eq. (A.8) with the constrain of zero magnetic specific heat at the lowest temperature. It should be noted that the estimation of C_{nuc} for Tb$_2$Ir$_2$O$_7$ is not very reliable. The Schottky anomaly of CEF, C_{CEF}, was calculated according to Eq. (A.6) within the CEF scheme of Ln^{3+}. The CEF scheme of Nd^{3+} was taken from the reported result in Ref [244]. The calculations of C_{CEF} for Tb$_2$Ir$_2$O$_7$, Dy$_2$Ir$_2$O$_7$, Er$_2$Ir$_2$O$_7$ and Yb$_2$Ir$_2$O$_7$ were considered the reported CEF results of their counterpart Tb$_2$Ti$_2$O$_7$ [35], Dy$_2$Ti$_2$O$_7$ [245], Er$_2$Sn$_2$O$_7$ [246] and Yb$_2$Ti$_2$O$_7$ [38]. As shown in purple lines, the C_{CEF} of Nd$_2$Ir$_2$O$_7$, Dy$_2$Ir$_2$O$_7$ and Yb$_2$Ir$_2$O$_7$ could be ignored below 25 K, as well as Er$_2$Ir$_2$O$_7$ below 10 K. This suggests a well-isolated CEF ground-state of the rare-earth ions. The obtained pure magnetic specific heat C_{mag} and the corresponding magnetic entropy are illustrated in the right panels of Appendix Figure A.1-5. The green line indicates the magnetic entropy of the paramagnetic state for a spin-1/2 system, $S_{mag} = R ln(2)$, while the blue line corresponds to the residual entropy of the classical spin-ice, $S_{mag} = \frac{R}{2} \ln\left(\frac{3}{2}\right)$. The C_{mag} of Nd$_2Ir_2O_7$ exhibits a λ-shape peak at 33 K, which is associated with the magnetic transition of the Ir^{4+} sublattice from paramagnetic state to the AIAO long-range order state. A unified feature of C_{mag} of these compounds is the broad hump at T_h = 5.0, 3.0 3.0 1.5 and 2.3 K for Nd$_2$Ir$_2$O$_7$ Tb$_2$Ir$_2$O$_7$, Dy$_2$Ir$_2$O$_7$, Er$_2$Ir$_2$O$_7$ and Yb$_2$Ir$_2$O$_7$, respectively. This relates to the development of short-rang order on the Ln^{3+} sublattice. Meanwhile, the obtained magnetic entropy completely releases in this process. The obtained S_{mag} approaches to the value of the parameter state for a spin-1/2 system at 20 K. Thus, no residual entropy associated to spin freezing process could be observed at lowest temperature in any of the compounds.
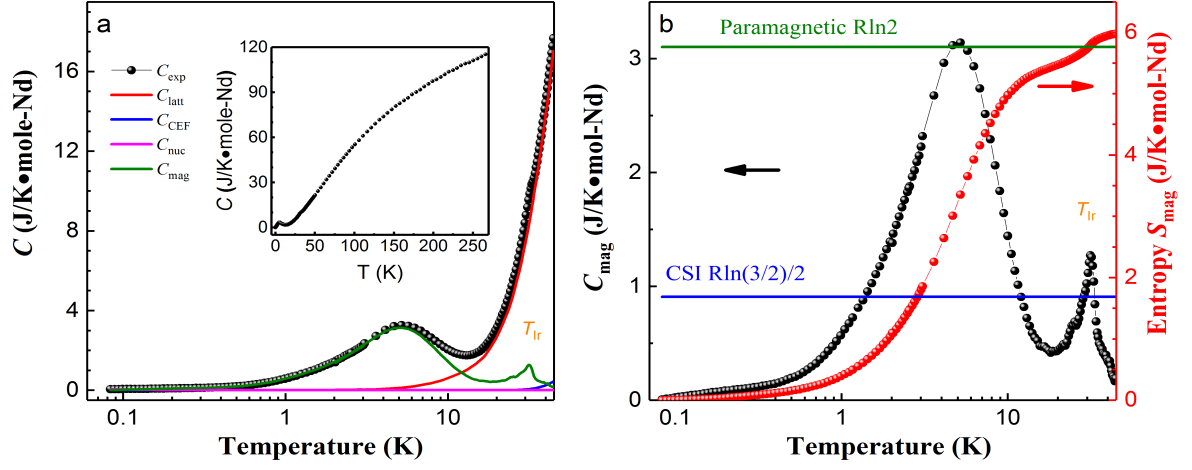
Appendix Figure A.1. (a) Analysis of the low-temperature specific heat of Nd$_2$Ir$_2$O$_7$. The insert shows the data from 0.1 to 270 K. (b) Obtained magnetic specific heat $C_{mag}(T)$ (black spheres) and the corresponding magnetic entropy $S_{mag}(T)$ (red spheres).
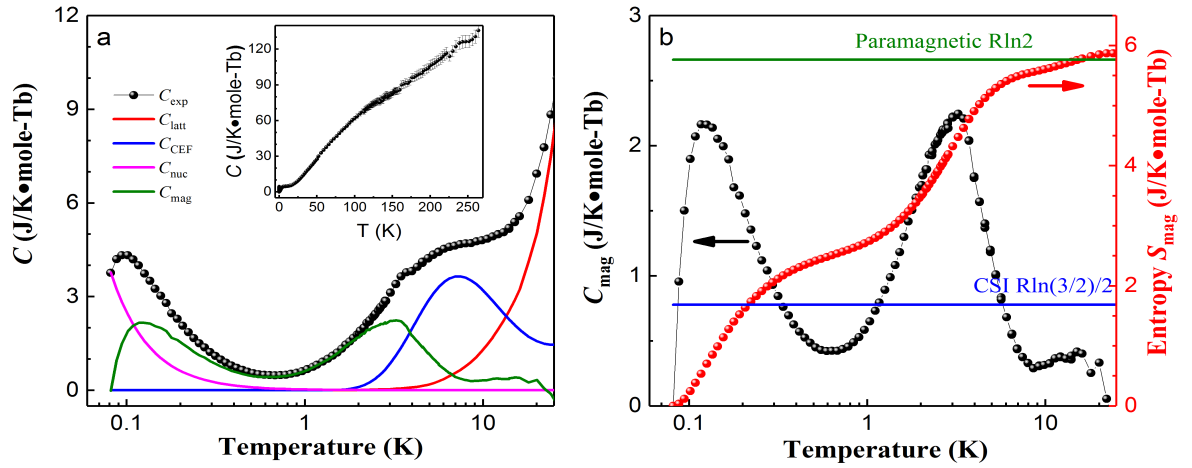
Appendix Figure A.2 (a) Analysis of the low-temperature specific heat of Tb$_2$Ir$_2$O$_7$. The insert shows the data from 0.1 to 270 K. (b) Obtained magnetic specific heat $C_{mag}(T)$ (black spheres) and the corresponding magnetic entropy $S_{mag}(T)$ (red spheres).

Appendix Figure A.3 (a) Analysis of the low-temperature specific heat of Dy₂Ir₂O₇. The insert shows the data from 0.1 to 200 K. (b) Obtained magnetic specific heat $C_{mag}(T)$ (black spheres) and the corresponding magnetic entropy $S_{mag}(T)$ (red spheres).
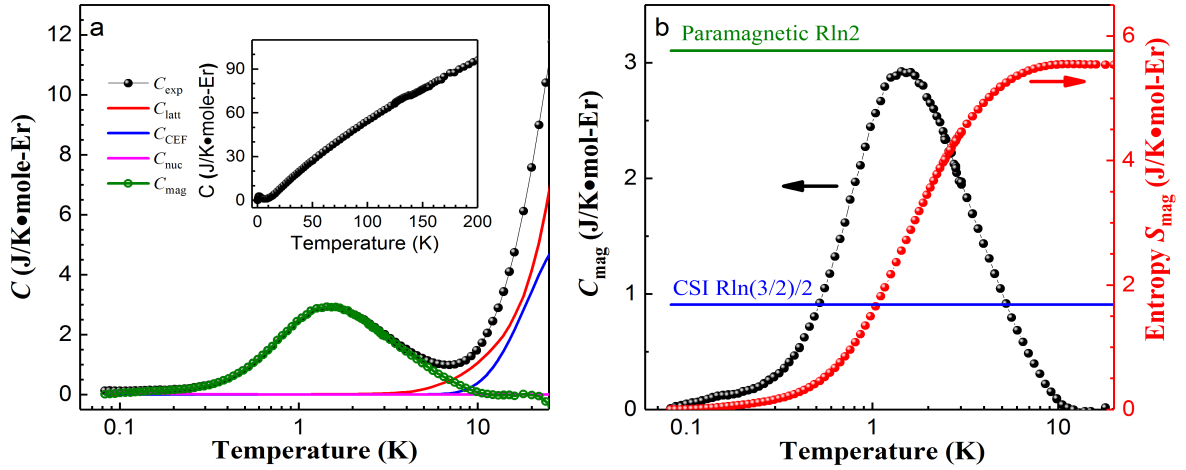
Appendix Figure A.4 (a) Analysis of the low-temperature specific heat of Er₂Ir₂O₇. The insert shows the data from 0.1 to 200 K. (b) Obtained magnetic specific heat $C_{mag}(T)$ (black spheres) and the corresponding magnetic entropy $S_{mag}(T)$ (red spheres).
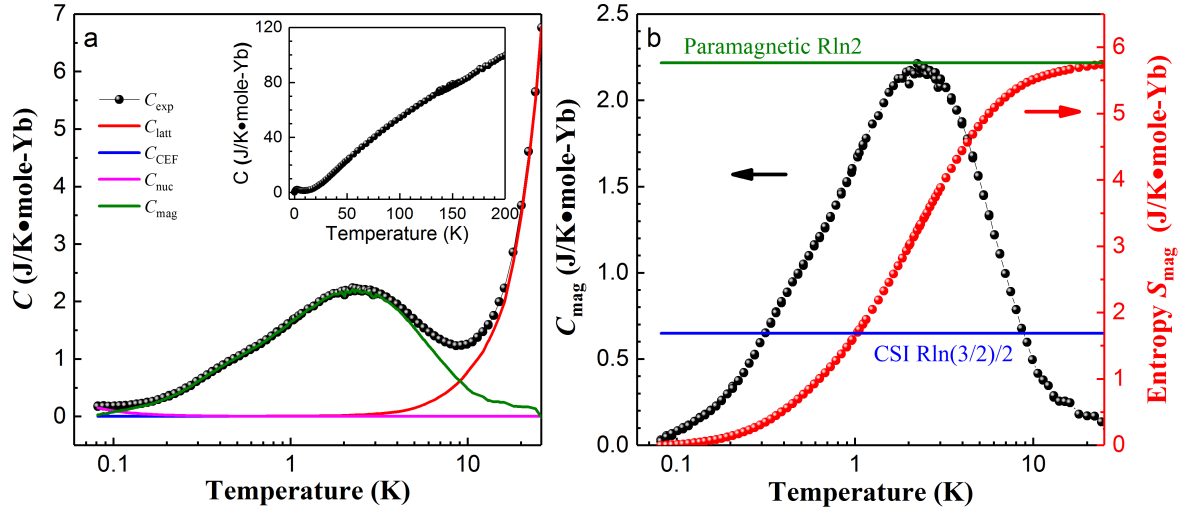
Appendix Figure A.5 (a) Analysis of the low-temperature specific heat of $Yb_2Ir_2O_7$. The insert shows the data from 0.1 to 200 K. (b) Obtained magnetic specific heat $C_{mag}(T)$ (black spheres) and the corresponding magnetic entropy $S_{mag}(T)$ (red spheres).

Appendix Table A.1 The CEF schemes of Ln^{3+} for the estimation of the Schottky anomaly in specific heat. The times of the energy denote the degeneracy of the corresponding CEF level.

Ln^{3+}	CEF scheme (meV)
Pr	[0, 0, 13, 60, 60]
Nd (NIO)	[0, 0, 26, 26]
Tb	[0, 0, 1.5, 1.5, 10.3, 16.1, 39.0, 39.0, 48.2, 48.8, 60.8, 60.8, 71.0]
Dy	[0, 0, 33, 33]
Er	[0, 0, 6, 6, 11, 11]
Yb	[0, 0, 76, 76]
Nd (NHO)	[0, 0, 24, 24]

B. Magnetic structure and diffraction pattern in pyrochlore

In this thesis, the irreducible representation (IR) analysis of space group is applied for magnetic structure determination. The principle of this method can be found in any textbook of crystallography. This section only presents the analysis results obtained from the software BASIREPS [151] and the corresponding magnetic NPD patterns. The pyrochlore compounds crystallize in the face-centered cubic lattice ($Fd\bar{3}m$ space group). The rare earth ions site at the 16d (1/2, 1/2, 1/2) position. Considering the propagation wavevector $\mathbf{k}$ = (0 0 0), the decomposition of the magnetic representation for the magnetic ions site is $\Gamma_{mag} = 1\Gamma_3^1 + 1\Gamma_5^2 + 1\Gamma_7^3 + 2\Gamma_9^3$, where the multiplicative factors represent the number of the times that the IRs occurs, and the dimensionality and the order of IRs are denoted as superscri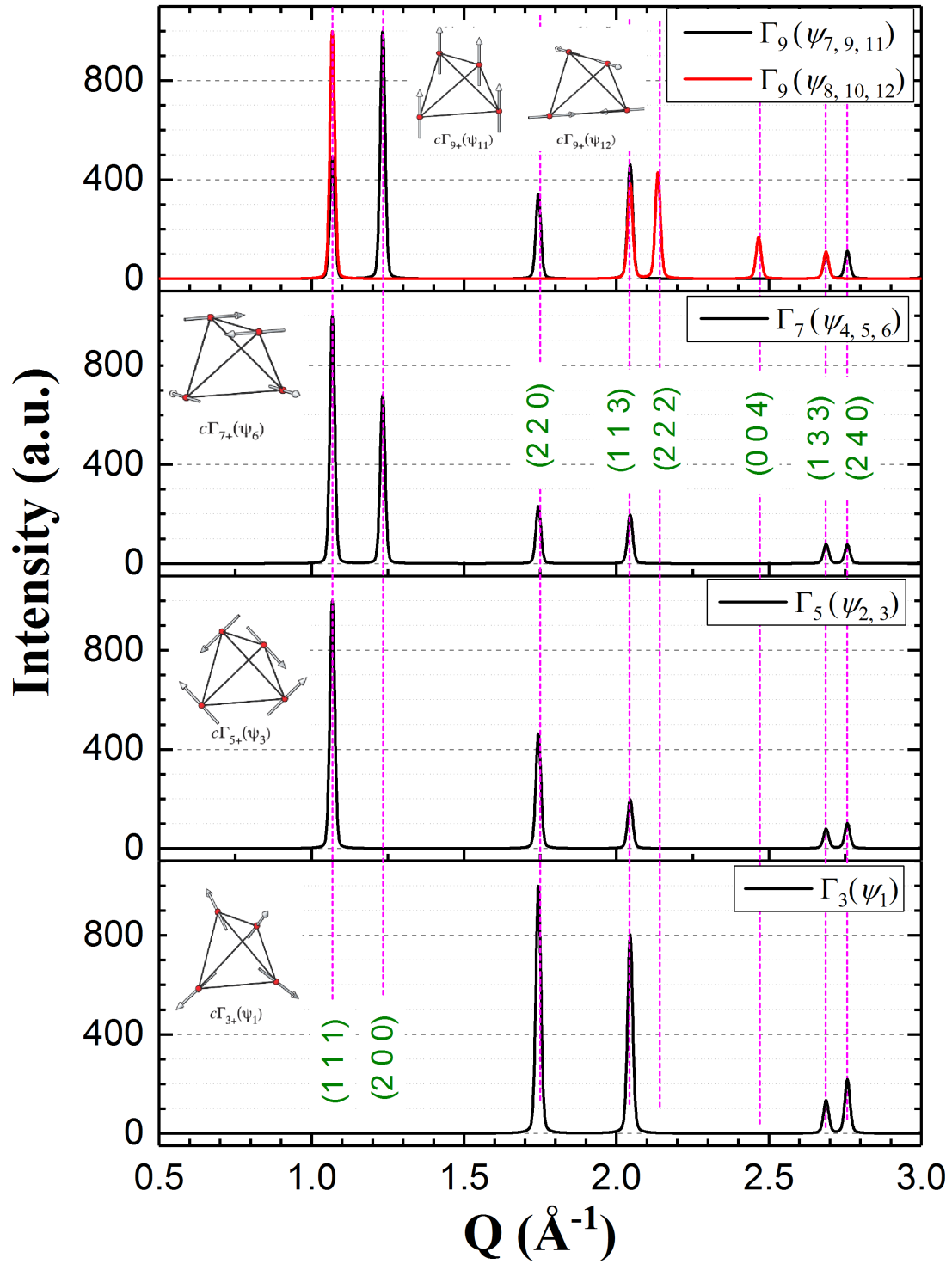pt and subscript. The IRs and the associated basis vectors (BVs) are listed in Appendix Table B.1. The simulated magnetic NPD patterns associated to each BVs are shown in Appendix Figure B.1

Appendix Table B.1 The BVs corresponding to each IR using the software BasIREPS. Note: the BVs are not normalized and Γ_9 is repeated twice.

IR	BV	(x, y, z)			$(-x+0.75, -y+0.25, z+0.5)$			$(-x+0.25, y+0.5, -z+0.75)$			$(x+0.5, -y+0.75, -z+0.25)$		
		m_x	m_y	m_z	m_x	m_y	m_z	m_x	m_y	m_z	m_x	m_y	m_z
Γ_3	ψ_1	1	1	1	-1	-1	1	-1	1	-1	1	-1	-1
Γ_5	ψ_2	1	$e^{\frac{4i\pi}{3}}$	$e^{\frac{2i\pi}{3}}$	-1	$e^{\frac{i\pi}{3}}$	$e^{\frac{2i\pi}{3}}$	-1	$e^{\frac{4i\pi}{3}}$	$e^{\frac{5i\pi}{3}}$	1	$e^{\frac{i\pi}{3}}$	$e^{\frac{5i\pi}{3}}$
	ψ_3	$e^{\frac{2i\pi}{3}}$	1	$e^{\frac{4i\pi}{3}}$	$e^{\frac{5i\pi}{3}}$	-1	$e^{\frac{4i\pi}{3}}$	$e^{\frac{5i\pi}{3}}$	1	$e^{\frac{i\pi}{3}}$	$e^{\frac{2i\pi}{3}}$	-1	$e^{\frac{i\pi}{3}}$
Γ_7	ψ_4	1	-1	0	-1	1	0	1	1	0	-1	-1	0
	ψ_5	0	1	-1	0	1	1	0	-1	-1	0	-1	1
	ψ_6	-1	0	1	-1	0	-1	1	0	-1	1	0	1
Γ_9	ψ_7	1	1	0	-1	-1	0	1	-1	0	-1	1	0
	ψ_8	0	0	1	0	0	1	0	0	1	0	0	1
	ψ_9	0	1	1	0	1	-1	0	-1	1	0	-1	-1
	ψ_{10}	1	0	0	1	0	0	1	0	0	1	0	0
	ψ_{11}	1	0	1	1	0	-1	-1	0	-1	-1	0	1
	ψ_{12}	0	1	0	0	1	0	0	1	0	0	1	0

Appendix Figure B.1 Simulated neutron diffraction patterns of magnetic peaks associated to different BVs. The corresponding magnetic structure in the unit of tetrahedral is shown in the insert. The cubic lattice constant is set to 10.19 Å during calculation

C. Absolute cross-section normalization of magnetic neutron scattering

Sometimes, obtaining the relative intensity in a neutron scattering experiment is sufficient, such as the Rietveld refinement of the neutron powder diffraction data. In this thesis, the quantitative analysis of the magnetic neutron scattering is used to examine the total moment sum rule. It is necessary to convert the magnetic scattering intensities to absolute units, i.e. in terms of magnet moments μ_B or spin (S) per site. The principle of this normalization process can be found in Ref [212,247,248]. This section presents a brief discussion of the absolute unit calibration and gives an example. The mentioned methods are specific for powder data.

C.1. Introduction

The neutron scattering intensity measured at the detector can be expressed as a convolution of the differential scattering cross-section $d^2\sigma/d\Omega dE$, which depends on the sample itself, and the instrument resolution function $R_{QE}(Q - Q', E - E')$, which is mainly determined by the instrument set-up:

$$\tilde{I}(Q,E) = C(E) \int dQ' dE' R_{QE}(Q - Q', E - E') \times \frac{d^2\sigma}{d\Omega dE'}(Q',E') \tag{C.1}$$

where $C(E)$ is the detector efficiency. The instrument resolution function is usually normalized to unity:

$$\int dQ' dE' R_{QE}(Q',E') = 1 \tag{C.2}$$

Making a necessary approximation to "decouple" the instrument resolution and the scattering response function, (C.1 can be approximated as

$$I_{raw}(Q,E) = R_0 \times \frac{k_i}{k_f} \frac{d^2\sigma}{d\Omega dE}(Q,E) \tag{C.3}$$

where $I_{raw}(Q,E)$ stands for the data obtained after standard data reduction, CR_0 is the resolution volume of the instrument. The task of the normalization is determining the resolution volume CR_0, as well as the sample molecular number N.

Generally, to obtain the resolution volume one could use the following reference cross sections: (i) standard sample incoherent elastic scattering (e.g., vanadium); (ii) sample incoherent elastic scattering; (iii) sample nuclear magnetic Bragg peaks; (iv) sample phonon scattering. Here we only discuss the first three methods, which are easily applied to powder

sample, because (iv) may introduce significant error due to the powder average effect of different phonon branches in powder sample.

C.2. Methods

(1) The incoherent elastic scattering of the experimental sample itself This is one of the most straight-forward methods to do absolute calibration. The cross section for the incoherent elastic scattering is quite simple:

$$\frac{d\sigma^{el}}{d\Omega_{inc}} = \frac{N}{4\pi} \sum_j \sigma_j^{inc} \exp(-2W_j) \tag{C.4}$$

where σ_j^{inc} is the incoherent neutron scattering cross section of the jth atom, and the summation is performed over all atoms in one molecule. According to (C.3, the energy integrated incoherent elastic scattering intensity

$$\int I_{raw}(Q,E)dE = \frac{N}{4\pi} \sum_j \sigma_j^{inc} \exp(-2W_j) \tag{C.5}$$

can be obtained by a numerical integration at a wave-vector transfer Q far away from any nuclear or magnetic Bragg peaks of the $I_{raw}(Q,E)$ data. Since $k_i = k_f$ in elastic scattering, we therefore can obtain the resolution volume:

$$CR_0 = \frac{4\pi \int I_{raw}(Q,E)dE}{N \sum_j \sigma_j^{inc} \exp(-2W_j)} \tag{C.6}$$

the Debye-Waller factor $\exp(-2W_j)$ can be assumed to unity at low Q, low temperature. Then, the intensity as function of Q and E can be normalized into the absolute unit barn/sr/f.u.

$$I(Q,E) = \frac{k_i}{k_f} \frac{d^2\sigma}{d\Omega dE}(Q,E) = \frac{I_{raw}(Q,E)}{CR_0} \tag{C.7}$$

here, the f.u. (formula unit) depends on the molecular number N. For example, the pyrochlore $Nd_2Hf_2O_7$, there are two Nd atoms per one molecule and 16 Nd atoms per simple cubic (s.c.) unit cell. If one wants to calibrate the intensity per Nd atom, then N = 1/2, the right side of Eq. (C.5) is $(2\times\sigma_{Nd}^{inc} + 2\times\sigma_{Hf}^{inc} + 7\times\sigma_O^{inc})/4\pi/2$.

(2) The incoherent elastic scattering of the standard sample Due to the relatively large spin-incoherent scattering cross section and nearly zero nuclear coherent scattering cross section, vanadium is a good solution as standard sample for normalization. The procedure is similar to the aforementioned normalization with the sample incoherent scattering. The masses and sizes of measured sample and vanadium sample in neutron beam have to be

considered. We assume the neutron beam flux B is uniformly distributed. The experimental sample was measured with the mass M_{sam} and the sectional area A_{sam} (illuminated in neutron beam), as well as the mass M_{vana} and the sectional area A_{vana} (illuminated in neutron beam) for the vanadium measurement. Then, Eq. (C.5) can be written as:

$$\int I_{raw}^{vana}(Q,E)dE = CR_0 \times BA_{vana} \times \frac{N_{vana}}{4\pi} \sigma_{vana}^{inc} \exp\left(-2W_{vana}\right) \tag{C.8}$$

for vanadium, where N_{vana} is the molecule number of vanadium, which can be obtained from M_{vana}.

$$I_{raw}^{sam}(Q,E) = CR_0 \times BA_{sam} \times N_{sam} \times \frac{k_i}{k_f} \frac{d^2\sigma}{d\Omega dE}(Q,E) \tag{C.9}$$

for experimental sample, where N_{sam} is the number of molecular of the sample, which can be obtained from M_{sam}. Here the double differential cross section $d^2\sigma/d\Omega dE$ should be set to per molecular. If both sample and vanadium data sets have been normalized to time or monitor counts, Eq. (C.7) has the follow expression

$$I(Q,E) = \frac{k_i}{k_f} \frac{d^2\sigma}{d\Omega dE}(Q,E) = \frac{I_{raw}^{sam}(Q,E) \cdot \sigma_{vana}^{inc}}{4\pi \int I_{raw}^{vana}(Q,E)dE} \times \frac{A_{vana}N_{vana}}{A_{sam}N_{sam}} \tag{C.10}$$

This method requires that the experimental sample and vanadium should be measured at the same condition, such as the shape and beam size.

(3) The nuclear or magnetic Bragg peaks of the sample This method is not suitable for single crystal due to the extinction in Bragg scattering and multiple scattering. Unlike the temperature dependent behavior of the magnetic Bragg peaks, the nuclear Bragg peak intensity usually keeps constant and is easy to handle for different temperature.

The Bragg scattering cross section for a powder sample takes the form [211]

$$\frac{d\sigma}{d\Omega} = N^* \sum_\tau \mathcal{I}(\tau)\delta(Q-\tau) \tag{C.11}$$

where the summation is over reciprocal lattice vectors, τ. The Q-integrated nuclear scattering intensity is

$$\mathcal{I}_{nuc}(\tau) = \frac{v^*}{4\pi\tau^2} \sum_{|\vec{\tau}'|=\tau} |F_{nuc}(\vec{\tau}')|^2 \tag{C.12}$$

where v^* is the volume of the reciprocal lattice unit cell and the structure factor is

$$F_{nuc}(\vec{Q}) = \sum_{\vec{d}} e^{-W_{\vec{d}}(\vec{Q})} b_{\vec{d}} \exp\left(i\vec{Q}\cdot\vec{d}\right) \tag{C.13}$$

For magnetic Bragg scattering the Q-integrated intensity is:

$$\mathcal{I}_{mag}(\tau) = r_0^2 \frac{v^*}{4\pi\tau^2} \sum_{|\vec{\tau}'|=\tau} \left|\frac{g}{2}f(\vec{\tau}')\right|^2 \left[\left|\vec{F}_{mag}(\vec{\tau}')\right|^2 \right.$$

$$\left. - \left|\hat{\tau}\cdot\vec{F}_{mag}(\vec{\tau}')\right|^2\right] \tag{C.14}$$

within the magnetic vector structure factor for a given spin configuration [249]

$$\vec{F}_{mag}(\vec{Q}) = \sum_{\vec{d}} e^{-W_{\vec{d}}(\vec{Q})}\vec{q}_d\langle\vec{S}_{\vec{d}}\rangle\exp(i\vec{Q}\cdot\vec{d}) \tag{C.15}$$

where $r_0^2 = (\frac{e^2\gamma}{m_ec})^2 = 0.2905$ barn, $\vec{q}_d = \vec{\mu}_{\vec{d}} - (\vec{k}\cdot\vec{\mu}_{\vec{d}})\vec{k}$ is the magnetic interaction vector, $\vec{k}$ is the unit vector parallel to the scattering vector, $\vec{\mu}_{\vec{d}}$ is the unit vector parallel to the ordered magnetic moment of the atom at position $\vec{d}$ with amplitude $\langle\vec{S}_{\vec{d}}\rangle$ in unit μ_B.

The Q-integrated intensity of nuclear Bragg peaks can be obtained by numerical integration or fitting of $I_{raw}(Q,E)$ in E and Q.

$$CR_0 = \frac{\iint I_{raw}(Q-\tau,E)dQdE}{\mathcal{I}_{nuc}} \tag{C.16}$$

the absolute intensity $I(Q,E)$ can obtain according to Eq. (C.7).

C.3.   Application for a real system

In practical measurement, one can use the reference sample such as vanadium to perform absolute unit calibration. However, the compounds including hafnium and iridium in this thesis are strong neutron absorbers. The self-attenuation correction has to be performed in the data reduction. On the other hand, the normalization with the spin-incoherent scattering cross section of vanadium is sometimes invalid. The normalization with the specific cross section of the sample itself has to be used, the so-called self-normalization.

For the data collected on the time-of-flight spectrometer IN6, LET and TOFTOF, one can use the nuclear Bragg peaks to perform the absolute unit calibration. Here is an example of powder $Nd_2Hf_2O_7$ data taken from IN6. As shown in Chapter 6, the diffraction patterns at different temperatures were obtained by integrating the spectra in the energy range from -0.3 to 0.3 meV, which is large enough to include all the elastic component. The Q-integrated intensity (named area) and the FWHM of each peak were carried out by a Gaussian profile fitting, as listed in Appendix Table C.1. Clearly, the area of the peak (2 2 0) and (1 1 3) increase at 57 mK due to the AIAO magnetic order of Nd^{3+} below $T_N = 535$ mK. In Appendix Table C.2, the theoretical intensities of nuclear and magnetic Bragg peaks were calculated according to Eq. (C.12) and Eq. (C.13). The m indicates the multiplicity of the peak. For the case of **k** = (0 0 0), the crystallographic unit cell and the magnetic unit cell are identical, as

well as the peak multiplicity. The nuclear structure factor and the squared magnetic structure factor were calculated in one simple cubic unit cell (s.c.) with lattice constant 10.52 Å. The Bragg peak intensities were normalized to per simple cubic cell and per Nd atom. The magnetic Bragg peak intensities were given with ordered moment 1 μ_B. Comparing with experimental and theoretical results of the nuclear Bragg peak (1 1 1), we obtain the normalization factor $CR_0 = \iint I_{bragg}^{obs}(Q - \tau, E)dQdE / \tilde{I}_{N-Nd}^{cal}(\tau) = 0.5846(323)$, giving rise to the systemic error 5.5%. applying $C\tilde{R}_0$ to Eq. (C.7), one can achieve the normalized inelastic neutron scattering intensity $I(Q, E)$ with the unit barn/sr/meV/Nd. Furthermore, the ordered magnetic moment of Nd^{3+} at T = 57 mK can be obtained according to $\mu_{order} = \sqrt{(I_{57mK}^{obs}(\tau) - I_{600mK}^{obs}(\tau) / (\tilde{I}_{M-Nd}^{cal}(\tau) \cdot NCR_0))} = 1.474(12) \; \mu_B$, in agreement with the result 1.523(22) μ_B according to Fullprof refinements within the error. This also is a cross check for the method and equations given above, as well as our MATLAB code. Another application of the $I(Q, E)$ is to estimate the fluctuating magnetic moment by calculating the spectra weight in a sufficient Q and E range [234,243]:

$$\delta m^2 = \mu_B^2 \frac{\iint Q^2 6I(Q, E)/|r_0 f(Q)|^2 dQdE}{\int Q^2 dQ} \tag{C.17}$$

where $f(Q)$ is the magnetic form factor of the corresponding magnetic ion.

Appendix Table C.1 The experimental results of Bragg peaks fitting. The units of the area and FWHM are arbitrary unit and Å^{-1}, respectively.

$\vec{\tau}$	Q^{obs}	I_{57mK}^{obs}		I_{600mK}^{obs}		I_{10K}^{obs}	
h k l	Å^{-1}	Area	FWHM	Area	FWHM	Area	FWHM
1 1 1	1.036	0.0167(5)	0.0255(9)	0.0150(5)	0.0262(11)	0.0155(6)	0.0265(10)
2 2 0	1.682	0.0451(5)	0.0209(3)	0.0108(5)	0.0205(10)	0.0114(5)	0.0218(11)
1 1 3	1.979	0.0910(5)	0.0196(2)	0.0605(5)	0.0199(2)	0.0619(5)	0.0201(2)

Appendix Table C.2 The calculated results of the nuclear and the magnetic Bragg peaks. The m indicates the multiplicity of peaks.

			Nuclear Contribution			Magnetic Contribution		
$\vec{\tau}$	m	Q^{cal}	F_N^{cal}	$\tilde{I}_N^{cal}/cell$	$\tilde{I}_N^{cal}/Nd$	$\left\|F_{M\perp}^{cal}\right\|^2$	$\tilde{I}_M^{cal}/cell$	$\tilde{I}_M^{cal}/Nd$
h k l		Å^{-1}	fm	barn/s.c.	barn/Nd	barn	barn/s.c./ μ_B^2	barn/Nd/ μ_B^2
1 1 1	8	1.035	-18.442	0.43105	0.02694	-	-	-
2 2 0	12	1.690	21.898	0.34187	0.02137	5.6607	0.40356	0.02522
1 1 3	24	1.981	45.898	2.18452	0.13653	3.9770	0.41241	0.02578

D. Equivalence of the fitting functions for INS data [148,235,250]

The signals of the inelastic neutron scattering and the quasielastic neutron scattering usually have a Lorentzian shape modified by the detailed balance factor. The fitting of the signals provides useful information, such as the peak position and FWHM, for further discussion. However, researchers somehow use different named functions to perform fitting process, which may confuse the readers. This section will explain the equivalence of the used fitting functions and reveal the relation of the fitting parameter among different functions.

The standard Lorentzian function is:

$$L(x) = \frac{2A}{\pi} \frac{w}{4(x - x_c)^2 + w^2} = \frac{A}{\pi} \frac{\Gamma_l}{(x - x_c)^2 + \Gamma_l^2} \tag{D.1}$$

where the w is the full-width at half maximum (FWHM) of the peak, $\Gamma_l = w/2$, x_c is the peak position, and A is the area (or integrated intensity) of the peak. The amplitude (or height) of the peak is $H = 2 * A/(\pi * w)$.

For the quasielastic neutron scattering of magnetic systems, the dynamic structure factor $S(Q, \omega, T)$, which is proportional to the imaginary part of the generalized susceptibility χ'', can be generally expressed as:

$$S(Q, \omega, T) = \hbar\omega(1 - \exp(-\hbar\omega/k_B T))^{-1} \cdot \chi''(Q, \omega, T) \tag{D.2}$$

where $(1 - \exp(-\hbar\omega/k_B T))^{-1}$ is the detailed balance factor standing for the difference in the scattering function of the neutron energy gain and loss side due to the thermal population. $\chi''(Q, \omega, T)$ is the generalized susceptibility taken as a Lorentzian-shaped quasielastic line with width Γ at sufficiently high temperature:

$$\chi''(Q, \omega, T) = \chi_0(Q, T) \frac{\Gamma_{QENS}(Q, T)}{\omega^2 + \Gamma_{QENS}^2(Q, T)} \tag{D.3}$$

The dynamic structure factor for quasielastic neutron scattering $S(E)$ at constant Q can be well described by a single Lorentzian as follow:

$$S(E) = \chi_0(T) \frac{\Gamma_{QENS}(T)}{E^2 + \Gamma_{QENS}^2(Q, T)} \cdot \frac{E}{1 - \exp(-E/k_B T)} \tag{D.4}$$

comparing with the Lorentzian function Eq. (D.1), one can obtain $\Gamma_{QENS} = w/2$ and $\chi_0 = A/\pi$.

For the case of inelastic neutron scattering, for example due to the intrinsic excitations of phonons or magnons in the sample, one can observe Lorentzian shape peaks appear in pair in both positive and negative energy side. One of the often-used fitting function for the dynamic structure factor is the damped harmonic oscillator function (DHO):

$$S(Q,E,T) = \frac{A_{DHO}E\Gamma_{DHO}}{(E^2 - E_{DHO}^2)^2 + (E\Gamma_{DHO})^2} \cdot \frac{1}{1 - \exp(-E/k_BT)} \tag{D.5}$$

where E_{DHO} is the renormalized excitation energy, A_{DHO} is the oscillator strength and Γ_{DHO} is the linewidth of the excitation. By using the relations $\Gamma_{DHO} = 2\Gamma_q$ and $E_{DHO}^2 = E_q^2 + \Gamma_q^2$, the DHO function can convert to double Lorentzian function form:

$$S_l(Q,E,T) = \frac{A_l}{\pi}\left[\frac{\Gamma_q}{\left(E - E_q\right)^2 + \Gamma_q{}^2} - \frac{\Gamma_q}{\left(E + E_q\right)^2 + \Gamma_q{}^2}\right]$$
$$\cdot \frac{1}{1 - \exp(-E/k_BT)} \tag{D.6}$$

where $A_l = \pi A_{DHO}/(2E_q)$ is the peak area of Lorentzian function, one can observe the peaks at $\pm E_q$ with FWHM of $2\Gamma_q$ or Γ_{DHO}.

The double Lorentzian function can be decomposed into two parts according the energy sign. In the bracket of the double Lorentzian function Eq. (D.6), the first term represents the neutron energy loss part, and is always positive (blue line in Appendix Figure D.1 (a)). The second term stands for the neutron energy gain part, which is always negative (red line in Appendix Figure D.1 (b)). This makes sense because the imaginary susceptibility χ'' is an odd function of energy. The detailed balance factor also changes sign from negative to positive energy (olive curve in Appendix Figure D.1 (a)). This leads to the dynamic structure factor being always positive. The summation of two parts gives an identical profile of the DHO function (Appendix Figure D.1 (b)). It should be noted that the detailed balance factor goes to infinite at the energy close to zero. The fitting process near zero energy should be done very careful.
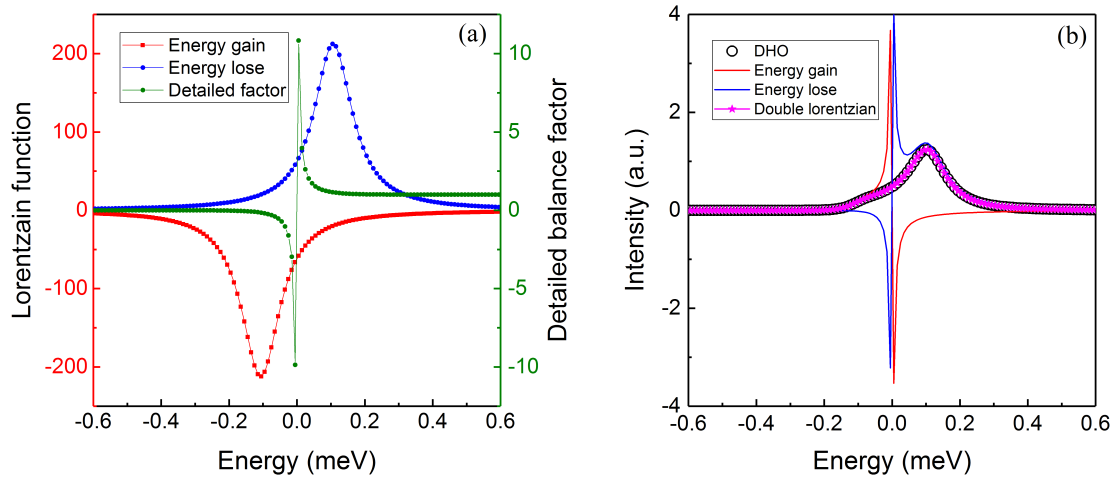
Appendix Figure D.1 (a) separated double Lorentzian function profiles in neutron energy gain (red curve) and energy lose (blue curve), and the detailed balance factor (olive) behavior in two energy part. (b) functions profiles: DHO function (black circles), double Lorentzian function multiplied by detailed balance factor (Magenta line with star symbols) and its neutron energy gain part (red line) and neutron energy loss part (blue).

E. TOFTOF results of Nd₂Hf₂O₇
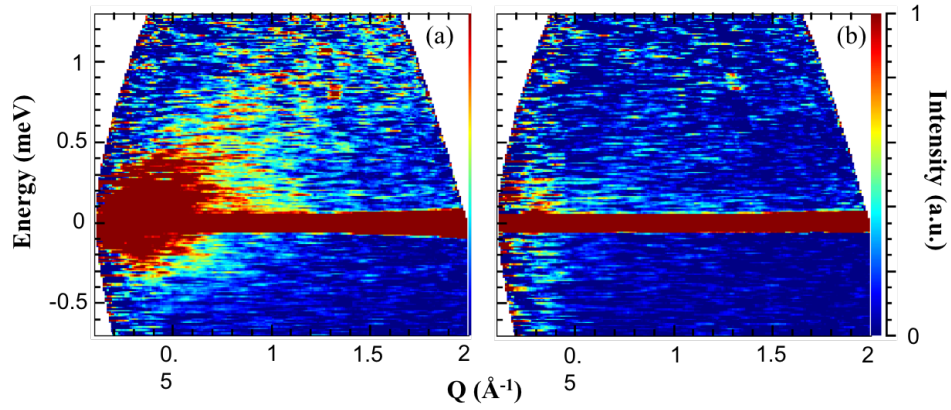
Appendix Figure E.1 INS results of the empty Cu container taken from TOFTOF with different He gas pressure in cryostat, (a) 25 mbar and (b) 2~3 mbar at 3.5 K.
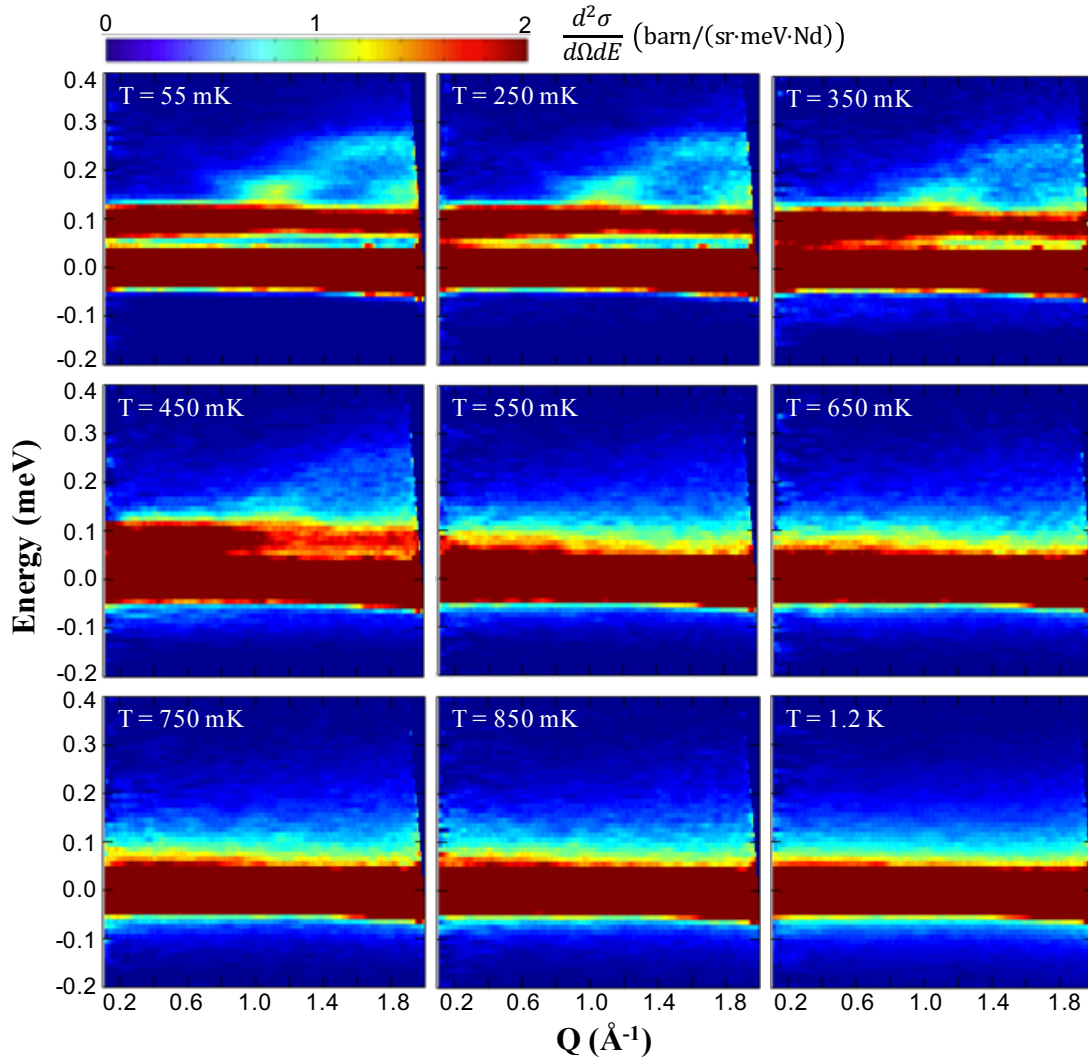
Appendix Figure E.2 Temperature dependence of the inelastic neutron scattering spectra of the powder Nd₂Hr₂O₇. The wavelength of the incident beam is 6 Å.
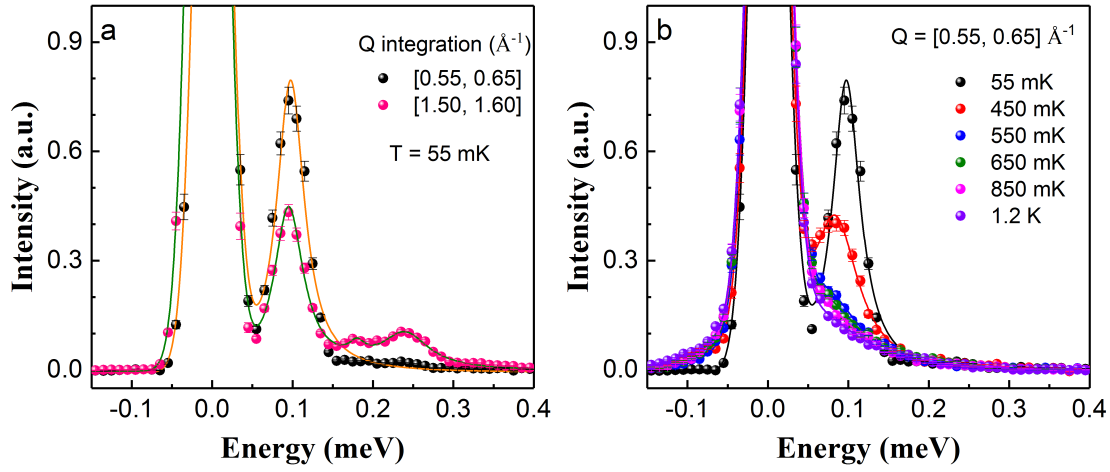
Appendix Figure E.3 (a) The DHO function fitted results of the spectra at 55 mK for the constant Q = 0.6 and 1.55 Å^{-1}. (b) Temperature dependence of the spectra at constant Q = 0.6 Å^{-1}.
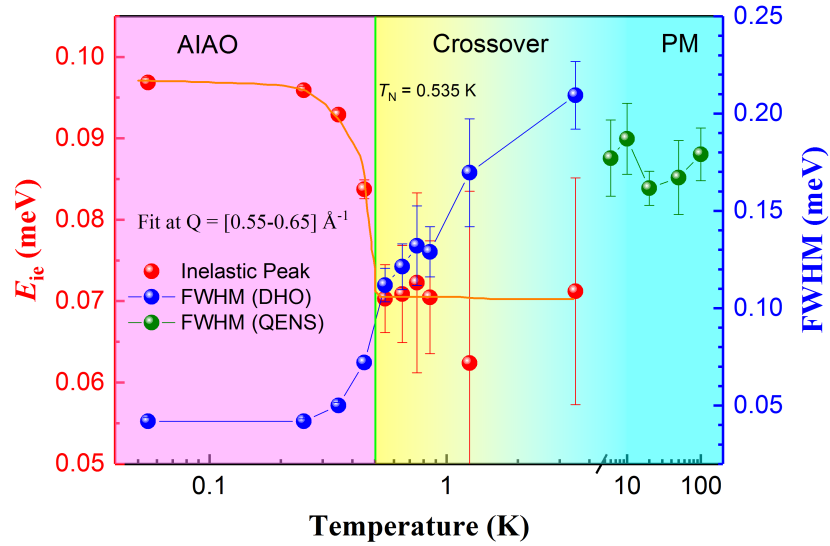
Appendix Figure E.4 Temperature dependence of the flat band position and the FWHM obtained by the fitting at constant Q = 0.6 Å^{-1}. The fitting functions could be found in Appendix D.

F. Examples of the PCR file for the Rietveld refinement by Fullprof

F.1.   Unpolarized neutron diffraction

```
COMM Refinement of Nd2Hf2O7 powder neutron
! Current global Chi2 (Bragg contrib.) =      1.167
! Files => DAT-file: Nd2Hf2O7.dat,  PCR-file: NHO_neutron_Npr7_ADP
!Job Npr Nph Nba Nex Nsc Nor Dum Iwg Ilo Ias Res Ste Nre Cry Uni Cor Opt Aut
   1  7  1 26  2  0  0  0  0  0  0  0  0  0  0  0  0  0  1
!
!Ipr Ppl Ioc Mat Pcr Ls1 Ls2 Ls3 NLI Prf Ins Rpa Sym Hkl Fou Sho Ana
   0  0  1  0  1  0  4  0  0  3 10  1  0  0  0  0  0
!
! Lambda1 Lambda2    Ratio    Bkpos    Wdt    Cthm     muR   AsyLim  Rpolarz  2nd-muR -> Patt# 1
 1.548320 1.548320 1.00000   10.000 40.0000 0.0000 0.3441 160.00   0.0000 0.0000
!
!NCY  Eps  R_at R_an R_pr R_gl     Thmin       Step     Thmax    PSD    Sent0
 10 0.10  1.00  1.00  1.00  1.00     0.9500  0.050019  151.9000  0.000   0.000
!
!2Theta/TOF/E(Kev)  Background  for Pattern#  1
       4.4524     5556.2837        0.00
       8.0833     3762.6165        0.00
      11.5357     2881.3640        0.00
      14.7500     2353.0837        0.00
      20.4345     1893.8644        0.00
      23.6786     1677.5648        0.00
      31.0680     1400.0378        0.00
      39.2313     1224.2581        0.00
      46.9796     1113.3431        0.00
      52.5918     1065.2941        0.00
      58.4626     1040.9934        0.00
      66.3878     1016.9235        0.00
      69.3129     1024.9980        0.00
      74.4940     1022.6277        0.00
      82.0536     1009.7409        0.00
      84.4345     1011.0252        0.00
      88.5714      996.8884       0.00
      94.1497      994.8542       0.00
     101.8027     1038.1161        0.00
     109.0119     1080.9722        0.00
     114.3988     1010.4091        0.00
     125.2313     1130.7930        0.00
     130.6735     1116.0804        0.00
     139.1072     1175.5215        0.00
     147.4762     1184.4120        0.00
     150.9456     1199.7860        0.00
!
! Excluded regions (LowT  HighT) for Pattern#  1
      0.00      5.00
    150.00    180.00
!
!
    18   !Number of refined parameters
!
! Zero   Code   SyCos   Code  SySin   Code  Lambda    Code MORE ->Patt# 1
 -0.04506  21.0 0.00000   0.0 0.00000   0.0 0.000000   0.00  0
!-------------------------------------------------------------------------------
! Data for PHASE number:  1  ==> Current R_Bragg for Pattern#  1:    2.75
!-------------------------------------------------------------------------------
pyrochlore
```

```
!
!Nat Dis Ang Pr1 Pr2 Pr3 Jbt Irf Isy Str Furth     ATZ    Nvk Npr More
   4  0  0 0.0 0.0 1.0  0  0  0  0  0   3490356.500  0  7  0
!
!
F d -3 m              <--Space group symbol
!Atom  Typ     X      Y      Z     Biso     Occ    In Fin N_t Spc /Codes
!  beta11 beta22 beta33 beta12 beta13 beta23 /Codes
Nd1   Nd    0.50000 0.50000 0.50000 0.00000  2.00000  0  0  2   0
            0.00    0.00    0.00    0.00     0.00
     0.00067  0.00067  0.00067 -0.00008 -0.00008 -0.00008
      141.00  141.00  141.00  171.00  171.00  171.00
Hf1   Hf    0.00000 0.00000 0.00000 0.00000  2.00000  0  0  2   0
            0.00    0.00    0.00    0.00     0.00
     0.00070  0.00070  0.00070  0.00010  0.00010  0.00010
      121.00  121.00  121.00  181.00  181.00  181.00
O1    O     0.33363 0.12500 0.12500 0.00000  6.00000  0  0  2   0
            0.00    0.00    0.00    0.00     0.00
     0.00151  0.00099  0.00099  0.00000  0.00000  0.00042
      131.00  161.00  161.00   0.00    0.00    151.00
O2    O     0.37500 0.37500 0.37500 0.00000  1.00000  0  0  2   0
            0.00    0.00    0.00    0.00     0.00
     0.00116  0.00116  0.00116  0.00000  0.00000  0.00000
       41.00   41.00   41.00   0.00    0.00     0.00
!-------> Profile Parameters for Pattern #  1
! Scale     Shape1    Bov     Str1    Str2    Str3   Strain-Model
 0.20468E-03  0.00000  0.00000  0.00000  0.00000  0.00000     0
   11.00000   0.000    0.000    0.000    0.000    0.000
!   U      V      W      X      Y     GauSiz  LorSiz Size-Model
  0.030704 -0.049776  0.108069  0.044869  0.000000  0.000000  0.000000   0
   51.000   61.000   71.000   81.000    0.000    0.000    0.000
!   a      b      c     alpha    beta    gamma     #Cell Info
 10.646323 10.646323 10.646323 90.000000 90.000000 90.000000
 31.00000 31.00000 31.00000  0.00000  0.00000  0.00000
! Pref1   Pref2    Asy1    Asy2    Asy3    Asy4    S_L    D_L
 0.00000 0.00000 0.20271 0.02105 -0.30659 0.00000 0.00000 0.00000
   0.00    0.00   91.00  101.00  111.00    0.00    0.00    0.00
! 2Th1/TOF1   2Th2/TOF2  Pattern to plot
    5.000   150.000     1
```

F.2. Polarized neutron diffraction (nuclear coherent scattering)

```
COMM Structure Refinement of Nd2Hf2O7 powder NPD at DNS
! Current global Chi2 (Bragg contrib.) =     69.91
! Files => DAT-file: NHO_89mK_nuc.dat,  PCR-file: NHO_89mK_ZFC_nuc
!Job Npr Nph Nba Nex Nsc Nor Dum Iwg Ilo Ias Res Ste Nre Cry Uni Cor Opt Aut
   1  0  1 14  2  0  0  0  0  0  0  0  0  0  0  0  0  0  1
!
!Ipr Ppl Ioc Mat Pcr Ls1 Ls2 Ls3 NLI Prf Ins Rpa Sym Hkl Fou Sho Ana
   0  0  1  0  1  1  4  0  0  3 10 -1  0  1  0  0  0
!
! Lambda1 Lambda2  Ratio  Bkpos   Wdt  Cthm   muR  AsyLim  Rpolarz 2nd-muR -> Patt# 1
 4.200000 4.200000 0.00000  40.000 4.0000 0.0000 0.0000 127.00   0.0000 0.0000
!
!NCY Eps R_at R_an R_pr R_gl  Thmin    Step    Thmax    PSD   Sent0
 20 0.10 1.00 1.00 1.00 1.00   13.0000 0.502252 124.5000 0.000 0.000
!
!2Theta/TOF/E(Kev)  Background  for Pattern#  1
     18.0000     0.2663     0.00
     25.5000     0.2184     0.00
```

```
      29.0000      0.2102      0.00
      34.5000      0.2284      0.00
      46.0000      0.2241      0.00
      48.5000      0.2268      0.00
      56.0000      0.2452      0.00
      63.5000      0.2772      0.00
      77.0000      0.3706      0.00
      92.5000      0.3188      0.00
     100.5000      0.3193      0.00
     107.5000      0.3025      0.00
     111.0000      0.2746      0.00
     123.0000      0.3970      0.00
!
! Excluded regions (LowT  HighT) for Pattern#  1
      0.00      8.50
    122.60    180.00
!
!
      5    !Number of refined parameters
!
! Zero   Code  SyCos   Code  SySin   Code  Lambda    Code MORE ->Patt# 1
 -0.80784  11.0 0.00000   0.0 0.00000   0.0 0.000000   0.00 0
!-------------------------------------------------------------------------------
! Data for PHASE number:   1  ==> Current R_Bragg for Pattern#  1:    3.62
!-------------------------------------------------------------------------------
pyrochlore
!
!Nat Dis Ang Pr1 Pr2 Pr3 Jbt Irf Isy Str Furth     ATZ    Nvk Npr More
   4  0  0 0.0 0.0 1.0  0  0  0  0  0   6059.208  0  0  0
!
!
F d -3 m              <--Space group symbol
!Atom Typ    X      Y      Z      Biso     Occ    In Fin N_t Spc /Codes
Nd1  Nd     0.50000 0.50000 0.50000 0.00000  0.08333  0  0  0  0
          0.00    0.00    0.00    0.00    0.00
Hf1  Hf     0.00000 0.00000 0.00000 0.00000  0.08333  0  0  0  0
          0.00    0.00    0.00    0.00    0.00
O1   O      0.33646 0.12500 0.12500 0.00000  0.25000  0  0  0  0
         41.00    0.00    0.00    0.00    0.00
O2   O      0.37500 0.37500 0.37500 0.00000  0.04167  0  0  0  0
          0.00    0.00    0.00    0.00    0.00
!-------> Profile Parameters for Pattern #  1
! Scale    Shape1    Bov    Str1    Str2    Str3  Strain-Model
 0.32749E-02  0.00000  0.00000  0.00000  0.00000  0.00000     0
   51.00000   0.000   0.000   0.000   0.000   0.000
!  U      V      W      X      Y     GauSiz  LorSiz Size-Model
  7.799441 -9.781798  9.338505  0.000000  0.000000  0.000000  0.000000  0
   0.000    0.000   31.000   0.000   0.000   0.000   0.000
!  a      b      c     alpha   beta   gamma    #Cell Info
 10.603503 10.603503 10.603503 90.000000 90.000000 90.000000
 21.00000 21.00000 21.00000  0.00000  0.00000  0.00000
! Pref1   Pref2   Asy1   Asy2   Asy3   Asy4
 0.00000 0.00000 0.00000 0.00000 0.00000 0.00000
   0.00    0.00    0.00    0.00    0.00    0.00
! 2Th1/TOF1   2Th2/TOF2  Pattern to plot
    18.540    121.520     1
```

F.3.   Polarized neutron diffraction (magnetic scattering)

COMM Magnetic structure Refinement of Nd2Hf2O7 powder NPD at DNS

! Current global Chi2 (Bragg contrib.) =   4.572

! Files => DAT-file: NHO_89mK_mag.dat, PCR-file: NHO_89mK_ZFC_mag

!Job Npr Nph Nba Nex Nsc Nor Dum Iwg Ilo Ias Res Ste Nre Cry Uni Cor Opt Aut

  1 0 1 9 2 0 0 0 0 0 0 0 0 0 0 0 0 0 0 1

!

!Ipr Ppl Ioc Mat Pcr Ls1 Ls2 Ls3 NLI Prf Ins Rpa Sym Hkl Fou Sho Ana

  0 0 1 0 1 1 4 0 0 3 10 1 0 1 0 0 0

!

! Lambda1 Lambda2 Ratio Bkpos Wdt Cthm   muR AsyLim Rpolarz 2nd-muR -> Patt# 1

 4.200000 4.200000 0.00000 40.000 4.0000 0.0000 0.0000 127.00   0.0000 0.0000

!

!NCY Eps R_at R_an R_pr R_gl   Thmin   Step   Thmax   PSD   Sent0

 20 0.10 1.00 1.00 1.00 1.00   13.0000 0.502252 124.5000 0.000 0.000

!

!2Theta/TOF/E(Kev) Background for Pattern# 1

      11.0000   0.0643   0.00

      22.5000   0.0804   0.00

      31.5000   0.0776   0.00

      40.5000   0.0772   0.00

      48.5000   0.0733   0.00

      62.0100   0.0707   0.00

      97.0100   0.0708   0.00

     106.5000   0.0691   0.00

     112.0100   0.0629   0.00

!

! Excluded regions (LowT HighT) for Pattern# 1

     0.00   7.00

   127.00   180.00

!

!

    1   !Number of refined parameters

!

! Zero   Code SyCos Code SySin Code Lambda   Code MORE ->Patt# 1

 -0.80784   0.0 0.00000   0.0 0.00000   0.0 0.000000   0.00 0

!---

! Data for PHASE number: 1 ==> Current R_Bragg for Pattern# 1:   21.35

!---

PIO Magnetic phase

!

!Nat Dis Mom Pr1 Pr2 Pr3 Jbt Irf Isy Str Furth   ATZ   Nvk Npr More

   1   0   0 0.0 0.0 1.0 1 -1 -2   0   0   0.000   1   0   0

!

!

F -1   <--Space group symbol for hkl generation

! Nsym   Cen Laue Ireps N_Bas

    4   1   1   -1   1

! Real(0)-Imaginary(1) indicator for Ci

  0

!

SYMM x,y,z

BASR 1 1 1

BASI 0 0 0

SYMM -x+3/4,-y+5/4,z-1/2

BASR -1 -1 1

BASI 0 0 0

SYMM -x+5/4,y-1/2,-z+3/4

BASR -1 1 -1

BASI 0 0 0

SYMM x-1/2,-y+3/4,-z+5/4

BASR 1 -1 -1

BASI 0 0 0

!

!Atom Typ Mag Vek X   Y   Z   Biso Occ   C1   C2   C3

!   C4   C5   C6   C7   C8   C9   MagPh

Nd1   JND3 1 1 0.50000 0.50000 0.50000 0.00000 1.00000 0.817 0.000 0.000

               0.00   0.00   0.00   0.00   0.00 11.00   0.00   0.00

   0.000   0.000   0.000   0.000   0.000   0.000 0.00000

    0.00   0.00   0.00   0.00   0.00   0.00   0.00

!-------> Profile Parameters for Pattern # 1

! Scale   Shape1   Bov   Str1   Str2   Str3 Strain-Model

 0.32749E-02 0.00000 0.00000 0.00000 0.00000 0.00000   0

   0.00000   0.000   0.000   0.000   0.000   0.000

!   U   V   W   X   Y   GauSiz LorSiz Size-Model

  7.799441 -9.781798 9.338505 0.000000 0.000000 0.000000 0.000000   0

   0.000   0.000   0.000   0.000   0.000   0.000   0.000

!   a   b   c   alpha   beta   gamma   #Cell Info

 10.603503 10.603503 10.603503 90.000000 90.000000 90.000000

  0.00000   0.00000   0.00000   0.00000   0.00000   0.00000

! Pref1   Pref2   Asy1   Asy2   Asy3   Asy4

 0.00000 0.00000 0.00000 0.00000 0.00000 0.00000

```
   0.00    0.00    0.00    0.00    0.00    0.00
```

! Propagation vectors:

```
  0.0000000  0.0000000  0.0000000       Propagation Vector  1
   0.000000   0.000000   0.000000
```

! 2Th1/TOF1   2Th2/TOF2 Pattern to plot

```
    18.540    121.520      1
```

G. Glossary

Symbol	Definition
AFM	Antiferromagnetic
AIAO	All-in-all-out spin configuration in alternating tetrahedra
a_d	Distance between two nearby tetrahedral center
a_{latt}	Lattice constant of the conventional cubic cell
$\boldsymbol{B_i}$	Lattice vector field mapped
$\{B_{mf}^{\mathrm{Ir}}, B_{mf,\parallel}^{\mathrm{Ir}}, B_{mf,\perp}^{\mathrm{Ir}}\}$	Molecular magnetic field and its two components along and perpendicular to the local $\langle 1\,1\,1 \rangle$ axis
B_n^m	CEF parameters
BVs	Basis vectors
BZ	Brillouin Zone
b_j	Scattering length of atom j
bg	Background
C_{CEF}	Specific heat of crystal-electric field contribution
C_{exp}	Measured specific heat
C_{latt}	Specific heat of lattice contribution
C_{mag}	Specific heat of magnetic contribution (magnetic moment from unpaired electrons)
C_{nuc}	Specific heat of nuclear contribution
C_p	Specific heat under constant pressure
C_{Sch}	Specific heat of Schottky anomaly
$C(E)$	Detector efficiency
CEF	Crystal electric field
CSI	Classical spin-ice
CW	Curie-Weiss
CR_0	Instrument resolution volume (normalization factor)
$\{\hat{c}_{i\alpha}, \hat{c}_{i\alpha}^{\dagger}\}$	Annihilation and its conjugate operator for an electron in orbital α at site i
DSI	Dipolar spin ice
D	Dipolar interaction constant
D_{nn}	Effective dipolar interaction constant between nearest neighbor spins
DHO	Damped harmonic oscillator function
$\hat{\boldsymbol{d}}_{ij}$	Unit vector of the Dzyaloshinskii-Moriya coupling
d_{hkl}	Distance between the parallel lattice plans with Miller indices (hkl)
E_i^{ie}	The i-th inelastic peak position

Appendices

$\{e_g, t_{2g}\}$	Doublet and triplet states of the d orbital band due to the octahedral CEF effect
$\{E_{\alpha i}, E_{\alpha f}\}$	Initial and finial energy of the sample in a neutron scattering experiment
FC	Field-cooling process (an external magnetic field is applied during system cooling)
FM	Ferromagnetic
FWHM	Full-width at half maximum of the peak
$\boldsymbol{F}_{mag}$	Magnetic vector structure factor
$F_{mag}^{\perp}$	Magnetic vector structure factor component perpendicular to $\boldsymbol{Q}$
F_{nuc}	Nuclear structure factor
f	Frustration index
$f(Q)$	Dimensionless magnetic form factor (depends on the magnetic ion)
$G(\theta_i)$	Peak shape function
GS	Ground state
g_J	Lande factor: $= \frac{2}{3} + \frac{S(S+1)-L(L+1)}{2J(J+1)}$
$\{g_\parallel, g_\perp\}$	Longitudinal and transverse spectroscopic factor
$\mathcal{H}_{CEF}$	The crystal-electric field Hamiltonian
$\mathcal{H}_{CSI}$	Classical spin ice Hamiltonian (involving only longitudinal exchange interaction)
$\mathcal{H}_{DB}$	Hamiltonian of the dumbbell model in the dipolar spin-ice
$\mathcal{H}_{eff-1/2}$	Anisotropic effective spin-1/2 Hamiltonian
$\mathcal{H}_{ex}$	Hamiltonian for the effective exchange couplings between the nearest neighbors in one tetrahedron
$\mathcal{H}_{Heisenberg}$	Heisenberg Hamiltonian
$\mathcal{H}_{Ising,AFM}$	Ising antiferromagnetic Hamiltonian in pyrochlore lattice considered by Anderson
$\mathcal{H}_{\mathcal{J}_1-\mathcal{J}_2}$	Hamiltonian for the $\mathcal{J}_1 - \mathcal{J}_2$ Ising model on a square lattice
$\mathcal{H}_{SO}$	Hamiltonian for the spin-orbit coupling
$\mathcal{H}_{XXZ}$	Quantum spin-ice Hamiltonian (XXZ model)
$\mathcal{H}_\perp$	Transverse exchange Hamiltonian (in XXZ model)
H	Applied magnetic field
$\hbar$	Reduced Plank constant
$\hbar\omega$	Energy transfer of neutrons in neutron scattering experiment
I	Insulator
$I(2\theta, t)$	Data form (intensity *vs* scattering angle and time) taken from TOF spectrometer.
$I(Q, E)$	INS data format (intensity *vs* scattering vector and energy transfer) with absolute units (barn/sr/meV/f.u.)

$I(Q)$	Intensity as function of Q
$I_{raw}(Q,E)$	INS data format (intensity *vs* scattering vector and energy transfer) with arbitrary unit
I_c	Superconducting critical current
$\{I_i^{cal}, I_i^{obs}\}$	Calculated and observed intensities in x-ray or neutron powder diffraction
INS	Inelastic neutron scattering
IR	Irreducible representation
IRF	Instrument resolution function/elastic line of $I(Q,E)$
$\mathcal{J}$	Exchange coupling constant
$\mathcal{J}_{DM}$	Dzyaloshinskii-Moriya interaction constant
$\mathcal{J}_{eff}$	Effective exchange coupling constant in DSI model
$\mathcal{J}_{iso}$	Isotropic exchange coupling constant
$\mathcal{J}_{nn}$	Exchange coupling constant between nearest neighbor spins
$\mathcal{J}_{pd}$	Pseudo-dipolar exchange coupling constant
$\mathcal{J}_{zz}$	Longitudinal exchange coupling constant in QSI model
$\mathcal{J}_{\pm}$	Transverse exchange coupling constant in QSI model
$\{\mathcal{J}_{zz}, \mathcal{J}_{\pm}, \mathcal{J}_{\pm\pm}, \mathcal{J}_{z\pm}\}$	Anisotropic exchange constants involved in $\mathcal{H}_{eff-1/2}$
$\hat{J}$	Total angular momentum operator
$\{\hat{J}_x, \hat{J}_y, \hat{J}_z\}$	x, y and z components of the total angular momentum operator
$\hat{J}_{\pm}$	Raising and lowering total angular momentum operators
J	Total angular momentum quantum number
J_{eff}	Effective total angular momentum quantum number
$\hat{L}$	Total orbital angular momentum operator
L	Total orbital angular momentum quantum number
$\{K_p, K_s\}$	Thermal conductance between the cryostat and the micro-calorimeter platform, and between the sample and the micro-calorimeter platform, respectively.
$\{\mathbf{k}_i, \mathbf{k}_f\}$	Incident and outgoing wavevectors of neutrons in a neutron scattering experiment
$\mathbf{k}_{mag}$	Magnetic propagation wavevector
LSWT	Linear spin wave theory
$L(\theta_i)$	Lorentz factor
M	Measured magnetization
M	Metal
M_{Ir}^{eff}	Net moment of Ir^{4+} parallel to the local $\langle 1\,1\,1 \rangle$ direction
MIT	Metal to inrulator transition
m	Neutron mass
m_{hkl}	Multiplicity of the Bragg reflection ($h\,k\,l$)

$\boldsymbol{m}_j$	Magnetic moment at site j
N	Number of nuclei or magnetic ions in the system
N_{mag}	Number of magnetic cells
N_{nuc}	Number of unit cells in the system
NPD	Neutron powder diffraction
$n_{i\alpha}$	Occupation number in orbital α at site i
nsf	Non-spin-flip
$\hat{O}_n^m$	Stevens operators
$P(t)$	Heating power
PC	Palmer-Chalker states
p	Magnetic scattering length per μ_B
p_{α_i}	Thermal population factor of the sample initial state $|\alpha_i\rangle$
p_{σ_i}	Polarization probability of the incident neutrons
$\boldsymbol{Q}$	Scattering vector
$\widehat{\boldsymbol{Q}}$	Scattering vector with unit length
QENS	Quasielastic neutron scattering
QSI	Quantum spin ice
QSL	Quantum spin liquid
q_m	Magnetic charge arising from the fragmentation of the magnetic moment
Q_α	Total magnetic monopole charge in a tetrahedron α
RVB	Resonating valence bond
RXS	Resonant x-ray scattering
$\boldsymbol{r}_{ij}$	Vector linking sites i and j
$\hat{\boldsymbol{r}}_{ij}$	Unit vector linking sites i and j
r_{nn}	Nearest neighbor distance between Ln^{3+} in pyrochlore lattice
$\hat{S}$	Total spin angular momentum operator
$\left\{\hat{S}_i^{x'}, \hat{S}_i^{y'}, \hat{S}_i^{z'}\right\}$	x, y and z components of the spin operators in the local coordinate system.
$\left\{\hat{S}_i^{+'}, \hat{S}_j^{-'}\right\}$	Raising and lowering spin operators in the local coordinate system
S	Total spin angular momentum quantum number
$\boldsymbol{S}(S^x, S^y, S^z)$	Classical spin treated as three dimensional vector
$S(\boldsymbol{Q}, \omega)$	Dynamic (nuclear) structure factor (or scattering function),
$S^{\alpha\beta}(\boldsymbol{Q}, \omega)$	Dynamic magnetic structure factor (or magnetic scattering function)
S_{CSI}	Pauling's residual entropy for water ice and spin ice
S_{mag}	Magnetic entropy
S_{PM}	Magnetic entropy of the paramagnetic state for spin-1/2 system
S_t	Total effective Ising spin per tetrahedron

SM	Semimetal
SOC	Spin-orbit coupling
sf	Spin-flip
$\{T_{bath}, T_p, T_s\}$	temperature of the cryostat, the platform and sample
T_c	Curie temperature for ferromagnetic ordering
T_h	Temperature at the magnetic specific heat hump maximum
T_{MI}	Metal-to-insulator transition temperature
T_N	Neel temperature for antiferromagnetic ordering
T_{tran}	Magnetic phase transition temperature
TI	Topolotical insulator
TRS	Time-reversal symmetry
U	Coulomb interaction/Hubbard repulsion potential
$\hat{U}$	Interaction operator between neutron and the sample
v_0	Unit cell volume
v_{mag}	Magnetic cell volume
WSM	Weyl semimetal
XRPD	X-ray powder diffraction
$\{x, y, z\}$	Global coordinate system based on the simple cubic coordinate system
$\{x', y', z'\}$	Local coordinate system based on the tetrahedron
$\{\tilde{x}, \tilde{y}, \tilde{z}\}$	Rotated local coordinate system in the (x', z') plane
ZFC	Zero-field cooling process (no external magnetic field is applied during system cooling)
α	"Schärpf angle", between the scattering vector and the x axis
$\{\lvert\alpha_i\rangle, \lvert\alpha_f\rangle\}$	Initial and final states of the sample in a neutron scattering experiment
χ	DC magnetic susceptibility
χ^2	Factor to minimized in the Rietveld refinement
$\delta(x)$	Dirac delta function
Δ_Z	Zeeman splitting energy
Δ_C	Estimated excitation level associated to T_h based the two levels assumption
μ	Magnetic moment per spin
μ_B	Electronic Bohr magneton,
μ_{CEF}	Effective magnetic moment of the ion under CEF condition.
μ_{eff}	Effective magnetic moment obtained from CW fitting of the DC susceptibility.
μ_{free}	Magnetic moment of the fre ion
$\hat{\boldsymbol{\mu}}$	Magnetic moment operator of the neutron

Appendices

$\hat{\boldsymbol{\sigma}}$	Pauli spin operator
μSR	Muon spin rotation/relaxation
2θ	Scattering angle
θ_{CW}	Curie-Weiss temperature
$\{\boldsymbol{\sigma}_i, \boldsymbol{\sigma}_f\}$	Spin states of the incident and outgoing neutrons
λ	Wavelength of the used radiation (x-ray or neutron)
λ_{SO}	Spin-orbit coupling constant
$\phi_0^{\pm}$	Wavefunction of the single ion ground state under CEF
γ	Gyromagnetic ratio
$\boldsymbol{\tau}$	Reciprocal lattice vector
$\{\tau^{x'}, \tau^{y'}, \tau^{z'}\}$	Pseudo-spin components in the local coordinate system
$\{\tilde{\tau}^{\tilde{x}}, \tilde{\tau}^{\tilde{y}}, \tilde{\tau}^{\tilde{z}}\}$	Pseudo-spin components in the rotated local coordinate system
Γ_n	The n-th CEF state/Irreducible representation label/FWHM of the inelastic peak
$\dfrac{d^2\sigma}{d\Omega d\omega}$	Partial (or double) differential cross section
$\dfrac{d\sigma}{d\Omega}$	Single differential cross section
$\dfrac{d\sigma}{d\Omega}\Big|_{coh}$	Single differential cross section of the coherent scattering
$\dfrac{d\sigma^{el}}{d\Omega_{inc}}$	cross section for the incoherent elastic scattering
$\left\{\dfrac{d\sigma}{d\Omega}\Big|_{mag}, \dfrac{d\sigma}{d\Omega}\Big|_{si}, \dfrac{d\sigma}{d\Omega}\Big|_{nuc}\right\}$	Magnetic, spin-incoherent and nuclear cross section
$\left\{\dfrac{d\sigma}{d\Omega}\Big|_x^{nsf}, \dfrac{d\sigma}{d\Omega}\Big|_x^{nsf}, \dfrac{d\sigma}{d\Omega}\Big|_x^{nsf}\right\}$	Non-spin-flip cross section for the incident neutrons with x, y and z polarization
$\left\{\dfrac{d\sigma}{d\Omega}\Big|_x^{sf}, \dfrac{d\sigma}{d\Omega}\Big|_x^{sf}, \dfrac{d\sigma}{d\Omega}\Big|_x^{sf}\right\}$	Spin-flip cross section for the incident neutrons with x, y and z polarization

Samples

NHO	$Nd_2Hf_2O_7$	DIO	$Dy_2Ir_2O_7$
LHO	$La_2Hf_2O_7$	HIO	$Ho_2Ir_2O_7$
PHO	$Pr_2Hf_2O_7$	EIO	$Er_2Ir_2O_7$
PIO	$Pr_2Ir_2O_7$	YbIO	$Yb_2Ir_2O_7$
NIO	$Nd_2Ir_2O_7$	YIO	$Y_2Ir_2O_7$
TIO	$Tb_2Ir_2O_7$		

Bibliography

[1] P. W. Anderson, *Science* **177**, 393 (1972).

[2] B. J. Kim *et al.*, *Physical Review Letters* **101**, 076402 (2008).

[3] W. Witczak-Krempa, G. Chen, Y. B. Kim, and L. Balents, *Annual Review of Condensed Matter Physics.* **5**, 57 (2014).

[4] S. T. Bramwell and M. J. P. Gingras, *Science* **294**, 1495 (2001).

[5] C. Castelnovo, R. Moessner, and S. L. Sondhi, *Nature* **451**, 42 (2008).

[6] S. Blundell, *Magnetism in condensed matter* (Oxford Univ. Press, 2001).

[7] J. Vannimenus and G. Toulouse, *Journal of Physics C: Solid State Physics* **10**, L537 (1977).

[8] J. Villain, *Journal of Physics C: Solid State Physics* **10**, 1717 (1977).

[9] R. M. F. Houtappel, *Physica* **16**, 425 (1950).

[10] G. H. Wannier, *Physical Review* **79**, 357 (1950).

[11] Y. Yafet and C. Kittel, *Physical Review* **87**, 290 (1952).

[12] P. W. Anderson, *Physical Review* **102**, 1008 (1956).

[13] G. Misguich and C. Lhuillier, *Frustrated spin systems*, 981 (2005).

[14] A. Kalz, A. Honecker, S. Fuchs, and T. Pruschke, *The European Physical Journal B* **65**, 533 (2008).

[15] A. I. Guerrero, D. A. Stariolo, and N. G. Almarza, *Physical Review E* **91**, 052123 (2015).

[16] L. Balents, *Nature* **464**, 199 (2010).

[17] A. Ramirez, *Annual Review of Materials Science* **24**, 453 (1994).

[18] C. Lhuillier and G. Misguich, *Introduction to Quantum Spin Liquids*, in *Introduction to Frustrated Magnetism: Materials, Experiments, Theory*, edited by C. Lacroix, P. Mendels, and F. Mila (Springer Berlin Heidelberg, Berlin, Heidelberg, 2011), pp. 23.

[19] G. Misguich, *Quantum Spin Liquids and Fractionalization*, in *Introduction to Frustrated Magnetism: Materials, Experiments, Theory*, edited by C. Lacroix, P. Mendels, and F. Mila (Springer Berlin Heidelberg, Berlin, Heidelberg, 2011), pp. 407.

[20] R. Moessner and S. L. Sondhi, *Physical Review B* **68**, 184512 (2003).

[21] S. Lucile and B. Leon, *Reports on Progress in Physics* **80**, 016502 (2017).

[22] Y. Zhou, K. Kanoda, and T.-K. Ng, *Reviews of Modern Physics* **89**, 025003 (2017).

[23] K. A. Ross, L. Savary, B. D. Gaulin, and L. Balents, *Physical Review X* **1**, 021002 (2011).

[24] H. Von Gaertner, *Geol. Palaeontol* **61**, 1 (1930).

[25] M. A. Subramanian, G. Aravamudan, and G. V. Subba Rao, *Progress in Solid State Chemistry* **15**, 55 (1983).

[26] R. Mouta, R. X. Silva, and C. W. A. Paschoal, *Acta Crystallographica Section B-Structural Science* **69**, 439 (2013).

[27] L. Cai, A. L. Arias, and J. C. Nino, *Journal of Materials Chemistry* **21**, 3611 (2011).

[28] M. Subramanian and A. Sleight, *Handbook on the physics and chemistry of rare earths* **16**, 225 (1993).

[29] R. t. Shannon and C. T. Prewitt, *Acta Crystallographica Section B: Structural Crystallography and Crystal Chemistry* **25**, 925 (1969).

[30] P. E. R. Blanchard, S. Liu, B. J. Kennedy, C. D. Ling, M. Avdeev, J. B. Aitken, B. C. C. Cowie, and A. Tadich, *The Journal of Physical Chemistry C* **117**, 2266 (2013).

[31] J. S. Gardner, M. J. P. Gingras, and J. E. Greedan, *Reviews of Modern Physics* **82**, 53 (2010).

[32] K. W. H. Stevens, *Proceedings of the Physical Society. Section A* **65**, 209 (1952).

[33] A. Princep, D. Prabhakaran, A. Boothroyd, and D. Adroja, *Physical Review B* **88**, 104421 (2013).

[34] J. Xu, V. K. Anand, A. K. Bera, M. Frontzek, D. L. Abernathy, N. Casati, K. Siemensmeyer, and B. Lake, *Physical Review B* **92**, 224430 (2015).

[35] A. J. Princep, H. C. Walker, D. T. Adroja, D. Prabhakaran, and A. T. Boothroyd, *Physical Review B* **91**, 8, 224430 (2015).

[36] A. Bertin, Y. Chapuis, P. D. de Reotier, and A. Yaouanc, *Journal of Physics-Condensed Matter* **24**, 6, 256003 (2012).

[37] A. M. H. J. Gaudet, A. I. Kolesnikov, B. D. Gaulin, *arxiv:1708.01176* (2017).

[38] J. Gaudet, D. D. Maharaj, G. Sala, E. Kermarrec, K. A. Ross, H. A. Dabkowska, A. I. Kolesnikov, G. E. Granroth, and B. D. Gaulin, *Physical Review B* **92**, 134420 (2015).

[39] A. Yaouanc *et al.*, *Physical Review Letters* **110**, 127207 (2013).

[40] S. E. Palmer and J. T. Chalker, *Physical Review B* **62**, 488 (2000).

[41] S. Guitteny, S. Petit, E. Lhotel, J. Robert, P. Bonville, A. Forget, and I. Mirebeau, *Physical Review B* **88**, 134408 (2013).

[42] S. Onoda and Y. Tanaka, *Physical Review B* **83**, 094411 (2011).

[43] O. Shigeki, *Journal of Physics: Conference Series* **320**, 012065 (2011).

[44] Y.-P. Huang, G. Chen, and M. Hermele, *Physical Review Letters* **112**, 167203 (2014).

[45] L. Savary and L. Balents, *Physical Review Letters* **118**, 087203 (2017).

[46] A. A. Biswas and Y. Jana, *Proceedings of the 54th DAE solid state physics symposium.* 1013 (2009).

[47] N. P. Raju, M. Dion, M. J. P. Gingras, T. E. Mason, and J. E. Greedan, *Physical Review B* **59**, 14489 (1999).

[48] R. Moessner and J. T. Chalker, *Physical Review B* **58**, 12049 (1998).

[49] B. Canals and C. Lacroix, *Physical Review B* **61**, 1149 (2000).

[50] B. Canals and C. Lacroix, *Physical Review Letters* **80**, 2933 (1998).

[51] J. D. M. Champion, A. S. Wills, T. Fennell, S. T. Bramwell, J. S. Gardner, and M. A. Green, *Physical Review B* **64**, 140407 (2001).

[52] J. R. Stewart, G. Ehlers, A. S. Wills, S. T. Bramwell, and J. S. Gardner, *Journal of Physics: Condensed Matter* **16**, L321 (2004).

[53] P. Bonville, J. A. Hodges, M. Ocio, J. P. Sanchez, P. Vulliet, S. Sosin, and D. Braithwaite, *Journal of Physics: Condensed Matter* **15**, 7777 (2003).

[54] A. S. Wills, M. E. Zhitomirsky, B. Canals, J P. Sanchez, P. Bonville, P. D. d. Réotier, and A. Yaouanc, *Journal of Physics: Condensed Matter* **18**, L37 (2006).

[55] M. J. Harris, S. T. Bramwell, D. F. McMorrow, T. Zeiske, and K. W. Godfrey, *Physical Review Letters* **79**, 2554 (1997).

[56] J. D. Bernal and R. H. Fowler, *The Journal of Chemical Physics* **1**, 515 (1933).

[57] L. D. C. Jaubert and P. C. W. Holdsworth, *Journal of Physics: Condensed Matter* **23**, 164222 (2011).

[58] R. Moessner, *Physical Review B* **57**, R5587 (1998).

[59] A. A. Zvyagin, *Low Temperature Physics* **39**, 901 (2013).

[60] C. L. Henley, *Annual Review of Condensed Matter Physics* **1,** 179 (2010).

[61] A. P. Ramirez, A. Hayashi, R. J. Cava, R. Siddharthan, and B. S. Shastry, *Nature* **399**, 333 (1999).

[62] K. Matsuhira, Y. Hinatsu, K. Tenya, H. Amitsuka, and T. Sakakibara, *Journal of the Physical Society of Japan* **71**, 1576 (2002).

[63] S. T. Bramwell and M. J. Harris, *Journal of Physics: Condensed Matter* **10**, L215 (1998).

[64] B. C. den Hertog and M. J. P. Gingras, *Physical Review Letters* **84**, 3430 (2000).

[65] G. M. Roger and J. P. G. Michel, *Journal of Physics: Condensed Matter* **16**, R1277 (2004).

[66] T. Fennell, P. P. Deen, A. R. Wildes, K. Schmalzl, D. Prabhakaran, A. T. Boothroyd, R. J. Aldus, D. F. McMorrow, and S. T. Bramwell, *Science* **326**, 415 (2009).

[67] H. Kadowaki, Y. Ishii, K. Matsuhira, and Y. Hinatsu, *Physical Review B* **65**, 144421 (2002).

[68] K. Matsuhira, Y. Hinatsu, K. Tenya, and T. Sakakibara, *Journal of Physics: Condensed Matter* **12**, L649 (2000).

[69] X. Ke, B. G. Ueland, D. V. West, M. L. Dahlberg, R. J. Cava, and P. Schiffer, *Physical Review B* **76**, 214413 (2007).

[70] H. D. Zhou *et al.*, *Nature Communications* **2**, 478 (2011).

[71] H. D. Zhou *et al.*, *Physical Review Letters* **108**, 207206 (2012).

[72] A. M. Hallas *et al.*, *Physical Review B* **86**, 134431 (2012).

[73] I. A. Ryzhkin, *Journal of Experimental and Theoretical Physics* **101**, 481 (2005).

[74] C. Castelnovo, R. Moessner, and S. L. Sondhi, *Annual Review of Condensed Matter Physics* **3,** 35 (2012).

[75] D. J. P. Morris *et al.*, *Science* **326**, 411 (2009).

[76] L. D. C. Jaubert and P. C. W. Holdsworth, *Nature Physcis* **5**, 258 (2009).

[77] K. K. K. Franziska, Felix Flicker, Amir Yacoby, Norman Y. Yao, Stephen J. Blundell, *arxiv 1711.00408* (2017).

[78] C. L. Henley, *Physical Review B* **71**, 014424 (2005).

[79] C. Paulsen, S. R. Giblin, E. Lhotel, D. Prabhakaran, G. Balakrishnan, K. Matsuhira, and S. T. Bramwell, *Nature Physics* **12**, 661 (2016).

[80] M. Hermele, M. P. A. Fisher, and L. Balents, *Physical Review B* **69**, 064404 (2004).

[81] M. J. P. Gingras and P. A. McClarty, *Reports on Progress in Physics* **77**, 056501 (2014).

[82] N. Shannon, O. Sikora, F. Pollmann, K. Penc, and P. Fulde, *Physical Review Letters* **108**, 067204 (2012).

[83] O. Benton, O. Sikora, and N. Shannon, *Physical Review B* **86**, 075154 (2012).

[84] M. Taillefumier, O. Benton, H. Yan, L. D. C. Jaubert, and N. Shannon, *Physical Review X* **7**, 041057 (2017).

[85] D. I. Khomskii, *Nature Communication* **3**, 904 (2012).

[86] S. Lee, S. Onoda, and L. Balents, *Physical Review B* **86**, 104412 (2012).

[87] S. H. Curnoe, *Physical Review B* **78**, 094418 (2008).

[88] B. Canals, M. Elhajal, and C. Lacroix, *Physical Review B* **78**, 214431 (2008).

[89] L. Savary and L. Balents, *Physical Review Letters* **108**, 037202 (2012).

[90] L. Savary and L. Balents, *Physical Review B* **87**, 205130 (2013).

[91] T. Fennell, *Collection SFN* **13,** 02004 (2014).

[92] H. R. Molavian, M. J. P. Gingras, and B. Canals, *Physical Review Letters* **98**, 4, 157204 (2007).

[93] T. Hiroshi, K. Hiroaki, J. S. Taku, W. L. Jeffrey, T. Yoshikazu, Y. Teruo, and M. Kazuyuki, *Journal of Physics: Condensed Matter* **24**, 052201 (2012).

[94] V. Peçanha-Antonio *et al.*, *Physical Review B* **96**, 214415 (2017).

[95] H. D. Zhou, C. R. Wiebe, J. A. Janik, L. Balicas, Y. J. Yo, Y. Qiu, J. R. D. Copley, and J. S. Gardner, *Physical Review Letters* **101**, 227204 (2008).

[96] K. Kimura, S. Nakatsuji, J. J. Wen, C. Broholm, M. B. Stone, E. Nishibori, and H. Sawa, *Nature Communications* **4**, 1934 (2013).

[97] R. Sibille, E. Lhotel, M. C. Hatnean, G. Balakrishnan, B. Fåk, N. Gauthier, T. Fennell, and M. Kenzelmann, *Physical Review B* **94**, 024436 (2016).

[98] L.-J. Chang, S. Onoda, Y. Su, Y.-J. Kao, K.-D. Tsuei, Y. Yasui, K. Kakurai, and M. R. Lees, *Nature Communications* **3**, 992 (2012).

[99] A. Poole, A. S. Wills, and E. Lelièvre-Berna, *Journal of Physics: Condensed Matter* **19**, 452201 (2007).

[100] S. Petit, E. Lhotel, F. Damay, P. Boutrouille, A. Forget, and D. Colson, *Physical Review Letters* **119**, 187202 (2017).

[101] Z. L. Dun *et al.*, *Physical Review B* **92**, 140407 (2015).

[102] A. M. Hallas, J. Gaudet, N. P. Butch, G. Xu, M. Tachibana, C. R. Wiebe, G. M. Luke, and B. D. Gaulin, *Physical Review Letters* **119**, 187201 (2017).

[103] Y. Q. Cai *et al.*, *Physical Review B* **93**, 014443 (2016).

[104] H. Yan, O. Benton, L. Jaubert, and N. Shannon, *Physical Review B* **95**, 094422 (2017).

[105] A. M. Hallas, J. Gaudet, and B. D. Gaulin, *Annual Review of Condensed Matter Physics* **9**, 105 (2018).

[106] S. Petit, J. Robert, S. Guitteny, P. Bonville, C. Decorse, J. Ollivier, H. Mutka, M. J. P. Gingras, and I. Mirebeau, *Physical Review B* **90**, 5, 060410 (2014).

[107] J. Oitmaa, R. R. P. Singh, B. Javanparast, A. G. R. Day, B. V. Bagheri, and M. J. P. Gingras, *Physical Review B* **88**, 220404 (2013).

[108] P. Fazekas, *Lecture notes on electron correlation and magnetism* (World Scientific, 1999).

[109] D. Pesin and L. Balents, *Nature Physics* **6**, 376 (2010).

[110] N. F. Mott, *Reviews of Modern Physics* **40**, 677 (1968).

[111] M. Imada, A. Fujimori, and Y. Tokura, *Reviews of Modern Physics* **70**, 1039 (1998).

[112] M. Z. Hasan and C. L. Kane, *Reviews of Modern Physics* **82**, 3045 (2010).

[113] X.-L. Qi and S.-C. Zhang, *Reviews of Modern Physics* **83**, 1057 (2011).

[114] X. Wan, A. M. Turner, A. Vishwanath, and S. Y. Savrasov, *Physical Review B* **83**, 205101 (2011).

[115] B. Yan and C. Felser, *Annual Review of Condensed Matter Physics* **8**, 337 (2017).

[116] G. Jackeli and G. Khaliullin, *Physical Review Letters* **102** (2009).

[117] T. Dey, A. V. Mahajan, P. Khuntia, M. Baenitz, B. Koteswararao, and F. C. Chou, *Physical Review B* **86** (2012).

[118] B. J. Kim, H. Ohsumi, T. Komesu, S. Sakai, T. Morita, H. Takagi, and T. Arima, *Science* **323**, 1329 (2009).

[119] F. Ye, S. Chi, B. C. Chakoumakos, J. A. Fernandez-Baca, T. Qi, and G. Cao, *Physical Review B* **87** (2013).

[120] K. Matsuhira, M. Wakeshima, R. Nakanishi, T. Yamada, A. Nakamura, W. Kawano, S. Takagi, and Y. Hinatsu, *Journal of the Physical Society of Japan* **76**, 3706 (2007).

[121] K. Matsuhira, M. Wakeshima, Y. Hinatsu, and S. Takagi, *Journal of the Physical Society of Japan* **80** (2011).

[122] M. Z. Hasan, S.-Y. Xu, I. Belopolski, and S.-M. Huang, *Annual Review of Condensed Matter Physics* **8**, 289 (2017).

[123] W. Witczak-Krempa and Y. B. Kim, *Physical Review B* **85** (2012).

[124] W. Witczak-Krempa, A. Go, and Y. B. Kim, *Physical Review B* **87**, 155101 (2013).

[125] T. Nobuyuki, W. Makoto, and H. Yukio, *Journal of Physics: Condensed Matter* **13**, 5527 (2001).

[126] S. Zhao, J. M. Mackie, D. E. MacLaughlin, O. O. Bernal, J. J. Ishikawa, Y. Ohta, and S. Nakatsuji, *Physical Review B* **83**, 180402 (2011).

[127] H. Guo, K. Matsuhira, I. Kawasaki, M. Wakeshima, Y. Hinatsu, I. Watanabe, and Z.-a. Xu, *Physical Review B* **88**, 060411 (2013).

[128] S. M. Disseler, *Physical Review B* **89**, 140413 (2014).

[129] H. Sagayama, D. Uematsu, T. Arima, K. Sugimoto, J. J. Ishikawa, E. O'Farrell, and S. Nakatsuji, *Physical Review B* **87**, 100403 (2013).

[130] C. Donnerer *et al.*, *Physical Review Letters* **117**, 037201 (2016).

[131] K. Tomiyasu et al., *Journal of the Physical Society of Japan* **81,** 034709 (2012).

[132] H. Guo, C. Ritter, and A. C. Komarek, *Physical Review B* **94**, 161102 (2016).

[133] M. C. Shapiro, S. C. Riggs, M. B. Stone, C. R. de la Cruz, S. Chi, A. A. Podlesnyak, and I. R. Fisher, *Physical Review B* **85** (2012).

[134] E. Lefrançois *et al.*, *Physical Review Letters* **114**, 247202 (2015).

[135] Z. Tian, Y. Kohama, T. Tomita, H. Ishizuka, T. H. Hsieh, J. J. Ishikawa, K. Kindo, L. Balents, and S. Nakatsuji, *Nature Physics* **12**, 134 (2016).

[136] L. Savary, E.-G. Moon, and L. Balents, *Physical Review X* **4**, 041027 (2014).

[137] G. Chen and M. Hermele, *Physical Review B* **86**, 235129 (2012).

[138] K. Ueda, J. Fujioka, Y. Takahashi, T. Suzuki, S. Ishiwata, Y. Taguchi, M. Kawasaki, and Y. Tokura, *Physical Review B* **89**, 075127 (2014).

[139] K. Ueda, J. Fujioka, B. J. Yang, J. Shiogai, A. Tsukazaki, S. Nakamura, S. Awaji, N. Nagaosa, and Y. Tokura, *Physical Review Letters* **115**, 056402 (2015).

[140] Y. Kamihara, T. Watanabe, M. Hirano, and H. Hosono, *Journal of the American Chemical Society* **130**, 3296 (2008).

[141] R. Xu and Q. Su, *High-temperature Synthesis*, in *Modern Inorganic Synthetic Chemistry* (Elsevier, Amsterdam, 2011), pp. 9.

[142] D. Yanagishima and Y. Maeno, *Journal of the Physical Society of Japan* **70**, 2880 (2001).

[143] J. N. Millican, R. T. Macaluso, S. Nakatsuji, Y. Machida, Y. Maeno, and J. Y. Chan, *Materials Research Bulletin* **42**, 928 (2007).

[144] J. F. Niven, M. B. Johnson, A. Bourque, P. J. Murray, D. D. James, H. A. Dąbkowska, B. D. Gaulin, and M. A. White, *Proceedings of the Royal Society of London A: Mathematical, Physical and Engineering Sciences* **470,** 0387 (2014).

[145] H. Tsujii, B. Andraka, K. A. Muttalib, and Y. Takano, *Physica B: Condensed Matter* **329**, 1552 (2003).

[146] T. Brückel, D. Richter, G. Roth, and R. Zorn, *Applications of Neutron Scattering - an Overview*, in *Lectures of the JCNS Laboratory Course Neutron Scattering* (Forschungszentrum Juelich GmbH, 2014).

[147] G. L. Squires, *Introduction to the theory of thermal neutron scattering* (Cambridge University press, 2012).

[148] G. Shirane, S. M. Shapiro, and J. M. Tranquada, *Neutron scattering with a triple-axis spectrometer: basic techniques* (Cambridge University Press, 2002).

[149] M. Hoelzel, A. Senyshyn, and O. Dolotko, *Journal of large-scale research facilities JLSRF* **1**, 5 (2015).

[150] P. Fischer *et al.*, *Physica B: Condensed Matter* **276**, 146 (2000).

[151] J. Rodríguez-Carvajal, *Physica B: Condensed Matter* **192**, 55 (1993).

[152] J. R. D. Copley and T. J. Udovic, *Journal of Research of the National Institute of Standards and Technology* **98,** 71 (1993).

[153] T. Unruh, J. Neuhaus, and W. Petry, *Nuclear Instruments and Methods in Physics Research Section A: Accelerators, Spectrometers, Detectors and Associated Equipment* **580**, 1414 (2007).

[154] M. Blume, *Physical Review* **130**, 1670 (1963).

[155] O. Halpern and M. H. Johnson, *Physical Review* **55**, 898 (1939).

[156] O. Schärpf and H. Capellmann, *physica status solidi (a)* **135**, 359 (1993).

[157] J. R. Stewart, P. P. Deen, K. H. Andersen, H. Schober, J.-F. Barthelemy, J. M. Hillier, A. P. Murani, T. Hayes, and B. Lindenau, *Journal of Applied Crystallography* **42**, 69 (2009).

[158] K. Kenta, O. Yasuo, and N. Satoru, *Journal of Physics: Conference Series* **320**, 012079 (2011).

[159] S. M. Disseler, C. Dhital, A. Amato, S. R. Giblin, C. de la Cruz, S. D. Wilson, and M. J. Graf, *Physical Review B* **86**, 014428 (2012).

[160] E. Lefrançois *et al.*, *Nature Communications* **8**, 209 (2017).

[161] B. J. Kennedy, B. A. Hunter, and C. J. Howard, *Journal of Solid State Chemistry* **130**, 58 (1997).

[162] H. J. Koo, M. H. Whangbo, and B. J. Kennedy, *Journal of Solid State Chemistry* **136**, 269 (1998).

[163] J. J. Ishikawa, E. C. T. O'Farrell, and S. Nakatsuji, *Physical Review B* **85,** 205104 (2012).

[164] W. K. Zhu, M. Wang, B. Seradjeh, F. Yang, and S. X. Zhang, *Physical Review B* **90,** 054419 (2014).

[165] T.-h. Arima, *Journal of the Physical Society of Japan* **82**, 013705 (2013).

[166] S. Tardif, S. Takeshita, H. Ohsumi, J.-i. Yamaura, D. Okuyama, Z. Hiroi, M. Takata, and T.-h. Arima, *Physical Review Letters* **114**, 147205 (2015).

[167] S. M. Disseler, S. R. Giblin, C. Dhital, K. C. Lukas, S. D. Wilson, and M. J. Graf, *Physical Review B* **87**, 060403 (2013).

[168] S. M. Disseler, C. Dhital, T. C. Hogan, A. Amato, S. R. Giblin, C. de la Cruz, A. Daoud-Aladine, S. D. Wilson, and M. J. Graf, *Physical Review B* **85**, 174441 (2012).

[169] S. T. Bramwell, M. N. Field, M. J. Harris, and I. P. Parkin, *Journal of Physics: Condensed Matter* **12**, 483 (2000).

[170] V. K. Anand and D. C. Johnston, *Physical Review B* **91**, 184403 (2015).

[171] H. W. J. Blöte, R. F. Wielinga, and W. J. Huiskamp, *Physica* **43**, 549 (1969).

[172] A. Tari, *The specific heat of matter at low temperatures* (Imperial Coll., 2003).

[173] S. Nandi *et al.*, *Physical Review B* **84**, 054419 (2011).

[174] R. Sachidanandam, T. Yildirim, A. B. Harris, A. Aharony, and O. Entin-Wohlman, *Physical Review B* **56**, 260 (1997).

[175] M. Rams, A. Zarzycki, A. Pikul, and K. Tomala, *Journal of Magnetism and Magnetic Materials* **323**, 1490 (2011).

[176] M. J. P. Gingras, B. C. den Hertog, M. Faucher, J. S. Gardner, S. R. Dunsiger, L. J. Chang, B. D. Gaulin, N. P. Raju, and J. E. Greedan, *Physical Review B* **62**, 6496 (2000).

[177] J. Zhang, K. Fritsch, Z. Hao, B. V. Bagheri, M. J. P. Gingras, G. E. Granroth, P. Jiramongkolchai, R. J. Cava, and B. D. Gaulin, *Physical Review B* **89**, 134410 (2014).

[178] S. Petit *et al.*, *Nature Physics* **12**, 746 (2016).

[179] M. Nakayama *et al.*, *Physical Review Letters* **117**, 056403 (2016).

[180] V. K. Anand *et al.*, *Physical Review B* **94**, 144415 (2016).

[181] S. Petit *et al.*, *Physical Review B* **94**, 165153 (2016).

[182] O. Benton, *arxiv: 1706.09238* (2017).

[183] R. Sibille *et al.*, *arxiv: 1706.03604* (2017).

[184] J. J. Wen *et al.*, *Physical Review Letters* **118**, 107206 (2017).

[185] T. Kondo *et al.*, *Nature Communications* **6**, 10042 (2015).

[186] S. Nakatsuji *et al.*, *Physical Review Letters* **96**, 087204 (2006).

[187] Y. Machida, S. Nakatsuji, Y. Maeno, T. Tayama, T. Sakakibara, and S. Onoda, *Physical Review Letters* **98**, 057203 (2007).

[188] Y. Machida, S. Nakatsuji, S. Onoda, T. Tayama, and T. Sakakibara, *Nature* **463**, 210 (2010).

[189] L. Balicas, S. Nakatsuji, Y. Machida, and S. Onoda, *Physical Review Letters* **106**, 217204 (2011).

[190] A. Ikeda and H. Kawamura, *Journal of the Physical Society of Japan* **77**, 073707 (2008).

[191] S. Onoda and Y. Tanaka, *Physical Review Letters* **105**, 047201 (2010).

[192] M. Udagawa, H. Ishizuka, and Y. Motome, *Physical Review Letters* **108**, 066406 (2012).

[193] H. Ishizuka, M. Udagawa, and Y. Motome, *Journal of the Physical Society of Japan* **81**, 113706 (2012).

[194] D. E. MacLaughlin, Y. Ohta, Y. Machida, S. Nakatsuji, G. M. Luke, K. Ishida, R. H. Heffner, L. Shu, and O. O. Bernal, *Physica B: Condensed Matter* **404**, 667 (2009).

[195] D. E. MacLaughlin, Y. Nambu, Y. Ohta, Y. Machida, S. Nakatsuji, and O. O. Bernal, *Journal of Physics: Conference Series* **225**, 012031 (2010).

[196] Y. Machida, S. Nakatsuji, H. Tonomura, T. Tayama, T. Sakakibara, J. van Duijn, C. Broholm, and Y. Maeno, *Journal of Physics and Chemistry of Solids* **66**, 1435 (2005).

[197] F. R. Foronda, F. Lang, J. S. Möller, T. Lancaster, A. T. Boothroyd, F. L. Pratt, S. R. Giblin, D. Prabhakaran, and S. J. Blundell, *Physical Review Letters* **114**, 017602 (2015).

[198] K. Kimura, Y. Ohta, and S. Nakatsuji, *Journal of Physics: Conference Series* **400**, 032040 (2012).

[199] D. E. MacLaughlin *et al.*, *Physical Review B* **92**, 054432 (2015).

[200] K. Matsuhira, C. Sekine, C. Paulsen, M. Wakeshima, Y. Hinatsu, T. Kitazawa, Y. Kiuchi, Z. Hiroi, and S. Takagi, *Journal of Physics: Conference Series* **145**, 012031 (2009).

[201] S. Lee, A. Paramekanti, and Y. B. Kim, *Physical Review Letters* **111**, 196601 (2013).

[202] H. Fukazawa, R. G. Melko, R. Higashinaka, Y. Maeno, and M. J. P. Gingras, *Physical Review B* **65**, 054410 (2002).

[203] Y. Tokiwa, J. J. Ishikawa, S. Nakatsuji, and P. Gegenwart, *Nature Materials* **13**, 356 (2014).

[204] R. Elliott and K. Stevens, *Proceedings of the Royal Society of London A: Mathematical, Physical and Engineering Sciences* (The Royal Society, 1953), pp. 553.

[205] J. Kondo, *Journal of the Physical Society of Japan* **16**, 1690 (1961).

[206] B. Bleaney, *Journal of Applied Physics* **34**, 1024 (1963).

[207] E. Bertin, P. Bonville, J. P. Bouchaud, J. A. Hodges, J. P. Sanchez, and P. Vulliet, *The European Physical Journal B - Condensed Matter and Complex Systems* **27**, 347 (2002).

[208] A. T. Boothroyd, *Spectre - a program for calculating spectroscopic properties of rare earth ions in crystals* (1990-2014).

[209] A. P. Kendig and C. J. Pings, *Journal of Applied Physics* **36**, 1692 (1965).

[210] G. Chen, *Physical Review B* **94**, 205107 (2016).

[211] S. H. Lee, C. Broholm, M. F. Collins, L. Heller, A. P. Ramirez, C. Kloc, E. Bucher, R. W. Erwin, and N. Lacevic, *Physical Review B* **56**, 8091 (1997).

[212] G. Xu, Z. Xu, and J. M. Tranquada, *Review of Scientific Instruments* **84**, 083906 (2013).

[213] T. Brückel, H. Capellmann, W. Just, O. Schärpf, S. Kemmler-Sack, R. Kiemel, and W. Schaefer, *Europhysics Letters* **4**, 1189 (1987).

[214] G. Ehlers, A. L. Cornelius, T. Fennell, M. Koza, S. T. Bramwell, and J. S. Gardner, *Journal of Physics: Condensed Matter* **16**, S635 (2004).

[215] L. R. Yaraskavitch, H. M. Revell, S. Meng, K. A. Ross, H. M. L. Noad, H. A. Dabkowska, B. D. Gaulin, and J. B. Kycia, *Physical Review B* **85**, 020410 (2012).

[216] T. Taniguchi *et al.*, *Physical Review B* **87**, 060408 (2013).

[217] H. Takatsu *et al.*, *Physical Review Letters* **116**, 217201 (2016).

[218] H. Kadowaki, H. Takatsu, T. Taniguchi, B. Fåk, and J. Ollivier, *SPIN* **05**, 1540003 (2015).

[219] G. C. Xu and Ping Yao, *arxiv: 1712.06534* (2017).

[220] A. Abragam and B. Bleaney, *Electron paramagnetic resonance of transition ions* (OUP Oxford, 2012).

[221] O. Benton, *Physical Review B* **94**, 104430 (2016).

[222] A. Bertin *et al.*, *Physical Review B* **92**, 144423 (2015).

[223] E. Lhotel, S. Petit, S. Guitteny, O. Florea, M. Ciomaga Hatnean, C. Colin, E. Ressouche, M. R. Lees, and G. Balakrishnan, *Physical Review Letters* **115**, 197202 (2015).

[224] L. Opherden, J. Hornung, T. Herrmannsdörfer, J. Xu, A. T. M. N. Islam, B. Lake, and J. Wosnitza, *Physical Review B* **95**, 184418 (2017).

[225] V. K. Anand, A. K. Bera, J. Xu, T. Herrmannsdörfer, C. Ritter, and B. Lake, *Physical Review B* **92**, 184418 (2015).

[226] M. E. Brooks-Bartlett, S. T. Banks, L. D. C. Jaubert, A. Harman-Clarke, and P. C. W. Holdsworth, *Physical Review X* **4**, 011007 (2014).

[227] S. V. Isakov, K. Gregor, R. Moessner, and S. L. Sondhi, *Physical Review Letters* **93**, 167204 (2004).

[228] J. Chun, P. G. Reuvekamp, D. Chen, C. Lin, and R. K. Kremer, *Journal of Materials Chemistry C* **3**, 491 (2015).

[229] V. K. Anand, D. L. Abernathy, D. T. Adroja, A. D. Hillier, P. K. Biswas, and B. Lake, *Physical Review B* **95**, 224420 (2017).

[230] K. A. Ross, T. Proffen, H. A. Dabkowska, J. A. Quilliam, L. R. Yaraskavitch, J. B. Kycia, and B. D. Gaulin, *Physical Review B* **86**, 174424 (2012).

[231] A. T. Boothroyd, J. P. Barratt, P. Bonville, P. C. Canfield, A. Murani, A. R. Wildes, and R. I. Bewley, *Physical Review B* **67**, 104407 (2003).

[232] M. T. Hutchings, *Point-Charge Calculations of Energy Levels of Magnetic Ions in Crystalline Electric Fields*, in *Solid State Physics*, edited by S. Frederick, and T. David (Academic Press, 1964), pp. 227.

[233] S. W. Lovesey, *Theory of Neutron scattering from condensed matter* (Clarendon Press, Oxford, 1984).

[234] M. Mourigal, S. Wu, M. B. Stone, J. R. Neilson, J. M. Caron, T. M. McQueen, and C. L. Broholm, *Physical Review Letters* **115**, 047401 (2015).

[235] S. W. Lovesey *Dynamics of Solids and Liquids by Neutron Scattering* (Springer-Verlag, New York, 1977).

[236] J. Snyder, B. G. Ueland, J. S. Slusky, H. Karunadasa, R. J. Cava, A. Mizel, and P. Schiffer, *Physical Review Letters* **91**, 107201 (2003).

[237] D. Pomaranski, L. R. Yaraskavitch, S. Meng, K. A. Ross, H. M. L. Noad, H. A. Dabkowska, B. D. Gaulin, and J. B. Kycia, *Nature Physics* **9**, 353 (2013).

[238] A. B. Sushkov, J. B. Hofmann, G. S. Jenkins, J. Ishikawa, S. Nakatsuji, S. Das Sarma, and H. D. Drew, *Physical Review B* **92**, 241108 (2015).

[239] K. Ueda, J. Fujioka, C. Terakura, and Y. Tokura, *Physical Review B* **92**, 121110 (2015).

[240] S. P. E. Lhotel, M. Ciomaga Hatnean, J. Ollivier, H. Mutka, E. Ressouche, M. R. Lees, G. Balakrishnan, *arxiv: 1712.02418* (2017).

[241] D. E. Bugaris and H.-C. zur Loye, *Angewandte Chemie International Edition* **51**, 3780 (2012).

[242] F. Freund, S. C. Williams, R. D. Johnson, R. Coldea, P. Gegenwart, and A. Jesche, *Scientific Reports* **6**, 35362 (2016).

[243] K. W. Plumb, J. R. Morey, J. A. Rodriguez-Rivera, H. Wu, A. A. Podlesnyak, T. M. McQueen, and C. L. Broholm, *Physical Review X* **6**, 041055 (2016).

[244] M. Watahiki, K. Tomiyasu, K. Matsuhira, K. Iwasa, M. Yokoyama, S. Takagi, M. Wakeshima, and Y. Hinatsu, *Journal of Physics: Conference Series* **320**, 012080 (2011).

[245] S. Rosenkranz, A. P. Ramirez, A. Hayashi, R. J. Cava, R. Siddharthan, and B. S. Shastry, *Journal of Applied Physics* **87**, 5914 (2000).

[246] P. M. Sarte, H. J. Silverstein, B. T. K. Van Wyk, J. S. Gardner, Y. Qiu, H. D. Zhou, and C. R. Wiebe, *Journal of Physics-Condensed Matter* **23**, 5, 382201 (2011).

[247] K. R. A. Ziebeck and P. J. Brown, *Journal of Physics F: Metal Physics* **10**, 2015 (1980).

[248] O. Steinsvoll, C. F. Majkrzak, G. Shirane, and J. Wicksted, *Physical Review B* **30**, 2377 (1984).

[249] E. H. Kisi and C. J. Howard, *Applications of neutron powder diffraction* (Oxford University Press, 2012), Vol. 15.

[250] E. F. Talbot, H. R. Glyde, W. G. Stirling, and E. C. Svensson, *Physical Review B* **38**, 11229 (1988).

Acknowledgements